UNIVERSITY OF ALBERTA

DEVELOPMENT OF A HIGH THROUGHPUT, MULTICAPILLARY DNA SEQUENCER

BY

H. JOHN CRABTREE ©

A thesis submitted to the Faculty of Graduate Studies and Research in partial fulfillment of the requirements for the degree of Doctor of Philosophy

Department of Chemistry

Edmonton, Alberta
Spring, 1997

National Library of Canada
Acquisitions and Bibliographic Services
395 Wellington Street
Ottawa ON K1A 0N4
Canada

Bibliothèque nationale du Canada
Acquisitions et services bibliographiques
395, rue Wellington
Ottawa ON K1A 0N4
Canada

Your file Votre référence

Our file Notre référence

The author has granted a non-exclusive licence allowing the National Library of Canada to reproduce, loan, distribute or sell copies of his/her thesis by any means and in any form or format, making this thesis available to interested persons.

The author retains ownership of the copyright in his/her thesis. Neither the thesis nor substantial extracts from it may be printed or otherwise reproduced with the author's permission.

L'auteur a accordé une licence non exclusive permettant à la Bibliothèque nationale du Canada de reproduire, prêter, distribuer ou vendre des copies de sa thèse de quelque manière et sous quelque forme que ce soit pour mettre des exemplaires de cette thèse à la disposition des personnes intéressées.

L'auteur conserve la propriété du droit d'auteur qui protège sa thèse. Ni la thèse ni des extraits substantiels de celle-ci ne doivent être imprimés ou autrement reproduits sans son autorisation.

0-612-21562-8

Canada

UNIVERSITY OF ALBERTA
LIBRARY RELEASE FORM

Name of Author: H. John Crabtree

Title of Thesis: Development of a High Throughput, Multicapillary DNA Sequencer

Degree: Doctor of Philosophy

Year this Degree Granted: 1997

Permission is hereby granted to the University of Alberta Library to reproduce single copies of this thesis and to lend or sell such copies for private, scholarly, or scientific research purposes only.

The author reserves all other publication and other rights in association with the copyright in the thesis, and except as hereinbefore provided, neither the thesis not any substantial portion thereof may be printed or otherwise reproduced in any material form whatever without the author's prior written permission.

John Crabtree

H. John Crabtree
4-10636-85th Ave.
Edmonton, Alberta
T6E 2K7

Dec 13th, 1996

Date

UNIVERSITY OF ALBERTA
FACULTY OF GRADUATE STUDIES AND RESEARCH

The undersigned certify that they have read, and recommend to the Faculty of Graduate Studies and Research for acceptance, a thesis entitled **Development of a High Throughput, Multicapillary DNA Sequencer** submitted by **H. John Crabtree** in partial fulfillment of the requirements for the degree of **Doctor of Philosophy**.

Dr. N. J. Dovichi

B. Kratochvil
Dr. B. Kratochvil

D. Clive
Dr. D. L. J. Clive

Dr. D. J. Harrison

M Brett
Dr. M. Brett

Michael
Dr. M. Thompson

December 4th, 1996

to my parents

ABSTRACT

A 16 capillary DNA sequencer was built which uses capillary gel electrophoresis and laser-induced fluorescence in a micromachined, multicapillary sheath flow cuvette to separate and detect DNA fragments. A variety of micromachined sheath flow cuvettes housing 1 to 48 capillaries were also built for use in other instruments.

Using the Applied Biosystems (ABI) 4 colour fluorescence detection scheme, the sequencer achieves high sample throughput by separating and detecting the fragments from 16 different DNA samples simultaneously. The sequence of the samples may be interpreted directly from the 16 electropherograms acquired during the separation. Under optimum conditions, the instrument has the potential to produce 8 Mb of raw sequence per year.

The sequencer's fluorescence detection system uses two chopped lasers and a four-colour filter wheel for spectral discrimination of the ABI dyes, stationary imaging optics, a discrete avalanche photodiode detector for each capillary's fluorescent spot in the cuvette, and an elaborate data acquisition system to produce a four spectral channel electropherogram for each capillary's separation. The 3σ detections limits range from 3800 to 23 000 molecules of fluorescein (~ 10^{-11} M).

The micromachined sheath flow cuvette detection cell used in the 16 capillary sequencer was the product of an iterative cuvette designing process. A reproducible microfabrication methodology was developed allowing numerous single and multicapillary cuvettes to be produced. 33 micromachined cuvette features were systematically evaluated, arriving at optimised features for the cuvette integrated into the 16 capillary sequencer. The cuvette yields even and reproducible spacing of the capillaries within, a significant advantage for a

multicapillary sequencer with fixed detection optics. Other cuvettes fabricated are in use in other single and multicapillary instruments used for DNA and protein separations.

ACKNOWLEDGEMENTS

My research greatly benefited from the knowledge, assistance and support of others. I thank all who have helped, and would further like to single out a few individuals whose contributions were substantial.

Norm Dovichi, my supervisor, graced me with his tremendous knowledge of things scientific and, of equal import, his very generous human spirit. I can only *hope* for equally positive, progressive and friendly bosses in the future. Sue Bay was an equal partner in the development and construction of the sequencer presented in Chapter 2, and contributed significantly to the cuvette research of Chapter 3; it has been a real opportunity and pleasure to work closely with such a sharp mind and good friend. Darren Lewis made very significant improvements to our instrument by way of electronic circuitry and data acquisition programming, without which the four colour data would not have been realised; I was the lucky beneficiary of his electronic wizardry, selflessness and cheerful friendship.

For most research, the researcher begins by standing on the shoulders of the giants who preceded him/her, and then taking his/her own steps from that vantage point; this thesis is no exception. In the area of instrument development, Jian Zhong Zhang built the first multicapillary instrument of this group, and his instrument provided both inspiration for, and a standard by which to measure, our own instrument. His kind tutelage in the area of optics is appreciated. As concerns sheath flow cuvette micromachining, I would like to thank Glen Fitzpatrick, Graham M^{c}Kinnon and Tran Tran at the Alberta Microelectronics Centre for their patience in bringing me up to speed with photolithography and other techniques at their facility, and the members of Dr. Jed Harrison's group for their help with glass annealing. I would also like to thank the members of the

machine and electronics shops who converted our concepts (often with refinement) into the working pieces of the sequencer.

Lastly, I would like to thank those whose contribution was moral support. I have made some very good friends in the Northern Lights Laser lab, around the department and university over the last five years; we have shared a lot of laughs, and I hope there are many more to come. I have friends from back home in Ontario whose continued warmth shrank the long distance feeling, if not the bill. And, of course, the members of my family, Mom, Dad, Paul, Rob, San, Carolyn and Dorothy, the purveyors of that crucial staple, unconditional love. I salute you and thank you from the bottom of my heart - I couldn't have done it without you!

John Crabtree
Edmonton, 1996

TABLE OF CONTENTS

CHAPTER 1: INTRODUCTION 1

1.1 Introduction **2**

1.2 Capillary Electrophoresis **3**

1.2.1 Capillary Zone Electrophoresis 3

1.2.1.A Electrophoretic Mobility 5

1.2.1.B Electroosmotic Mobility 7

1.2.1.C Efficiency and Resolution 10

1.2.2 Capillary Gel Electrophoresis 12

1.3 DNA and DNA Sequencing Methods **20**

1.3.1 DNA 20

1.3.1.A Importance of DNA 20

1.3.1.B Structure of DNA 21

1.3.2 DNA Sequencing Methods 25

1.3.2.A Sanger Sequencing Protocol 25

I. Fragment Generation 25

II. Separation of Fragments 31

III. Interpretation of Separation 31

IV. Sequencing Strategies, Accuracy and Redundancy 33

1.3.2.B Modifications to Sanger Sequencing for Fluorescence Detection 37

1.3.2.C Other Sequencing Methods 39

1.4 Sheath Flow Cuvettes and Micromachining **40**

1.4.1 Glass structure and etching 40

1.4.2 Micromachining 43

1.4.2.A Creation of a master mask 44
1.4.2.B Substrate preparation 44
1.4.2.C Application of metal film(s) 46
1.4.2.D Application of photoresist 47
1.4.2.E Exposure 47
1.4.2.F Development 47
1.4.2.G Pattern metal layers 48
1.4.2.H Etch substrate to desired depth 48
1.4.2.I Remove remaining photoresist and metal 48
1.5 Conclusion 48
1.6 References 50
CHAPTER 2: MULTICAPILLARY DNA SEQUENCER 57
2.1 Introduction 58
2.1.1 Instrument Approach 58
2.1.2 GRIN Lenses and Avalanche Photodiodes 62
2.1.2.A GRIN Lenses 62
2.1.2.B Avalanche Photodiodes 64
2.2 Instrument Development 71
2.2.1 General Description of Instrument 71
2.2.2 Separation Apparatus 76
2.2.2.A Capillary Preparation & Gel Pouring 76
2.2.2.B DNA Sample 82
2.2.3 Data Acquisition 83
2.2.3.A 4-Colour Data Encoding 83
2.2.3.B Sequential Data Acquisition 85
2.2.4 Optics 97

2.2.4.A Routine Optical Alignment 100
2.2.4.B GRIN Lens Alignment 103
2.2.4.C Optical Fibre and GRIN Lens Connections 112
2.2.5 Detection Electronics 116
2.2.5.A APD Cooling 116
2.2.5.B APD Biasing 123
2.2.5.C APD Stabilisation 125
2.2.5.D APD Power Supply 125
2.2.5.E Bucking Current 131
2.2.5.F APD Noise and Data Acquisition Mis-Triggering 131
2.2.5.G Low-Pass Filter Performance 135
2.2.5.H Calculation of Low-Pass Filter Cut Off Frequency 140

2.3 Instrument Performance 144

2.3.1 Sensitivity Evaluation 144
2.3.1.A Limits of Detection 145
2.3.1.B S/N Comparison of Linear Vs. Geiger APDs 156
2.3.2 Example of Four-Colour DNA Sequencing 156

2.4 Conclusions 171

2.5 References 172

CHAPTER 3: SHEATH FLOW CUVETTES 174

3.1 Introduction 175

3.2 Experimental 177

3.2.1 Micromachining 177
3.2.1.A Mask 177
3.2.1.B Substrate preparation and metal plating 180
3.2.1.C Photolithography 184

3.2.1.D Etching and Solutions 184
3.2.2 Cuvette Assembly 185
3.2.2.A Cutting 185
3.2.2.B Assembly 186
3.2.2.C Cutting and Polishing 195
3.2.3 Cuvette Testing 195
3.2.3.A Cuvette Holder 195
3.2.3.B Testing 199
3.3 Results and Discussion 202
3.3.1 Micromachining Methodology 202
3.3.2 Cuvette Design 207
3.3.2-A Capillary Stoppers 212
3.3.2-B Capillary Guides 221
3.3.2-C Cover Slips, Guides 228
3.3.2-D Aspect Ratio 231
3.4 Conclusions 234
3.5 References 235
CHAPTER 4: CONCLUSIONS AND FUTURE DIRECTIONS 236
4.1 Conclusions 237
4.2 Future Directions 238
4.3 References 242
APPENDIX 1: DNA SEQUENCING RUN 243
APPENDIX 2: SHEATH FLOW CUVETTE HOLDER 275

LIST OF TABLES

CHAPTER 1: INTRODUCTION 1

CHAPTER 2: MULTICAPILLARY DNA SEQUENCER 57

Table 2.1: Dye Absoption and Emission Data. 84

Table 2.2: GRIN Lens Positions on Mounting Plate. 109

Table 2.3: Avalanche Photodiode Biasing Voltage Optimisation 126

Table 2.4: Low-Pass Filter Response vs. Frequency Generator Input. 136

Table 2.5: 3σ Limit of Detection for Each Capillary 147

Table 2.6: Base-Calling Comparison with Known Sequence. 164

Table 2.7: Base-Calling Accuracy. 168

CHAPTER 3: SHEATH FLOW CUVETTES 174

Table 3.1: Annealing Programmes for Pyrex 7740 183

Table 3.2: Effect of Etching Conditions and Annealing for Pyrex 7740 203

Table 3.3: Cuvette Design Features. 208

LIST OF FIGURES

CHAPTER 1: INTRODUCTION 1

Figure 1.1: Movement of Ions in CZE. 6

Figure 1.2: Polymerisation of Acrylamide 14

Figure 1.3: DNA Reptation 19

Figure 1.4: Components of DNA and RNA. 22

Figure 1.5: Single Strand of DNA. 24

Figure 1.6: Base-Pairing. 26

Figure 1.7: Gene Cloning and Cycle Sequencing 28

Figure 1.8: DNA Fragment Separation and Sequence Interpretation. 32

Figure 1.9: Shot Gun Sequencing and Primer Walking 35

Figure 1.10: Crystalline and Amorphous Silica 42

Figure 1.11: Photolithographic Patterning. 45

CHAPTER 2: MULTICAPILLARY DNA SEQUENCER 57

Figure 2.1: Conventional and GRIN Lenses 63

Figure 2.2: Diodes and Avalanche Photodiodes 66

Figure 2.3: Avalanche Photodiode Biasing Curve. 68

Figure 2.4: Box Diagram of Separation Apparatus 73

Figure 2.5: Detection Apparatus. 75

Figure 2.6: Photo of Sequencer in Operation. 77

Figure 2.7: Photo of Some Detection Electronic and Optical Copmponents 79

Figure 2.8: Rotation of Filters Through Optical Path. 86

Figure 2.9: Timing of Data Acquisition Programme. 89

Figure 2.10: Timing of Data Acquisition Programme - Verification......93
Figure 2.11: Arrangement of Detection Optics..98
Figure 2.12: Optical Alignment of Fluorescent Spots...........................101
Figure 2.13: Working Distance Correction for Cuvette Wall.............105
Figure 2.14: GRIN Lens Positions on Mounting Plate........................110
Figure 2.15: Effect of Optical Filters on GRIN Lens Alignment........113
Figure 2.16: Optical Fibre Connections..115
Figure 2.17: Detection Electronics for One Capillary...........................117
Figure 2.18: APDs in Cooling Box..120
Figure 2.19: LED-GRIN Lens Aligner Used as APD Light Source....124
Figure 2.20: APD Biasing Curves..128
Figure 2.21: Shielding APD Leads from Interference...........................134
Figure 2.22: Low-Pass Filter Response Curves....................................137
Figure 2.23: Filter Wheel Geometry...142
Figure 2.24: Absence of Cross Talk in LOD Studies...........................154
Figure 2.25: Example of 4-Colour DNA Sequencing Electropherogram...158
Figure 2.26: Base-Calling...162
Figure 2.27: Comparison of 16 Electropherograms..............................166
CHAPTER 3: SHEATH FLOW CUVETTES____________________**174**
Figure 3.1: Photo of 6 Capillary Micromachined Sheath Flow Cuvette...178
Figure 3.2: Photo of Photolithography Mask...181
Figure 3.3: Cuvette Design...187
Figure 3.4: Cuvette Assembly I: Orientation and Crude Alignment..189
Figure 3.5: Cuvette Assembly II: Fine Alignment................................191

Figure 3.6: Cuvette Assembly III: Glue Curing,
Cutting and Polishing. 193
Figure 3.7: Photo of Striations on Outer Cuvette Surface 196
Figure 3.8: Finished Cuvette 198
Figure 3.9: Photos of 16 Capillary Sheath Flow Cuvette
Mounted in Holder 200
Figure 3.10: Scanning Electron Micrographs of
Etched Glass Surfaces 204
Figure 3.11: Photo of Capillaries, Guides and Stoppers in
a 6 Capillary Cuvette. 210
Figure 3.12: Capillary Stoppers. 213
Figure 3.13: Photo of Capillary Ends and Square Peg Stoppers. 217
Figure 3.14: Shape of V in Capillary Stoppers 219
Figure 3.15: Capillary Guide-Capillary Stopper Separation. 222
Figure 3.16: Effect of Capillary Guide Spacing 224
Figure 3.17: Photo of Evenly and
Unevenly Spaced Capillaries in Cuvette. 226
Figure 3.18: Cover Slip Thickness 229
Figure 3.19: Cover Slip Guides. 230
Figure 3.20: Aspect Ratio Observed During Etching. 232

LIST OF ABBREVIATIONS

ABI	Applied Biosystems, Inc.
APD	avalanche photodiode
BOE	buffered oxide etch
CCD	charge-coupled device
CGE	capillary gel electrophoresis
CZE	capillary zone electrophoresis
ddNTP	dideoxynucleotide triphosphate
DNA	deoxyribonucleic acid
dNTP	deoxynucleotide triphosphate
dsDNA	double stranded DNA
FITC	fluorescein isothiocyanate
GRIN	gradient refractive index
ID	inner diameter
LED	light-emitting diode
LIF	laser-induced fluorescence
LOD	limit of detection
LPF	low-pass filter
MALDI	matrix-assisted laser desoption/ionisation
MECC	micellar electrokinetic capillary chromatography
NA	numerical aperture
nmr	nuclear magnetic resonance
OD	outer diameter
PMT	photomultiplier tube
RNA	ribonucleic acid
SBH	sequencing by hybridisation

SPCM	single photon counting module
ssDNA	single stranded DNA
TBE	tris-borate-ethylenediaminetetraacetic acid
TEMED	tetramethylethylenediamine
UV	ultraviolet

Chapter 1

INTRODUCTION

1.1 Introduction

If DNA is the blueprint of life, then DNA sequencing is the ability to read that blueprint. Consequently, DNA sequencing is an indispensable tool for geneticists and scientists of other biological fields, and is key to the increasing demand for genetic information. The International Human Genome Project[1], "a worldwide research effort with the goal of analyzing the structure of human DNA and determining the location of the estimated 100 000 human genes", was begun in response to this demand. The American programme, which has in part funded the research of this thesis, states amongst its objectives[2] the need to "develop technology for high-throughput sequencing", and the capacity to sequence at 50 Mb/year by 1998, such that the entire human genome is sequenced by the year 2005; the genomes of other "model" organisms are also being sequenced in this project. Further, sequencing is used for genetic assaying, which is becoming more important as genetic diseases become better understood.

The development of a 16 capillary, high throughput DNA sequencer described in this thesis takes direct aim at the needs of the Human Genome Project. This sequencer alone is designed for a capacity of ~ 1 Mb/year of (finished) sequence information. While designed specifically for DNA sequencing, the instrument could easily be applied to other capillary electrophoresis applications where high throughput is advantageous.

The development of the sequencer occurred in two main areas. First in chronological order, a micromachined, multicapillary sheath flow cuvette (the flow-through detection cell of the sequencer) was developed, and second, the sequencer instrumentation (with the micromachined sheath flow cuvette integrated) was developed. The sequencer instrumentation is described first in Chapter 2 to establish the context for the use of the sheath flow cuvette, whose development is described next in Chapter 3. In Chapter 4, general conclusions about sheath flow cuvettes, the DNA sequencer and their performance are drawn, and some ideas for directions in future research related to this project are offered.

It is important to mention at the outset that much of this work, namely testing of the third and all of the fourth of the five cuvette iterations in Chapter 3 and all of the sequencer instrumentation development of Chapter 2, is a collaborative effort with Sue Bay of this research group.

In Chapter 1, background information is introduced concerning fundamental or applied science which is brought to bear on topics discussed later in Chapters 2 or 3, and which is thought perhaps not to be common knowledge for an analytical chemist. The main areas discussed are capillary electrophoresis, DNA and DNA sequencing methods, and sheath flow cuvettes and micromachining.

1.2 Capillary Electrophoresis

Discussion of capillary electrophoresis is divided into free zone- and gel-based methods.

1.2.1 Capillary Zone Electrophoresis

Electrophoresis can be described most simply as the movement of charged particles in an electric field. In 1809, Reuss observed the migration of particles of clay in an aqueous dispersion with an applied electric field[3]. In 1937, Tiselius[4] introduced moving boundary electrophoresis; in the moving boundary method, the sample is continuously applied, and the leading edges of the sample constituents are resolved, but all but the fastest constituent overlap with others from the sample mixture. In contrast, in zone electrophoresis, the sample is applied only briefly, after which the injection end of the separation chamber is re-immersed in carrier electrolyte, such that the sample constituents are resolved into discrete zones by electrophoresis. A zone separation has distinct advantages as an analytical tool or preparative method over a moving boundary separation, since the spatially resolved sample constituents can be individually detected or collected.

A limiting feature of zone electrophoresis is generation of heat and resultant convection due to the current passed in the separation medium. Convection acts to broaden zones and degrade the separation. In the first example of capillary zone electrophoresis (CZE), Hjertén[5] addressed the convective movement of the liquid electrophoretic medium of his separations by putting it "into a periodic orbit" - an elaborate apparatus was developed to rotate the 3 mm inner diameter (ID), 7.8 mm outer diameter (OD) quartz electrophoresis capillary during the separation. Mikkers and coworkers[6] and Jorgenson and Lukacs[7] made use of narrow-bore capillaries to suppress convection. While thin glass capillaries offer exceptional separation capabilities (N > 400 000, N = number of theoretical plates)[7], it has been shown that sample concentration must be kept low (relative to carrier concentration) to avoid asymmetric peaks[6, 8]; low sample concentrations and small detection volumes demand a sensitive detection system. Many detection systems have been successfully applied to capillary electrophoresis[9].

Strictly speaking, CZE includes all forms of zone electrophoresis in a capillary; in practice, it is used to refer only to *free* zone electrophoresis, excluding zone electrophoresis with a gel sieving medium (capillary gel electrophoresis, CGE, described in section 1.2.2 below).

It is instructive to revisit chromatographic figures of merit such as efficiency and resolution as applied to CZE. The equations for analyte motion during the separation must first be defined, as they differ significantly from those in chromatography. The next three sections deal with electrophoretic mobility

(1.2.1.A), electroosmotic mobility (1.2.1.B), and efficiency and resolution (1.2.1.C); electrophoretic and electroosmotic mobilities and their summation are shown in Figure 1.1.

1.2.1.A Electrophoretic Mobility

Kuhr has shown a simple derivation for electrophoretic mobility[10]. Consider an open cylindrical tube (capillary) of length L and radius r_{cap} filled with a running buffer (a conductive, electrolytic solution, often pH-buffered to sample requirements), and having both ends immersed in reservoirs of the running buffer. If a potential V is applied along the capillary axis by means of electrodes in the running buffer reservoirs to generate an electric field E = V/L, then electrophoresis of the ions in the capillary occurs. Each ion of gyration radius r_{ion} and of charge q has a force applied by the field, F_{ep}:

$$F_{ep} = qE \tag{1.1}$$

The force of friction in solution, F_{fr}, encountered by the ion moving with a velocity, v_{ep}, is:

$$F_{fr} = 6\pi\eta r_{ion} v_{ep} \tag{1.2}$$

where η is the viscosity of the running buffer. If v_{ep} is constant, then the two forces are equal and opposite:

$$qE = 6\pi\eta r_{ion} v_{ep}$$

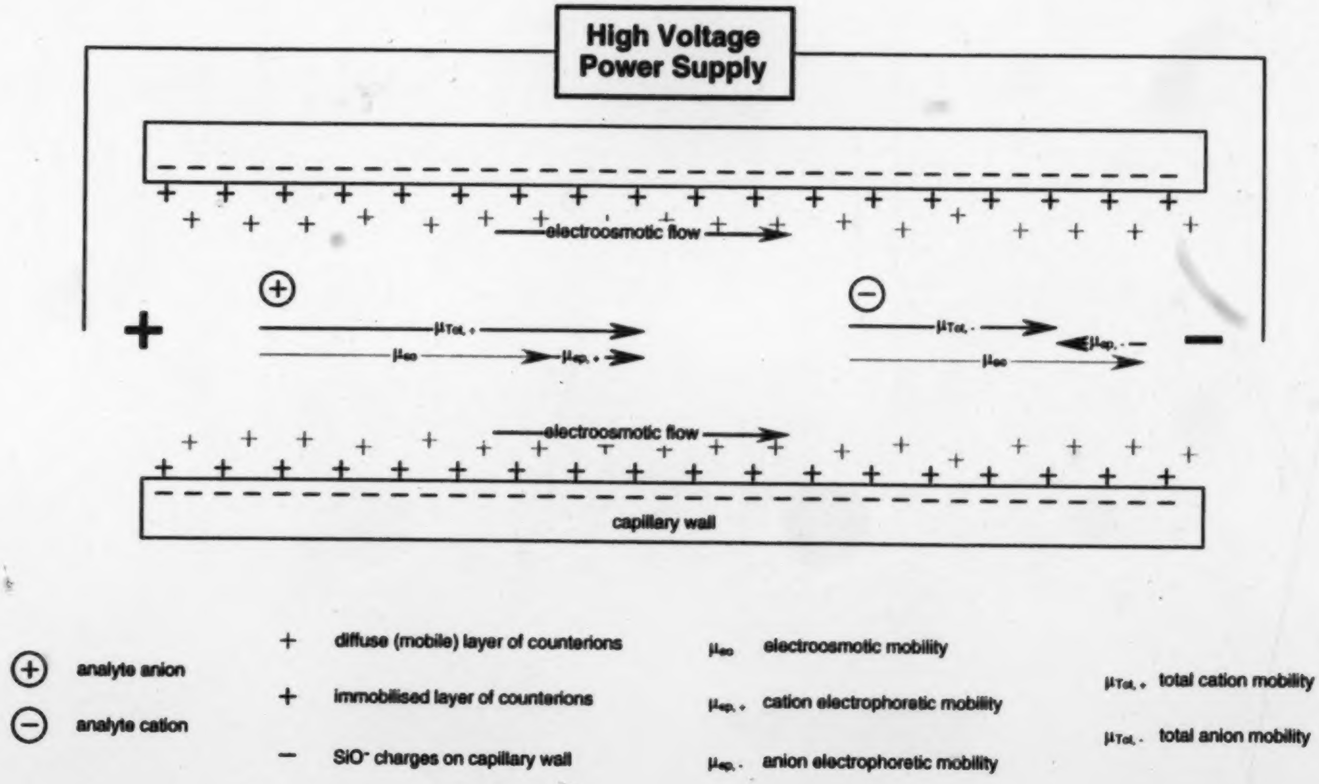
High Voltage Power Supply
electroosmotic flow
+
$\mu_{Tot,+}$
μ_{eo}
$\mu_{ep,+}$
−
$\mu_{Tot,-}$
$\mu_{ep,-}$
μ_{eo}
electroosmotic flow
capillary wall
⊕ analyte anion
⊖ analyte cation
+ diffuse (mobile) layer of counterions
+ immobilised layer of counterions
− SiO⁻ charges on capillary wall
μ_{eo} electroosmotic mobility
$\mu_{ep,+}$ cation electrophoretic mobility
$\mu_{ep,-}$ anion electrophoretic mobility
$\mu_{Tot,+}$ total cation mobility
$\mu_{Tot,-}$ total anion mobility

Figure 1.1: Movement of Ions in CZE

Rearranging,

$$v_{ep} = \frac{qE}{6\pi\eta r_{ion}} \qquad (1.3)$$

The electrophoretic mobility, μ_{ep}, is defined as the velocity normalised to the field:

$$\mu_{ep} = \frac{v_{ep}}{E} = \frac{q}{6\pi\eta r_{ion}} \qquad (1.4)$$

The velocity and mobility of an ion are seen to be functions of its charge to size ratio, q/r_{ion}.

It should be noted that the variables E, F_{ep}, F_{fr}, v_{ep} and μ_{ep} are all vector quantities, but since their direction is either anodic or cathodic, their scalar value taken with their sign and that of q accurately describe the ion's motion. This convention is used throughout.

Other authors have defined an ion's electrophoretic mobility slightly differently[11], or have defined it in terms of the ion's zeta potential[12, 13].

1.2.1.B Electroosmotic Mobility

When the capillary of the electrophoretic separation has a charged inner surface (as for glass or quartz capillaries, or if the surface is otherwise derivatised), then an additional component to an ion's movement, electroosmosis, must be considered.

Electroosmosis in a capillary may be described as the movement of the bulk solution caused by the migration of the capillary wall's counterions towards the cathode or anode, wherein the charge of the counterions determines the direction of flow. As an illustration, the specific example of a quartz or glass capillary will be used to describe electroosmosis, although the same argument applies to capillaries derivatised to have oppositely charged walls, excepting that the direction of flow is reversed.

In an underivatised glass or quartz capillary, the capillary surface has many silanol (Si-OH) groups which are deprotonated[11] at $pH > 2$. The $Si\text{-}O^-$ groups attract cations from the bulk solution to the walls; the aggregation of counterions at the wall surface (or to the surface of a charged particle in solution) is due to electroneutrality and results in the formation of an *electrical double layer*[3]. The double layer may be visualised as an immobile layer of cations adjacent to the wall, and a second, more diffuse and mobile layer of cations extending into the bulk[14] (see Figure 1.1). The concentration, $c_i(x)$, of a counterion, i, at a distance, x, from the surface is given by[3]:

$$c_i(x) = c_i(\infty) \bullet \exp\left(\frac{-q_i e \zeta_{wall}(x)}{k_B T}\right) \qquad (1.5)$$

where $c_i(\infty)$ is the bulk ($x \rightarrow \infty$) concentration of an ion i, e is the charge of an electron, k_B is the Boltzmann constant, T is the absolute temperature and $\zeta_{wall}(x)$ is the potential between the wall and the solution, termed the zeta potential, at a distance, x, from the surface. For a flat plane (on a molecular scale, the curvature of a ~ 50 μm ID capillary is negligible), the zeta potential may be described as[3]:

$$\zeta_{wall}(x) = \zeta_{wall}(0) \bullet \exp\left(\frac{-x}{t_{DL}}\right) \qquad (1.6)$$

where $\zeta_{wall}(0)$ is the potential at the wall ($x = 0$) and t_{DL} is the thickness of the double layer, both of which depend on the nature of the solid surface and liquid[14]. In a mixture of electrolytes, $1/t_{DL}$ is defined as[3]:

$$\frac{1}{t_{DL}} = \sqrt{\frac{2F^2\mu_{is}}{\varepsilon_0\varepsilon RT}} \qquad (1.7)$$

where F is the Faraday constant, μ_{is} is the ionic strength, ε_0 is the permittivity of free space, ε is the permittivity of the medium and R is the universal gas constant. At $x = t_{DL}$, the zeta potential has dropped to $\zeta_{wall}(0) \bullet \exp(-1)$; this is the centre of mass of the double layer[3]. The boundary between the immobile and diffuse layers occurs at $x = \delta$. This boundary plane is called the shear plane, as the counterions of the diffuse layer move adjacent to the immobile layer when a field is applied in the direction of the capillary axis. In a capillary, the cationic counterions migrate to the cathode, entraining their water of hydration[11] and the bulk solution. Unlike the parabolic flow profile of pressure-driven flow, electroosmosis creates a flat flow profile[15] across the diameter of the capillary, providing $r_{cap} >> t_{DL}$. The resulting electroosmotic mobility, μ_{eo}, which *all ions and neutrals in solution* experience, is[11]:

$$\mu_{eo} = \frac{\varepsilon\zeta_{wall}(\delta)}{4\pi\eta} \qquad (1.8)$$

The presence of electroosmosis in CZE has several ramifications. First, since the bulk flow in an uncoated capillary is to the cathode, anions and cations alike may be analysed together. Second, because of its flat, plug-like flow, it does not cause band broadening. Third, by altering the inner capillary surface of running buffer solution, μ_{eo} can be adjusted to enhance resolution (described below). Lukacs and Jorgenson[16] have shown the pH dependence of μ_{eo} for Pyrex, quartz and Teflon capillaries. Last, outside the double layer, the electroosmotic mobility is independant of capillary radius.

1.2.1.C Efficiency and Resolution

Giddings'[17] expressions for efficiency and resolution are:

$$N = \frac{L^2}{\sigma^2} \tag{1.9}$$

where N is the number of plates, L is the length of the column, σ^2 is the spatial variance of a band in the separation, and:

$$R_s = \frac{\sqrt{N}}{4} \bullet \frac{v_2 - v_1}{v_{avg}} \tag{1.10}$$

where R_s is the resolution, v_1, v_2 and v_{avg} are the individual and average velocities of solutes 1 and 2. Building upon Giddings' equations, Jorgenson and Lukacs have shown:

$$N = \frac{V(\mu_{eo} + \mu_{ep})}{2D} \tag{1.11}$$

where D is the solute's molecular diffusion constant, and:

$$R_s = \frac{\mu_{ep.1} - \mu_{ep.2}}{4\sqrt{2}} \sqrt{\frac{V}{D(\mu_{ep.avg} + \mu_{eo})}} \tag{1.12}$$

where $\mu_{ep,1}$ and $\mu_{ep,2}$ are for solutes 1 and 2, and $\mu_{ep,avg}$ is their average.

These important results show that efficiency and resolution improve with higher applied potential, and that generating an electroosmotic flow to be nearly equal and opposite to μ_{ep} of the solutes yields high resolution, but at the cost of analysis time, t_{mig}. Since $t_{mig} = L/v$, and $v = v_{ep} + v_{eo} = (\mu_{ep} + \mu_{eo})\ V/L$, t_{mig} may be expressed as:

$$t_{mig} = \frac{L^2}{V(\mu_{eo} + \mu_{ep})} \tag{1.13}$$

Thus a compromise between high resolution and migration time must be made.

There is also a limit to the resolution which may be achieved by increasing the applied potential, since the process of Joule heating acts to degrade the separation. The heat generated in the capillary comes from the power, P, supplied to the separation[11]:

$$P = \frac{\pi r_{cap}^2 \Lambda c_{RB} V^2}{L} \tag{1.14}$$

where Λ is the molar conductivity of the solution and c_{RB} is the concentration of the running buffer. Most of this power is converted to thermal flux (heat/time), and is generated uniformly across the capillary radius. Dissipation of the heat occurs only at the capillary-running buffer interface, which generates a thermal gradient along r_{cap}, such that $T_{centre} > T_{wall}$. Mobilities increase with temperature, so central ions in a zone speed up relative to the outer ions, causing bandbroadening. The temperature difference also induces convection. Both bandbroadening and convection detract from separation efficiency and resolution[11]. Obviously, high voltages will generate amounts of heat which cannot be dissipated by the capillary. Lowering the c_{RB} and using thin capillaries will reduce the production of heat.

1.2.2 Capillary Gel Electrophoresis

In this section, repeated reference will be made to "DNA fragments", "DNA ions", "series of fragments", etc. While the nature of DNA and the DNA fragments used in sequencing are discussed at length in section 1.3, it can merely be pointed out for the purpose of this section that typical DNA sequencing (or Sanger sequencing) samples consist of a series of DNA fragments, varying in length from ~ 60 to 3400 Å, and that DNA is a polymer, so that a DNA fragment behaves somewhat like a chain whose links are its constituent monomers.

In free zone electrophoresis, electrophoretic mobility varies with the charge-to-size ratio, q/r; unfortunately this ratio is essentially unchanged for DNA fragments of all sizes[18]. In basic aqueous solution (such as DNA's natural medium), the charge carried by the polymer is -N for a piece of single stranded DNA N nucleotides long, since each phosphate is deprotonated. Thus a change in DNA fragment size (as measured by its radius of gyration, R_g) is accompanied by a proportional change in charge, q, and its mobility is unchanged. The independence of mobility from size in zone electrophoresis has been shown experimentally to be true[18].

To effect a separation of DNA, a sieving medium such as a gel or entangled polymer is used in combination with the electric field, E. Here the analyte DNA ions must find a path through the gel in which the gel pores are large enough to accommodate the size of the DNA fragment. In general, the electrophoretic migration time increases as a function of analyte size, allowing ions of different size (such as in Sanger sequencing) to be resolved. This separation process will be described first by examining the sieving medium, and second by looking at the migration behaviour of DNA ions therein.

Sieving media used in DNA separations are of two basic types: gels and entangled polymers. Entangled polymers are essentially solutions of long, straight chain polymers which, although not cross linked, are sufficiently concentrated to form a "mesh"[19]. The concentration at which the polymer becomes entangled is termed the entanglement or overlap threshold, and is a function of the molar mass of the polymer[19]. The pore size of the polymer mesh is a function of the polymer concentration[19]. In contrast, in a gel the polymer chains are cross-linked with each other, either chemically (as for cross-linked polyacrylamide) or physically (as for agarose). A gel's pore size can be controlled by the amount of cross-linker used in the polymerisation reaction, in the case of a chemical gel[20].

The reaction for the polymerisation of acrylamide[21] (polyacrylamide is commonly used for DNA sequencing separations) is shown in Figure 1.2. The free-radical reaction between two monomers of acrylamide or bisacrylamide is initialised by ammonium persulphate ($(NH_4)_2S_2O_8$) and catalysed by N, N, N', N'-tetramethylethylenediamine (TEMED). Whether the chain extends or branches depends on which monomer, acrylamide or bisacrylamide, is incorporated. The extent to which the polymer branches depends on the fraction of total monomer which the bisacrylamide cross-linker constitutes; the concentrations of the monomers are described as %T, %C, where %T (total) is the mass fraction of the solution of both monomers combined, and %C (cross-linker) is the fraction of the monomers which is cross-linker.

Gels act as both the sieving medium for size-dependent separations, and as an anticonvective medium, to reduce bandbroadening. An advantage arising from the use of capillaries is their efficient dissipation of Joule heat, and the resultant suppression of convection[22], which in turn allows the use of entangled polymers, such as straight chain polyacrylamide (in the preparation of which no bisacrylamide is used) in lieu of gels for capillary-based separations of DNA.

Figure 1.2: Polymerisation of Acrylamide.

a) monomers, initialiser and catalyst; b) straight chain and branched chain polymerisation

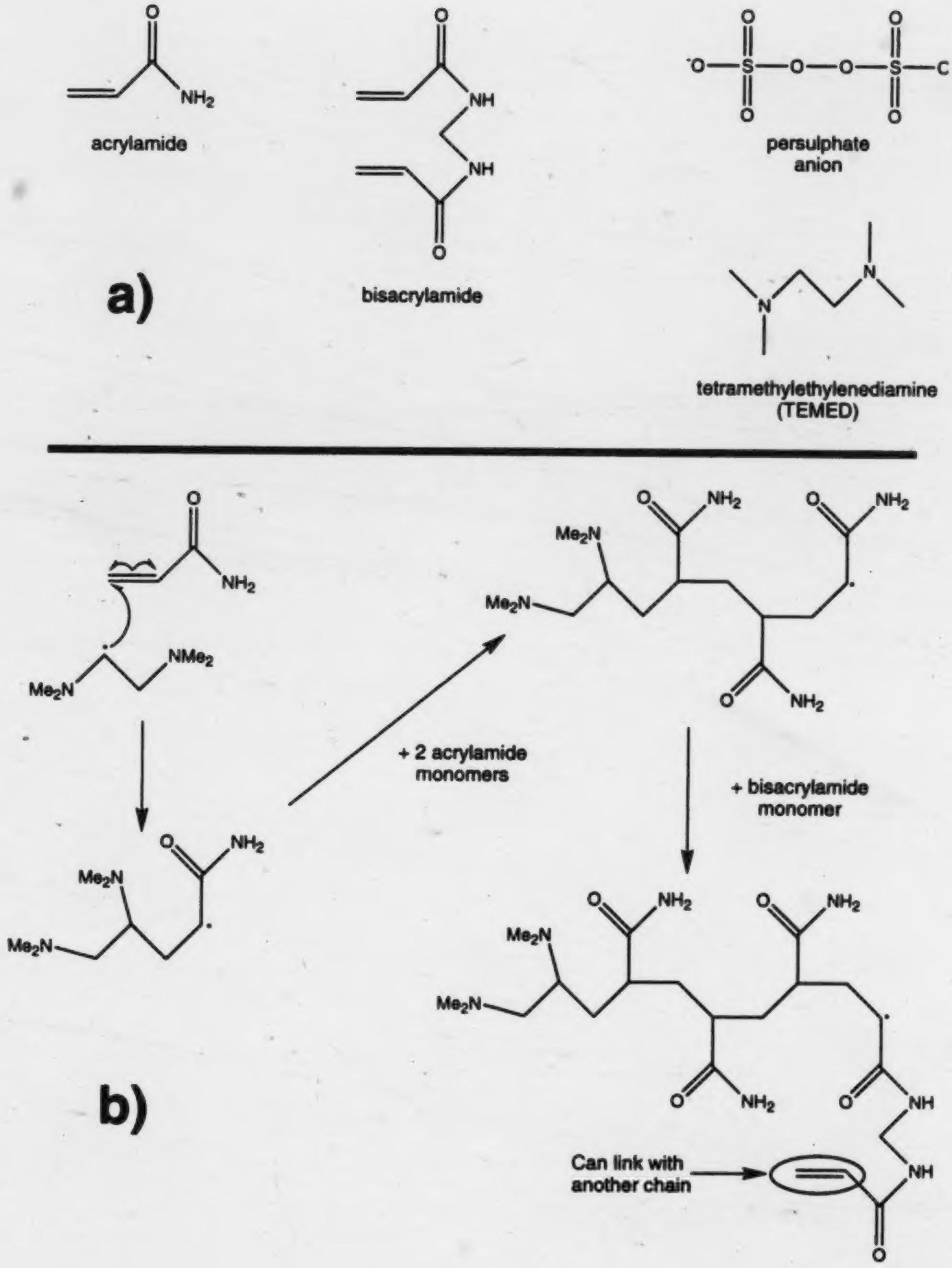
a)
acrylamide
NH2
O
bisacrylamide
NH
persulphate anion
tetramethylethylenediamine (TEMED)
N
b)
Me2N
NMe2
+ 2 acrylamide monomers
+ bisacrylamide monomer
Can link with another chain

Entangled polymer solutions are less viscous and thus more amenable to pressurised replacement than gels, which should yield faster turnaround times, since only the gel and not the capillary need be replaced between (DNA sequencing) runs[20]. It should be noted that while gels and entangled polymers are distinct from each other (and despite the exploitation of the advantages of entangled polymers in capillaries), capillary electrophoresis with a sieving medium is usually referred to as "capillary gel electrophoresis", or CGE, regardless of whether a gel or entangled polymer is used.

The complexity of migration behaviour of DNA anions in sieving media has stimulated a great deal of research[18-20, 22-36], and the current theories have been well described qualitatively[22, 23] and quantitatively[25-28, 30, 31]. The method by which the long chain DNA polyanion migrates depends on the relative sizes of the DNA fragment and of the mesh pore, and on the electric field applied. The electric field, E, and pore size, a, can be controlled experimentally[19]; the size of the DNA fragment is measured by its radius of gyration, R_g. Above a certain length called the persistence length, p, DNA of length L folds into a globular shape, and R_g may be estimated as:

$$R_g = \frac{pL}{3}\left(1 - \frac{p}{L} + \frac{p}{L} \bullet \exp(-L/p)\right) \qquad (1.15)$$

For $R_g < a$, the DNA migrates according to the Ogston model, while for $R_g > a$, the reptation model prevails[23].

In the Ogston model[26-28], the globular DNA passes through the pores of the matrix unperturbed with a mobility, μ, described by:

$$\frac{\mu}{\mu_0} = f = \exp(-2\pi\nu L R_g^2) \qquad (1.16)$$

where μ_0 is the free solution mobility of the DNA ion (note that in gel electrophoresis, electroosmosis is suppressed by the sieving matrix, so mobilities are electrophoretic), f is the fraction of the total volume of the sieving medium which can accommodate ions of a particular size, ν is the number of fibres/mL and 2L is the length of fibre. The mobility has also been expressed with different but related variables as the exponential argument[23]:

$$\frac{\mu}{\mu_0} = \exp(-Ab(R_g + r)^2) \qquad (1.17)$$

$$\frac{\mu}{\mu_0} = \exp\left(-\frac{\pi}{4}\left(\frac{R_a + r}{a}\right)^2\right) \qquad (1.18)$$

where A is the gel or polymer concentration, r is the gel fibre radius, b is a constant chosen for the units of A, and a is the average pore size.

In the reptation model[22-25, 29-36], the DNA must deform from its globular shape to fit through the pores - it "reptates" or "snakes" its way through a tube of connected pores. Within the reptation model, there are two main regimes to consider: reptation without orientation, and reptation with orientation or stretching ("biased reptation"). For lower E and/or shorter DNA fragment lengths in a given sieving matrix, the ion snakes through the pores and partially deforms, but still retains some of its globular shape[22]; the mobility of the fragment scales with the reciprocal of its length:

$$\mu \propto \frac{1}{N} \qquad (1.19)$$

As the fragments become longer and/or the field increases, the fragments become stretched in the direction of the field and are thought to snake straight through. In this biased reptation regime, the fragment mobility is independent of length, and dependent on E. Above a certain length, all fragments migrate with the same mobility. The effect of electric field on fragment shape, as well as a pictoral representation of reptation are shown in Figure 1.3.

Slater and Noolandi[25] have proposed an expression which encompasses both regimes:

$$\mu = \frac{Q}{3\xi_c}\left[\frac{1}{N} + \left(\frac{qE\alpha}{3k_BT}\right)^2 + \cdots\right] \tag{1.20}$$

where Q is the total charge for a DNA fragment of N segments, each with a charge q and length α, ξ_c is the chain friction coefficient, k_B is the Boltzmann constant, and T is the absolute temperature. For short fragment lengths (low N) and weak field (low E), the first term predominates and, since both Q and ξ_c scale with N, $\mu \alpha$ 1/N. For longer fragment lengths and high field, the second term predominates, and $\mu \alpha E^2$ - size separation is no longer achieved. A somewhat different theoretical approach to reptation by Duke and co-workers yielded the biased reptation with fluctuations model, in which $\mu \alpha E$ for this same long fragment, high field regime[35].

The gel separations of DNA sequencing make use of the regime of *reptation without orientation,* such that equation (1.19) is valid and thus $t_{mig} \alpha$ N. Therefore the electropherogram from a separation of Sanger sequencing fragments (which differ in length by whole numbers of nucleotides) will consist of a series of peaks spaced evenly in time.

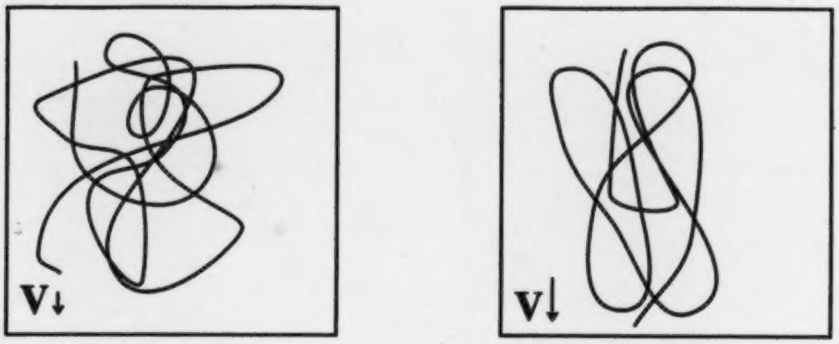

a) Weak field

b) Medium field

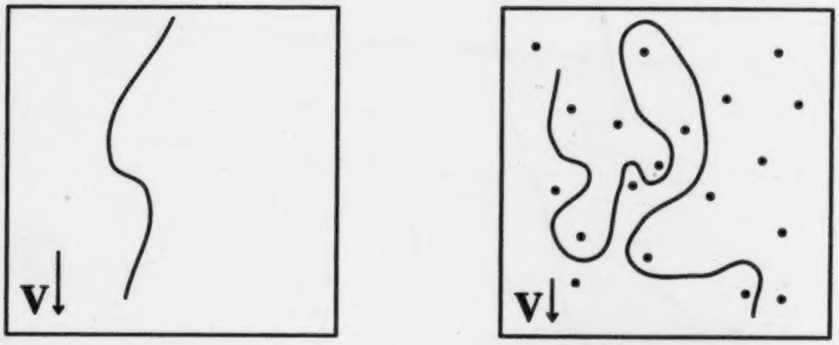

c) Strong field

d) Reptation of a DNA polymer through the sieving mesh

Figure 1.3: DNA Reptation.

The effect of electric field on DNA polymer shape (a)-c)), and an example of DNA reptating through the sieving medium at a moderate field (d)).

(Adapted from P. D. Grossman and D. S. Soane, Biopolymers **31,** 1221 (1991))

1.3 DNA and DNA Sequencing Methods

An overview of the structure of DNA and methods by which it is sequenced is given in this section.

1.3.1 DNA

This section deals with the importance and structure of DNA.

1.3.1.A Importance of DNA

Deoxyribonucleic acid, or DNA, is likely the single most important biological molecule known. Watson and Crick[37] elucidated its structure in 1953 by means of clever model building and with the benefit of the detailed crystallographic studies of Wilkins[38] and Franklin[39]. The impact of the discovery of DNA as the genetic blueprint of life is unquestionably enormous, and includes the birth of the field of Molecular Genetics. Indeed, Watson, Crick and Wilkins shared the 1962 Nobel Prize for their groundbreaking research (Franklin died before the prize was awarded)[40].

On a basic level, DNA is the digital code for the synthesis of proteins, the doers and builders in any living cell. Proteins and DNA are both long chain polymers; proteins have 20 different kinds of monomers, called amino acids, while DNA has only 4 kinds of monomers, called nucleotides. The four nucleotides, adenosine, cytidine, guanosine and thymidine are referred to as A, C, G and T in shorthand (a complete description follows). Just as a sequence of 1s and 0s are used to encode information in binary code, the sequence of As, Cs, Gs and Ts encodes protein information: every three nucleotides of DNA (called a codon) along a gene encodes for one amino acid in the synthesis of a protein. The human genome is estimated to be 3 000 000 000 nucleotides long - stretched out, this would measure ~ 1 m!

Proteins themselves perform many crucial functions as enzymatic catalysts of a myriad of reactions and processes, and are also integral parts in structures such as cell membranes, where they control flow in and out of the cell. Given the central role of proteins and the fact that they are fully described in DNA, the need to study DNA is paramount. One of the first steps in the study of DNA is to read the sequence along a particular gene of interest so that it may be interpreted by geneticists and biochemists. This need for sequencing is the raison d'être of this thesis.

1.3.1.B Structure of DNA

To understand the methods by which DNA is sequenced, knowledge of its structure is necessary; a more detailed look at DNA structure may be found elsewhere as a chapter[41] or as a complete volume[42]. As mentioned, DNA is a long chain polymer made up of monomers. In its normal "B-form", DNA has two such chains linked together to form a right-handed double helix, with a full turn occurring every 34 Å along the axis; each turn is 10 nucleotides long, meaning that the nucleotides are 3.4 Å apart. The structure may be examined on three levels: the structure of a nucleotide, the linking of nucleotides into a chain of "single stranded" DNA (ssDNA), and the pairing of two such chains to form "double stranded" DNA (dsDNA).

Figure 1.4-a shows the structure of 2'-deoxycytidinetriphosphate - the 2'-deoxynucleotidetriphosphate form is that taken when a nucleotide is not linked in a chain. The three components of a nucleotide are the phosphate, the sugar and the base. In DNA, the four bases are cytosine, thymine (the pyrimidines), guanine and adenine (the purines), as depicted in Figure 1.4-b, and the sugar is 2'-deoxyribose, the central structure of Figure 1.4-c. 2'-Deoxyribose is bonded at carbon 1' to the nitrogen 1 of a pyrimidine, and nitrogen 9 of a

a) 2'-deoxycytidinetriphosphate

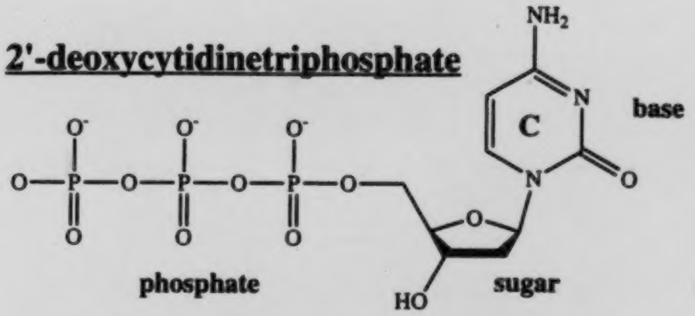
NH2
base
C
phosphate
sugar
HO

b) Bases:

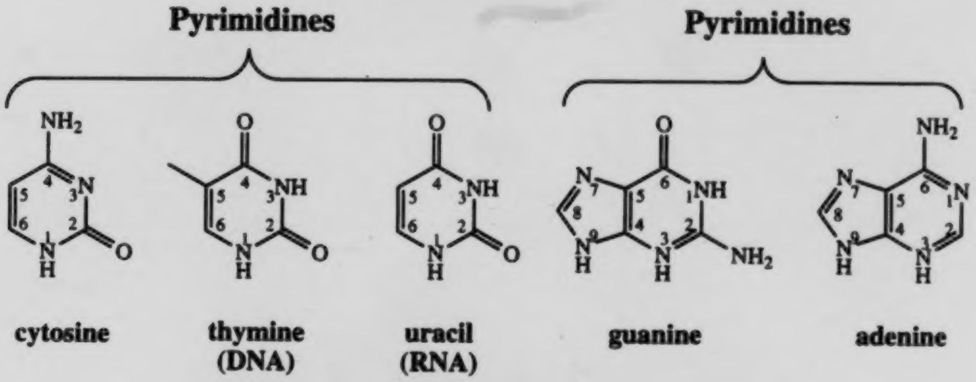
Pyrimidines
Pyrimidines
cytosine
thymine
(DNA)
uracil
(RNA)
guanine
adenine

c) Sugars:

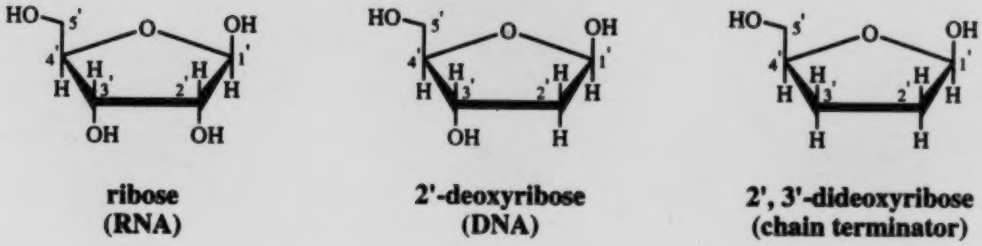
ribose
(RNA)
2'-deoxyribose
(DNA)
2', 3'-dideoxyribose
(chain terminator)

Figure 1.4: Components of DNA and RNA.

a) as they occur in a nucleotide triphosphate of DNA, b) the five possible bases, and c) the sugars of RNA, DNA and ddNTPs purine. In ribonucleic acid, or RNA (the "working copy" of DNA), ribose is the sugar, and while cytosine, guanine and adenine are retained, uracil replaces thymine (uracil is identical to thymine except for the lack of the methyl group at position 5).

In the formation of ssDNA, an enzyme attaches the last nucleotide of the chain at its 3' hydroxy group to the incoming 2'-deoxynucleotidetriphosphate at its α-phosphorus to make a phosphodiester bond between sugars ($HP_2O_7^{-3}$ is a byproduct of the reaction). Since chain extension can only occur at the 3'-hydroxy group, the absence of this group in 2', 3'-dideoxynucleotides stops chain extension; 2', 3'-dideoxynucleotides are used for this very purpose, as seen in section 1.3.2.A. Together, the sugars and phosphates are referred to as the sugar-phosphate backbone. Figure 1.5 shows the four nucleotides in a segment of single stranded DNA, or oligomer. Two additional features of this figure should be noted. First, at pH > 2, the phosphates are deprotonated[42] and so DNA carries a negative charge of -N, for a strand N nucleotides long. Second, a direction is ascribed to any nucleotide or ssDNA chain by virtue of the carbon-numbering in sugar(s) of the sugar-phosphate backbone. The end with the free 3'-hydroxy group is referred to as the 3' end, and the other end where the 5'-carbon attaches to the phosphate is referred to as the 5' end. The direction is thus expressed as either 3'→5' or 5'→3'; in Figure 1.5, the strand is 5'→3' going top to bottom.

DNA in the double stranded B-form has the two chains linked together by hydrogen bonds between paired bases from nucleotides of opposing strands. Adenosine always pairs with thymidine (or uracil in RNA) by means of two hydrogen bonds and cytidine with guanosine by means of three; this pairing means that the sequences of the two strands of dsDNA are complementary. It

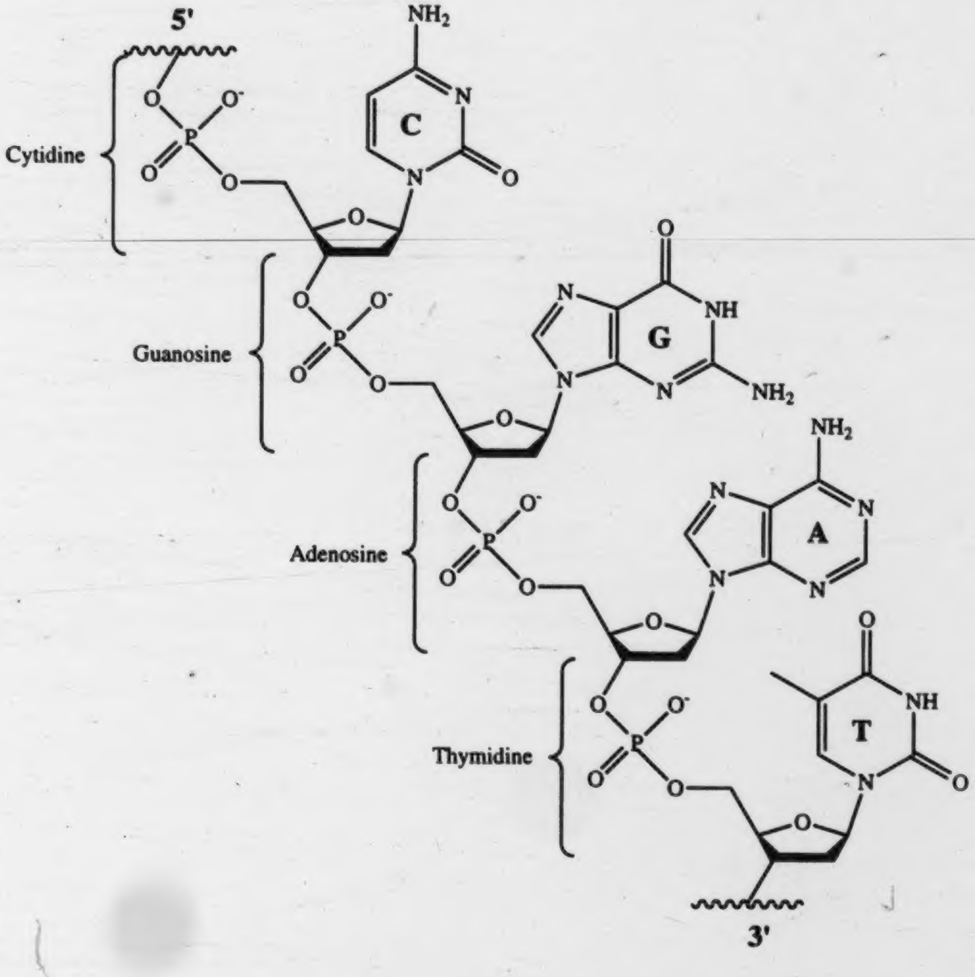
5'
Cytidine
Guanosine
Adenosine
Thymidine
C
G
A
T
NH2
N
O
NH
O-
P
3'

Figure 1.5: Single Strand of DNA.

should also be noted that two paired strands are in opposite directions, or antiparallel. An example of base pairing in dsDNA is shown in Figure 1.6.

1.3.2 DNA Sequencing Methods

DNA sequencing is the determination of the order of the nucleotides in a strand of unknown DNA. Methods for sequencing DNA are discussed in three parts. Sanger sequencing, while nearly 20 years old, is still the method of choice today (Frederick Sanger received his *second* Nobel Prize in 1980 in recognition of his contribution to DNA sequencing), and so it is discussed first in section 1.3.2.A. Secondly, the modifications which have been introduced to the Sanger sequencing protocol for fluorescent detection are mentioned in section 1.3.2.B. Lastly, the more recently developed methods for sequencing (including refinements in the separation of Sanger sequencing fragments, as well as alternatives to the Sanger sequencing protocol) are discussed in section 1.3.2.C.

1.3.2.A Sanger Sequencing Protocol

The Sanger sequencing method[43] sequences a given strand of unknown DNA in three steps: **I.** generation of a series of DNA fragments differing from each other by one nucleotide in length, **II.** separation of these fragments in a gel sieving medium so that, under suitable conditions, the migration time varies linearly with fragment length, and **III.** interpretation of the separation of fragments to determine the sequence of the original unknown DNA. In part **IV**, sequencing strategies, accuracy and redundancy are briefly mentioned.

I Fragment Generation

One common method for generating DNA fragments is cycle sequencing in which single stranded fragments complementary to the original unknown

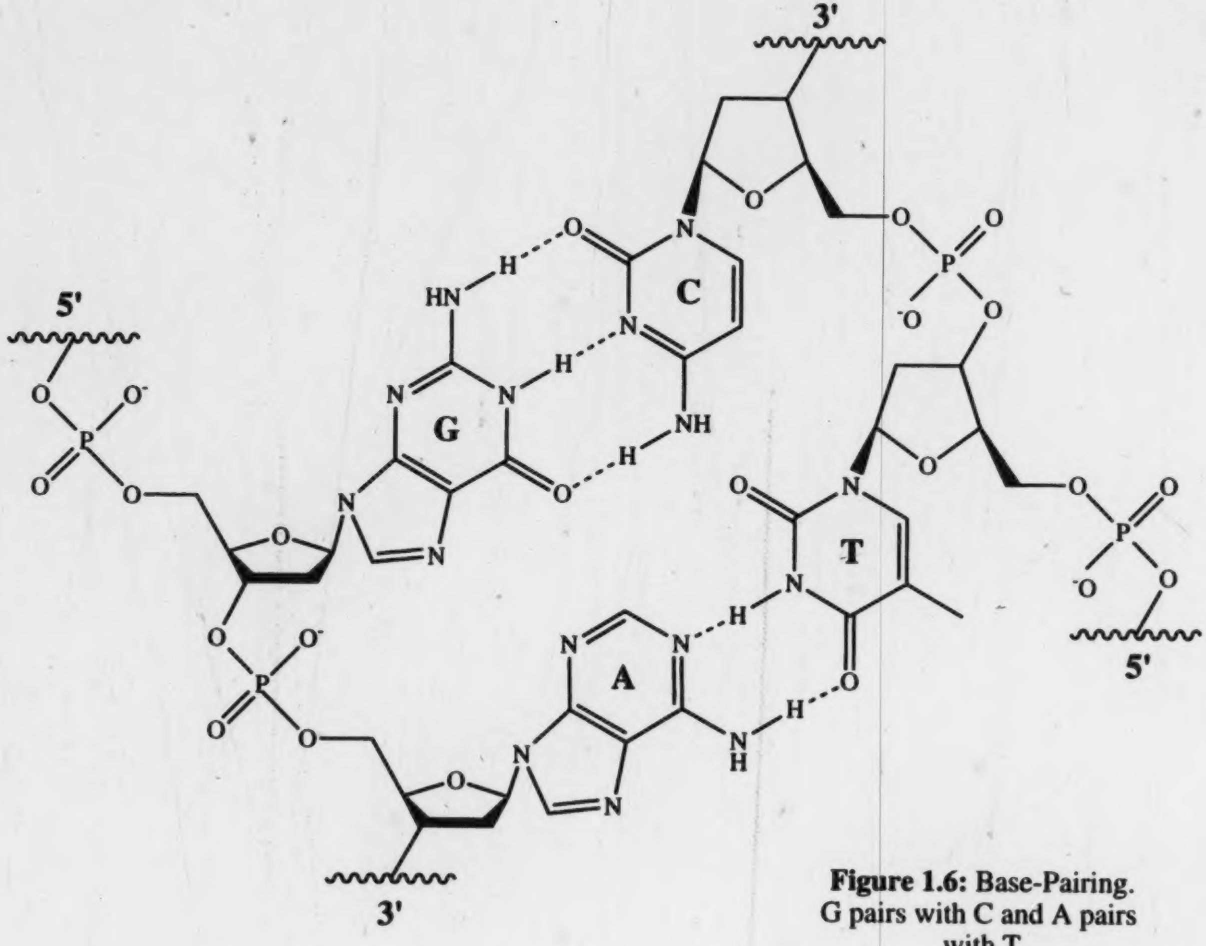

Figure 1.6: Base-Pairing. G pairs with C and A pairs with T

template are made. Figure 1.7 illustrates the general procedure for fragment generation in cycle sequencing, beginning with gene cloning. Note that the base sequences used are hypothetical.

Gene cloning is a method by which a segment of DNA can be amplified (the number of identical copies of the DNA is increased), and is performed before cycle sequencing on the unknown DNA. To begin, the DNA segment of unknown sequence, or template, is enzymatically inserted into a circular cloning vector (Figure 1.7-a), a circular piece of DNA of known sequence. The insertion point into the cloning vector is the same for all inserts using a given enzyme, meaning that the sequence just before the insert is the same; this characteristic is used to advantage when targetting the primers (discussed below). The vector and insert are amplified in bacteria (such as *Escherichia coli*) (Figure 1.7-b, -c), isolated (Figure 1.7-d), and divided into four vials.

To each vial are added a number of reagents (whose functions and reactions become clear in the ensuing paragraph on chain extension): a radiolabelled primer (radioactively-labelled oligonucleotide, ~ 15 - 25 nucleotides long), the four 2'-deoxynucleotide triphosphates or "dNTPs" (dATP, dCTP, dGTP and dTTP), some version of a DNA polymerase enzyme (often Taq polymerase from *Thermus aquaticus* is used), and one of the four 2', 3'-dideoxynucleotide triphosphates or "ddNTPs" (ddATP, ddCTP, ddGTP or ddTTP). The vials are put a into thermocycler which is set to alternate between two temperatures: 70 °C for annealing and chain extension, and 95 °C for denaturing the fragments produced.

70 °C: The primer (an oligomer, usually 15 - 25 nucleotides in length) is synthesised to bind or "anneal" specifically to the vector's universal binding sites (located at or near the 5' end of the template, Figure 1.7-e), and is required for the DNA polymerase enzyme to perform chain extension. Once the primer has

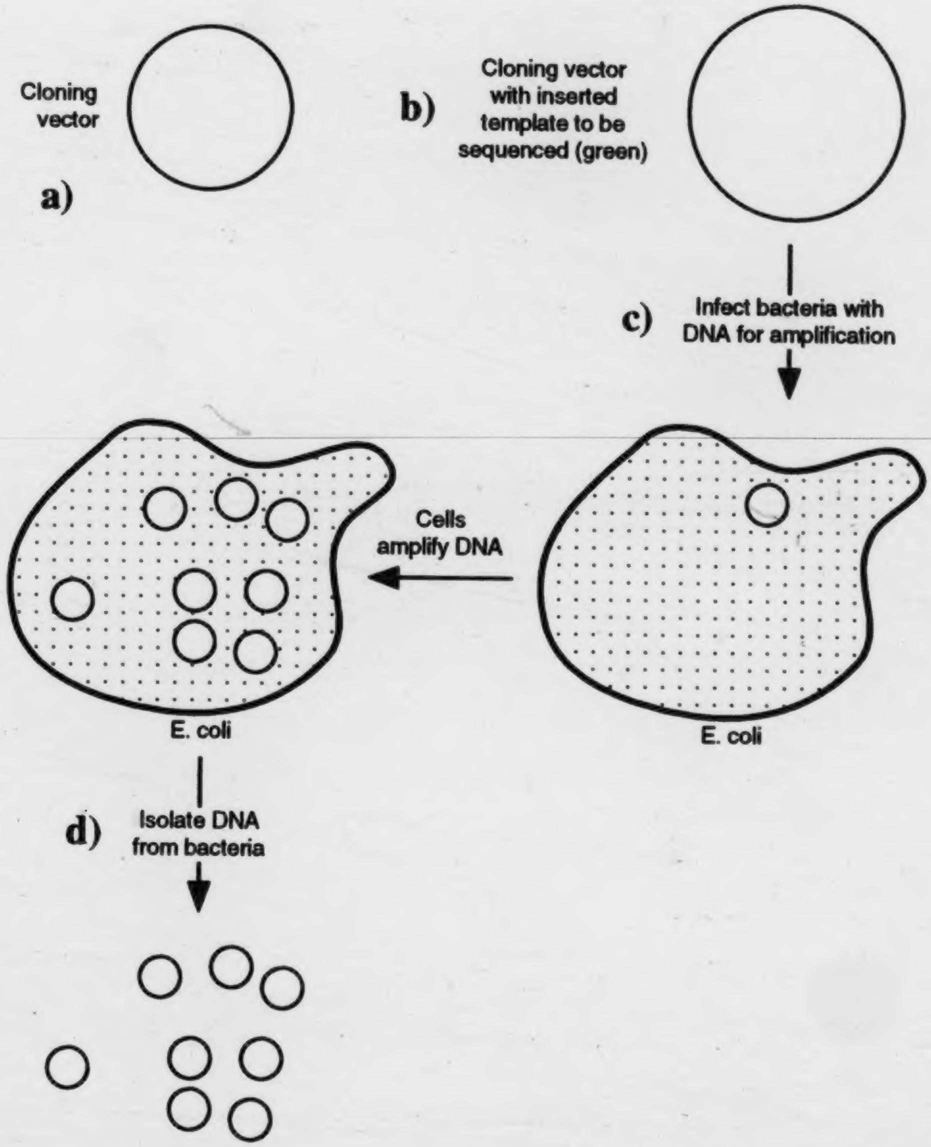
Cloning vector
a)
b)
Cloning vector with inserted template to be sequenced (green)
c)
Infect bacteria with DNA for amplification
Cells amplify DNA
E. coli
E. coli
d)
Isolate DNA from bacteria

Figure 1.7: Gene Cloning and Cycle Sequencing.

a-d: gene cloning; e-g: cycle sequencing (see text for description)

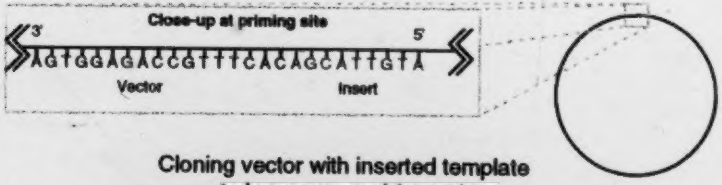
Close-up at priming site
3'
5'
AGTGGAGACCGTTTCACAGCATTGTA
Vector
Insert

e) Cloning vector with inserted template to be sequenced (green)

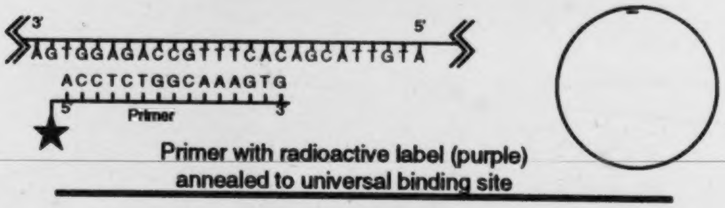
3'
5'
AGTGGAGACCGTTTCACAGCATTGTA
ACCTCTGGCAAAGTG
5'
Primer
3'

f) Primer with radioactive label (purple) annealed to universal binding site

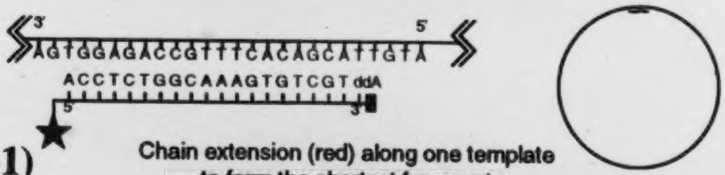
3'
5'
AGTGGAGACCGTTTCACAGCATTGTA
ACCTCTGGCAAAGTGTCGT ddA
5'
3'

g-1) Chain extension (red) along one template to form the shortest fragment

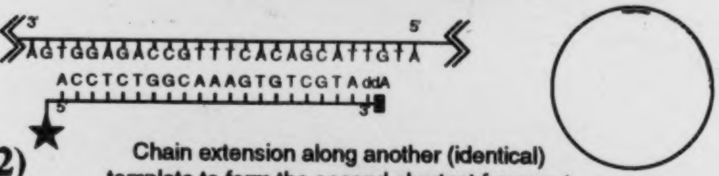
3'
5'
AGTGGAGACCGTTTCACAGCATTGTA
ACCTCTGGCAAAGTGTCGTA ddA
5'
3'

g-2) Chain extension along another (identical) template to form the second shortest fragment

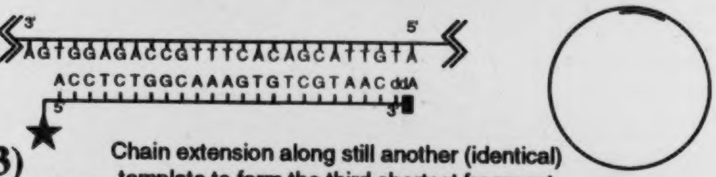
3'
5'
AGTGGAGACCGTTTCACAGCATTGTA
ACCTCTGGCAAAGTGTCGTAAC ddA
5'
3'

g-3) Chain extension along still another (identical) template to form the third shortest fragment

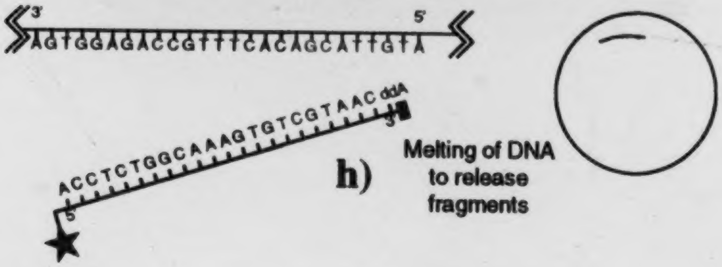
3'
5'
AGTGGAGACCGTTTCACAGCATTGTA
ACCTCTGGCAAAGTGTCGTAAC ddA
5'
3'

h) Melting of DNA to release fragments annealed, DNA polymerase proceeds to attach at the 3' end dNTPs complementary to the template (cleaving off a pyrophosphate, $P_2O_7^{-4}$, for each dNTP added); the chain extension reaction terminates when the enzyme incorporates a ddNTP, since 2', 3'-dideoxyribose (see Figure 1.4) has no 3' hydroxy group, where the next nucleotide's phosphate attaches (Figure 1.7-g-1).

Consider the "A" vial with ddNTP = ddATP. Many reactions are occurring simultaneously in this vial, with the ddATPs being incorporated at different chain lengths, so all the possible A-terminated fragments are produced in the "A" vial (the three shortest fragments are shown in (Figure 1.7-g-1, -g-2 and -g-3). Similarly, the same procedure (using ddCTPs, ddGTPs or ddTTPs) performed in the other 3 vials produces C-, G- and T-terminated fragments. This stage takes about 45 s.

It should be noted that because the primer binds to the cloning vector at a specific, known location (the universal priming site), and not to the unknown DNA insert, an identical primer may be used for any unknown DNA (regardless of its sequence) inserted at that location; such a primer is called a universal primer.

95 °C: At this slightly higher temperature, double stranded DNA melts - the two strands come apart. Thus the fragments just produced are now released into the solution (Figure 1.7-h). It is these complementary fragments which are separated in the gel.

For the beginning of the next cycle, the thermocycler returns to 70 °C, new primer anneals, and another series of fragments is produced.

The cycle is repeated as many times as required to amplify the sample. For each cycle, the concentration of the sample fragments increases by an amount equal to the concentration of the cloning vector-insert units. Sufficient reagents are added once, at the beginning, to last the n-cycle duration (typically ~ 30 cycles[44]).

II. Separation of Fragments

Once the four series of fragments have been generated, they are separated by means of gel electrophoresis (see section 1.2.2, which deals with capillary gel electrophoresis; whether in the form of a slab, as described below, or in a capillary, as used in Chapter 2, the principle of separation is the same).

A gel polymer solution (typically polyacrylamide) is prepared and poured into a slab form; once the gel is set, the DNA sample fragments are applied in four lanes of the gel at the cathodic, or negatively charged, end (one lane for each of the A-, C-, G- and T-terminated series of fragments, Figure 1.8-a), and a potential is applied along the length of the gel (~ 10-50 V/cm). The fragments migrate under the influence of the field, separating on the basis of size (as described in section 1.2.2 above) such that the shortest fragments (primers) migrate the fastest and the furthest, the next shortest (primer + 1 nucleotide) migrate second furthest, etc. After sufficient time (8-14 h), the electrophoretic separation is complete, and the position of the fragments on the gel must be determined.

III. Interpretation of Separation

All the fragments of a given length migrate at approximately the same velocity within a band; a distinct band exists for each possible fragment length. The different fragment lengths may be compared using the distance through the gel migrated by each band of fragments, so it is the relative positions of these bands which need to be determined.

The positions of the four series of fragments are determined by making an X-ray image, or autoradiograph, of the gel. The X-ray sensitive photographic

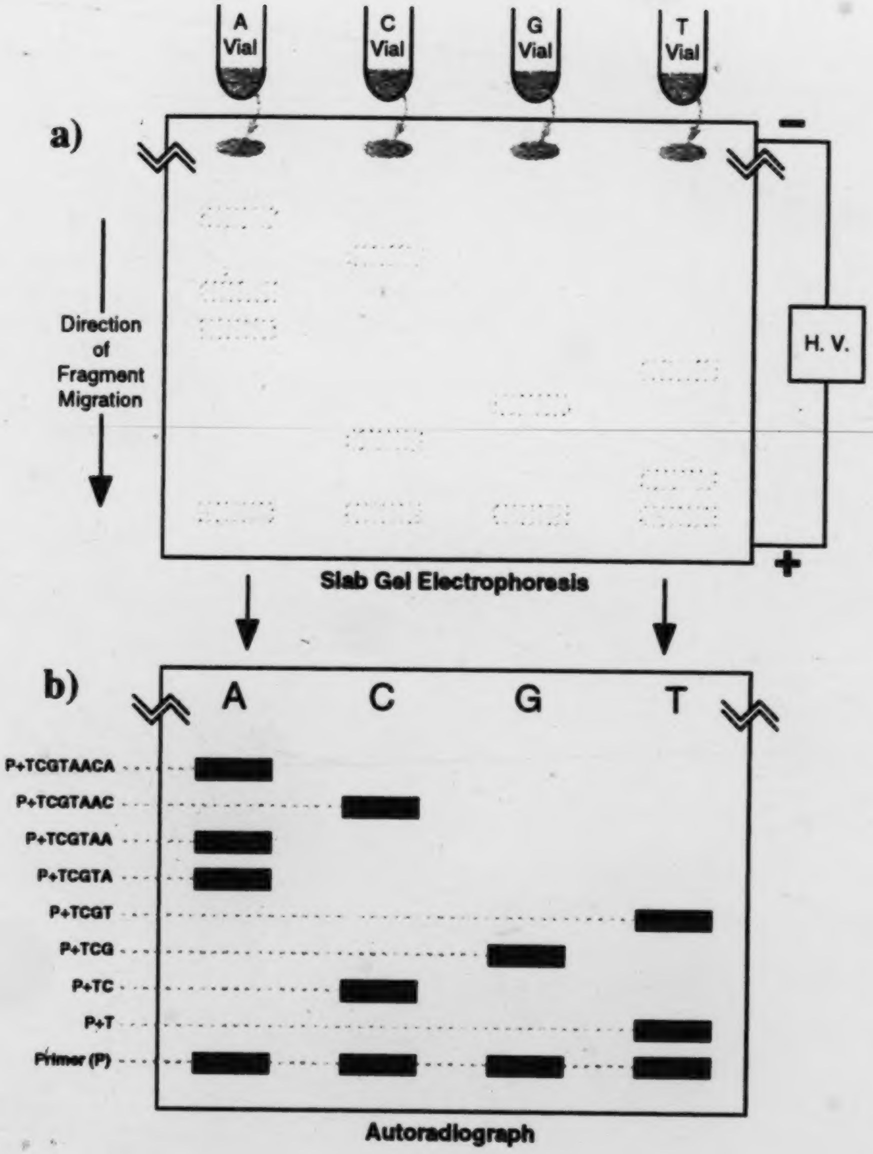
a)
A Vial
C Vial
G Vial
T Vial
−
Direction of Fragment Migration
H. V.
+
Slab Gel Electrophoresis
b)
A
C
G
T
P+TCGTAACA
P+TCGTAAC
P+TCGTAA
P+TCGTA
P+TCGT
P+TCG
P+TC
P+T
Primer (P)
Autoradiograph

Figure 1.8: DNA Fragment Separation and Sequence Interpretation.

a) slab gel separation of DNA fragments, and

b) reading the sequence from the bands in the autoradiograph plate is placed on top of the slab gel, and the bands of fragments mark their position by means of their radioactively labelled primers. The *complementary* sequence can then be read directly from the autoradiograph; in the following example, the hypothetical autoradiograph of Figure 1.8-b is used. Beginning at the anodic (or positively charged) end of the image, the first band is for the shortest fragment, the primer, and is seen in all four lanes. The second band is the primer + 1 nucleotide and is seen only in the T lane, so the terminal nucleotide (the first of the unknown sequence) is a T, and thus the unknown sequence begins with 5'-T-3'. The third band is the primer + 2 nucleotides, and is seen in only in the C lane, so the terminal nucleotide (the second of the unknown sequence) is a C, and thus the unknown sequence begins 5'-TC-3'. The fourth band in the G lane means the sequence begins 5'-TCG-3'; using the bands of progressively longer fragments, the sequence may be read as 5'-TCGTAACA-3'. The original sequence (complementary to that read on the gel) is thus 3'-AGCATTGT-5' in this region of the template. The procedure of reading the sequence directly from the autoradiograph is called base-calling (it is common practice to refer to nucleotides by their bases). Approximately 500 bases of sequence are typically generated per run.

IV. Sequencing Strategies, Accuracy and Redundancy

Let us assume we wish to sequence a substantial length of DNA, say a particular gene which codes for a protein of interest. An extremely short[41] gene of 75 bases may simply be cycle sequenced in one run, however longer genes (some are known to be in excess of 2300 kb (kb = kilobase)) cannot, given the ~ 500 base/run limitation in read length (which stems from biased reptation, discussed in section 1.2.2). For the longer gene, two main sequencing stategies exist for providing the template DNA (from which Sanger sequencing may proceed) in such a way that the whole gene is sequenced: the random strategy, also referred to as shotgun sequencing, and the directed strategy consisting of several variations of which only one, primer walking, will be discussed. These two strategies are illustrated in Figure 1.9.

Shotgun Sequencing: Using shotgun sequencing[45], the gene would first be physically broken into smaller fragments, 2-4 kb average length, usually by sonication. The fragment ends are then repaired enzymatically, and the fragments are electrophoresed through a slab gel to select the fragments in the 1.5-3 kb size range which are suitable for Sanger sequencing, performed next as described above. Since the generation of fragments is random, a statistical approach is invoked: to obtain the continuous sequence for the whole gene, enough fragments must be sequenced so that there is sequence overlap between the fragments, allowing the gene sequence to be constructed from the consensus of the overlapping fragment sequences. The base-called sequence of each fragment is termed the *raw* sequence, while the sequence arrived at by consensus of fragment raw sequences is called the *finished* sequence (and not *consensus* sequence, which has a different meaning in genetics). Sequencing the number of fragments required is equivalent, in terms of length, to sequencing the entire gene 5 to 10 times over, which is referred to as 5 to 10 times redundancy; shotgun sequencing is illustrated in Figure 1.9-a. In one example of shotgun sequencing[46], a total of 94.6 kb of DNA required 1577 fragments of average read length of 441 bases for an overall redundancy of $1577 \bullet 441/94\,600 = 7.4$; in a second example[47], a 35.3 kb length required an average redundancy of 8.4. That both large amounts of DNA must be sequenced, and that equally large amounts of raw sequence must be processed are the shotgun strategy's biggest flaws; to its credit, however, are the facts that the universal primer may be used for all templates, and that template generation is random and relatively easy to perform.

a) Shotgun Sequencing

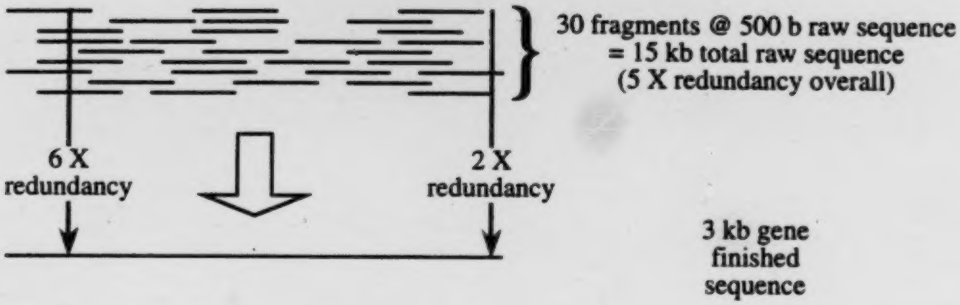
30 fragments @ 500 b raw sequence
= 15 kb total raw sequence
(5 X redundancy overall)
6 X
redundancy
2 X
redundancy
3 kb gene
finished
sequence

b) Primer Walking
(directed priming)

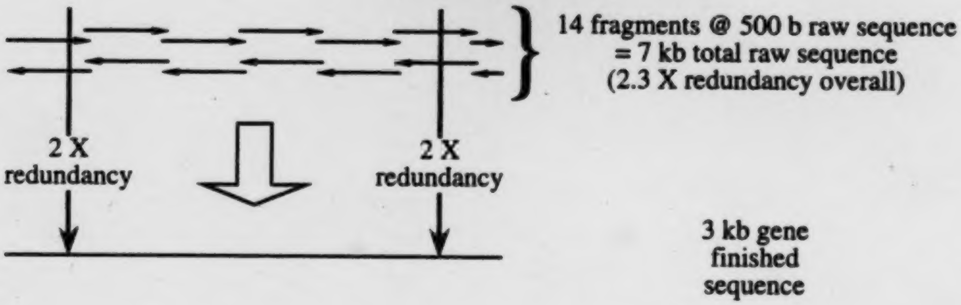
14 fragments @ 500 b raw sequence
= 7 kb total raw sequence
(2.3 X redundancy overall)
2 X
redundancy
2 X
redundancy
3 kb gene
finished
sequence

Figure 1.9: Shot Gun Sequencing and Primer Walking. Finished Sequence assembled from a) random DNA fragments by Shotgun sequencing with high redundancy, and b) ordered, successive fragments by primer walking with low redundancy

Included in the redundancy factor must be the fact that, for various reasons, the accuracy of the base-called sequence in each run is not perfect. This applies to both random and directed strategies. Errors in the experimentally determined sequence may arrise from the fact that some of ssDNA Sanger sequencing fragments double onto themselves over some fraction of their length, making their effective length shorter, causing their band to migrate with the shorter fragments, and creating a hole in the band pattern (and hence base-called sequence) where their band would occur at full length. This phenomenon is referred to as a compression, and is more pronounced in GC-rich DNA templates, owing to stronger GC base pairing compared to AT pairing (three hydrogen bonds for GC versus two for AT). Also, base-calling errors due to weak or unresolved bands contributes to sequence inaccuracy. Acceptable raw sequencing accuracy is considered to be ≥ 97%. With each base in the sequence detemined several times in different fragments, an error in one fragment is made obvious by the consensus in sequence of the other overlapping fragments.

Primer Walking: The simplest directed method (conceptually), primer walking, is described as an illustration to the directed strategy; the reader is directed to other sources for other types of directed sequencing[48, 49]. In the simplest form of primer walking [46, 50-52], called *directed priming*[50], the entire gene (or an enzymatically cleaved fraction if the whole gene is too large) is incorporated into the cloning vector, and, for the first run, Sanger sequencing is primed at the universal primer site. The first ~ 500 bases of sequence are determined and the last portion of sequence in the first run is used to design a primer for the second run. The second run is therefore begun very close to the end of the first, minimising overlap, and the sequence is extended another 500 bases; this is continued for the entire length of the gene being sequenced, and repeated in the opposite direction with the complementary strand, as illustrated in

Figure 1.9-b. In a faster (albeit less efficient in terms of redundancy) version of primer walking, called *random priming*[50], several randomly generated primers are used to start sequencing at several points along the gene, and then directed priming is used to fill in the sequence between primers. The gain in sequencing speed for random priming (since several areas can be sequenced at once) comes at the cost of slightly higher redundancy.

Either of these two methods of primer walking is much more efficient than shotgun sequencing in terms of redundancy. The redundancy for primer walking depends on the length of the primer and whether directed or random priming is used, but ranges[50, 53] between 2 and 3; in essence, the redundancy need only account for sequencing inaccuracy. However, the main drawback of primer-walking is that a new primer must be synthesised for each run, and primer synthesis is time-consuming and costly. The concept of modular primers[50-52], wherein any primer is generated as the sum of several shorter oligonucleotides drawn from a pre-made library, has been proposed to negate this deficiency.

In practice, shotgun sequencing is used out of convenience in nearly all large-scale sequencing projects[54] for the majority (95%) of the sequencing length, and primer walking is used to fill in any gaps in the sequence.

1.3.2.B Modifications to Sanger Sequencing for Fluorescence Detection

Several fluorescence detection modifications to Sanger sequencing have been introduced and integrated into commercial sequencers, three of which are briefly discussed below.

The ABI 373 and 377 slab gel sequencers (Applied Biosystems, Foster City, California) and a number of non-commercial sequencers, including the one described herein, make use of a four colour, laser induced fluorescence (LIF) detection scheme, in lieu of the traditional autoradiography method just described. The first such instrument used an Ar^+ laser alternately filtered for the 488 or 514 nm line, and a 2 mm ID gel-filled capillary; this was the ABI prototype[55]. The principle incentive for moving to fluorescence detection is the relative ease with which it can be automated for base-calling. Another advantage is 4X higher throughput, since the A-, C-, G- and T-terminated fragment series can be run on a single lane of a slab gel or in a single gel-filled capillary.

There are two differences in the Sanger sequencing protocol. First, instead of using a single radiolabelled primer in all four fragment-generating reactions, four spectrally distinct, fluorescently labelled primers are used, one in each reaction. Since each of the A-, C-, G- and T-terminated fragment series fluoresces at a different wavelength, they can all be run on the same lane or capillary. The second difference is that the detection system is obviously no longer an X-ray photographic plate, but an LIF detection system located at the anodic end of the gel which spectrally discriminates between the four primer dyes. Detection is accomplished with one or two lasers as excitation sources and (1) a rotating filter wheel with optical filters at the emission wavelengths of the four dyes, or (2) a dispersive element (prism or grating), either of which is paired with photocells (photomultiplier tubes (PMTs), avalanche photodiodes (APDs) or a charge coupled device (CCD)) to measure the fluorescence amplitude. The signals from the photocell and dispersive element are recorded by a computer and generate a four colour electropherogram. Peaks in the electropherogram confirm the presence of a "band" of a particular fragment, while the colour of the fluorescence determines whether the terminal nucleotide of the fragment is A-, C-, G- or T.

The du Pont prototype[56] (E. I. du Pont de Nemours & Company, Wilmington, Delaware), while resembling the ABI system, is distinguished from the latter by several differences. Fluorescently-labelled ddNTPs are used instead of labelled primers (allowing the four A-, C-, G- and T-terminated fragment series to be synthesised together in one step), and the four dyes, excited with only the 488 nm line of the Ar^+ laser, have very closely spaced emission maxima (all four only span 21 nm). Detection of the fluorescence from a band occurrs simultaneously at two PMTs, each with different optical filters, such that the relative intensity of the signals from the two PMTs is characteristic of the fluorescing dye.

The Pharmacia approach[57] is most similar to the radiolabelled strategy in that only one fluorescently-labelled primer is used for all four DNA fragment series. This means that four separate reactions are carried out to generate the four fragment series, and that each series must be applied to its own lane. While the design affords no gains in sample throughput or in the efficiency of sample preparation, it does not suffer from difficulties in spectral overlap of the four dyes used in the ABI or du Pont systems, which simpifies base-calling.

1.3.2.C Other Sequencing Methods

Gel-sieving methods have seen considerable growth since the inception of the Sanger sequencing protocol[43] in 1977, at which time the preferred method was slab gel electrophoresis with autoradiograph images for detection. Since then, gel-filled capillaries[58-63], gel-filled micromachined capillaries[64] and ultrathin slab gels[65, 66] have been employed for DNA sequencing, all three of which have significantly better heat dissipating abilities compared to conventional slab gels; this greatly reduces the amount of Joule heating observed and allows higher electric fields (by a factor of ~ 4 or more) to be applied, resulting in shortened run times. Several instruments[61-63, 67-70] have been constructed in which many capillaries are arranged in parallel to increase sample throughput, similar to parallel lanes in a gel.

DNA sequencing technology has witnessed substantial diversification over the last 20 years. Quite apart from the traditional approach of gel-sieving of fragments, a number of innovative, non-separation methods have appeared. Mass spectrometry with various ionisation methods have been applied to sequencing[71-74]. While promising in terms of its ability to perform exceedingly rapid analyses with simplified sample preparation, mass spectrometry faces challenges in terms of sample consumption and read length (number of bases sequenced per run); using matrix assisted laser desorption/ionisation (MALDI), approximately 50 nucleotides may sequenced from a single sample[73, 74]. Another interesting approach is sequencing by hybridisation, or SBH[75, 76]. In this method, a library of short oligonucleotide probes of known sequence are exposed to unknown DNA; where the sequence is complementary, hybridisation occurs, and the labelled immobilised complex is detected. The information is processed with a reconstruction algorithm. While offering high sample throughput capabilities for sequencing, SBH may not be as successful in regions of DNA with multiple tandem repeats[76], but would at least be useful as a complementary sequencing method to traditional gel separations.

1.4 Sheath Flow Cuvettes and Micromachining

Sheath flow cuvettes are flow-through detection cells used in this and other instruments. The glass cuvette employed in the sequencer described in Chapter 2 was custom designed by the process of micromachining, and so micromachining in glass is described next.

1.4.1 Glass structure and etching

In subsequent sections, the procedures involved in patterning glass and producing detection cells are outlined. Since the chemical and physical treatment of various glasses will be referred to, a brief introduction to the nature of glass and its treatment seems warranted.

Simply put, a glass is an amorphous solid; for a substance to be amorphous in chemical terms means that it is not crystalline, or has no long range order to its molecular structure. While certain materials are more disposed to form glasses than others, the property of being glassy or vitreous is not wholly inherent. In fact it is possible to make glasses from materials whose structures are normally ordered, such as metals, and conversely make crystals from normally glassy materials. The process of "splat cooling" is used to very rapidly cool and solidify molten metals without crystallisation[77]. Diamond and graphite are well known allotropes of carbon, but a glassy allotrope may also be prepared, and is used to make the carbon fibres used for structural reinforcement in skis, tennis racquets, etc.[77]. Quartz (SiO_2) has both a glassy and a crystalline structure, as shown[78, 79] in Figure 1.10. The building block of both forms is a tetrahedron with a central silicon atom covalently bonded to four oxygen atoms, one at each apex. From Figure 1.10, one may see that in glassy quartz, there is order over a short range, but that the order deteriorates over several silicon-oxygen tetrahedra. In crystalline quartz, there is a regular, repeating series of these tetrahedra.

Most glasses which are designed for visible wavelength transparency may be thought of as impure quartz: their composition is mostly silica (SiO_2), with other oxides (those of boron, phosphorus, and of a variety of metals including Li, Na, K, Mg, Ca, Al, Pb) added to obtain certain chemical or physical properties. Decorative "crystal" is a given higher refractive index (allowing it to glitter) by the addition of PbO. Thermal expansion is reduced by the addition of boron oxide (B_2O_3)[79]; such glasses are referred to as borosilicates. The composition of the glass used in all the patterning in this work, Pyrex #7740 (Corning Glass

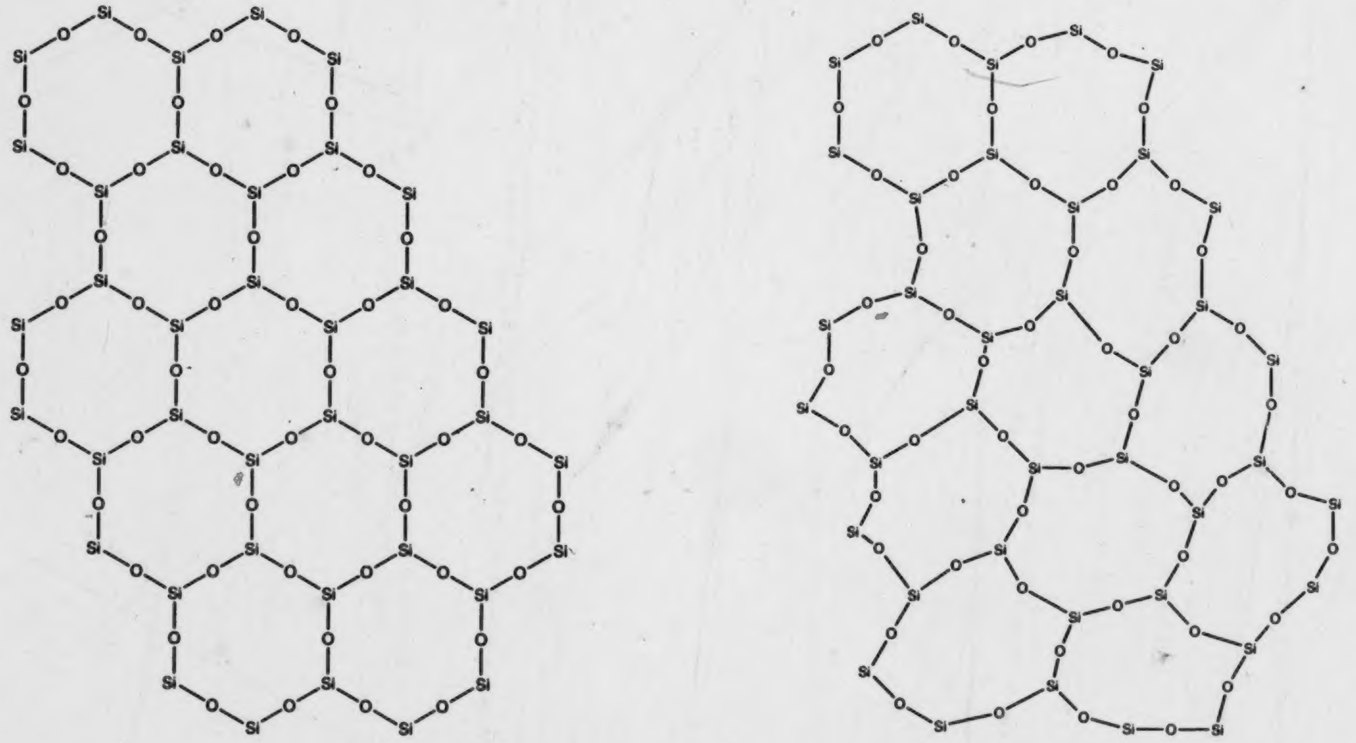

Figure 1.10: Crystalline and Amorphous Silica.
Two dimensional views of crystalline (left) and amorphous (right) silica
(adapted from Doremus' "Glass Science" and Maloney's "Glass in the Modern World")

Works, Corning, New York), is 80.6% SiO_2, 13.0% B_2O_3, 4.0% Na_2O, 2.3% Al_2O_3 and 0.1% miscellaneous traces[80].

Etching of borosilicate glass (henceforth referred to as "glass") is usually accomplished with hydrofluoric acid in any of a number of aqueous solutions. The reactions of HF with SiO_2 are not altogether clear, with many workers[79, 81-83] in the field making reference to an article by Judge[84] in 1971. Judge showed that silica is dissolved by both HF and HF_2^-, but that the latter is much more reactive. The rate of reaction varies linearly with [HF] and [HF_2^-], and is temperature dependent. A variety of products are thought to result, one of which is possibly the hexafluorosilicate anion, SiF_6^{-2}. One likely reaction[81] is thus:

$$SiO_2 + 6HF \rightarrow H_2SiF_6 + 2H_2O \qquad (1.21)$$

Aqueous solutions used for glass etching are usually either buffered or unbuffered solutions of HF. The advantage of buffering HF with NH_4F is to stabilise concentrations over the time span of one or several etches. However, it is likely the fluoride anion which is being buffered[81], controlling the relative concentrations of F^-, HF and HF_2^-.

Increasing glass porosity (porosity is a measure of non silica constituents in the glass) tends to increase the rate of the etching reaction, since the dissolution of given amount of silica backbone liberates more material in a borosilicate glass than in pure silica.

1.4.2 Micromachining

"Micromachining is the surface treatment of a solid material to obtain mechanical microstructures by using film deposition, photolithography, etching and bonding."[85] Micromachining has been applied to a multitude of fields, including sensors for pressure[86] and for micro flow systems[87], a feedback flow control system[88] and analytical separations. Within separation science, micromachining has been used for gas chromatography[89], liquid chromatography[90] and capillary electrophoresis[64, 91-93]. Some good reviews of micromachining as applied to silicon[94] and as applied to analytical separations[95] have been written. Micromachining owes its impressively miniature and precise capabilities to the microelectronics industry which developed silicon patterning techniques for producing chip-sized integrated circuits.

A simple example of micromachining a plus sign (+) protruding from the surface of a glass substrate is depicted in Figure 1.11. *General procedures and considerations* for each of the steps are outlined below (specific experimental details are found in section 3.2.1):

1.4.2.A Creation of a master mask

The mask serves as the design template, and is a tool used in the fabrication of the patterned substrate. For very simple designs, a photocopied transparency or a photographic slide may be used. If finer resolution is needed, the design is drawn with the use of software and the mask is commercially fabricated by plating metal (in the design pattern) onto a glass plate to specified tolerances.

1.4.2.B Substrate preparation

The substrate is the piece of silicon or glass which is to be patterned; it must be scrupulously clean so that the subsequently added layers (often silica for silicon substrates, metal(s) for glass substrates) adhere properly. Poor adhesion of these adsorbed layers has been shown to cause dramatic undercutting and loss of resolution of the pattern being applied[82]. A variety of cleaning methods are used for cleaning the substrate, including simple scrubbing with soap and water,

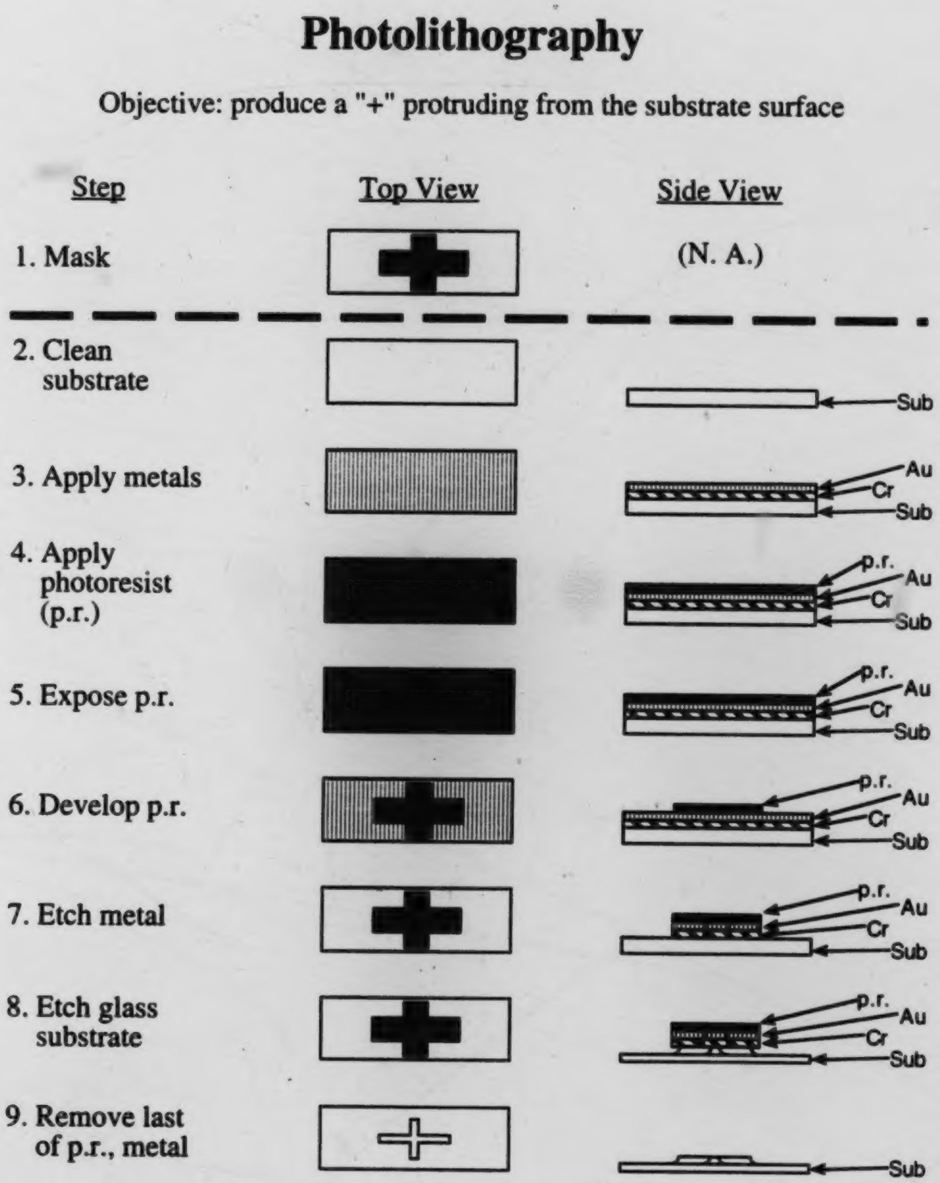
Photolithography
Objective: produce a "+" protruding from the substrate surface
Step
Top View
Side View
1. Mask
(N. A.)
2. Clean substrate
Sub
3. Apply metals
Au
Cr
Sub
4. Apply photoresist (p.r.)
p.r.
Au
Cr
Sub
5. Expose p.r.
p.r.
Au
Cr
Sub
6. Develop p.r.
p.r.
Au
Cr
Sub
7. Etch metal
p.r.
Au
Cr
Sub
8. Etch glass substrate
p.r.
Au
Cr
Sub
9. Remove last of p.r., metal
Sub

Figure 1.11: Photolithographic Patterning.

(see text for details)

sonication, organic solvent washes, acid washes and plasma cleaning[82]. Surface stress (as may be incurred by polishing) is also thought to affect the rate of etching[81]; in the case of glass, these stresses can be relieved by annealing[79]. Fan and Harrison found that annealing a Pyrex substrate dramatically improved the quality of its patterned surface[96].

1.4.2.C Application of metal film(s)

For glass micromachining, metal layers are intermediate masking layers, and serve to support the photoresist in later steps of wet chemical etching. (In working with silicon, often layers of silica or silicon nitride, Si_3N_4, are grown or deposited). Methods for depositing metal layers include vacuum evaporation and sputtering. In the evaporation method, the substrate is placed inside a large bell jar, which is evacuated to ~ 10^{-7} Torr; the metal to be coated vapourises in a resistively-heated crucible, and condenses on the inside of the jar where the substrates are held. In sputtering a metal film, an Ar^+ plasma bombards a target made of the coating metal, producing a metal vapour; the gaseous metal atoms then condense on the substrate as in the evaporation method. Several descriptions of the process of evaporating[97, 98] and sputtering[97, 99] films have been written.

One or several discrete layers of metals (such as Cr, Au, Cu, Ni, Al) or alloys may be deposited. Chromium adheres well to glass, and is usually applied first; gold fills in the pinholes in the chromium layer, and is adhered to by the photoresist (to which the design pattern is first imparted) better than chromium, and so is often added after the chromium and before the photoresist.

1.4.2.D Application of photoresist

The film of photoresist is analogous to photographic film: where the photoresist film is exposed to UV light, a photochemical reaction occurs, and upon development, an image is visible.

Either a positive or negative photoresist is selected, depending on whether the transparent areas of the mask are to be etched or not, respectively. The viscous photoresist liquid is poured onto the centre of the substrate, and the latter is spun for ~ 30 s. The thickness of the film depends on the spinning speed used. This process is called spin-coating.

Before exposure, the film is given a "soft bake" to dry the photoresist (remove the solvent).

1.4.2.E Exposure

Exposure of the photoresist to UV light is equivalent to "taking the picture". The substrate and master mask are mounted in a mask aligner, aligned and brought together, with the substrate's photoresist in direct contact with the mask's metal pattern. The UV radiation is then shone through the mask onto the substrate for a few seconds. The length of exposure depends on the thickness and type of photoresist and on the age of the lamp.

1.4.2.F Development

The photoresist which was exposed to UV radiation in the previous step is washed away during development. A positive, 1:1 reproduction of the master mask design has therefore been imparted to the photoresist.

During development, the substrate is treated alternately with developer solution and water in an automated instrument. The duration of the development cycle is related to the length of exposure[100]. After developing, the substrate is subjected to a "hard bake", which serves to harden the photoresist, inhibitting its flow, and hence which preserves the pattern as it is reproduced in the layers beneath.

1.4.2.G Pattern metal layers

The pattern in the photoresist layer is now to be propagated through any underlying metal layers. The propagation is accomplished by simply immersing the substrate into appropriate acids (the choice of acid(s) depends on the metal(s) used) to etch away metal not protected by photoresist; the etch lasts until the metal layer is seen to disappear.

1.4.2.H Etch substrate to desired depth

As mentioned earlier, there is a range of buffered and unbuffered hydrofluoric acid solutions from which to choose. The choice of etching solution and conditions will depend on time and surface quality requirements.

The depth of etch can be monitored with a profilometer and regulated by timing.

1.4.2.I Remove remaining photoresist and metal

Once the glass has been etched to the desired depth, the masking layers of photoresist and metal are removed with acetone and acids to leave the bare, patterned substrate.

1.5 Conclusion

It is hoped that the fundamental and applied areas of research which pertain to the work described in next three chapters and which perhaps lie outside the knowledge of the average analytical chemist have been addressed in this first chapter.

The following chapters deal with the actual design, construction and performance of the 16 capillary DNA sequencer (Chapter 2), followed by the design, construction and performance of the sequencer's micromachined detection cell, or sheath flow cuvette (Chapter 3), and finally, a summary of the work done as well as future directions which are recommended based upon this work (Chapter 4).

1.6 References

1. *Understanding our Genetic Inheritance: The U. S. Human Genome Project-The First Five Years 1991-1995 (NIH Publication No. 90-1590)*; National Institutes of Health (U.S.), 1990.
2. *Human Genome News*; NIH/DOE (U.S.), 1993; Vol. 5, No. 4.
3. J. T. G. Overbeek and B. H. Bijsterbosch In *Electrokinetic Separation Methods*; Righetti, P. G., Oss, C. J. v., Vanderhoff, J. W., Eds.; Elsevier/North Holland Biomedical Press, 1979, pp 1-32.
4. A. Tiselius, *Transactions of the Faraday Society* **33,** 524-531 (1937).
5. S. Hjertén, *Chromatographic Reviews* **9,** 122-219 (1967).
6. F. E. P. Mikkers, F. M. Everaerts and T. P. E. M. Verheggen, *Journal of Chromatography* **169,** 11-20 (1979).
7. J. W. Jorgenson and K. D. Lukacs, *Analytical Chemistry* **53,** 1298-1302 (1981).
8. F. E. P. Mikkers, F. M. Everaerts and T. P. E. M. Verheggen, *Journal of Chromatography* **169,** 1-10 (1979).
9. N. J. Dovichi In *Capillary Electrophoresis - Theory and Practice*; Camilleri, P., Ed.; CRC Press: Boca Raton, 1993, pp 25-64.
10. W. G. Kuhr In *Capillary Electrophoresis - Theory and Practice*; Camilleri, P., Ed.; CRC Press: Boca Raton, 1993, pp 65-116.
11. H. J. Issaq, G. M. Janini, K. C. Chan and Z. E. Rassi, *Advances in Chromatography* **35,** 101-169 (1995).
12. D. C. Henry, *Proceedings of the Royal Society of London A* **133,** 106-129 (1931).
13. R. A. Mosher, D. Dewey, W. Thormann, D. A. Saville and M. Bier, *Analytical Chemistry* **61,** 362-366 (1989).

14. V. Pretorius, B. J. Hopkins and J. D. Schieke, *Journal of Chromatography* **99,** 23-30 (1974).

15. C. L. Rice and R. Whitehead, *Journal of Physical Chemistry* **69 (11),** 4017-4024 (1965).

16. K. D. Lukacs and J. W. Jorgenson, *Journal of High Resolution Chromatography & Chromatography Communications* **8,** 407-411 (1985).

17. J. C. Giddings, *Separation Science* **4 (3),** 181-189 (1969).

18. B. M. Olivera, P. Baine and N. Davidson, *Biopolymers* **2,** 245-257 (1964).

19. C. Heller, *Journal of Chromatography A* **698,** 19-31 (1995).

20. D. Figeys and N. J. Dovichi, *Journal of Chromatography* **645,** 311-317 (1993).

21. T. Tanaka, *Scientific American* **244 (1),** 124-138 (1981).

22. P. D. Grossman and D. S. Soane, *Biopolymers* **31,** 1221 (1991).

23. G. W. Slater and J. Noolandi, *Biopolymers* **28,** 1781-1791 (1989).

24. G. W. Slater and J. Noolandi, *Physical Review Letters* **55 (15),** 1579-1582 (1985).

25. G. W. Slater and J. Noolandi, *Biopolymers* **25,** 431-454 (1986).

26. D. Rodbard and A. Chrambach, *Proceedings of the National Academy of Sciences, USA* **65,** 970-977 (1970).

27. A. G. Ogston and C. F. Phelps, *Biochemical Journal* **78,** 827-833 (1961).

28. A. G. Ogston, *Transactions of the Faraday Society* **54,** 1754-1757 (1958).

29. O. J. Lumpkin, P. Déjardin and B. H. Zimm, *Biopolymers* **24,** 1573-1593 (1985).

30. O. J. Lumpkin and B. H. Zimm, *Biopolymers* **21,** 2315-2316 (1982).

31. L. S. Lerman and H. L. Frisch, *Biopolymers* **21,** 995-997 (1982).

32. L. Mitnik, L. Salomé, J. L. Viovy and C. Heller, *Journal of Chromatography A* **710,** 309-321 (1995).

33. P. G. deGennes, *Journal of Chemical Physics* **55 (2),** 572-579 (1971).

34. M. Doi and S. F. Edwards, *Journal of the Chemical Society - Faraday Transactions II* **74,** 1789-1801 (1978).

35. T. Duke, J.-L. Viovy and A. N. Semenov, *Biopolymers* **34,** 239-247 (1994).

36. C. Heller, T. Duke and J. L. Viovy, *Biopolymers* **34,** 249-259 (1994).

37. J. D. Watson and F. H. C. Crick, *Nature* **171,** 737 (1953).

38. M. H. F. Wilkins, A. R. Stokes and H. R. Wilson, *Nature* **171,** 738 (1953).

39. R. E. Franklin and R. G. Gosling, *Nature* **171,** 740 (1953).

40. J. D. Watson, *The Double Helix*; W. W. Norton & Company: New York, 1980.

41. T. A. Brown, *Genetics: a Molecular Approach*, 2nd ed.; Chapman and Hall: London, 1992.

42. W. Saenger, *Principles of Nucleic Acid Structure*; Springer-Verlag: New York, 1984.

43. F. Sanger, S. Nicklen and A. R. Coulson, *Proceedings of the National Academy of Science, USA* **74,** 5463 (1977).

44. P. Roos, Personal Communication, 1996.

45. A. Martin-Gallardo, J. Lamerdin and A. Carrano In *Automated DNA Sequencing and Analysis*; Academic Press: London, 1994, p 368.

46. T. Hunkapiller, R. J. Kaiser, B. F. Koop and L. Hood, *Science* **254,** 59-67 (1991).

47. B. F. Koop, L. Rowan, W.-Q. Chen, P. Deshpande, H. Lee and L. Hood, *BioTechniques* **14 (3),** 442-447 (1993).

48. C. H. Martin, C. A. Mayeda, C. A. Davis, M. P. Strathmann and M. J. Palazzolo In *Automated DNA Sequencing and Analysis*; Academic Press: London, 1994, p 368.

49. C. M. Berg, G. Wang, K. Isono, H. Kasai and D. E. Berg In *Automated DNA Sequencing and Analysis*; Academic Press: London, 1994, p 368.

50. F. W. Studier, *Proceedings of the National Academy of Science, USA* **86,** 6917-6921 (1989).

51. J. Kieleczawa, J. J. Dunn and F. W. Studier, *Science* **258,** 1787 (1992).

52. L. Kotler, I. Sobolev and L. Ulanovsky, *BioTechniques* **17 (3),** 554-558 (1994).

53. H. Voss, S. Wiemann, D. Grothues, C. Sensen, J. Zimmermann, C. Schwager, J. Stegemann, H. Erfle, T. Rupp and W. Ansorge, *BioTechniques* **15 (4),** 714-721 (1993).

54. E. Y. Chen In *Automated DNA Sequencing and Analysis*; Academic Press: London, 1994, p 368.

55. L. M. Smith, J. Z. Sanders, R. J. Kaiser, P. Hughes, C. Dodd, C. R. Connell, C. Heiner, S. B. H. Kent and L. E. Hood, *Nature* **321,** 674-679 (1986).

56. J. M. Prober, G. L. Trainor, R. J. Dam, F. W. Hobbs, C. W. Robertson, R. J. Zagursky, A. J. Cocuzza, M. A. Jensen and K. Baumeister, *Science* **238,** 336-341 (1987).

57. W. Ansorge, B. S. Sproat, J. Stegemann and C. Schwager, *Journal of Biochemical and Biophysical Methods* **13,** 315-323 (1986).

58. H. Swerdlow, J. Z. Zhang, D. Y. Chen, H. R. Harke, R. Grey, S. Wu and N. J. Dovichi, *Analytical Chemistry* **63,** 2835 (1991).

59. H. Lu, E. Arriaga, D. Y. Chen and N. J. Dovichi, *Journal of Chromatography A* **680,** 497 (1994).

60. S. Carson, A. S. Cohen, A. Belenkii, M. C. Ruiz-Martinez, J. Berka and B. L. Karger, *Analytical Chemistry* **65,** 3219 (1993).

61. K. Ueno and E. S. Yeung, *Analytical Chemistry* **66,** 1424 (1994).

62. S. Takahashi, K. Murakami, T. Anazawa and H. Kambara, *Analytical Chemistry* **66,** 1021 (1994).

63. X. C. Huang, M. A. Quesada and R. A. Mathies, *Analytical Chemistry* **64,** 2149 (1992).

64. A. T. Woolley and R. A. Mathies, *Analytical Chemistry* **67,** 3676 (1995).

65. D. Chen, M. D. Peterson, R. L. Brumley, Jr., M. C. Giddings, E. C. Buxton, M. Westphall, L. Smith and L. M. Smith, *Analytical Chemistry* **67,** 3405 (1995).

66. A. J. Kostichka, M. L. Marchbanks, R. L. Brumley, Jr., H. Drossman and L. M. Smith, *Bio/Tecnology* **10,** 78 (1992).

67. R. A. Mathies and X. C. Huang, *Nature* **359,** 167-169 (1992).

68. R. J. Zagursky and R. M. McCormick, *BioTechniques* **9 (1),** 74-79 (1990).

69. H. Kambara and S. Takahashi, *Nature* **361,** 565-566 (1993).

70. J. A. Taylor and E. A. Yeung, *Analytical Chemistry* **65,** 956-960 (1993).

71. C. J. McNeal, S. A. Narang, R. D. MacFarlane, H. M. Hsiung and R. Brousseau, *Proceedings of the National Academy of Science, USA* **77,** 735-739 (1980).

72. L. Grotjahn, H. Blöcker and R. Frank, *Biomedical Mass Spectrometry* **12,** 514 (1985).

73. C. H. W. Chen, N. I. Taranenko and S. L. Allman, *AMS '95: Third International Conference on Automation in Mapping and DNA Sequencing*, Berkeley, California, 1995; 34.

74. W. H. Benner, S. D. Fuerstenau, J. M. Jaklevic and M. J. Palazzolo, *AMS '95: Third International Conference on Automation in Mapping and*

DNA Sequencing, November 5th -8th, 1995, Berkeley, California, 1995; 35.

75. S. P. A. Fodor, R. P. Rava, X. C. Huang, A. C. Pease, C. P. Holmes and C. L. Adams, *Nature* **364,** 555 (1993).

76. R. Drmanac, S. Drmanac, Z. Strezoska, T. Paunesku, I. Labat, M. Zeremski, J. Snoddy, W. K. Funkhouser, B. Koop, L. Hood and R. Crkvenjakov, *Science* **260,** 1649 (1993).

77. I. S. Butler and J. F. Harrod, *Inorganic Chemistry: Principles and Applications*; Benjamin/Cummings: Redwood City, CA, 1989.

78. F. J. T. Maloney, *Glass in the Modern World - A Study in Materials Development*; Doubleday & Company: Garden City, New York, 1967.

79. R. H. Doremus, *Glass Science*; John Wiley and Sons: Toronto, 1973.

80. *Laboratory Glassware Specifications Guide*; Corning Glass Works, Corning, New York, 1985.

81. S. K. Ghandhi, *VLSI Fabrication Principles*; John Wiley and Sons, 1983.

82. W. Kern and C. A. Deckert, *Chemical Etching*; Academic Press: New York, 1978.

83. W. Kern, *RCA Review* **47,** 186 (1986).

84. J. S. Judge, *Journal of the Electrochemical Society* **118 (11),** 1772 (1971).

85. A. Manz, J. C. Fettinger, E. Verpoorte, H. Lüdi, H. M. Widmer and D. J. Harrison, *Trends in Analytical Chemistry* **10 (5),** 144 (1991).

86. Y. Kewamura, K. Sato, T. Teasawa and S. Tanaka, *Tansducers '87 (4th International Conference on Solid-state Sensors and Actuators, June 2nd - 5th, 1987, Tokyo, Japan)*, Tokyo, 1987; 283.

87. M. Nagata, N. Swart and A. Nathan, *Tansducers '95 (8th International Conference on Solid-state Sensors and Actuators, June 25th - 29th, 1995, Stockholm, Sweden)*, Stockholm, 1995; 447.

88. M. Esashi, *Sensors and Actuators* **A21-A23,** 161 (1990).

89. S. C. Terry, J. H. Herman and J. B. Angell, *IEEE Transactions on Electron Devices* **26,** 1880 (1979).

90. G. Ocvirk, E. Verpoorte, A. Manz, M. Grasserbauer and H. M. Widmer, *Analytical Methods and Instrumentation* **2 (2),** 74 (1995).

91. A. Manz, D. J. Harrison, E. Verpoorte, J. C. Fettinger, A. Paulus, H. Lüdi and H. M. Widmer, *Journal of Chromatography* **593,** 253 (1992).

92. S. C. Jacobson, A. W. Moore and J. M. Ramsey, *Analytical Chemistry* **67,** 2059 (1995).

93. C. S. Effenhauser, A. Manz and H. M. Widmer, *Analytical Chemistry* **67,** 2284 (1995).

94. K. E. Petersen, *Proceedings of the IEEE* **70,** 420 (1982).

95. A. Manz, D. J. Harrison, E. Verpoorte and H. M. Widmer, *Advances in Chromatography* **33,** 1 (1993).

96. Z. H. Fan and D. J. Harrison, *Analytical Chemistry* **66,** 177 (1994).

97. W. H. Ko, *Sensors - A Comprehensive Survey*; VCH Publishers: New York, 1989.

98. C. V. Deshpandey and R. F. Bunshah In *Thin Film Processes II*; Vossen, J. L., Kern, W., Eds.; Academic Press: New York, 1991, pp Chapter II-2.

99. R. Parsons In *Thin Film Processes II*; Vossen, J. L., Kern, W., Eds.; Academic Press: New York, 1991, pp Chapter II-4.

100. C. A. Deckert and D. A. Peters, *Solid State Technology* **23 (1),** 76 (1980).

Chapter 2

CONSTRUCTION AND EVALUATION OF A MULTICAPILLARY DNA SEQUENCER

2.1 Introduction

Chapter 2 deals with the construction and evaluation of a 16 capillary DNA sequencer, and is divided into four main sections: the introduction, 2.1, instrument development, 2.2, instrument performance, 2.3, and finally conclusions, 2.4. This order deviates from the traditional format for presenting research, usually categorised as introduction, experimental procedure, results and discussion, and conclusions. Due to the emphasis on instrument building in this chapter, the experimental work is presented in two main sections: instrument development (2.2), focussing on the construction and optimisation of the instrument and its components, and instrument performance (2.3), focussing on the performance of the instrument, in terms of sensitivity and on an example of four-colour DNA sequencing. Within these sections are several areas of experimentation, each of which is described in whole, from concept to results, without interruption. The last section of the chapter, 2.4, contains conclusions drawn from both the development and characterisation sections, 2.2 and 2.3.

Three principal areas are introduced in section 2.1. In the first section of the introduction, section 2.1.1, a general discussion of the instrument's design and its perceived advantages as applied to DNA sequencing are presented. In section 2.1.2, a few key and perhaps less well-known components, namely the avalanche photodiodes (or APDs, the detection system's transducers) and the gradient refractive index lenses (or GRIN lenses, part of the detection system's optics) are discussed.

2.1.1 Instrument Approach

The International Human Genome Project has provided incentive to build high sample throughput DNA sequencers[1, 2]; the sequencer described herein is targeted specifically at the need for high throughput.

The design of the instrument allows for high throughput and ease of automation. In simple terms, the instrument described in this chapter consists of an array of 16 gel-filled capillaries as the electrophoretic DNA separation medium, a micromachined sheath flow cuvette detection cell into which the capillaries are inserted (discussed at length in Chapter 3) for post column detection, non-scanning imaging detection optics including a rotating filter wheel used to discriminate between the four series of DNA fragments (see section 1.3.2.B on fluorescently-labelled DNA fragments), and APD transducers with their associated electronics (see section 2.2.5).

The instrument's design offers several advantages for DNA sequencing. First, the high separation speed which will be shown in section 2.3.2 yields ~ 500 bases of raw sequence/capillary over ~ 2 hrs; the use of 16 capillaries in parallel to increase sample throughput, similar to parallel lanes in a slab gel seen in other work[3], means that the parallel instrument design yields higher throughput at decreased cost. Second, capillaries are very easily amenable to automated sample injection schemes, such as using gold-plated microtiter plates[4]. Third, the use of a micromachined, multicapillary sheath flow cuvette described in Chapter 3 allows laser-induced fluorescence detection to achieve high sensitivity[5], which, in turn reduces the amount of sample required; the cuvette also allows capillary arrays to be changed frequently while conserving precise optical alignment.

Four other instruments used for[6-10] or intended for[11, 12] DNA sequencing have been constructed in which many capillaries are arranged in parallel.

Zagursky and McCormick[7] modified a Genesis 2000 DNA slab gel sequencer, essentially replacing the slab gel with 12 capillaries; an Ar^+ laser beam, perpendicular to the capillary array plane, mechanically scans across the array of 50 cm-long capillaries 10 cm from the detection ends, where polyimide has been removed over 0.5 cm of the capillary length for on-column detection. The fluorescence from the sequentially scanned capillaries originating from the ddNTP-labelled fragments is collected by two stationary photomultiplier tubes, or PMTs, equipped with optical filters. All four dyes used are excited with the Ar^+ laser at 488 nm. They report > 98% sequencing accuracy out to 415 bases using M13mp18 DNA template (M13 is a bacteriophage virus). No detection limits were given.

The 25-capillary array sequencer from Mathies' group[6, 10] similarly uses on-column detection with a single, 488 nm Ar^+ laser inducing fluorescence in the capillaries sequentially as the array translates beneath the stationary laser beam and detection confocal optics. A two label, two colour binary-encoded detection system is employed with an emission beamsplitter and two PMTs. The authors achieved read lengths up to 350 nucleotides in M13mp18 in about 2 hours[10], but encountered base-calling accuracy problems due to the fact that in the binary code employed, C-terminated fragments were inferred by the *absence* of a peak; a 5.4% error rate over 280 bases was owing to this problem alone. They also reported a limiting sensitivity of 10 attomoles of fluorescently-labelled DNA, or approximately 6 million molecules.

Yeung's group[12] developed a 100 capillary array intended for DNA sequencing which also uses on-column detection with a single, multi-line Ar^+ laser, but in this system, there are no moving parts; the laser beam is split with a prism, the 488 nm and 514 nm lines are expanded into planes to cover the wide capillary array, and are each incident at different locations along the capillaries, 37 cm from the injection end at 45° to the plane of capillaries. A wide angle lens and CCD camera are used to collect and detect the fluorescence. No actual sequence data were presented, but detection limits (3σ) were reported ranging between 4.0×10^{-10} to 6.2×10^{-9} M fluorescein, depending on detection optical geometry.

Challenges mentioned were cross-talk between capillaries (<10%), and weak signal for outer capillaries in the array.

Finally, Kambara and Takahashi have produced a 20-capillary instrument with a post-column, sheath flow detection cell, where the DNA fragments exiting the capillaries are excited by the beams of two lasers (Ar^+, 488 nm, and YAG, 532 nm) simultaneously passing beneath the linear array of capillaries, through each capillary's sheathed stream. Concentric capillaries are used to create the sheath flow. Fluorescence from DNA fragments passes through lenses, a prism and filters before reaching the CCD detector which simultaneously records all four wavelengths and capillaries. The ABI four-colour dye system is used. Sequencing read lengths of > 300 bases of M13mp18 are reported (sequencing accuracy is not mentioned), as are impressive 2σ detection limits of 600 molecules or 1×10^{-13} M Texas Red for single colour detection or 2×10^{-12} M for four colour detection mode with the ABI dyes.

The construction and optimisation of a 16 capillary gel electrophoresis DNA sequencer is described, and its use with an M13mp18 DNA sample is demonstrated in this Chapter. It should be noted that, while the instrument was designed specifically for DNA sequencing, it could easily be modified for other types of separations for which high throughput is desirable such as DNA fingerprinting, or open tube separations by means of CZE or micellar electrokinetic capillary chromatography, MECC, a variation on CZE in which a micellar phase is added to the separation medium so that neutral as well as ionic species may be analysed in an electrophoretic separation[13].

2.1.2 GRIN Lenses and Avalanche Photodiodes

A brief description of GRIN lenses, which are used in the instrument's detection optics, and avalanche photodiodes, the transducers used in the instrument, is given next in sections 2.1.2.A and B.

2.1.2.A GRIN Lenses[14, 15]

Gradient refractive index lenses, or GRIN lenses, are different from conventional optical lenses principally in that the variable index of refraction within the lens, and not the curvature of the lens surface, is used to focus beams of light. To describe a GRIN lens, it is useful to briefly review a conventional lens, and then contrast a GRIN lens with the conventional lens. Figure 2.1 depicts the two types of lenses.

Snell's Law dictates that light rays from medium #1 with refractive index n_1 which are incident at an angle θ_1 upon medium #2 of refractive index n_2 will emerge in that second medium at an angle θ_2 according to the equation $n_1 \sin\theta_1 = n_2 \sin\theta_2$. In conventional optics, the lens element(s) each have homogeneous chemical composition and hence index of refraction within the lens, but the curvature of the lens surfaces, which represents the boundary of index of refraction between the two media, air ($n = 1.0$) and glass ($n = 1.5$), is such that parallel incident rays at different radial displacements refract to different extents to come to a point focus. This concept is illustrated in Figure 2.1-a; the incident light rays are refracted twice, once at each air-glass interface, but the paths outside and inside the lens are straight, since the index of refraction in each medium is constant.

In GRIN lenses, the index of refraction is made to vary continuously as a function of the lens radius, and the optical surfaces of the lens through which light passes are usually flat. Specifically, the index of refraction decreases with

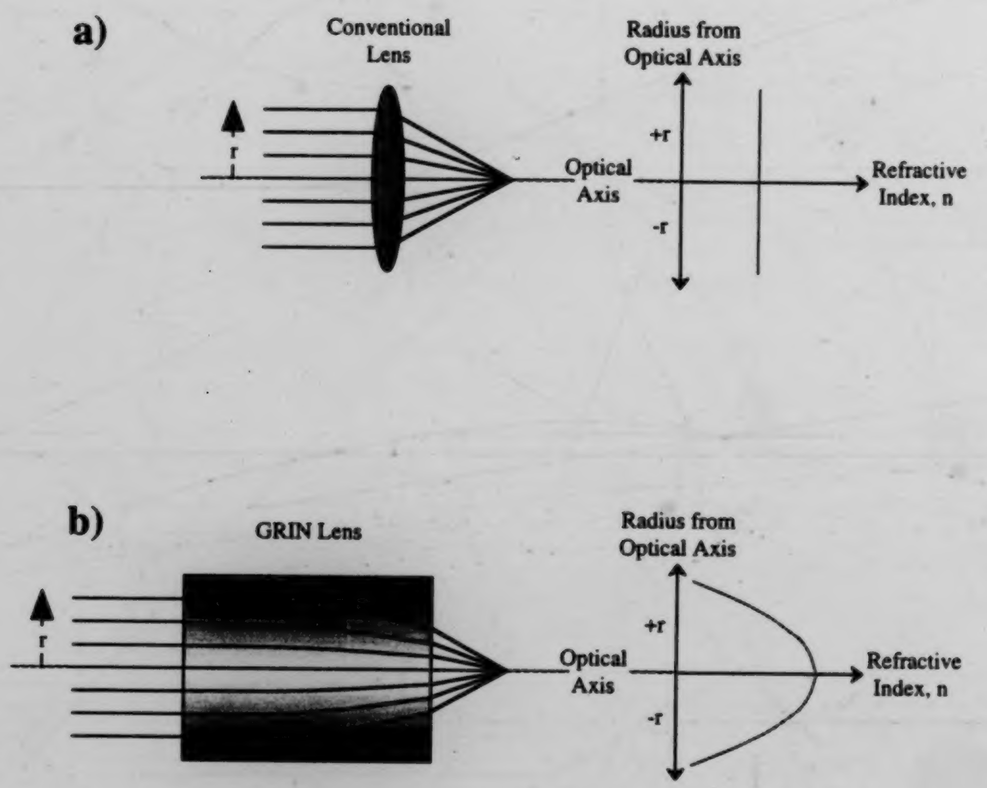
a)
Conventional Lens
Radius from Optical Axis
r
+r
Optical Axis
Refractive Index, n
-r
b)
GRIN Lens
Radius from Optical Axis
r
+r
Optical Axis
Refractive Index, n
-r

Figure 2.1: Conventional and GRIN Lenses.

a) stepwise refraction in conventional optics, and

b) continuous refraction in gradient refractive index optics the square of the radius. In their application in this work, the lenses are used to focus light onto an optical fibre; if the lens is the correct length or pitch, parallel rays incident at one end of the lens are gradually refracted over the length of the lens towards the lens' optical axis, coming to a focus at or just beyond the lens' other surface. GRIN lens focussing is illustrated in Figure 2.1-b; the incident light rays are refracted continuously within the lens, due to the changing index of refraction. The optical fibre is placed at the focal point of the GRIN lens to receive the light.

The GRIN lenses used (lenses SLW-180-025-C2 in collimators FCM-OF-050-063, NSG America, Inc., Somerset, N. J) are cylinders of length 4.63 mm, of radius 0.9 mm, with numerical aperture of 0.46, whose index of refraction, n(r), decreases with radius, r (mm), according to the equation[14]:

$$n(r) = n_o\left(1 - \frac{A}{2}r^2\right) \qquad (2.1)$$

where n_o is the refractive index along the optical axis, and A is the square of the gradient constant. Given the lens radius of 0.9 mm, the axial index of refraction of $n_o = 1.6075$ and the gradient constant at 630 nm of $A^{0.5} = 0.339$, the index of refraction at $r = 0.9$ mm may be calculated with equation (2.1) to be 1.5327.

2.1.2.B Avalanche Photodiodes

In low light detection applications where point detection, as opposed to 1- or 2-dimensional detection, is required, the conventional choice for a light transducer is a photomultiplier tube, or PMT. Quantum efficiency of a PMT or other transducer is defined as {number of detected photons}/{total number of photons incident on the photosensitive surface}; while dependent on the PMT's photocathode composition and the wavelength being detected, quantum efficiency is typically[16] over 10%. The internal gain of a PMT, defined as the number of electrons generated per incident photon, is high, typically[16] 10^4 to 10^7. Taken together, the quantum efficiency and high gain of PMTs underlie their widespread use in analytical instruments for atomic or molecular absorption, emission and fluorescence.

Avalanche photodiodes, or APDs, are transducers which are meant for the same, low light applications as PMTs; while they are newer, less proven and less common in instrumentation, they present comparable performance characteristics, and are in some ways more practical than PMTs. APDs have typical quantum efficiencies of 20-50%, and have achieved values as high as 95%[17]. Depending on which mode of operation chosen, linear or Geiger (discussed below), their internal gain is about 10^2 to 10^3 in the linear mode and inferior to that of PMTs, or as high as 10^8 in the Geiger mode, but variable from photon to photon. However, the low gain of the linear mode can be supplemented with high-gain amplifiers, and pulse counting electronics can be used to generate a linearly-varying signal in the Geiger mode. Compared with PMTs, APDs are compact (~ 5 mm X 5 mm X 5 mm), inexpensive (~ $400 CDN), and insensitive to damage by overexposure when powered up.

Since APDs are not commonplace in analytical instrumentation or described in analytical textbooks, a description of the process of transduction is given next. Avalanche photodiodes evolved from diodes and photodiodes, and are most easily understood as modifications of the latter devices, therefore an explanation of an APD begins with diodes and photodiodes; the concepts are illustrated in Figure 2.2. An excellent description of diodes and photodiodes, on which the following is based, can be found elsewhere[18].

A diode is an electrical component which in essence allows current to flow

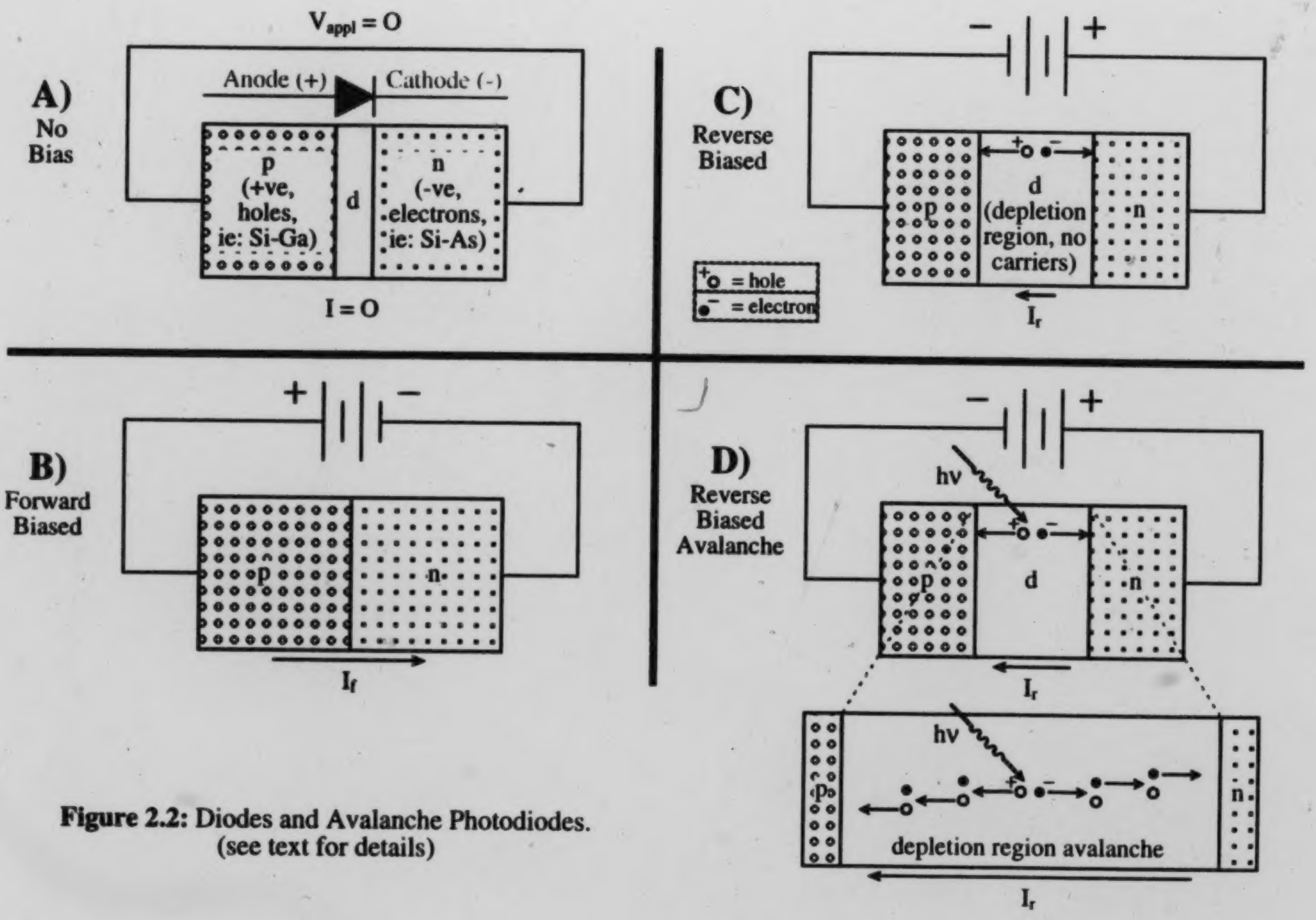
V_appl = O
A)
No
Bias
Anode (+)
Cathode (-)
p
(+ve,
holes,
ie: Si-Ga)
d
n
(-ve,
electrons,
ie: Si-As)
I = O
C)
Reverse
Biased
−
+
p
d
(depletion
region, no
carriers)
n
I_r
o = hole
• = electron
B)
Forward
Biased
+
−
p
n
I_f
D)
Reverse
Biased
Avalanche
−
+
hv
p
d
n
I_r
hv
p
n
depletion region avalanche
I_r

Figure 2.2: Diodes and Avalanche Photodiodes.
(see text for details)

in one direction only. It is formed from two types of silicon, "n-type" and "p-type", for negative and positive (silicon is commonly used, but germanium, another semiconductor, can also be used). n-type silicon (n-Si) consists of pure silicon into which a group V element (As, Sb) is purposely introduced as an impurity to make the silicon electron-rich - the fifth valence electron, not involved in the bonding of the crystal lattice, is easily promoted to the semiconductor's conduction band; conversely, p-type silicon (p-Si) has a group III element (B, Ga) introduced which, with only three valence electrons, makes the silicon electron-deficient. In n-Si, charge can be carried by the excess electrons, while in p-Si, the charge carriers are the *missing electrons*, or *holes.* Holes may move about in the p-Si lattice, and so can be thought of as charge carriers equal in magnitude and opposite in sign to the excess electrons; when electrons and holes meet, they are mutually eliminated as charge carriers in the silicon. When n- and p-Si are adjacent to each other and no external bias is applied, as in Figure 2.2-a, the excess n-Si electrons are attracted to the positive holes of the p-Si along the n-Si/p-Si boundary, or pn junction, and mutual elimination occurs; this creates a narrow strip of silicon depleted of either of the charge carriers, which is referred to as the depletion region, denoted as "d" in the diagram. The movement of charge carriers to create the depletion region at the pn junction establishes a potential from the n-Si to the p-Si. When the diode is conducting current in the normal fashion, a small forward bias, V_f, is applied to negate the potential at the pn junction and greatly reduce the depletion zone, allowing the charge carriers to move across the pn junction, and hence allowing the diode to conduct *in the forward direction* with current I_f, as shown in Figure 2.2-b. This particular forward bias is called the junction contact potential, V_{cp}, and is shown in the current-voltage curve of Figure 2.3; any forward bias in excess of V_{cp} results in a dramatic increase in I_f. If a reverse bias, V_r, is applied, then the applied bias and

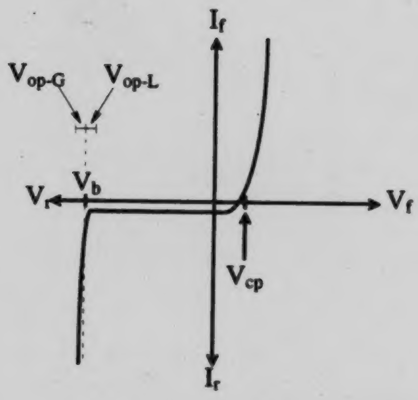

Figure 2.3: Avalanche Photodiode Biasing Curve.

Figure 2.3: Avalanche Photodiode Biasing Curve.

Current to voltage plot shows behaviour of an APD in different biasing regimes. As used in this project, the APDs were used in the linear avalanche mode, biased at V_{op-L}.

the junction potential, which exists with no applied bias, are summed, and the depletion zone grows; this is shown in Figure 2.2-c. Despite the wide depletion zone, a small reverse current, I_r, is observed, due to the thermal generation of electron-hole pairs in the depletion region; once produced, the electron and hole move to the n- and p-Si, respectively, as dictated by the applied electric field. Naturally, the magnitude of this thermal current is temperature-dependent; this dependence is used to advantage by cooling the APDs as described in section 2.2.5.A. In a photodiode, the depletion region of the silicon surface is exposed such that light of the appropriate energy can create electron-hole pairs to generate a small reverse current, analogous to the thermal current, and this photocurrent is proportional to the incident light flux; this is depicted in Figure 2.2-d.

In a reverse-biased diode or photodiode, the depletion region created by the applied bias is like an insulator; at a sufficiently high reverse bias, the whole depletion region may break down if an electron-hole pair is created. At this applied potential, two thermally- or photoelectrically-generated charge carriers accelerate across the depletion zone due to the electric field to an extent that, before they reach the n- or p-Si, they generate other electron-hole pairs by virtue of the kinetic energy they transfer during collisions with other atoms in the lattice; these secondary charge carriers may also generate electron-hole pairs before reaching the n- or p-Si, and so on. This cascade of charge carriers in the depletion region initiated by a single incident photon is termed an avalanche, and the resulting reverse current can be seen as the breakdown of the insulating ability of the depletion region; this avalanche is responsible for the internal gain of avalanche photodiodes. The potential at which the depletion region breaks down, V_b, is characteristic of the particular device and is temperature-dependent. The large reverse current incurred at V_b is seen in Figure 2.3.

As mentioned above, avalanche photodiodes are operated in one of two modes: the linear mode, for which the bias applied to the APD, or operating voltage, $V_{op\text{-}L}$, is just less than V_b; or the Geiger mode, for which the operating voltage, $V_{op\text{-}G}$, is somewhat greater than V_b (see Figure 2.3). Therefore, at a constant temperature, the bias applied to the APD is crucial as it determines in which mode the APD will operate, and to a large degree its performance characteristics in that mode.

In the Geiger mode, the current produced is not proportional to the incident light flux, and so current pulses are counted. The gain, which may be as much as 10^8 in this mode[19], is variable[17]: some photons cause the whole diode to discharge, while others produce a more modest cascade of gain 1-10^4. The APD current measured is thus not proportional to the incident light flux, and so a frequency counter is used instead to measure the number of pulses produced per unit time by discrete photons which are above a certain current threshold. A voltage which is proportional to the frequency of counted peaks is produced by the counting electronics; this voltage is proportional to the incident light flux and is used as the analytical signal from the transducer.

In the linear mode, the voltage across the depletion zone is slightly less than in the Geiger mode. While avalanches of charge-carriers are still produced for incident photons, the avalanches are smaller, resulting in lower internal gain of ~ 10^2 to 10^3, and the current is proportional to incident light flux. The current can be amplified and converted to a voltage, and the voltage is used as the analytical signal from the APD.

The APDs used in the instrument described in this chapter (C30902S, EG&G Optoelectronics Canada, Vaudreuil, Québec, Canada) are rated as having a typical gain of 250 and a quantum efficiency of 77% at 830 nm when used in the linear mode at 22°C. As used, the APDs were in the linear mode, but were cooled to -20.0 °C (see section 2.2.5.A).

2.2 Instrument Development

Instrument development is subdivided into five main areas: an overview of the whole instrument is given first, followed by more detailed descriptions of discrete or interrelated components in the areas of capillary separation, data acquisition, optics and detection electronics. The topics are listed on the next page.

2.2.1 General Description of Instrument

To explain the basic layout and functioning of the instrument as a DNA sequencer, the *general procedure* for injecting and running a Sanger sequencing sample (see section 1.3.2:A, B) to produce electropherograms from which the DNA sequence may be directly read is first described *in as much as it illustrates the functioning of the instrument.*

The instrument may be broken down into two main parts, the separation apparatus, where the Sanger sequencing fragments are analysed, and the detection apparatus, where the analysed fragments are detected by their fluorescence which is converted into an electropherogram containing the DNA sequence information.

A box diagram of the sample injection and separation apparatus is illustrated in Figure 2.4, showing the array of 16 gel-filled capillaries through which the DNA fragments migrate and are separated. The DNA samples are injected by inserting the capillaries and Pt electrode into a microcentrifuge tube containing the DNA dissolved in water and by applying an electric field of ~ 100 V/cm for ~ 40 s with a negative high voltage power supply (Spellman CZE

Topic	Section
•General Description of Instrument	2.2.1
•Separation Apparatus	2.2.2
•Capillary Preparation & Gel Pouring	2.2.2.A
•DNA Sample	2.2.2.B
•4-Colour Data Acquisition	2.2.3
•Data Encoding	2.2.3.A
•Sequential Data Acquisition	2.2.3.B
•Optics	2.2.4
•Routine Optical Alignment	2.2.4.A
•GRIN Lens Alignment	2.2.4.B
•Optical Fibre and GRIN Lens Connections	2.2.4.C
•Detection Electronics	2.2.5
•APD Cooling	2.2.5.A
•APD Biasing	2.2.5.B
•APD Stabilisation	2.2.5.C
•APD Power Supply	2.2.5.D
•Bucking Current	2.2.5.E
•APD Noise and Data Acquisition Mis-Triggering	2.2.5.F
•Low-Pass Filter Performance	2.2.5.G
•Calculation of Low-Pass Filter Cut Off Frequency	2.2.5.H

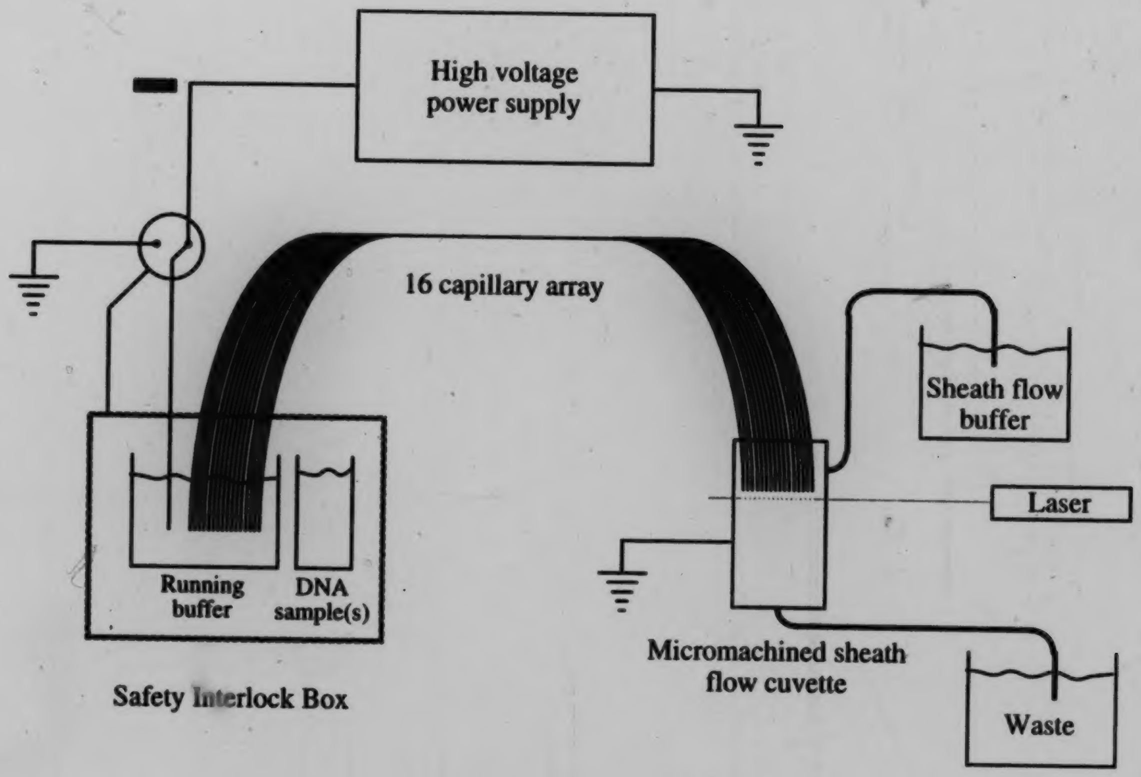
High voltage power supply
16 capillary array
Sheath flow buffer
Laser
Running buffer
DNA sample(s)
Safety Interlock Box
Micromachined sheath flow cuvette
Waste

Figure 2.4: Box Diagram of Separation Apparatus (not to scale)

1000PN30, Plainview, N. Y.) connected to the Pt electrode. The capillaries and electrode are then switched into a 1XTBE running buffer (1XTBE described in section 2.2.2.A) and the separation of the injected fragments is effected at a field of ~ 200 V/cm over ~ 2 hrs. The injection ends of the capillaries and high voltage electrode are housed in a Plexiglas safety interlock box, which interrupts the high voltage if the door to the box is opened. The DNA fragments migrate through the polyacrylamide gel matrix, and exit from the capillaries into the sheath flow cuvette glass detection cell in order of increasing size. Once the fragments migrate from a capillary, they are swept by the 1XTBE sheath flow into one of two laser beams which are aligned to pass directly beneath the capillaries; the dye-labelled primer attached to the DNA fragments fluoresces at a wavelength characteristic of the terminal nucleotide. The sample fragments and sheath flow then pass through the cuvette out into a waste vial.

The fluorescence from the DNA fragments is translated into an electropherogram by the detection system depicted as a box diagram (not to scale) in Figure 2.5. The fluorescent spots are generated by two lasers, a blue Ar^+ laser at 488 nm (Cyonics 2213-755L, San Jose, California) operated at 30 mW and a green, frequency-doubled, 10 mW Nd-YAG laser at 532 nm (Coherent 532-10, Santa Clara, California). The laser beams reflect off a pair of mirrors and then alternately pass through a chopper wheel rotating at 2 Hz; a mirror and dichroic beamsplitter (reflects blue, transmits green; 505 DRLP, Omega Optical Inc., Brattleboro, Vermont) serve to combine the two beams along the same optical path through a focussing objective (1X, 0.05 N. A.; Melles Griot, Nepean, Canada), into the cuvette, passing directly beneath the capillaries' ends. From one side of the cuvette, a microscope is u[illegible]iew the cuvette, the capillaries and their fluorescent spots produced by the DNA flowing from the capillaries. From the other side, the spots are imaged by a microscope objective (18x,

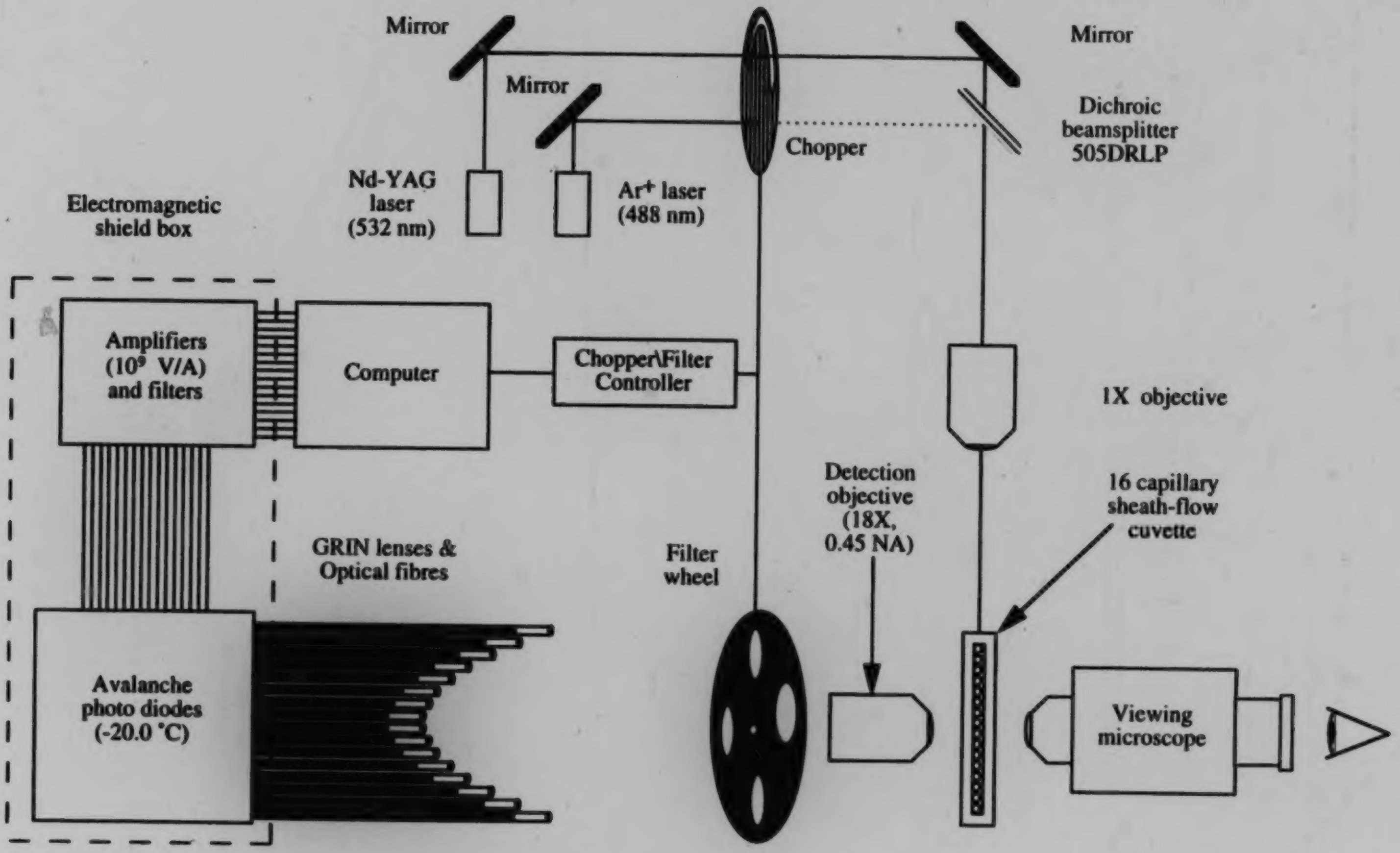
Mirror
Mirror
Mirror
Dichroic
beamsplitter
505DRLP
Chopper
Electromagnetic
shield box
Nd-YAG
laser
(532 nm)
Ar+ laser
(488 nm)
Amplifiers
(10^9 V/A)
and filters
Computer
Chopper\Filter
Controller
1X objective
Detection
objective
(18X,
0.45 NA)
16 capillary
sheath-flow
cuvette
GRIN lenses &
Optical fibres
Filter
wheel
Avalanche
photo diodes
(-20.0 °C)
Viewing
microscope

Figure 2.5: Detection Apparatus (not to scale)

0.45 N. A., Melles Griot) through a rotating filter wheel synchronised with the chopper (see section 2.2.3 below on data acquisition) onto an array of GRIN lenses (FCM-OF-050-063, NSG America, Inc., Somerset, N. J.), one lens for each capillary's spot. The GRIN lenses focus the images of the fluorescent spots onto optical fibres coupled to a second set of optical fibres (optical fibres and connectors from Radiant Communications, South Plainfield, N. J.) leading to 16 avalanche photodiode (APD) transducers which produce a current proportional to the incident light flux. High gain (10^9 V/A) transimpedance amplifiers amplify the signals, which are then filtered by single pole, active 7 Hz low pass filters (electronics are discussed in more detail below). The APD signals are then digitised (16 bit) and, together with the synchronisation pulse from the filter and chopper wheels, are collected on an Apple Power MacIntosh 7100/66 (Apple Computer Inc., Cupertino California) computer with a custom-made Labview programme (National Instruments, Austin Texas; data acquisition software programmed by Darren Lewis of this group) to generate 16 simultaneous four-colour electropherograms, one for each capillary.

The photos of Figures 2.6 and 2.7 serve to illustrate the sequencer in operation, as well some of the components of the detection optics and electronics.

2.2.2 Separation Apparatus

2.2.2.A Capillary Preparation & Gel Pouring

Before the capillaries can be inserted into the detection cell, their detection ends are cut with a wafer dicing saw (Micro Automation model 1100, General Signal, Freemount, California), to ensure clean, blunt ends; cleanly-cut ends are crucial to optical alignment, as discussed in section 2.2.4.A. The capillaries are mounted with tape onto a microscope slide, and the slide is mounted onto the

Figure 2.6: Photo of Sequencer in Operation.

The beams from two lasers in the background of the photo reflect off mirrors (just out of the photo), pass through the rotating chopper wheel to produce segments of light in time, and are combined at the beamsplitter in the foreground to alternately pass through a focussing lens and on into the sheath flow cuvette along the same axis. The array of capillaries comes out of the top of the sheath flow cuvette and appear as a red line curving to the left towards the transparent Plexiglas sample injection box. A large white bottle supplies sheath solution to the cuvette at a constant pressure. Lying behind the sheath solution bottle and the sheath flow cuvette is a black box which houses the detection optics.

Figure 2.7: Photo of Some Detection Electronic and Optical Components.
With the box covering the detection optics removed, orange optical fibres terminating in ~ 2mm diameter GRIN lenses in their black plastic holders can be seen, five of which are mounted on an aluminum stage. The GRIN lenses point towards the sheath flow cuvette to the left; coming out of the top of the cuvette and bending to the left into a falcon tube are gold coloured capillaries with their white labels. A blue styrofoam box behind the aluminum GRIN lens stage houses the avalanche photodiode (APD) transducers whose temperature is controlled at -20.0°C; black optical fibres coupled to the APDs come out of the top of the styrofoam box and are connected to the orange optical fibres.

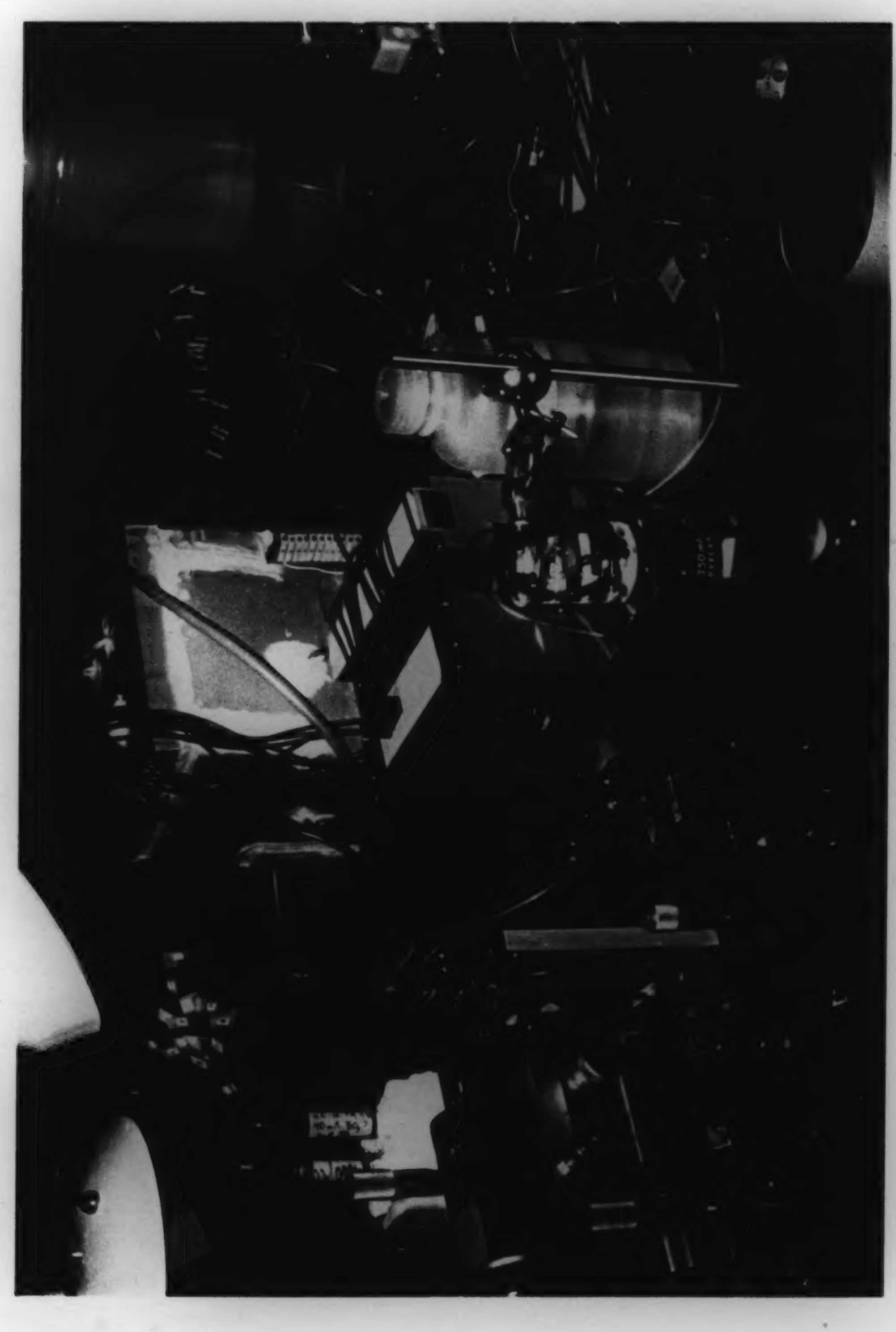

horizontal chuck of the wafer dicing saw. The saw, equipped with a 0.25 mm thick resinoid blade which is made of a diamond-impregnated resin and is spinning at 22 000 rpm, is programmed to cut depthwise through the 145 μm O. D. capillaries and an additional 0.25 mm of the 1mm microscope slide in a single pass, advancing horizontally at 1-2 mm/s. Several hundred capillaries may be cut at once, and the resulting clean, blunt ends are very reproducible.

For capillary zone electrophoresis (as used in LOD studies), fused silica capillaries (~ 50 μm I. D. and 40 cm long, exterior polyimide coating to enhance flexibility; Polymicro Technologies, Phoenix, Arizona) are directly inserted and sealed into the sheath flow cuvette after cutting. An aligning solution (~ 10 nM fluorescein, BDH, Toronto, Canada) is electrophoresed through the capillaries to verify optical alignment (see section 2.2.4.A) and capillary gel quality.

For DNA sequencing, the capillaries are filled with gel prior to insertion. To covalently bond the gel polymer to the capillary walls, a silanising solution of 20 μL γ–methacryloxypropyltrimethoxysilane (Sigma, St. Louis, Missouri) in 500 μL of each of glacial acetic acid and water must be passed through the capillaries by vacuum. To draw a solution through the capillaries, the injection ends are placed in the solution, the detection ends (cut by the saw) are sealed in an Erlenmeyer filter flask (the capillaries are pinched between the neck of the flask and a rubber stopper), and vacuum is applied to the flask. The silanising solution inhibits movement of the gel inside the capillary under electroosmotic flow. The gel is typically a ~ 10 mL, 5%T, 0%C acrylamide (Gibco BRL, Gaithersburg, Maryland) solution, prepared under argon, which is 7 M in urea (ICN Biomedicals, Aurora, Ohio; urea is used as a denaturing agent, to prevent compressions in the sequence - see section 1.3.2.A, part D), 1XTBE (a "1X" concentration of tris (89 mM tris(hydroxymethyl)aminomethane, Sigma), borate (89 mM boric acid, H_3BO_3 from BDH) and EDTA (2.0 mM ethylenediaminetetraacetic acid, BDH) at pH = 8.0), and has been degassed by vacuum and filtered (0.22 μm pore size filter, #SCGS 050 12, Millipore, Mississauga, Ontario, Canada). Just before the gel is drawn into the capillaries by vacuum as described above, 10 μL of 10% ammonium persulphate (Boehringer Mannheim, Indianapolis, Indiana) and 5 μL N, N, N', N'-tetramethylethylenediamine (TEMED, Gibco BRL) are added to initiate and catalyse the reaction. The gel solution is then drawn through the capillaries by vacuum and is left to polymerise inside overnight. The next morning, the capillaries are inserted and sealed into the sheath flow cuvette, an aligning solution of 400 nM labelled primer is electrophoresed through for 30 minutes at ~ 150 V/cm to verify gel quality and optical alignment. Capillaries which do not generate a fluorescent spot from the aligning solution have inferior gels (gel may have bubbles or may not have polymerised). Note that the detection ends of the capillaries are kept in aqueous solution from the moment the gels are drawn into the capillaries through to the end of the DNA sequencing separation; this is to keep the gel from drying out. The injection ends which are left exposed to the air do dry out, but 1-2 cm are cut from these ends to expose fresh, wet gel just prior to running the aligning solution; from this point on, the injection ends are also kept in aqueous solution.

2.2.2.B DNA Sample

Cycle sequencing was used to prepare Sanger sequencing fragments from the bacteriophage M13mp18; while M13mp18 is normally used as the cloning vector into which the template is inserted in cycle sequencing, it served as the template in this case. Approximately 400 ng of M13mp18 from Amersham (Amersham Life Sciences, Buckinghamshire, England) in combination with pyrophosphatase, Thermal Sequenase (DNA polymerase), dNTPs and ddNTPs from an Amersham RPN 2536 kit, and fluorescently-labelled forward dye primers from an Applied Biosystems 401487 kit (Applied Biosystems Inc. (ABI), Foster City, California) were used in a PTC -100 Programmable Thermal Controller (MJ Research, Watertown, Massachusetts) for cycle sequencing. The primers use the ABI fluorescent labels FAM, JOE, TAMRA, and ROX. The sample is then cleaned using Microcon tubes (Microcon 30, Amicon Inc., Beverly, Massachusetts) yielding the DNA dissolved in ~ 10-20 μL of water. The DNA sample is then injected and analysed as described in section 2.2.1.

2.2.3 Data Acquisition

2.2.3.A 4-Colour Data Encoding

The combination of the chopper and filter wheels allows the data for each capillary to be segregated into four spectral channels, one for each dye and nucleotide (see section 13.2.A, B on Sanger sequencing). The terminal nucleotide, its corresponding dye, the dye's absorption maximum (λ_{abs}), excitation laser, emission maximum (λ_{em}) and detection wavelength (λ_{det}) are shown in Table 2.1.

The 1" circular optical filters in the filter wheel are centred at the wavelengths listed in the table, and have a 10 nm bandwidth (540DF10, 560DF10, 580DF10, 610DF10; Omega Optical Inc., Brattleboro, Vermont). These 540, 560, 580 and 610 nm filters are referred to as the blue, green, yellow and red emission or optical filters, respectively.

Spectral discrimination is achieved by synchronising the chopper wheel with the filter wheel: when the chopper allows the blue Ar^+ laser beam to pass beneath the capillaries, the filter wheel brings the C and A emission filters into the

Terminal Nucleotide of Fragment	Primer Dye Label	λ_{abs} (nm)	Excitation Laser (λ_{ex} (nm))	λ_{em} (nm)	λ_{det} (nm)
C	FAM	494	Ar$^+$ (488)	521	540
A	JOE	525		555	560
G	TAMRA	555	Nd-YAG (532)	580	580
T	ROX	585		605	610

Table 2.1: Dye Absoption and Emission Data.

Terminal nucleotides, their corresponding dyes, the dyes' absorption maxima, excitation lasers, emission maxima and detection wavelengths optical path sequentially; the chopper then alternates to the green Nd-YAG laser, and the G and T filters rotate into place.

The two wheels are kept in phase by interrupters which sense narrow notches on each wheel, and by circuitry, built in-house specifically to align the wheels and drive the wheel motors at 2.00 Hz; the circuitry provides continuous phase monitoring, and immediately corrects for any misalignment[20].

The data acquisition system writes one point per capillary for each spectral filter; for every rotation of the filter wheel, 64 points are acquired. The temporal information indicating which filter is in alignment, and hence which dye is being detected, is fed to the computer along with the fluorescence amplitude coming from the avalanche photodiode transducers, so that the fluorescent peaks from the DNA fragments passing through the laser beam are colour coded.

2.2.3.B Sequential Data Acquisition

An additional complication in data acquisition, namely that the signal from all 16 capillaries through one optical filter cannot be acquired simultaneously, arises from the facts that the optical filters rotate through the optical path horizontally as illustrated in Figure 2.8, and that the electronic signal has a rise time associated with the low pass filters used. When an optical filter has rotated squarely in front of the lens and fluorescence from the spots can reach the GRIN lenses as at time = t_2 in Figure 2.8, each APD will have been exposed for different durations, the duration decreasing in the direction of rotation of the filter wheel. Because of the electronic filtering, the signals from those APDs which have only been exposed briefly will not have reached their maximum. As a result, the signal from all 16 capillaries cannot be acquired simultaneously, and instead each is acquired sequentially, at the moment before the trailing edge of the filter eclipses the fluorescent spot from its GRIN lens, for example capillary 1 at time = t_2, or

Figure 2.8: Rotation of Filters Through Optical Path.
The rotating filter wheel and rise time associated with the electronic signal necessitate that the signal for each capillary be acquired just prior to its eclipse by the rotating filter wheel, as for capillary 5 at time t_3.

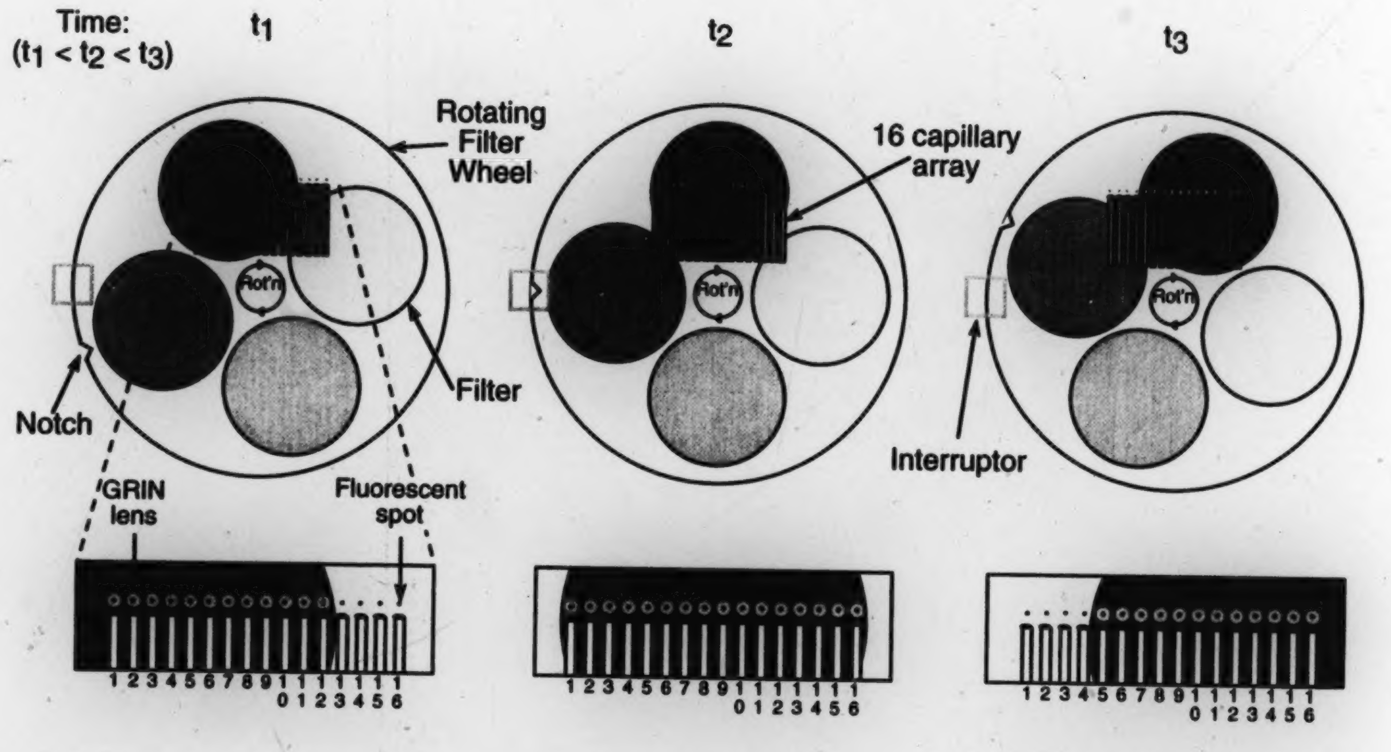
Time:
($t_1 < t_2 < t_3$)
t_1
t_2
t_3
Rotating Filter Wheel
16 capillary array
Rot'n
Filter
Notch
Interruptor
GRIN lens
Fluorescent spot
1 2 3 4 5 6 7 8 9 10 11 12 13 14 15 16

Right-most capillaries eclipsed

All capillaries "seen"
Exposure time: cap 1 » cap 16

Left-most capillaries eclipsed;
capillary 5 to be sampled

capillary 5 at time = t_3 in Figure 2.8. This procedure maximises the signal intensity acquired for each capillary.

The mechanism by which this timing is achieved is somewhat involved, and has been iterated several times with the invaluable assistance of Darren Lewis and Dr. Scott Delinger of this Department. To produce 16 simultaneous four colour electropherograms, one per capillary, sampled at 2 Hz, 64 points must be collected every 0.5 s: one point for each of 16 capillaries for each of the four emission filters. Such a 0.5 s array of 64 points is referred to as a *scan*. Therefore, what is sought is a series of peaks in precise alignment with the rotation of the chopper and filter wheels which dictates to the data acquisition programme *when* these points should be acquired for each capillary and for each optical filter. The current timing and data acquisition system will first be described, followed by an earlier, less successful methodology employed, and the reasons for its failure.

Current Data Acquisition System: Figure 2.9 illustrates the currently used timing sequence for spectral separation and data acquisition. Three pulse trains and a time scale are shown. The first pulse train is the signal from the interrupter on the filter wheel; since the filter wheel rotates at 2 Hz, a narrow pulse is seen every 500 ms. This signal is received by Labview, which in turn generates two dependent pulse trains. The "primary" Labview pulse train is a 16 Hz signal, begun simultaneously with the filter wheel pulse. This square wave merely serves to initiate Labview's "secondary" pulse train, consisting of 7 intermittent packets of 16 pulses at 345 Hz; it is from these pulses that the data acquisition is triggered.

Inflexibility in the Labview programme has two repercussions which impact on the secondary 345 Hz pulse train, and on the design of the filter wheel. Since only 4 packets of 16 pulses are required every scan (16 pulses per packet, one for each capillary, and one packet per filter), the initial design of the current

Figure 2.9: Timing of Data Acquisition Programme.
For each 500 ms rotation of the filter wheel, 64 points are acquired , a point for each of 16 capillaries and each of the 4 filters. Each 64 point scan is triggered by a pulse from the filter or chopper wheel, from which Labview generates two pulse trains. It is the secondary pulse train, with its 7 packets of 16 pulses per 500 ms filter wheel rotation, which actually triggers the data acquisition; of the 7 pulse packets, only the four packets which are temporally aligned with the blue, green, yellow and red emission filters on the filter wheel are used.

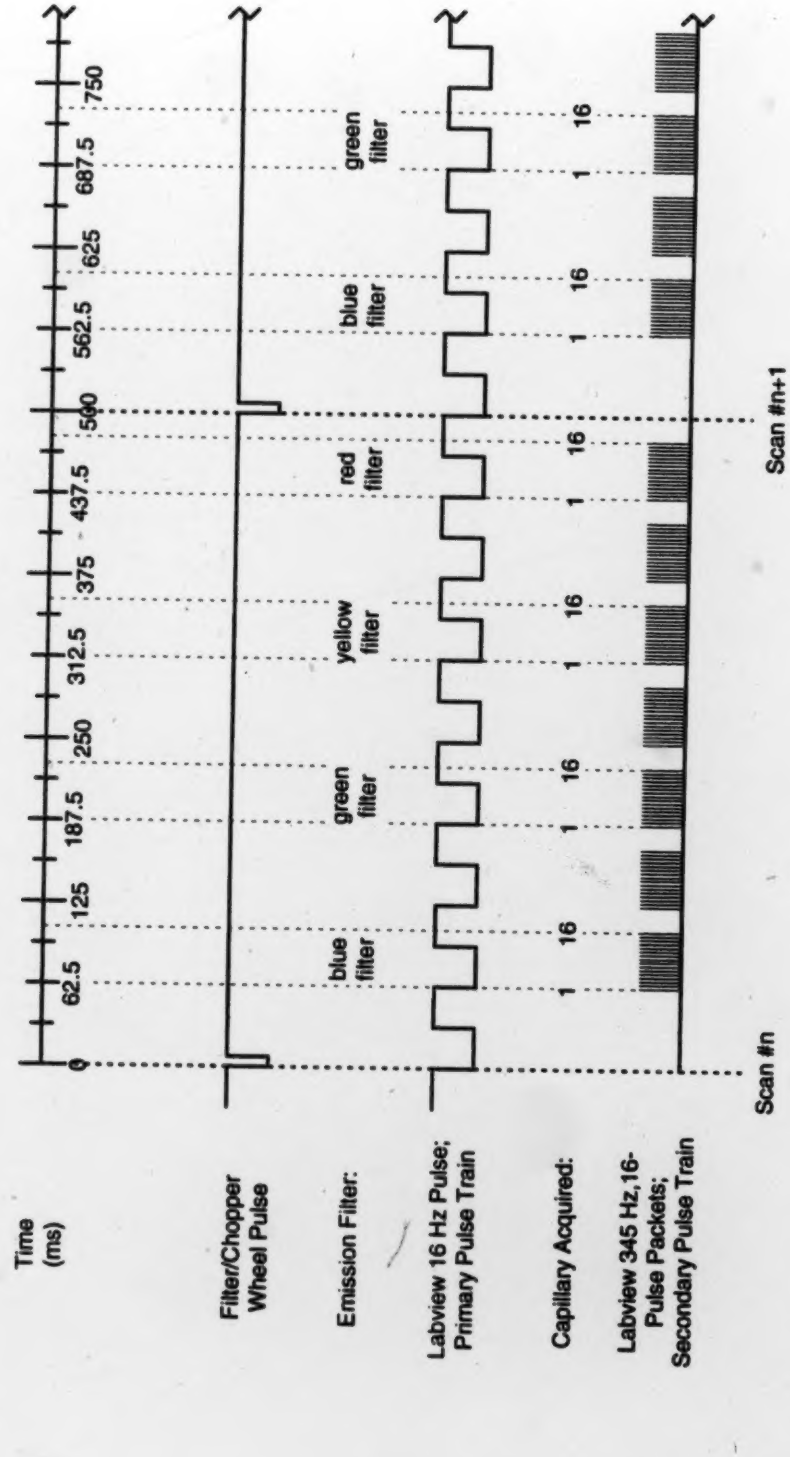
Time (ms)
0
62.5
125
187.5
250
312.5
375
437.5
500
562.5
625
687.5
750
Filter/Chopper Wheel Pulse
Emission Filter:
blue filter
green filter
yellow filter
red filter
blue filter
green filter
Labview 16 Hz Pulse; Primary Pulse Train
Capillary Acquired:
1
16
1
16
1
16
1
16
1
16
1
16
Labview 345 Hz, 16-Pulse Packets; Secondary Pulse Train
Scan #n
Scan #n+1

programme used an *8 Hz* primary pulse to trigger the 345 Hz secondary packets. Labview, however, cannot generate the secondary pulse train (345 Hz) until one full period of the primary pulse has passed, so triggering 4 packets of 16 pulses off the *8 Hz* primary pulse train put the fourth packet in the subsequent cycle, causing the routine to crash. The solution described above using the 16 Hz primary pulse train generates 7 packets (the eighth is omitted so as not to run into the next cycle) of which the first, third, fifth and seventh are properly positioned 125 ms apart for data acquisition on the four filters; the other three packets are ignored. The first packet is still offset by one period of the primary pulse or 62.5 ms after the filter wheel pulse, which means that the notch in the filter wheel must pass through the interrupter 62.5 ms before the capillary 1 is to be sampled. The physical position of the notch must therefore be 62.5 ms/500 ms X 360° = 45° past the interrupter when the blue filter is about to eclipse capillary 1.

The speed of the chopper and filter wheel stepper motors is controlled at 2 Hz by the clock in the driving circuitry (built by Darren Lewis of this group), and has been measured with a digital oscilloscope to be 2.00 Hz. However, since the chopper wheel/filter wheel controller and computer have independent clocks, it is desirable to sample the filter wheel position regularly and trigger the Labview pulse train off of the filter wheel; this design inhibits the two pulse trains from falling out of phase. To that end, the 16 Hz primary pulse train is triggered by an interruptor sensing a notch in the filter wheel once per rotation. In the rare event that a filter wheel pulse did not trigger Labview for whatever reason, the entire scan, or array of 64 points = 4 filters X 16 capillaries, pending that trigger pulse were omitted in the data file; in other words, a 0.5 s gap in the data occurred. Such mistriggers occur approximately once every two minutes of data acquired, and are thus inconsequential.

The spacing of the pulses in the secondary pulse train was determined by physical measurements on the filter wheel. The phase angle between the two positions of the filter wheel just prior to eclipsing capillary 1 and just prior to eclipsing capillary 16 was measured; dividing this angle by 15 gives the angular separation between any two capillaries. The inter-capillary angular separation is converted to a temporal separation for the rotating filter wheel, and the corresponding frequency (345 Hz) is directly entered into the data acquisition programme to control the secondary pulse train.

The timing of the data acquisition was empirically verified and fine tuned by comparing the temporal alignment of the secondary pulse train with the signal emanating from any particular capillary's electronically filtered APD signal. In particular, the position of the filter wheel notch and the secondary pulse train frequency were directly evaluated.

First, the alignment of the filter wheel notch was checked. White light from a flashlight was shone from the position of the observing microscope through the cuvette and rotating filter wheel onto the GRIN lenses. APD #1's signal, taken after the low pass filter, was one input of a dual trace oscilloscope. Viewed on the scope, the signal traced the typical exponential rise and decay curves expected for a low pass filter, as the white light blinked on the GRIN lens due to the rotating filter wheel. The second input to the scope was the digital output of Labview's secondary pulse train, used internally to trigger data acquisition. With the filter wheel notch properly aligned, the first peak of each of the four 16-packets used arrived late on the plateau of APD #1's signal, ensuring that the APD signal was being sampled at near-maximum intensity. This timing can be seen by comparing the signal from APD #1 (chopper wheel & filter wheel aligned) to secondary pulse train in Figure 2.10.

Figure 2.10: Timing of Data Acquisition Programme - Verification.
To verify that the filter wheel notch position and primary and secondary pulse frequencies controlling data acquisition timing were correct, the APD signal profiles were compared directly with the triggering pulses generated by the data acquisition programme. Proper alignment is shown when the nth pulse in a 16 pulse packet from the secondary pulse train for capillary #n arrives late on the plateau of the signal from APD #n.

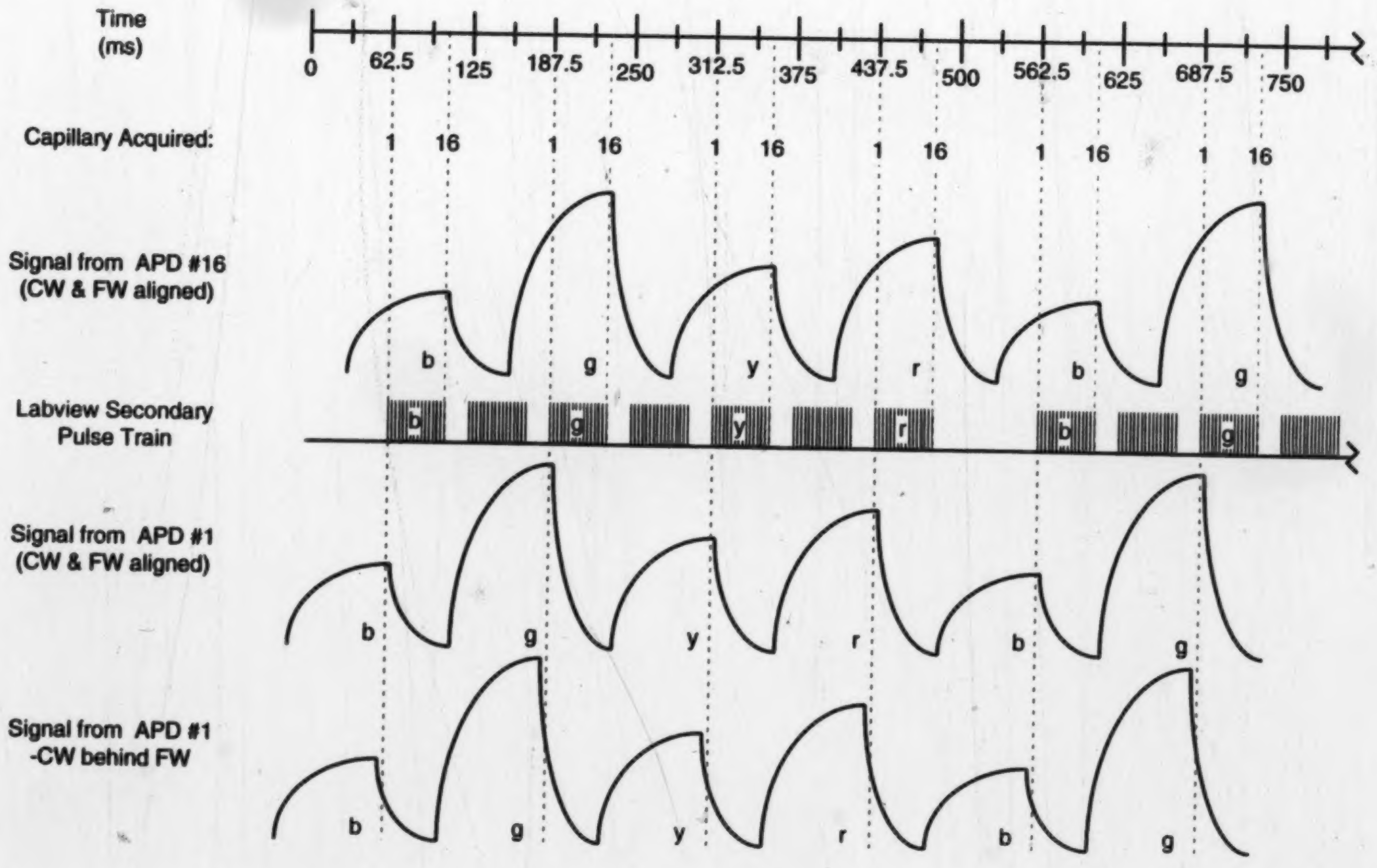
Time
(ms)
0
62.5
125
187.5
250
312.5
375
437.5
500
562.5
625
687.5
750
Capillary Acquired:
1
16
1
16
1
16
1
16
1
16
1
16
Signal from APD #16
(CW & FW aligned)
b
g
y
r
b
g
Labview Secondary
Pulse Train
b
g
y
r
b
g
Signal from APD #1
(CW & FW aligned)
b
g
y
r
b
g
Signal from APD #1
-CW behind FW
b
g
y
r
b
g

Once the filter wheel notch was aligned, the intercapillary spacing could be verified. The scope's inputs were changed to APD #16 and the secondary pulse train. When the latter was properly adjusted, the 16th pulse of each of the four 16-packets was lined up late on the plateau of APD #16's signal: compare the signal from APD #16 (chopper wheel & filter wheel aligned) to secondary pulse train in Figure 2.10. This direct monitoring allowed precise temporal alignment of the data acquisition.

Early Data Acquisition System: In the previous iteration, the chopper wheel/filter wheel synchronisation was achieved only by an initial, stationary alignment; when both wheels were started up, the heavier filter wheel lagged behind the chopper wheel by 3 to 8 steps, usually by 3 to 6 steps. To compensate for discrepancy, the chopper wheel notch was adjusted to give the chopper wheel a 4.5 step handicap at the start, which usually nullified the discrepancy. The phase aligment was verified after start-up with an oscilloscope.

Furthermore, with this chopper/filter wheel combination, if the two wheels fell out of phase, there was no correction circuit. This weakness was crucial, since the data acquisition was triggered from the chopper wheel pulse, not the filter wheel as above. The driving circuitry for the chopper wheel and filter wheel stepper motors also developed an elusive loose connection, and so after an initial alignment verified on the scope, the two wheels would occasionally fall out of phase by one to six steps (a step is 3.6°, or 5 ms at 2 Hz) - it is because of this problem that the presently used version has an autoalignment circuit, actively keeping the wheels in phase. With regard to the laser/emission filter alignment, a small phase difference is tolerable since the chopper wheel changes the lasers in between emission filters, with the fluorescence temporarily blocked from the GRINs by the solid part of the filter wheel. However, with regard to data acquisition, a small error in timing can be very detrimental. If, for example, the chopper wheel began to lag behind the filter wheel, then the location of the secondary pulse triggering the data acquisition would be on the rapidly decreasing slope of the signal, reflecting the fact that the fluorescent spot was eclipsed before sampling: observe the temporal alignment of the signal from APD #1 (chopper wheel behind filter wheel) with the secondary pulse train in Figure 2.10.

Another difference in this early version is that, while the data acquisition was triggered by a series of 16 packets, they were not generated internally by Labview. Instead, the synchronising pulse from the chopper wheel or filter wheel was the input to "Pandora's Box", a pulse generator specifically designed and built for this system by Darren Lewis of this group. Pandora's output was four packets of 16 pulses, with control over the inter- and intra-packet spacing, analogous to altering the frequencies of the primary and secondary pulse trains of Labview in the currently used system. This system was conceptually sound, but had troubles interfacing with Labview; cleaning up the signal emanating from Pandora's Box by placing an opto-isolator between Pandora and the computer significantly reduced Labview's tendency to crash mid-run. In the opto-isolator, Pandora's signal controls the pulsing of an LED, which is transduced by a photocell; the signal from the photocell in the opto-isolator is then sent to trigger the data acquisition in the computer. This configuration impeded fluctuations in Pandora's ground potential from causing a mistrigger in the Labview programme, and while it significantly reduced programme crashes, it fell short of curing them.

One of the most serious weaknesses of this earlier version was that *all* the data points acquired in the run were directly triggered from the Pandora pulse generator, and that, when a point was missed, the integrity of the 64 point X N-scan data file was lost. If 63 points points were acquired for a particular scan, scan #1, then the first point from scan #2 was used incorrectly as the 64th point of scan #1, meaning that the order of capillaries and filters does not correspond to the order of the data in the file acquired. Given that for *each datum*, the triggering pulse was transduced at the interruptor of the chopper or filter wheel, again at the opto-isolator, and that peak-height discrimination was used by the Labview programme to recognise the pulse, and given that a typical DNA sequencing run lasts ~ 2 hours or consists of 2 h • 3600 s/h • 2 scan/s • 64 pts/scan = 921 600 points, it is not surprising that at least one trigger pulse was misinterpreted and either caused the data acquisition programme to crash or compromised the integrity of the data file. This weakness is not present in the currently used system. First, as described above, the programme is only triggered *once* per scan, making it less susceptible to a noisy triggering signal. Second, in the event of a mistriggering, the programme does not crash, nor is the capillary and filter order correspondence to data point order compromised; instead, the entire scan is simply omitted from the data file, and since this happens once every ~ 2 minutes, this loss is negligible.

2.2.4 Optics

The components of the detection optics are shown in Figure 2.11; the fluorescent spots from the capillaries are imaged through the 18 X lens, through one of the filters in the filter wheel, onto the GRIN lenses, one spot per lens.

A number of factors influencing the optical alignment will be discussed, and are divided into two areas. Section 2.2.4.A deals with those factors which are encountered in routine sequencing use, including positioning of both laser beams by mirrors, beamsplitter and focussing lens, focussing of the laser beams, capillary positioning within the cuvette, cuvette positioning along the laser beam axis, and sheath flow rate and composition. Section 2.2.4.B deals with those factors which affect GRIN lens alignment and were part of the instrument

Figure 2.11: Arrangement of Detection Optics.

The positions of the cuvette, imaging objective, filter wheel and GRIN lenses; with the exception of the positions of the GRIN lenses on their mounting plate, the diagram is to scale. GRIN lens positions on the mounting plate are given in Figure 2.14.

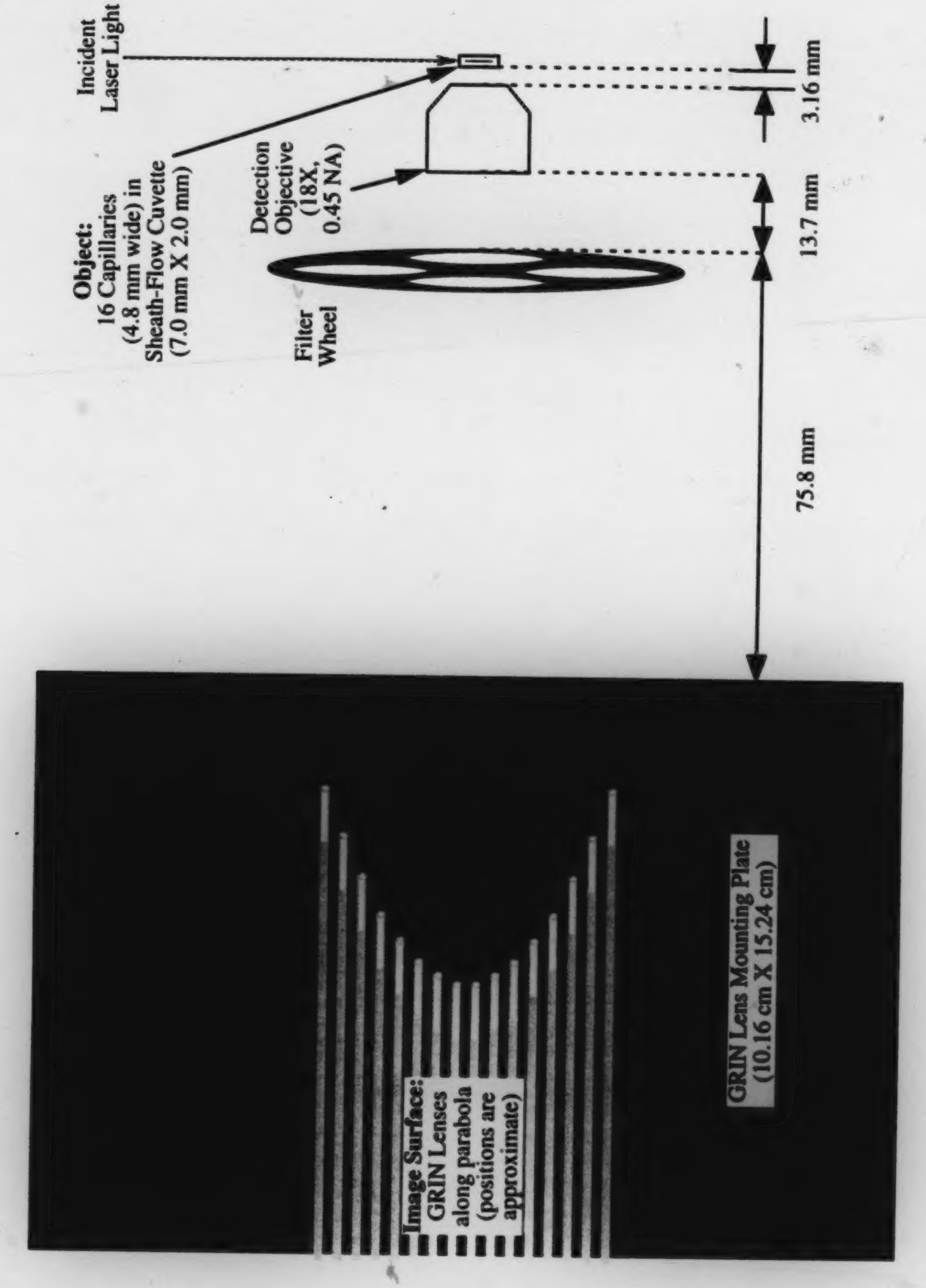
Incident Laser Light
Object: 16 Capillaries (4.8 mm wide) in Sheath-Flow Cuvette (7.0 mm X 2.0 mm)
Detection Objective (18X, 0.45 NA)
Filter Wheel
3.16 mm
13.7 mm
75.8 mm
Image Surface: GRIN Lenses along parabola (positions are approximate)
GRIN Lens Mounting Plate (10.16 cm X 15.24 cm)

development and construction, which are set once, and, unless they are disturbed, do not need to be reset, such as choice of imaging objective (18 X, 0.45 N. A.), cuvette-18X objective distance, 18X objective-GRIN lens distance and GRIN lens angle, and optical bandpass filters. Finally, the protocol for making optical fibre connections to GRIN lenses and fibre connectors is described in section 2.2.4.C.

2.2.4.A Routine Optical Alignment

Positioning and focussing of laser beams: Good optical alignment, as illustrated in Figure 2.12-a, is achieved when the images of the fluorescent spots beneath the capillaries are coincident with the GRIN lenses, and are approximately the same size as the latter. To verify this alignment, a fluorescent solution, ~ 400 nM in FAM- and JOE-labelled primer, is passed through the capillaries by electrophoresis, one of the two laser beams is focussed underneath the capillaries, and a lamp is shone back through the GRIN lenses to make them backlit (the lamp is shone into the FC connectors linked to the GRIN lenses via optical fibres - see section 2.2.4.C); both the fluorescent spots and the GRIN lens spots can thus be seen through the viewing microscope, and should overlap. The verification of GRIN lens/fluorescent spot alignment is then repeated using the other laser.

The laser beams are each positioned by *two* reflective surfaces, two mirrors for the Nd-YAG laser, or a mirror and beamsplitter for the Ar^+ laser (see Figure 2.5), allowing both the beam angle to be changed and the beam to be translated horizontally or vertically with regard to the cuvette. Both beams should pass through the centres of the capillary streams (horizontal laser beam adjustment), and should be level with the backlit GRIN lenses (vertical laser beam adjustment). The laser beams should also be focussed by the 1X objective so that the beam waist, the narrowest part of the beam, is in the centre of the cuvette; each laser

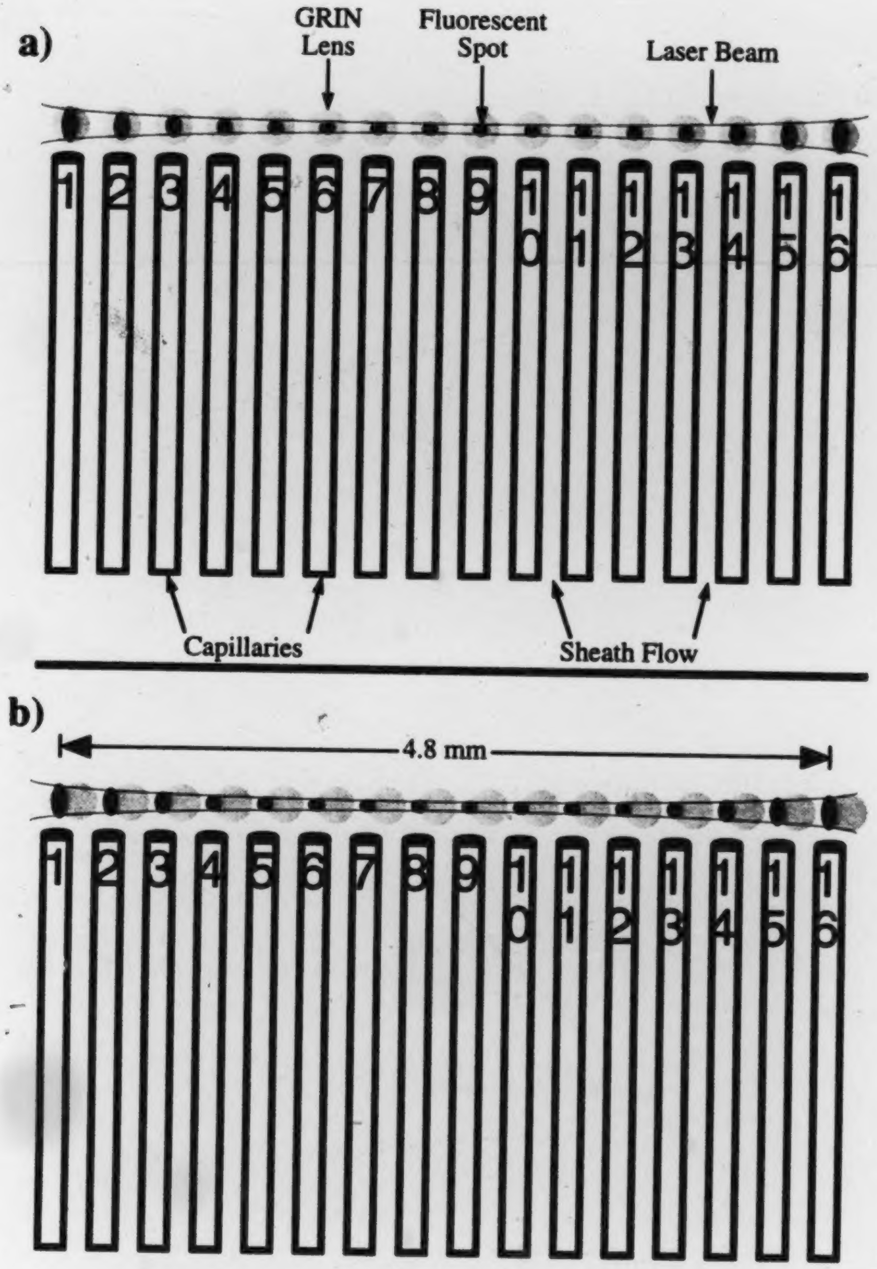
a)
GRIN Lens
Fluorescent Spot
Laser Beam
1
2
3
4
5
6
7
8
9
10
11
12
13
14
15
16
Capillaries
Sheath Flow
b)
4.8 mm
1
2
3
4
5
6
7
8
9
10
11
12
13
14
15
16

Figure 2.12: Optical Alignment of Fluorescent Spots. a), aligned; b), misaligned; capillaries are shown inverted, as they appear through the viewing microscope

beam thus forms a bow-tie shape, as seen in Figure 2.12. The laser beams should pass through the centre of the objective.

Capillary positioning within the cuvette: While discussed at length in Chapter 3, capillary positioning within the cuvette is briefly overviewed here. In the cuvette used, the micromachined features position the capillaries 300 μm centre to centre, stop all the capillaries at the same height, and ensure that the capillary array is flat so that a laser beam can intersect all streams simultaneously. The capillary positioning is quite reproducible when the capillaries are changed from run to run and, providing the capillaries have clean, blunt ends, the fluorescent spot positioning will also be very reproducible. Capillaries which have polyimide burrs attached or irregularly shaped ends cause disturbances in the sheath flow, which disrupts the alignment of the fluorescent spots with their GRIN lenses.

Cuvette positioning along the laser beam axis: With the routine replacement of the capillaries from run to run, however, the cuvette holder, and hence cuvette, is sometimes moved left or right, and the fluorescent spots become accordingly misaligned, as seen in Figure 2.12-b and should be realigned. To realign, an aligning solution is electrophoresed through the gel-filled capillaries usually for 20 minutes before each DNA sequencing run, and the position of the cuvette is moved along the laser beam axis to regain the optimum overlap of the fluorescent spot with the image of the GRIN lens.

Sheath flow: The sheath flow is the solution passing outside of the capillaries and inside the cuvette, ensheathing the streams coming out of the capillaries and drawing them straight down to the laser beam; the faster the sheath flow, the narrower are the fluorescent streams. The sheath flow buffer, which is kept in a wide, $\phi = \sim 4"$, container, enters through the top of the cuvette holder, passes down through the cuvette, and exits the cuvette and holder at the bottom to a waste vial; the difference in height between the liquid levels of the buffer reservoir and waste vial determines the sheath flow rate. The wide container ensures that the slowly draining sheath flow reservoir does not change height too quickly, disrupting spot sizes. The sheath flow composition should be the same as the running buffer used to separate the analyte in capillary zone electrophoresis to ensure no index of refraction boundary at the capillary stream perimeter (which will cause laser and fluorescence scatter); in capillary gel electrophoresis, there is no bulk flow from the capillaries, so index of refraction matching is not a concern.

2.2.4.B GRIN Lens Alignment

Choice of imaging objective: In setting up the imaging optics, the choice of lens was made considering several parameters. The magnification of the lens must be sufficient to spread out the fluorescent spot images ~ 4 mm apart, the width of the GRIN lens in its holder; the lens must be able to image the whole 4.8 mm object; the working distance of the lens (between the lens and object) must be greater than the 1 mm thickness of the cuvette wall, taking into account the differences in refractive index for air and glass; and last, the numerical aperture should be as high as possible to maximise collection efficiency, the fraction of total light emitted by the source which is collected.

Collection efficiency and the lens' numerical aperture (N. A.) are related by[21]:

$$\text{collection efficiency} = \sin^2\left(\frac{\arcsin(\text{N.A.}/n)}{2}\right) \qquad (2.2)$$

where n is the refractive index of the surrounding medium. In microscope objectives, higher magnification and better optical design at a given magnification share the advantage of higher N. A. and hence better collection efficiency.

Given the cuvette chosen in which the spots are 300 μm apart, a 18 X lens separates the spot images by 18 x 300 μm = 5400 μm or 5.4 mm, which is sufficient to accommodate the GRIN lenses in their holders, and to allow them to be manipulated into place. The working distance of the 18 X lens is 4.2 mm, well in excess of the 1 mm required. Several higher magnification (20, 25 X) and N. A. (0.6, 0.7 N. A.) lenses were investigated, but it was found that due to the large object size, not all of the fluorescent spots could be imaged at once, and/or the working distance was insufficient. Thus the 18 X, 0.45 N. A. lens was chosen. Used in air (n = 1.0), the collection efficiency of this lens is 5.3%.

Cuvette-18X objective distance: The 4.2 mm working distance given is for a surrounding medium of air (n = 1), meaning that the distance will have to be corrected for the 1 mm glass wall (n = 1.5) of the cuvette. An air thickness, t_a, equivalent to the glass cuvette wall thickness, t_g (t_g = 1.0 mm) can be determined, so that the cuvette-to-18 X lens distance, $D_{C\text{-}L}$, can be calculated as:

$$D_{C\text{-}L} = 4.2 \text{ mm} - t_a \qquad (2.3)$$

Figure 2.13 depicts the cuvette wall and closest lens element of the 18 X lens to scale, and shows the effect of the 1 mm glass cuvette wall in the path of the cone of light emanating from a fluorescent spot which reaches the lens. The light gray cone is for an air-only medium specified by the lens manufacturer, and the dark gray, dual-angle cone is for air *and* glass media, as experienced imaging through a cuvette; cone dimensions are approximate. The two cones differ only for that portion in the glass, which is magnified in the diagram for the purpose of

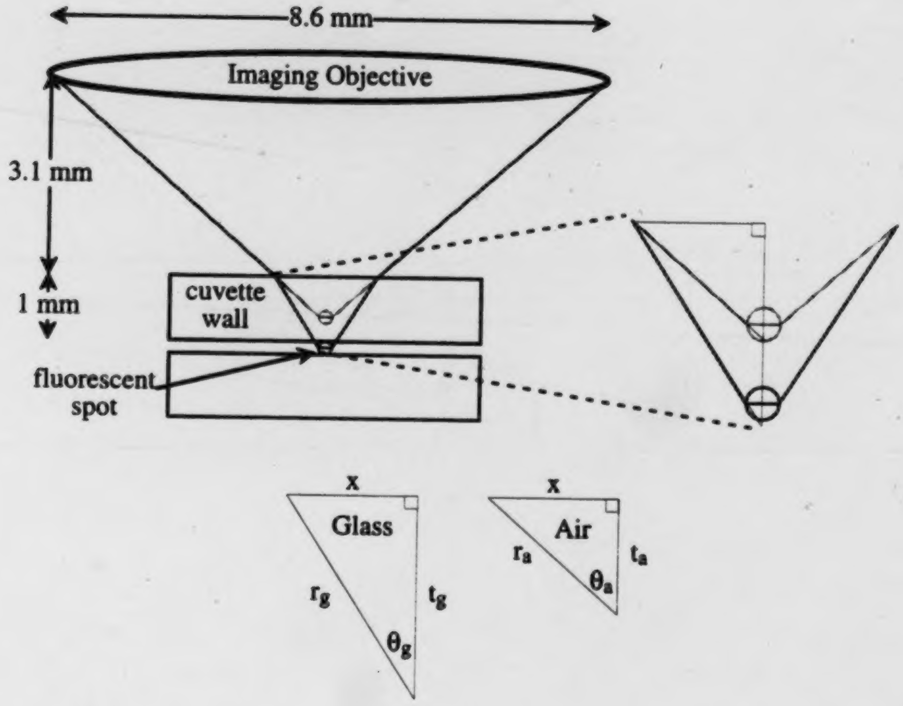
8.6 mm
Imaging Objective
3.1 mm
1 mm
cuvette wall
fluorescent spot
x
Glass
r_g
t_g
θ_g
x
Air
r_a
t_a
θ_a

Figure 2.13: Working Distance Correction for Cuvette Wall.
The change in optical medium from air to glass requires the imaging objective to be moved further from the object than would be the case if no glass were present. Diagram is to scale, and represents the optical geometry *currently used*, as discussed in section 2.2.4.B-18X objective-GRIN lens distance and GRIN lens angle (see text for calculations).

geometric calculations. Using the two triangles drawn for these cones, trigonometry and substitution yield:

$\cos\theta_a = t_a / r_a$ $\qquad\qquad$ $\cos\theta_g = t_g / r_g$

$\sin\theta_a = x / r_a$ $\qquad\qquad$ $\sin\theta_g = x / r_g$

Substituting for r_a and r_g,

$$\sin\theta_a = x \bullet \cos\theta_a / t_a \tag{2.4}$$

$$\sin\theta_g = x \bullet \cos\theta_g / t_g \tag{2.5}$$

Given indices of refraction n_a and n_g for air and glass, Snell's Law may be written as:

$$n_g \sin\theta_g = n_a \sin\theta_a \tag{2.6}$$

or

$$\frac{n_g}{n_a} = \frac{\sin\theta_a}{\sin\theta_g} \tag{2.7}$$

Substitution of equations (2.4) and (2.5) into (2.7) yields:

$$\frac{n_g}{n_a} = \frac{t_g \bullet \cos\theta_a}{t_a \bullet \cos\theta_g} \tag{2.8}$$

For axial rays (those which pass through the centre of the lens), $\theta_a = \theta_g = 0°$, so $\cos\theta_a = \cos\theta_g = 1$, and the equivalent air thickness, t_a, for 1 mm of glass, is determined from equation (2.9):

$$t_a = t_g \bullet \frac{n_a}{n_g} = 1\,\text{mm} \bullet \frac{1}{1.5} = 0.66\,\text{mm} \qquad (2.9)$$

For rays passing through the outer edges of the lens, or marginal rays, the angle to the normal in air, θ_a, is seen from Figure 2.13 to be approximately 45°; for $\theta_a = 45°$, Snell's Law yields $\theta_g = 28.1°$, and equation (2.9) becomes:

$$t_a = t_g \bullet \frac{n_a \bullet \cos\theta_a}{n_g \bullet \cos\theta_g} = 1\,\text{mm} \bullet \frac{1 \bullet \cos 45°}{1.5 \bullet \cos 28.1°} = 0.53\,\text{mm}$$

That equivalent air thickness ranged from 0.53 to 0.66 mm was overlooked when the cuvette-18 X lens distance was initially determined, but this oversight was immaterial due to other optical constraints described next.

A value of 0.66 mm was used as the equivalent air thickness, t_a, for the purpose of determining $D_{C\text{-}L}$ from equation (2.3):

$$D_{C\text{-}L} = 4.2\text{ mm} - 0.66\text{ mm} = 3.54\text{ mm}$$

The 3.54 mm cuvette-to-18 X lens distance calculated was employed to position the GRIN lenses, but because of the distorted image plane, complications arose which forced the distance to be changed to 3.16 mm. GRIN lens positioning and the aforementioned complications are dealt with in the next section.

18X objective-GRIN lens distance and GRIN lens angle: The initial positioning of the GRIN lenses to capture the images of the fluorescent spots was non-trivial. The planar array of fluorescent spots (the object) is imaged by the 18 X lens onto an image surface. Each GRIN lens captures the image of one capillary's fluorescent spot, and must therefore lie at the spot's corresponding location along the image surface. Given such a large object, namely the 4.8 mm width of 16 capillaries' spots spaced 300 μm apart, the 18 X lens image surface is curved in an approximately parabolic shape. Further, the angle of acceptance of a GRIN lens is small since light entering the GRIN lens must almost be parallel with the optical axis of the latter, and so each GRIN lens along the parabola must fixed exactly at its particular angle. In Figure 2.11, the approximate layout of the GRIN lenses on their mounting plate is shown; the exact positions, as measured with a caliper, and angles of the GRIN lenses on that plate are given in Table 2.2, and are depicted graphically in Figure 2.14.

Experimental: With the cuvette placed 3.54 mm from the 18 X lens, fluorescent spots beneath the capillaries, and the GRIN lenses backlit with a lamp at the FC connectors (see section 2.2.4.C on FC connectors), the GRIN lenses and fluorescent spots could be seen with the viewing microscope. The GRIN lens' position was determined by moving the GRIN lens along the image surface across the mounting plate from top to bottom in Figure 2.11 so that the GRIN lens' spot was centred on a particular capillary's fluorescent spot; then, with the two spots coincident, the GRIN lens-18 X lens distance was changed moving across the mounting plate from left to right in Figure 2.11 to put the GRIN lens in sharp focus. The GRIN lens in its locally made plastic holder was then fixed at that position on the mounting plate with 5-minute epoxy and double sided tape. This procedure was repeated for all 16 GRIN lenses.

Grin Lens	x_{bottom} (cm)	y_{bottom} (cm)	x_{top} (cm)	y_{top} (cm)	Angle (°)
1	4.33	1.83	4.09	2.86	-13.13
2	4.60	2.30	4.40	3.34	-10.58
3	4.63	4.39	4.46	5.42	-9.81
4	4.69	7.05	4.54	8.11	-7.96
5	5.28	5.90	5.17	6.94	-5.57
6	5.62	7.02	5.54	8.06	-4.58
7	6.10	7.35	6.04	8.39	-3.35
8	6.52	8.13	6.49	9.17	-1.39
9	7.03	8.20	7.02	9.25	-0.14
10	7.44	7.32	7.47	8.37	1.38
11	7.92	6.97	7.97	8.03	2.48
12	8.35	7.00	8.41	8.04	3.64
13	8.71	6.07	8.81	7.12	5.52
14	9.02	5.02	9.15	6.07	7.06
15	9.32	4.17	9.47	5.21	8.37
16	9.52	2.98	9.70	4.02	9.69

Table 2.2: GRIN Lens Positions on Mounting Plate.

Bottom and top of the GRIN lens holders are illustrated in Figure 2.14; angles are in the plane of the plate, with respect to the 18 X lens optical axis (-ve angles are to the left, +ve angles are to the right).

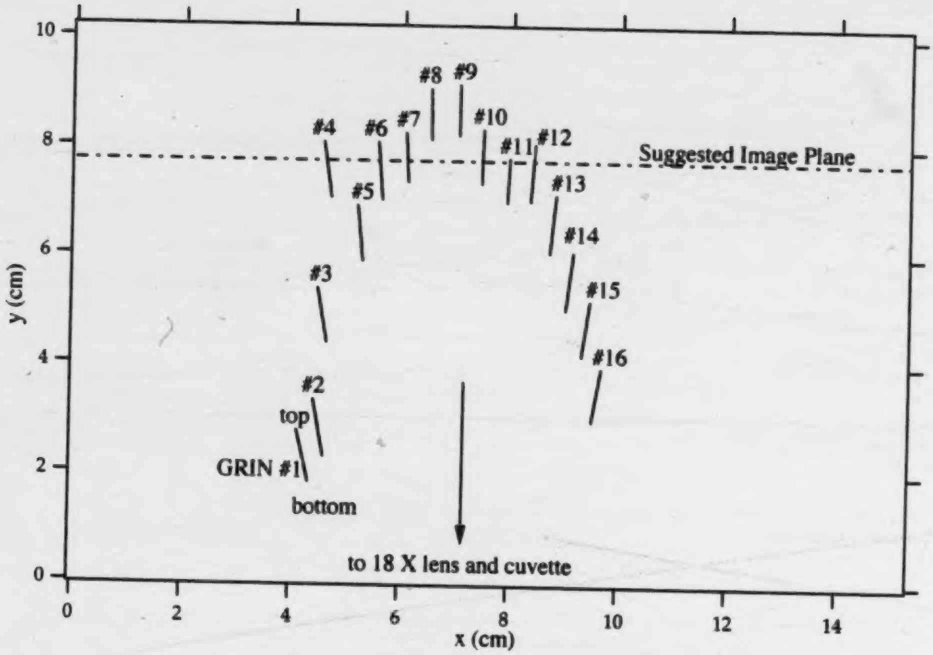

Figure 2.14: GRIN Lens Positions on Mounting Plate.

This diagram is complementary to Figure 2.11, showing the exact locations of the 16 GRIN lenses on their 10.16 X 15.24 cm mounting plate. The approximately parabolic image surface can be seen; the image plane suggested by the manufacturer of the 18 X imaging objective is shown as a reference.

Results and discussion: As attempted with the cuvette-18 X lens distance of 3.54 mm, the GRIN lenses closest to the cuvette, #1 and #16, were in focus at positions between the mounting plate and the 18 X lens, and thus could not be mounted on the plate. Two possible solutions were moving the plate closer to the 18 X lens, or moving the image plane away from the 18 X lens by moving the cuvette closer to the 18 X lens; while the former was the easier of the two options, it would encroach on the space required for the filter wheel. Thus the cuvette-18 X lens distance was changed to 3.16 mm so that all the GRIN lenses were accommodated on the plate.

While the images for the central GRIN lenses were located close to the distance from the 18 X objective specified by the manufacturer, 15.0 cm, those on the outside were markedly closer. It should be noted that, first, moving the cuvette closer than 3.54 mm from the lens would move the image plane to further than 15.0 cm, and second, as used, the 18 X lens had most (1.71 cm) of its metal barrel removed without altering any optical components, simply meaning that in Figure 2.11, the image plane should be 15.0 cm + 1.71 cm = 16.7 cm back from the lens. In terms of the GRIN lens y coordinates listed Table 2.2, the image plane would be located at:

$$\begin{aligned} y &= 16.7\,\mathrm{cm} - (18\,\mathrm{X\ lens} - \mathrm{mounting\ table\ distance}) \\ &= 16.7\,\mathrm{cm} - (7.58 + 1.37)\,\mathrm{cm} \\ &= 7.75\,\mathrm{cm} \end{aligned}$$

A line is drawn in Figure 2.14 showing where on the mounting plate GRIN lenses #8 and #9 would lie if the cuvette were 3.54 mm from the lens, and where all the GRIN lenses would lie without the distortion of the image plane.

The parabolic distortion of the image surface may be due to the use of marginal rays[16], which is exacerbated by the large 4.8 mm object imaged.

Optical bandpass filters: A further complication in the positioning the GRIN lenses was that, as seen from the viewing microscope, the GRIN lens spots moved as the filter wheel rotated; this movement with respect to a capillary in the cuvette is depicted in Figure 2.15. Two distinct problems could be seen as shown in Figure 2.15-a: for all filters, the spots moved when one filter was switched for the next, termed inter-filter movement, and, for the blue and yellow filters, the spots moved *during* the passage of that filter, termed intra-filter movement. Left unresolved, these made four spot positions for each GRIN lens, rendering the alignment of an immobile fluorescent spot to a moving GRIN lens spot impossible. These problems were minimised by altering the filter positions in the wheel, and by positioning the GRIN lenses with the filter wheel rotating.

Inter-filter movement is partly due to non-coplanarity of the filters; adding shims to the seats of the filters in the filter wheel to bring the filters in parallel with each other significantly reduced the problem, as seen in Figure 2.15-b. Intra-filter movement is thought to be due to imperfections in the filter. The blue and yellow (540 nm and 580 nm) filters displayed this abnormality; for the blue filter, the filter was rotated such that the defect never came into the optical path, while for the yellow filter, the defect spanned the entire filter, and could not be avoided, as seen in Figure 2.15-c. The yellow filter was therefore rotated to centre the intra-filter movement of the GRIN lens spot for that filter on the three other now nearly coincident spots through the three other filters.

2.2.4.C Optical Fibre and GRIN Lens Connections

As supplied, the APDs were connected to ~ 60 cm of optical fibre(C30902 SQC-01, APDs coupled to 50 μm core, 125 μm cladding optical fibres, EG&G

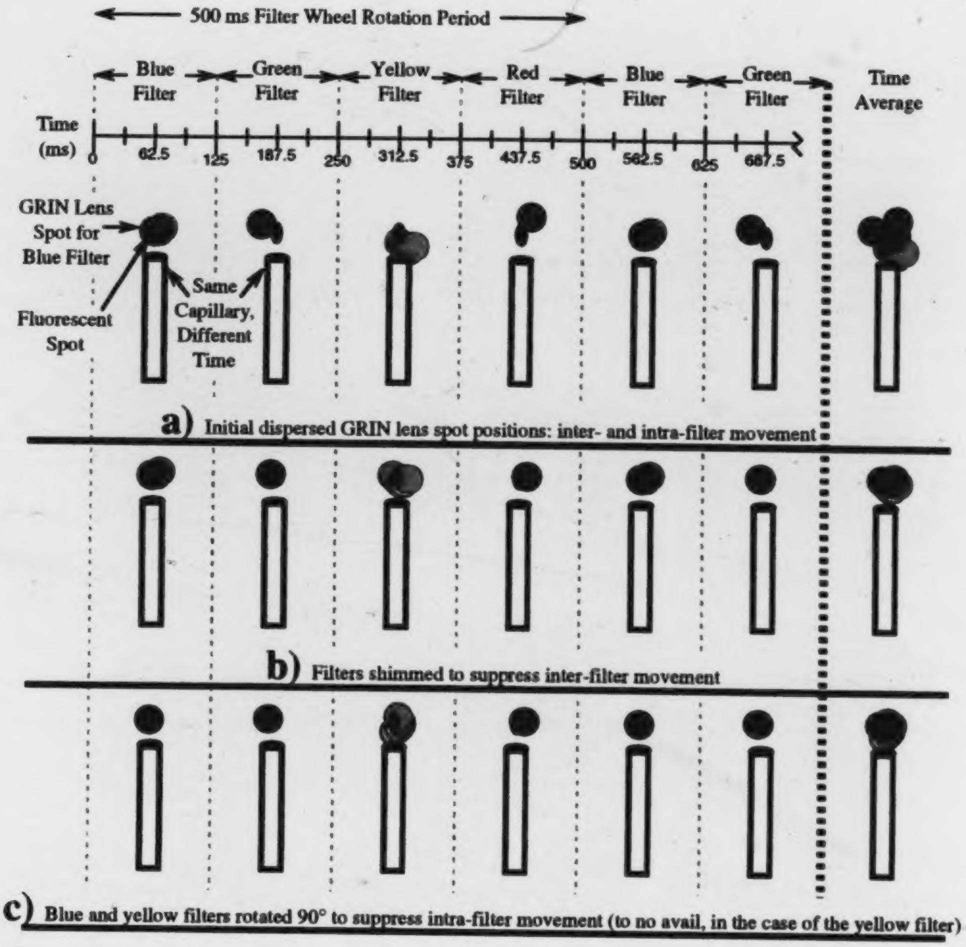
500 ms Filter Wheel Rotation Period
Blue Filter
Green Filter
Yellow Filter
Red Filter
Blue Filter
Green Filter
Time Average
Time (ms)
0
62.5
125
187.5
250
312.5
375
437.5
500
562.5
625
687.5
GRIN Lens Spot for Blue Filter
Fluorescent Spot
Same Capillary, Different Time
a) Initial dispersed GRIN lens spot positions: inter- and intra-filter movement
b) Filters shimmed to suppress inter-filter movement
c) Blue and yellow filters rotated 90° to suppress intra-filter movement (to no avail, in the case of the yellow filter)

Figure 2.15: Effect of Optical Filters on GRIN Lens Alignment. a) shows *inter*-filter movement of the GRIN lens image (image in different positions for each filter), and *intra*-filter movement (image shifting *during* a filter), as seen above a single capillary; b) shimming the filters to coplanarity to eliminate inter-filter movement; c) rotation of filters to eliminate intra-filter movement.

Optoelectronics, Vaudreuil, Québec, Canada) and could have been connected directly to the GRIN lenses (lenses SLW-180-025-C2 in collimators FCM-OF-050-063, NSG America, Inc., Somerset, N. J). However, for the optical alignment mentioned above, a fibre-to-fibre connection is required. These connections, as well as the connections to the GRIN lenses, were made in-house. The procedure followed is as outlined in the kit used (#TK-8, Radiant Communications Corp., South Plainfield, New Jersey), and is depicted in Figure 2.16 and briefly described below.

Experimental: For both the fibre-to-fibre and fibre-to-GRIN connections, the optical fibre first had its outer insulation and cladding removed, leaving the 50 μm diameter fibre exposed (Figure 2.16-a). The fibre was then inserted into a housing (slightly different for the two types of connections) such that the fibre protruded slightly from the other end, and a drop of 5 minute epoxy was applied to secure the fibre in place (Figure 2.16-b). Once the epoxy had hardened, the end of the fibre was cleaved at the surface of the epoxy with a diamond cutter. A series of four polishing pads with grit sizes of 12, 3, 1 and 0.3 μm were then used successively to polish the fibre end and epoxy together to a smooth surface, as inspected with a 100X microscope (Figure 2.16-c). For a fibre to GRIN lens connection, the fibre in its housing and a spacer were inserted into the metal sleeve holding the GRIN lens; with light shone back through the fibre, the GRIN lens was inspected to ensure that the fibre end was in focus. The lens sleeve and fibre housing were then epoxied together. Heat shrink tubing was applied over fibre-GRIN lens connection to add mechanical strength (Figure 2.16-d). For the fibre-to-fibre connections, the connector housing was crimped onto the outer fibre insulation, and the connectors were threaded into an aligning seat (Figure 2.16-e).

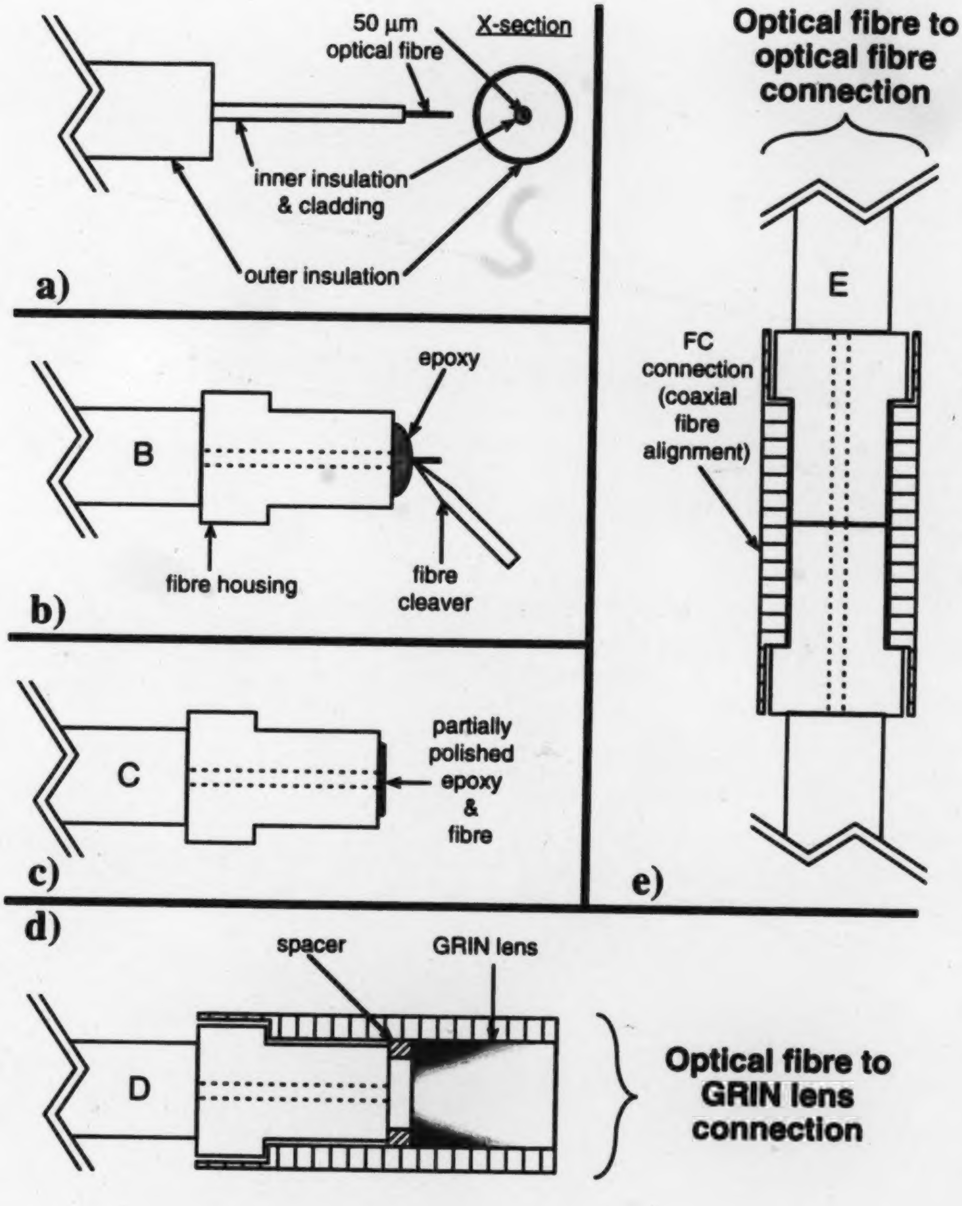
50 μm
optical fibre
X-section
inner insulation
& cladding
outer insulation
a)
epoxy
B
fibre housing
fibre
cleaver
b)
C
partially
polished
epoxy
&
fibre
c)
d)
spacer
GRIN lens
D
Optical fibre to
GRIN lens
connection
Optical fibre to
optical fibre
connection
E
FC
connection
(coaxial
fibre
alignment)
e)

Figure 2.16: Optical Fibre Connections.

a) - c), preparation of fibre in its housing; d) fibre to GRIN connection;

e) fibre to fibre connection

2.2.5 Detection Electronics

The general description of the detection electronics is most easily followed by looking at the circuit diagram of the detection electronics for one of the 16 capillaries, shown in Figure 2.17. Photons travelling along the optical fibre from that particular capillary's GRIN lens are incident upon the depletion region of the avalanche photodiode (APD) transducer. The depletion zone in the APD is created by a reverse bias of approximately -200 V applied by a high voltage power supply to the positive electrode of the APD (a description of the procedure used to bias each individual APD can be found later in section 2.2.5.B) such that some of the incident photons create avalanches of electrons, as described earlier in section 2.1.2.B. A weak current signal, on the order of nanoamperes, is produced from the APD, and is sent to a high gain transimpedance amplifier. The "bucking" current, an adjustable, weak current opposing that from the APD, joins the latter before it reaches the amplifier, and serves to counter any thermal current generated by the APD; it is a circuit for adjusting the position of the baseline (described in more detail in section 2.2.5.E). The net current reaching the high gain transimpedance amplifiers is converted to voltage and amplified by 10^9 V/A. The voltage signal is then passed through low-pass filters to screen out any high frequency noise (the cut-off frequency is 7.2 Hz - see section 2.2.5.G). This filtered and amplified APD signal is then sent along with the synchronisation pulse from the chopper/filter wheel electronics (see section 2.2.3) to the computer to be collected as an electropherogram.

2.2.5.A APD Cooling

The need for temperature control of the APDs at low temperature (-20.0 to -30.0 °C) is fourfold. The photo-current generated by an APD is very sensitive to the proximity of the APD's applied reverse bias to the breakdown voltage, which

Figure 2.17: Detection Electronics for One Capillary.
APD is reverse-biased by a discrete power supply and generates a weak current in response to incident light from the optical fibre. A bucking current opposes the APD background current and allows the baseline to be adjusted. The APD current is then amplified and converted to a voltage, and finally put through a 7 Hz low pass filter before being sent along with the synchronisation pulse from the filter/chopper wheels to the computer for data acquisition.

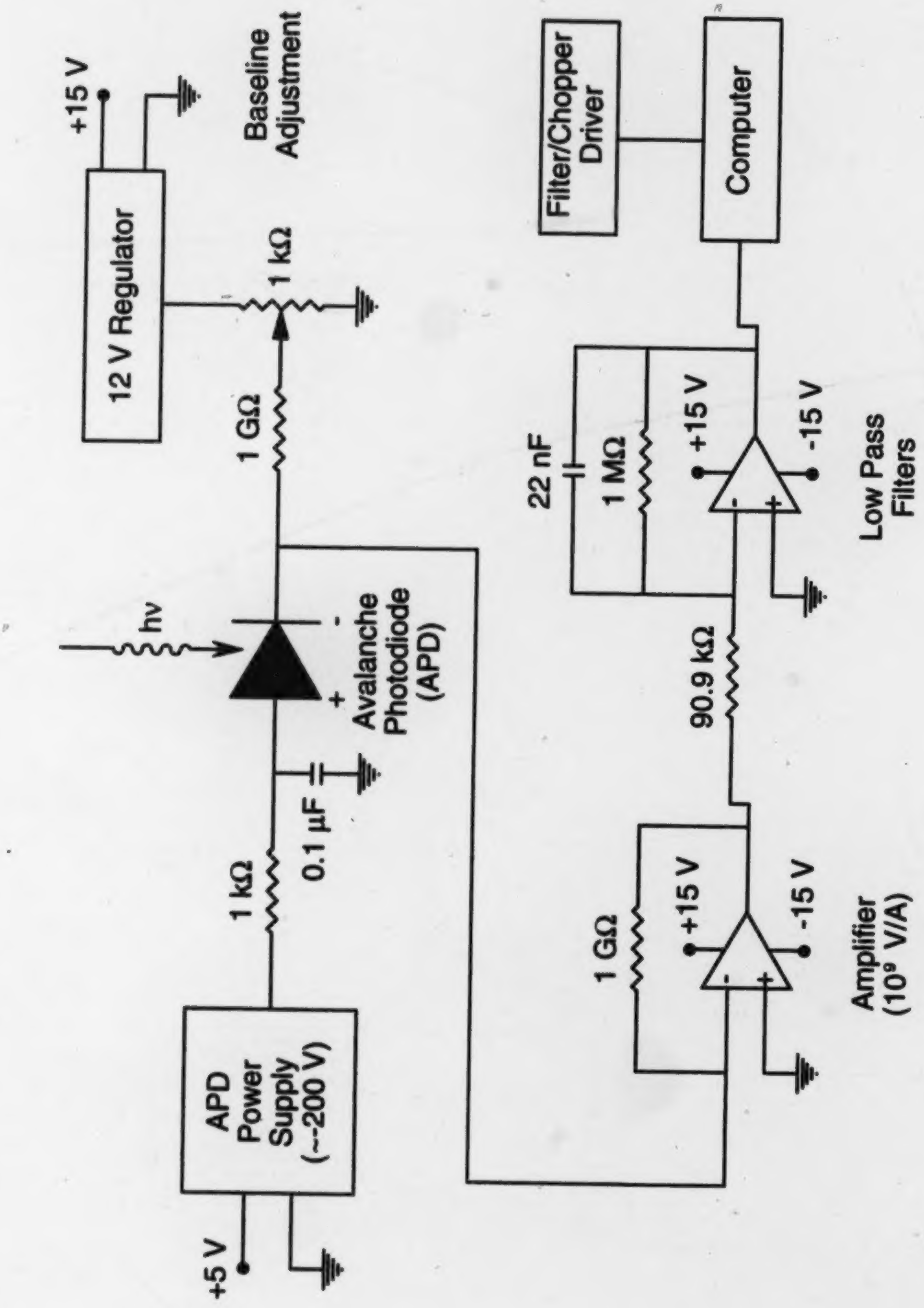
+15 V
Baseline Adjustment
12 V Regulator
1 kΩ
1 GΩ
hν
-
+
Avalanche Photodiode (APD)
0.1 µF
1 kΩ
APD Power Supply (~-200 V)
+5 V
Filter/Chopper Driver
Computer
22 nF
1 MΩ
+15 V
-
+
-15 V
Low Pass Filters
90.9 kΩ
1 GΩ
+15 V
-
+
-15 V
Amplifier (10^9 V/A)

is temperature dependent; the photo-current is superimposed on a background of thermal current, which is also temperature dependent. Keeping the APDs at a *constant* temperature stabilises both the background, as well as the breakdown voltage and hence signal. Operation of the APDs at *low* temperature produces two more benefits: the thermally generated background signal is greatly reduced, and the background is much less sensitive to temperature fluctuations. Keeping the APDs at a *constant, low* temperature yields a more stable signal on a lower, more stable background.

Experimental: The APDs (EG&G Optoelectronics C30902S, Vaudreuil, Québec, Canada) are housed in an aluminum U-block inside a Styrofoam box, as shown in Figure 2.18; the box is ~ 3" X 3" X 3" inside, and the walls are 2" thick. Holes were bored into the walls and lid of the box to bring in electrical leads, dry N_2, etc., and all holes and pieces of Styrofoam used to make the box were sealed together with silicone (RTV 102, G. E. Silicones Canada, Pickering, Ontario, Canada). Dry nitrogen is left continuously flowing through the box to purge it of moisture. During operation, the APDs are cooled in two stages to -20.0 °C. In the first stage, the heat is drawn from the aluminum block with a Peltier cooler (Melcor CP-1.4-71-10L, Trenton, N. J.). The Peltier cooler is switched between zero and maximum current by a power supply (Kepco MSK 10-10M, Flushing, N. Y.). The duty cycle of the power supply, ~ 58% with second stage cooling at ~ -4 °C, is in turn precisely controlled by a proportional temperature controller (ERO μPC, ERO Electronic S.p.A., Milan, Italy; the settings used were: set point = -20.0 °C, proportional band = 2.0%, reset = 30 s, rate = 0 s, antireset = 0%, deadband/cycle = 2%, manual reset = 50%) which uses a platinum resistance temperature detector mounted directly on the aluminum block for feedback. The heat is pumped from the hot side of the Peltier cooler by a locally made copper heat sink through which an ethylene glycol/water solution is

Figure 2.18: APDs in Cooling Box.

APDs are mounted directly into an aluminum U-block which is cooled to -20.0°C by a Peltier cooler and a circulating water bath. A 2 inch sealed Styrofoam box insulates the assembly, contains desiccant and is purged continuously with dry N_2 to ensure that the APD environment is moisture-free.

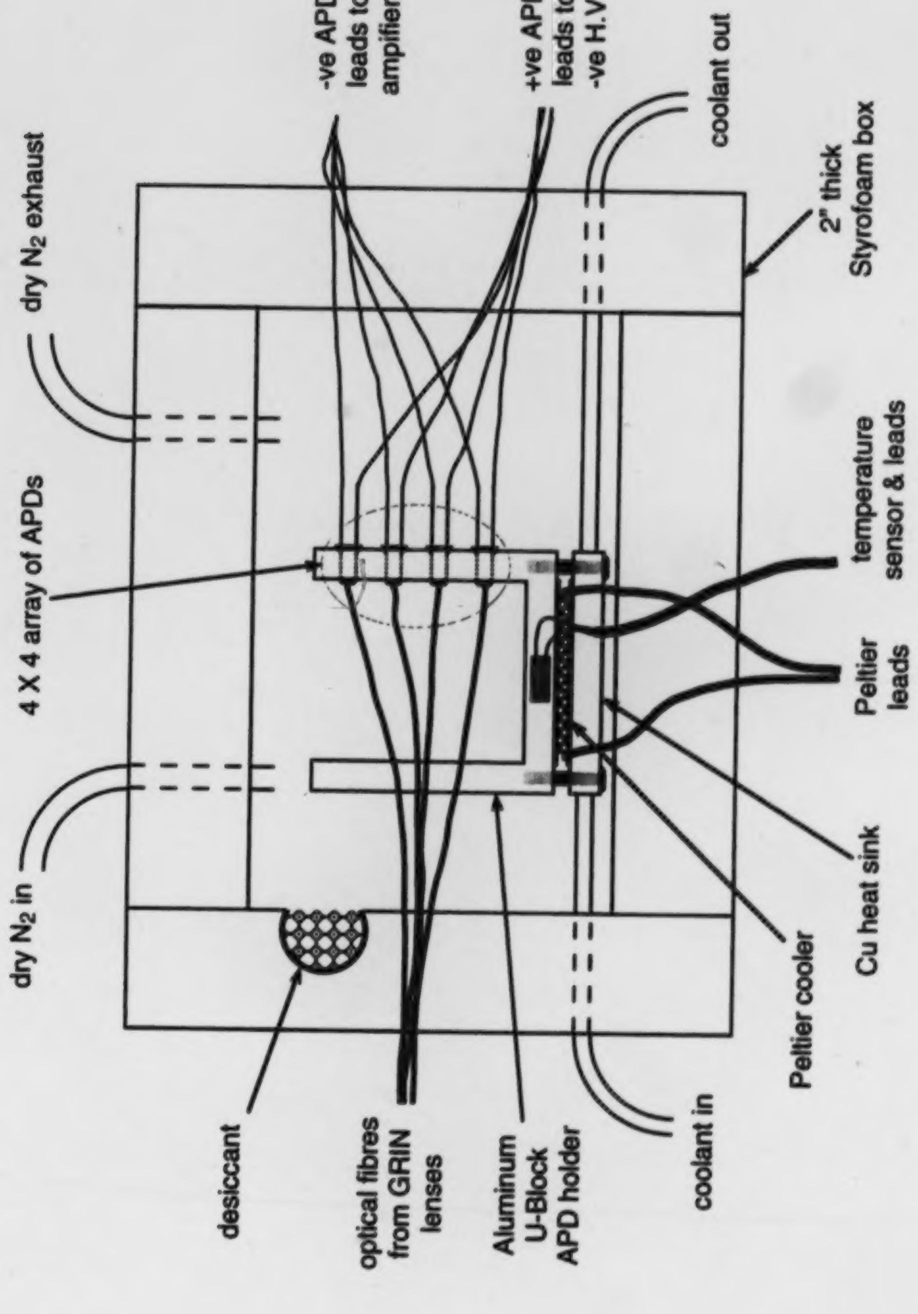
4 X 4 array of APDs
dry N_2 in
dry N_2 exhaust
-ve APD leads to ampifiers
+ve APD leads to -ve H.V.
coolant out
2" thick Styrofoam box
temperature sensor & leads
Peltier leads
Cu heat sink
Peltier cooler
coolant in
Aluminum U-Block APD holder
optical fibres from GRIN lenses
desiccant

circulated by a water bath operated at ~ -4 °C (MGW Lauda-Brinkmann RC20 (bath) and B2R (thermostat), Messgeräte-Werk Lauda, West Germany). As operated, the temperature of the block does not deviate from -20.0 °C by more than 0.1 °C.

Results and Discussion: The choice of APD temperature was a compromise between reduced background at lower temperatures and reduced water condensation at higher temperatures. During early experimentation, the cooling system was as described in the preceding paragraph except that the second stage of cooling was cold tap water instead of the circulating water-ethylene glycol bath, and so the minimum achievable temperature was ~ -34°C; to minimise background magnitude and fluctuation, the APDs were cooled to -30.0 °C, the minimum temperature that could be tightly controlled. However, APD signal observed at -30.0° on a digital oscilloscope (PM 3375, Philips, Eindhoven, Holland) showed frequently-occurring current spikes, despite biasing the APDs well beneath the breakdown voltage (see section 2.1.2.B); these spikes were thought to be due to intermittent short-circuits created by ice crystal formation on the cold APD leads[22]. Several steps were taken to hinder ice-crystal formation. The dry nitrogen flow was made non-stop, and a replaceable cylinder of Drierite was added to the box as a crude gauge of moisture content in the styrofoam box. The temperature was set for -20.0 °C, and the APDs were optimised for -20.0 °C (in section 2.2.5.B on APD Biasing); while only 378 ppm of water are required for a dew point of -30 °C, 1020 ppm are required at -20 °C[23]. With these changes, higher signal-to-noise values were obtained, and the current spikes disappeared.

2.2.5.B APD Biasing

As purchased from EG&G, the APDs were supplied with data sheets giving the operating and breakdown voltages for operation at 22 °C, and with an approximate temperature correction factor of 0.6 V/°C, allowing the operation voltage to potentially be corrected for the lower operating temperature of -20.0 °C used (the need for, and mechanism of, temperature control is discussed in section 2.2.5.A). However, the response of the transducers was very sensitive to small changes in bias at the recommended, extrapolated operating voltage, and so it was thought that a somewhat more rigourous approach should be adopted for determining the biasing voltage. The optimal reverse bias potentials applied to the APDs (distinct for each APD) were determined by maximising their signal to noise ratio, S/N.

Experimental: Each APD was tested individually. An assembly consisting of a 2 cm X 2 cm X 8 cm black plastic holder aligning a small LED (light-emitting diode) to a GRIN lens connected to the APD being tested is shown in Figure 2.19. The plastic holder has a slot allowing for neutral colour density filters (÷ 1.26, ÷ 2, ÷ 4, and ÷ 10, Kodak Wratten Gelatin Filter, Eastman Kodak, Rochester, New York) to reduce the LED intensity; light-tight seals were made at this slot, and where the GRIN and LED enter the holder to block all light except that from the LED from reaching the GRIN lens. This assembly was used as a reproducible light source for the APDs. For each APD, several biasing voltages were chosen in a 5-10 V range in the linear avalanche region, just before the breakdown voltage at which point the APD changes to Geiger mode. With a given APD biased at a given voltage, the LED was set to flash at approximately 0.5 Hz, and the amplified, filtered APD signal was collected on the Apple computer using a simple Labview 1-channel programme. The intensity of the

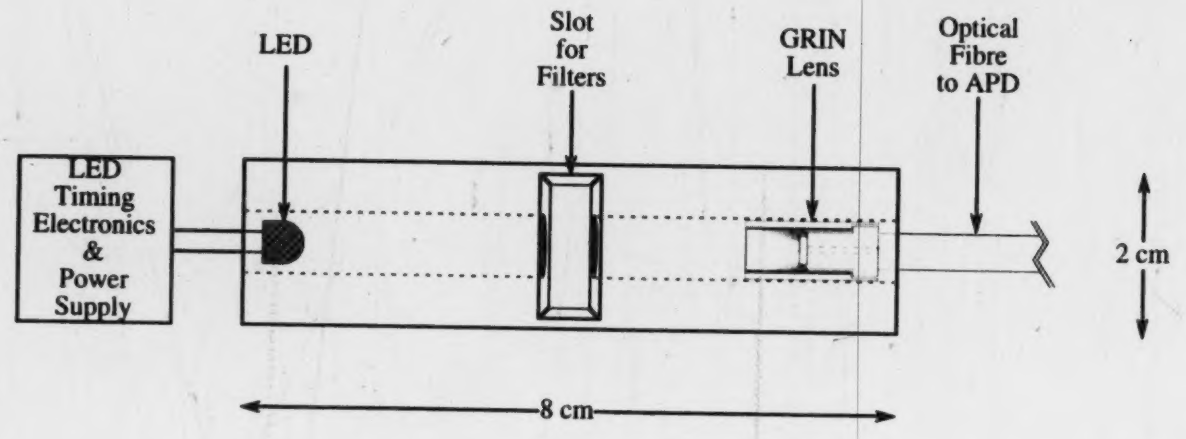
LED
Slot
for
Filters
GRIN
Lens
Optical
Fibre
to APD
LED
Timing
Electronics
&
Power
Supply
2 cm
8 cm

Figure 2.19: LED-GRIN Lens Aligner Used as APD Light Source.
(LED and GRIN lens are magnified for clarity)

LED was reduced with neutral density filters so that the APD signal was on-scale. In the resulting square wave signal trace, the height of the square wave represented the signal, S, and the standard deviation of the signal with the LED on represented the noise in the signal, N; these values were determined by statistical analysis of the traces in Igor Pro (WaveMetrics, Inc., Lake Oswego, Oregon), a data manipulation programme.

Results and Discussion: The results of these tests at -20.0 °C are shown in Table 2.3; for each APD, the optimal biasing voltage (to which the APD was set following the test) is italicised and boldscripted. The results are also depicted graphically in Figure 2.20. In some cases, APDs displayed multiple-maxima for their S/N over the range studied; in these cases, the values chosen were for the S/N maxima thought to be most central to the biasing voltage range for which high S/N was seen.

2.2.5.C APD Stabilisation

When the APDs have been cooled down to -20.0 °C and are first turned on, the signal collected over the first ~ 30 minutes shows significant baseline drift; to circumvent this problem, the detection electronics were all powered up for at least 30 minutes prior to data collection.

2.2.5.D APD Power Supply

The reverse bias for each APD is supplied by a discrete power supply (-20 to -350 V, Analog Modules model 522, Longwood, Florida), and is decoupled from any high frequency ripple by a passive, 1.6 kHz low-pass filter (see Figure 2.17) before reaching the transducer.

APD #1		APD #2		APD #3		APD #4		APD #5		APD #6	
V_{bias}	S/N	V_{bias}	S/N	V_{bias}	S/N	V_{bias}	S/N	V_{bias}	S/N	V_{bias}	S/N
-154	5.8	-207.5	6.6	-205	6.1	-208.1	3.3	-203.9	3.7	-207.5	3.8
-154.5	***7.1***	-208.6	6.1	-206	7.1	***-209.2***	***5.3***	-205.7	4.3	-209.5	6.8
-155.6	4.7	-209	4.6	-207.1	6.8	-210	4.2	-206.8	5.6	-210.4	7.5
-156.2	4.6	-210.4	4.2	***-208***	***7.9***	-210.9	4.7	***-207.5***	***5.7***	-211.6	6.6
-156.8	3.6	***-211.4***	***6.5***	-208.9	6.4	-211.8	4.9	-208.8	5.4	-212.6	9.5
-157.9	3.4	-213.6	5.2	-209.9	7.3	-212.3	3.7	-209.8	2.8	***-213.4***	***11.4***
		-215.3	4.5	-212.1	5.8	-213	3.1			-214.5	7.4
				-214	3.1	-213.8	3.4			-215.7	3.9

Table 2.3: Avalanche Photodiode Biasing Voltage Optimisation. Signal-to-noise values obtained at biases near the breakdown voltage; optimal values are italicised. APDs 1-6 this page, 7-16 next page

APD #7		APD #8		APD #9		APD #10		APD #11	
V_{bias}	S/N	V_{bias}	S/N	V_{bias}	S/N	V_{bias}	S/N	V_{bias}	S/N
-207.1	4.9	-210.5	4.8	-206.4	3.8	-208.2	6	-209.8	5.1
-208.2	5.1	-211.5	5.2	-207.9	4.5	-209.6	4.9	-212.2	7
-209	4.9	***-212.4***	***8.4***	-208.9	4.6	***-210.4***	***6.2***	-213.2	5.4
-210.1	4.7	-213.4	6.3	***-210***	***5.6***	-211.2	4.5	-214.2	7.5
-211.3	***8.7***	-214.4	6.7	-211.1	5.4	-212.2	5.9	***-215.1***	***9.1***
-212.3	5.6	-215.5	4.9	-212.3	5.4	-213.7	4.9	-216.1	4.7
-213.2	4.6	-216.6	5.8	-213.2	4.8	-214.6	3.7	-218.1	5.1
				-214.2	5.6	-215.6	3.4	-218.9	4.3
								-220.1	1.8

APD #12		APD #13		APD #14		APD #15		APD #16	
V_{bias}	S/N	V_{bias}	S/N	V_{bias}	S/N	V_{bias}	S/N	V_{bias}	S/N
-198.5	3.3	-210.3	4.7	-203.9	7.4	-204.9	4.3	-200.9	3.3
-199.4	***7.1***	-212.5	5.2	-204.9	8.6	-206	7	-202.1	5
-200.5	4.9	-213.5	5.9	-205.9	7.2	-206.9	4.9	***-203.1***	***6.2***
-201.5	5	***-215.4***	***6.4***	***-207***	***8***	***-207.8***	***7.8***	-203.8	3.9
-202.4	4.5	-216.5	4	-208.2	5.9	-208.8	5.2	-205.1	3.9
-203.4	2.8	-217.6	3.4	-209.9	4.2	-210	5.7	-206.1	5.7
-205.9	2.6			-211.9	2.5	-211	4.4	-207.1	2.8

Figure 2.20: APD Biasing Curves.

Signal-to-noise plotted against biasing voltage near the breakdown voltage for each APD.

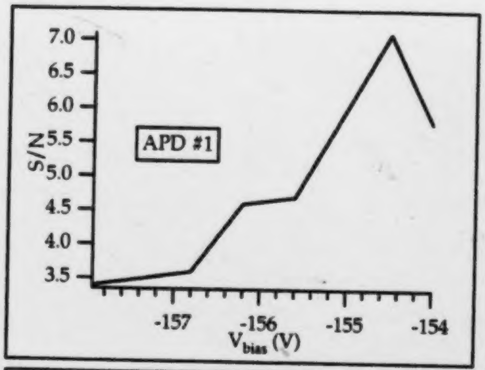
APD #1
S/N
7.0
6.5
6.0
5.5
5.0
4.5
4.0
3.5
-157
-156
-155
-154
V_{bias} (V)

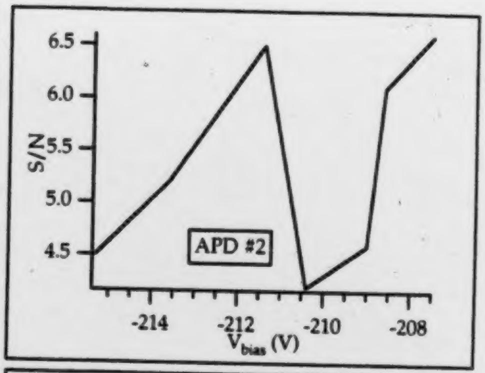
APD #2
S/N
6.5
6.0
5.5
5.0
4.5
-214
-212
-210
-208
V_{bias} (V)

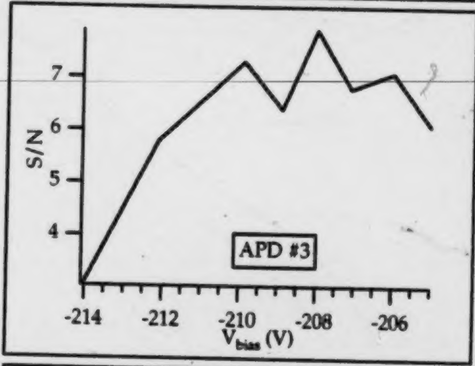
APD #3
S/N
7
6
5
4
-214
-212
-210
-208
-206
V_{bias} (V)

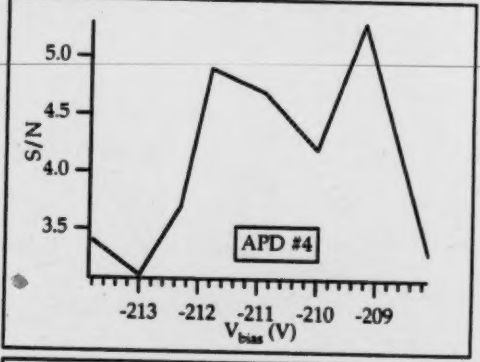
APD #4
S/N
5.0
4.5
4.0
3.5
-213
-212
-211
-210
-209
V_{bias} (V)

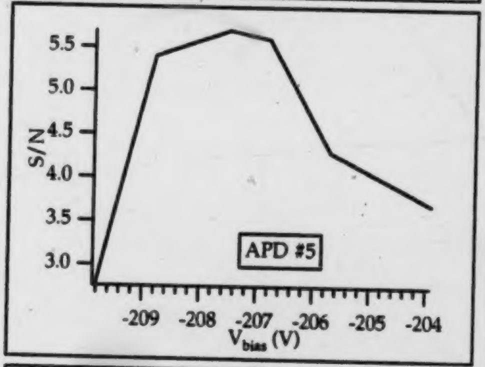
APD #5
S/N
5.5
5.0
4.5
4.0
3.5
3.0
-209
-208
-207
-206
-205
-204
V_{bias} (V)

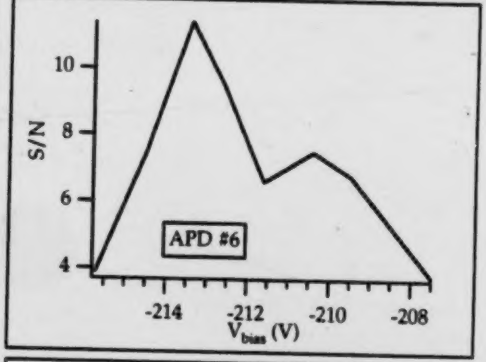
APD #6
S/N
10
8
6
4
-214
-212
-210
-208
V_{bias} (V)

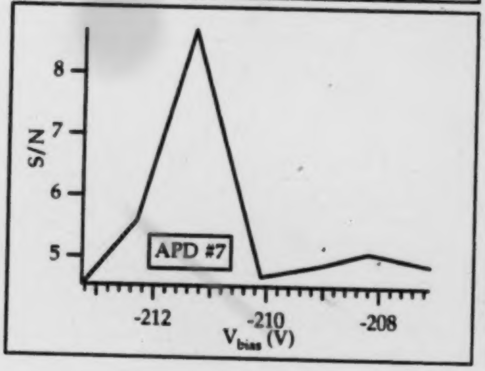
APD #7
S/N
8
7
6
5
-212
-210
-208
V_{bias} (V)

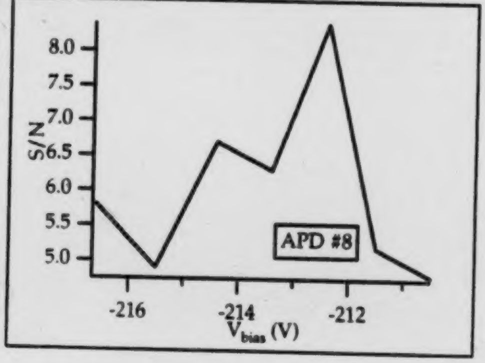
APD #8
S/N
8.0
7.5
7.0
6.5
6.0
5.5
5.0
-216
-214
-212
V_{bias} (V)

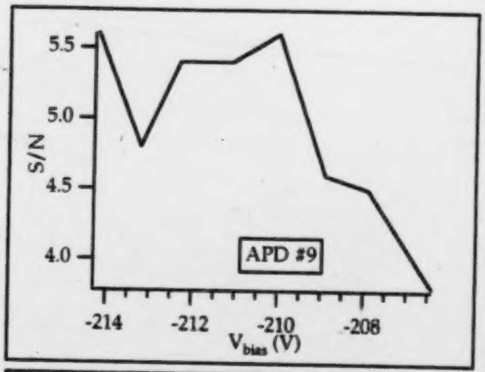
5.5
5.0
4.5
4.0
S/N
APD #9
-214
-212
-210
-208
V_{bias} (V)

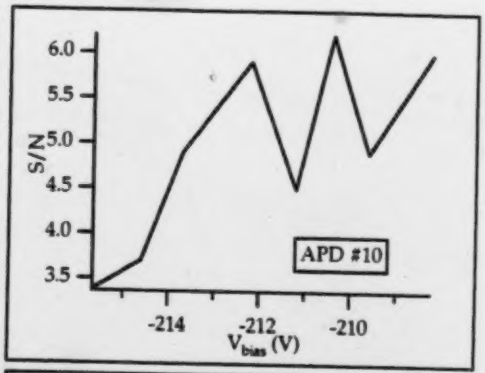
6.0
5.5
5.0
4.5
4.0
3.5
S/N
APD #10
-214
-212
-210
V_{bias} (V)

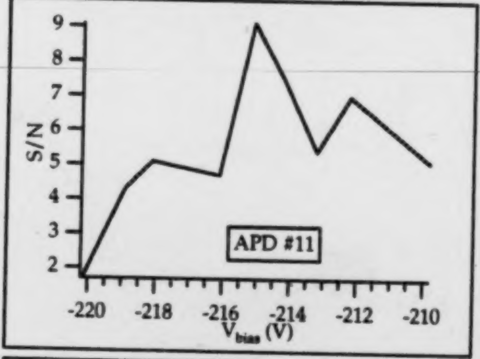
9
8
7
6
5
4
3
2
S/N
APD #11
-220
-218
-216
-214
-212
-210
V_{bias} (V)

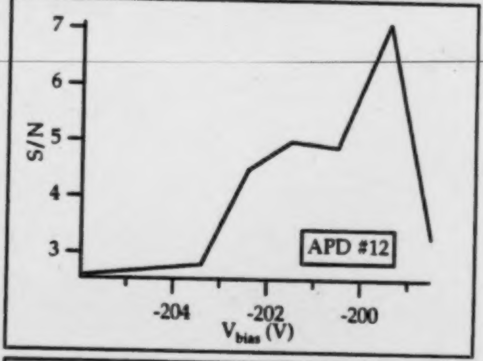
7
6
5
4
3
S/N
APD #12
-204
-202
-200
V_{bias} (V)

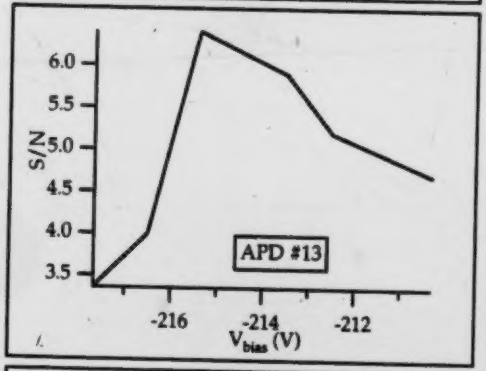
6.0
5.5
5.0
4.5
4.0
3.5
S/N
APD #13
-216
-214
-212
V_{bias} (V)

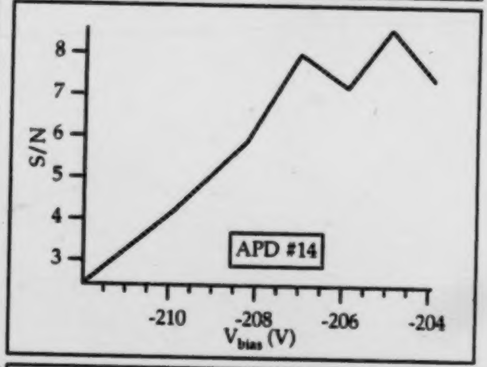
8
7
6
5
4
3
S/N
APD #14
-210
-208
-206
-204
V_{bias} (V)

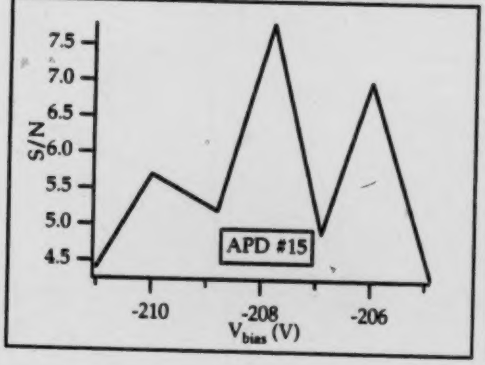
7.5
7.0
6.5
6.0
5.5
5.0
4.5
S/N
APD #15
-210
-208
-206
V_{bias} (V)

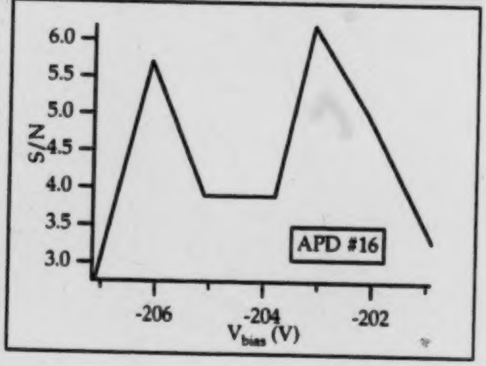
6.0
5.5
5.0
4.5
4.0
3.5
3.0
S/N
APD #16
-206
-204
-202
V_{bias} (V)

2.2.5.E Bucking Current

A circuit for baseline adjustment was also implemented, enabling the baseline to be shifted at will. A 0-12 V supply was dropped across a 1 GΩ resistor to produce a weak current opposing that of the APD, added before amplification, between the APD and the transimpedance amplifier; this current is referred to as the bucking current. This current was added to offset the thermal current generated by the APDs and extend the dynamic range. However, operating the APDs at -20.0 °C results in the reduction of the thermal current to a negligible magnitude. The baselines are thus adjusted to merely space the traces of the different APDs out on the screen during data acquisition.

2.2.5.F APD Noise and Data Acquisition Mis-Triggering

One drawback of the homemade design and construction of the detection electronics was its susceptibility to environing noise sources. During the ~ 2-year course of instrument development, three major kinds of electronic noise were isolated and eliminated or reduced to tolerable levels with help from Larry Coulson and Darren Lewis of this Department. Two were observed directly in the signals emanating from the APD detectors, while the third was seen in the triggering signal to the software data acquisition.

The noise seen in the post-filter APD signals was observed on a digital oscilloscope with the APDs on, cooled to -30 °C, amplifiers, low-pass filters and base-line adjustment circuit on, and all light to the GRIN lenses blocked. The first type of noise observed was an 80 MHz, 1-5 mV peak-to-peak signal seen with varying amplitudes on all 16 channels. As a reference to the reader, typical signal amplitudes generated by DNA samples, while varying from APD to APD, were on the order of hundreds of millivolts, so a 5 mV noise was not insignificant. Though initially seen with all the above-mentioned components powered up, the noise was also observed with only the low-pass filters connected to the scope, and with all the components including the low-pass filters turned off (refer to Figure 2.17). This last observation means the point of entry is after the low-pass filters and before the computer. The noise proved hard to shunt to ground, but was circumvented by amplifying the signal in the filters themselves. Refering to Figure 2.17, R_1 had previously been 1 MΩ, such that the filter gain, R_2/R_1, was one. By adding to each of the 16 low-pass filter circuits a 100 kΩ resistor in parallel with the the R_1 1 MΩ resistor, the new value for R_1 and the filter gain became:

$$R_1 = \frac{1}{\frac{1}{100\,\mathrm{k\Omega}} + \frac{1}{1000\,\mathrm{k\Omega}}} = 91\,\mathrm{k\Omega} \qquad (2.10)$$

and:

$$\mathrm{Gain} = \frac{R_2}{R_1} = \frac{1000\,\mathrm{k\Omega}}{91\,\mathrm{k\Omega}} = 11 \qquad (2.11)$$

After the alteration, the amplitude of the 80 MHz noise did not change, meaning that the signal would be amplified 11 times relative to that particular source of noise.

The source of this noise is thought to originate from outside of the laboratory. A simple antenna conceived of by Larry Coulson of this department consisting of a 10 X electronic probe (P6062B, Tektronix, Beaverton, Oregon) with its ground clamp connected to the probe clip with a bare coil of copper wire was used to try to locate the origin of the 80 MHz signal. With instruments turned off, all the optical tables in the laboratory could be seen to receive this signal, as did any large metal obect on several floors of the same wing of the building; it is thought to perhaps originate from one of the powerful nmr instruments in the department.

The second type of noise observed was 60 Hz line noise in the APD signals. In contrast to the 80 MHz noise, the line noise was only evident when the detection electronics were powered up. The point of entry, determined by moving a ~ 30 cm X 30 cm sheet of Ad-Mu foil (Ad-Vance Magnetics Inc., Rochester, Indiana) about the electronics and watching for the suppression of the noise signal as observed on the scope, was seen to be the APD leads coated only with nail polish prior to their connection with the shieldel coaxial cable leading the signal to the transimpedance amplifiers. A schematic of the U-block housing the APDs, their bare leads and coaxial cable may be seen in Figure 2.21. The bare leads are in a 4 X 4 array, in the form of a box; providing grounded shielding for all six sides dramatically reduced the magnitude of the interference of line noise from 2 V to 20 mV peak-to-peak noise amplitude, versus typical sample signal amplitude on the order of volts with the modified, amplifying low-pass filters. The shielding was accomplished by grounding the aluminum U-block on one side of the box, forming a grounded cylinder of Ad-Mu foil around the APD leads, parallel to them, shielding the four box sides touching the aluminum U-block, and finally wrapping foil around the outside of the styrofoam box to shield the last side of the box.

Additional shielding for the detection signal electronics (but not triggering electronics) was provided by placing the APDs, their high voltage power supplies, amplifiers, low pass filters and baseline adjusters on a grounded copper sheet (~ 30 cm X 60 cm) on a Plexiglas base, and covering the assembly with a grounded stainless steel box (~ 30 cm X 30 cm X 60 cm). The copper sheet acted as a ground plane to which the ground leads and/or casings from all the electronic

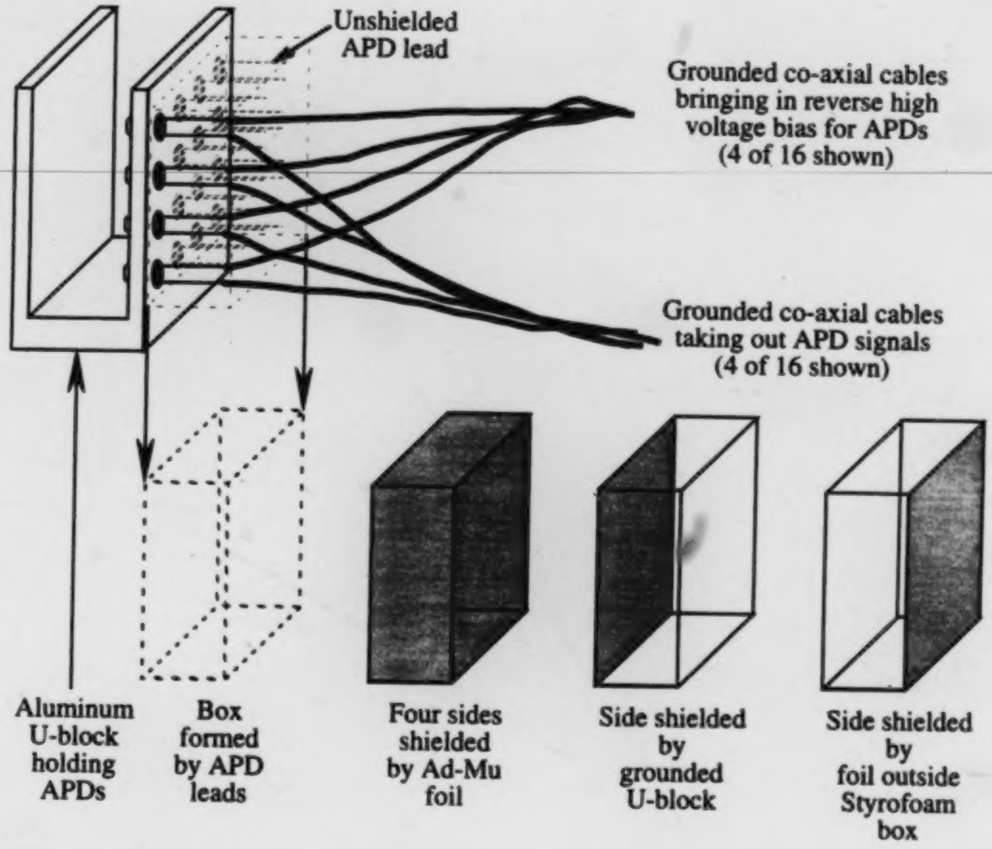
Unshielded
APD lead
Grounded co-axial cables
bringing in reverse high
voltage bias for APDs
(4 of 16 shown)
Grounded co-axial cables
taking out APD signals
(4 of 16 shown)
Aluminum
U-block
holding
APDs
Box
formed
by APD
leads
Four sides
shielded
by Ad-Mu
foil
Side shielded
by
grounded
U-block
Side shielded
by
foil outside
Styrofoam
box

Figure 2.21: Shielding APD Leads from Interference.

(see text for explanation)

components as well as the shielding box were attached. Shielded, grounded coaxial cable was used to carry the signal from the APDs to the amplifiers, on to the low-pass filters and finally to the connector box which was interfaced with the computer's ribbon cable; it was also used to carry the high voltage bias to the APDs.

The third type of noise was interference in the interruptor signal from the filter and chopper wheels. This interference manifested itself in the occurrence of 1 point signal spikes occurring in acquired, four colour, electropherograms - large, 1 point deviations from the electropherogram's profile (software data acquisition is described in detail in section 2.2.3.B); in some cases, the frequency of these spikes was such that analyte peaks were obscured. The programmer of the data acquisition software, Darren Lewis of this group, was able to virtually eliminate this effect by wrapping in grounded aluminum foil the cables from the chopper and filter wheel motors to their driving circuitry, as well as the circuitry itself, the cable from the circuitry to the computer ribbon cable, and the communications ethernet connection to the computer.

2.2.5.G Low-Pass Filter Performance

As a check on the performance of the low-pass filters, the frequency dependance of their outputs was verified. A function generator emitting a sine wave was input into each of the filters, and the input and output voltages at five different frequencies were measured on the digital scope. The results may be viewed in Table 2.4, or in graphic form in the log (V_{out}/V_{in}) vs. log $f_{freq.\ gen.}$ plots of Figure 2.22; such log-log plots are referred to as Bode plots. The form of a Bode plot essentially consists of two linear functions: for $f_{freq.\ gen.} < f_{cut\ off}$, the low-pass filter is expected to transmit the signal undampened, so log (V_{out}/V_{in}) should be constant, while for $f_{freq.\ gen.} > f_{cut\ off}$, the single stage filter dampens[18] the signal by.

$f_{freq. gen.}$ (Hz)	V_{out}/V_{in}							
	LPF #1	LPF #2	LPF #3	LPF #4	LPF #5	LPF #6	LPF #7	LPF #8
4	9.7	8.9	9.6	9.7	9.0	9.0	9.4	9.4
7	7.7	7.8	8.0	8.7	8.1	7.9	8.0	8.4
10	6.5	6.4	6.8	6.4	6.8	7.2	7.0	6.0
30	2.6	2.5	2.4	2.9	2.8	2.5	2.6	2.9
70	1.2	1.1	1.2	1.4	1.3	1.3	1.2	0.97
Roll-off (dB/decade)	-17.4	-18.1	-17.8	-15.6	-17.0	-17.6	-18.1	-18.7

$f_{freq. gen.}$ (Hz)	V_{out}/V_{in}							
	LPF #9	LPF #10	LPF #11	LPF #12	LPF #13	LPF #14	LPF #15	LPF #16
4	9.4	9.1	9.7	12.3	9.1	9.1	9.7	9.7
7	8.2	7.8	7.5	8.0	7.5	7.2	7.8	8.2
10	6.7	6.7	6.6	7.4	6.3	6.3	6.8	6.7
30	2.8	2.7	2.6	3.0	2.5	2.2	2.8	2.8
70	1.2	1.1	1.2	1.4	1.3	1.3	1.2	0.97
Roll-off (dB/decade)	-17.7	-18.6	-17.5	-17.1	-16.2	-16.2	-17.8	-19.9

Table 2.4: Low-Pass Filter Response vs. Frequency Generator Input. Filter response is calculated as V_{out}/V_{in} (± 0.1); generator input is $f_{freq. gen}$. Roll-off, the slope of log (V_{out}/V_{in}) vs log $f_{freq. gen.}$ for high frequencies, is ± 1.6 dB, and is calculated here for the 10 and 70 Hz points.

Figure 2.22: Low-Pass Filter Response Curves.

Low-pass filter response, V_{out}/V_{in} (± 0.1), vs. frequency generator input, $f_{freq.\ gen}$.

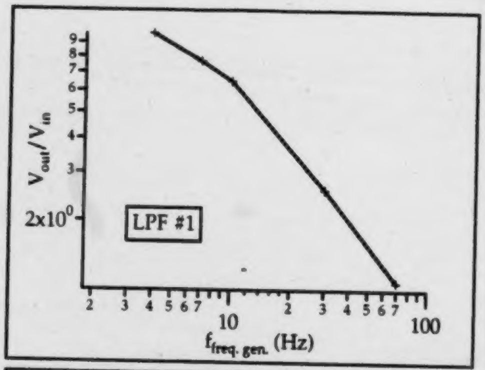
LPF #1
Vout/Vin
9 8 7 6 5 4 3 2x10⁰
2 3 4 5 6 7 10 2 3 4 5 6 7 100
ffreq. gen. (Hz)

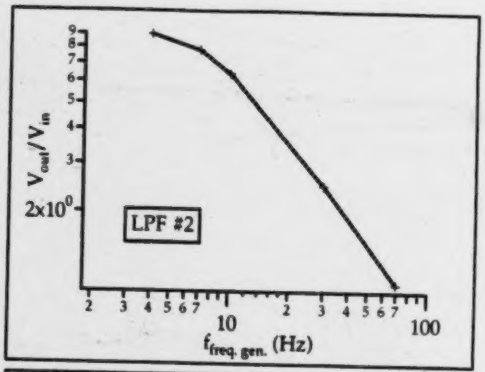
LPF #2
Vout/Vin
9 8 7 6 5 4 3 2x10⁰
2 3 4 5 6 7 10 2 3 4 5 6 7 100
ffreq. gen. (Hz)

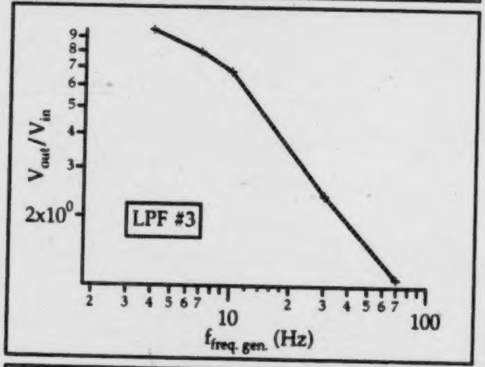
LPF #3
Vout/Vin
9 8 7 6 5 4 3 2x10⁰
2 3 4 5 6 7 10 2 3 4 5 6 7 100
ffreq. gen. (Hz)

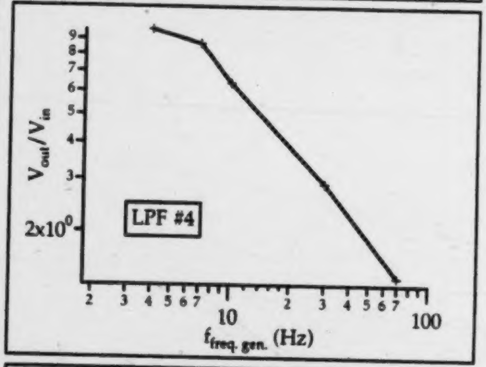
LPF #4
Vout/Vin
9 8 7 6 5 4 3 2x10⁰
2 3 4 5 6 7 10 2 3 4 5 6 7 100
ffreq. gen. (Hz)

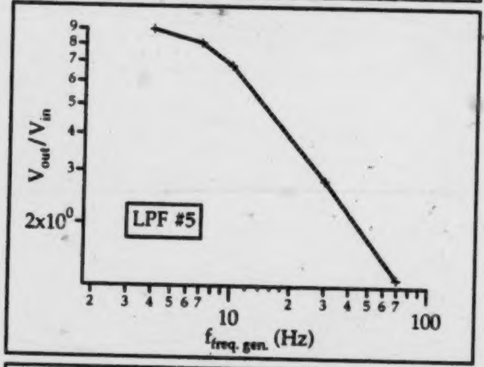
LPF #5
Vout/Vin
9 8 7 6 5 4 3 2x10⁰
2 3 4 5 6 7 10 2 3 4 5 6 7 100
ffreq. gen. (Hz)

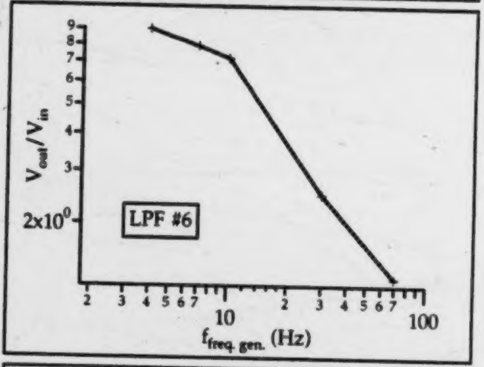
LPF #6
Vout/Vin
9 8 7 6 5 4 3 2x10⁰
2 3 4 5 6 7 10 2 3 4 5 6 7 100
ffreq. gen. (Hz)

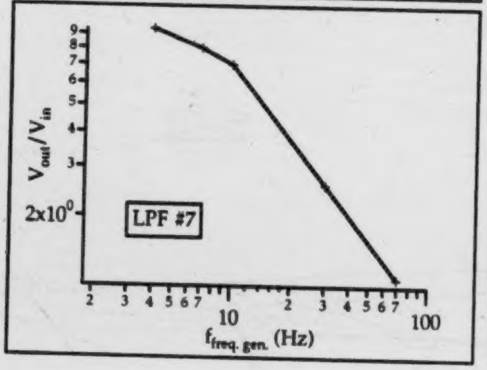
LPF #7
Vout/Vin
9 8 7 6 5 4 3 2x10⁰
2 3 4 5 6 7 10 2 3 4 5 6 7 100
ffreq. gen. (Hz)

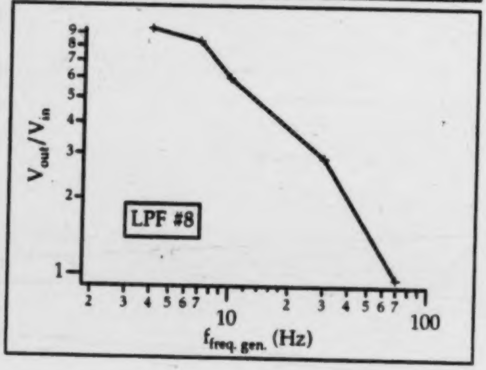
LPF #8
Vout/Vin
9 8 7 6 5 4 3 2 1
2 3 4 5 6 7 10 2 3 4 5 6 7 100
ffreq. gen. (Hz)

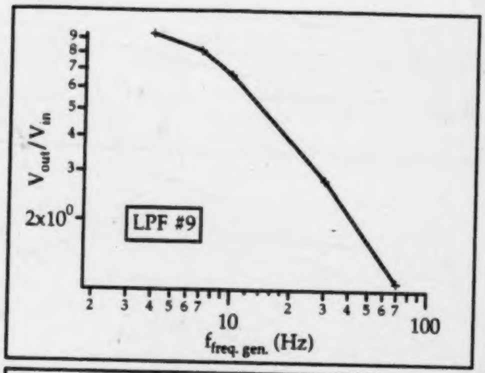
LPF #9
V_{out}/V_{in}
9 8 7 6 5 4 3 2x10⁰
2 3 4 5 6 7 10 2 3 4 5 6 7 100
$f_{freq.\ gen.}$ (Hz)

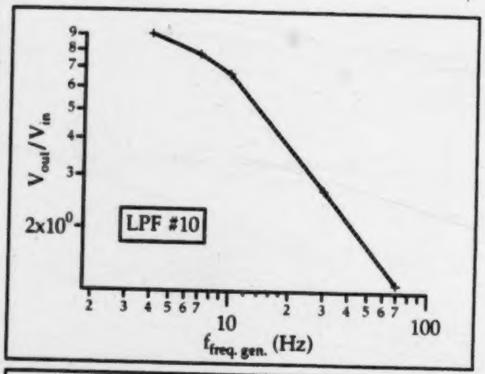
LPF #10
V_{out}/V_{in}
9 8 7 6 5 4 3 2x10⁰
2 3 4 5 6 7 10 2 3 4 5 6 7 100
$f_{freq.\ gen.}$ (Hz)

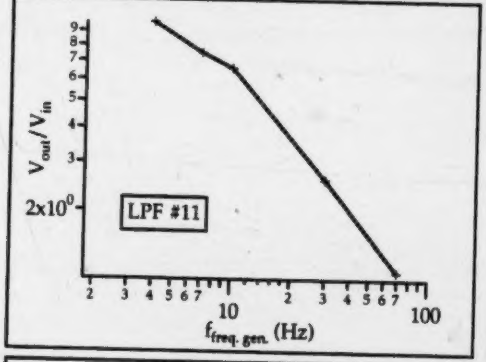
LPF #11
V_{out}/V_{in}
9 8 7 6 5 4 3 2x10⁰
2 3 4 5 6 7 10 2 3 4 5 6 7 100
$f_{freq.\ gen.}$ (Hz)

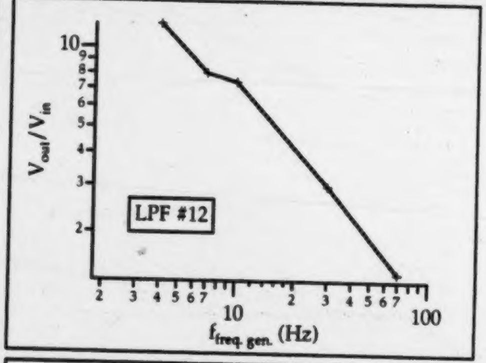
LPF #12
V_{out}/V_{in}
10 9 8 7 6 5 4 3 2
2 3 4 5 6 7 10 2 3 4 5 6 7 100
$f_{freq.\ gen.}$ (Hz)

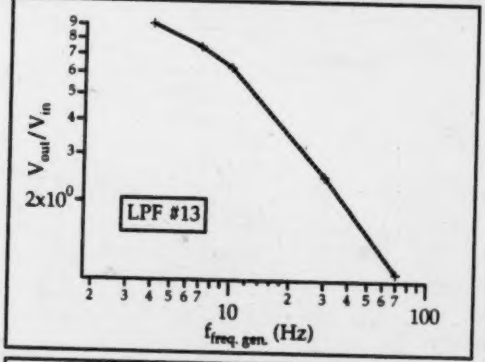
LPF #13
V_{out}/V_{in}
9 8 7 6 5 4 3 2x10⁰
2 3 4 5 6 7 10 2 3 4 5 6 7 100
$f_{freq.\ gen.}$ (Hz)

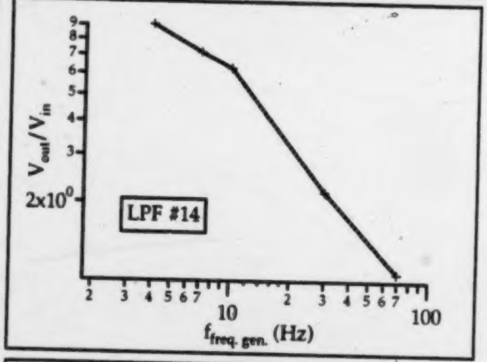
LPF #14
V_{out}/V_{in}
9 8 7 6 5 4 3 2x10⁰
2 3 4 5 6 7 10 2 3 4 5 6 7 100
$f_{freq.\ gen.}$ (Hz)

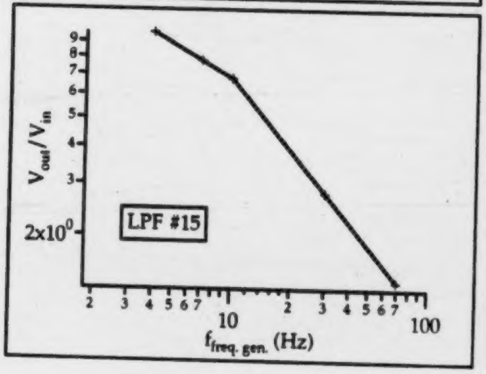
LPF #15
V_{out}/V_{in}
9 8 7 6 5 4 3 2x10⁰
2 3 4 5 6 7 10 2 3 4 5 6 7 100
$f_{freq.\ gen.}$ (Hz)

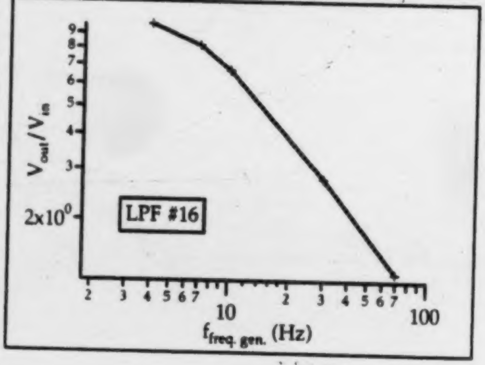
LPF #16
V_{out}/V_{in}
9 8 7 6 5 4 3 2x10⁰
2 3 4 5 6 7 10 2 3 4 5 6 7 100
$f_{freq.\ gen.}$ (Hz)

or "rolls off at", 20 dB/(frequency decade), which is the slope of the plot for these high frequencies. The equation for voltage gain expressed in dB (deciBels) is:

$$\text{Gain} = 20\log\left(\frac{V_{out}}{V_{in}}\right)\text{dB} \tag{2.12}$$

Two such filters in series (2 stage) would roll off at 40 dB/decade[22]. The Bode plot curves at the intersection of the two lines, and the signal suppression at their intersection where $f_{freq.\ gen.} = f_{cut\ off}$ should be by a factor of $2^{-0.5}$; this is called the "3 dB point", since 20 log ($2^{-0.5}$) dB = -3.01 dB.

The experimental plots of Figure 2.22 show the roll off section of the Bode plots, and are approaching full gain of 11 at 4 Hz, the lowest frequency measured, as the curves tend towards constant functions at low frequencies. For the sake of comparison, the roll-off was calculated for the linear region between 10 and 70 Hz for each of the plots; in the calculation, the 10 Hz and 70 Hz points were used to define the line. The roll-off values are shown in Table 2.4, and are close to the ideal -20 dB/decade.

At the cut-off frequency (7.2 Hz), the amplitude of a sine wave is expected to be dampened by a factor of $2^{-0.5}$; the filters used were given a gain of 11, so a value of $2^{-0.5} \times 11 = 7.8$ for V_{out}/V_{in} is expected at 7.2 Hz, and a value moderately higher at 7.0 Hz, in agreement with those seen in Table 2.4.

2.2.5.H Calculation of Low-Pass Filter Cut Off Frequency

The choice of the 7.2 Hz cut-off frequency for the low pass filters was based on geometric and temporal calculations, and was designed to filter out the broadest high frequency range while transmitting the transduced fluorescent signal with ≥ 97% efficiency. In other words, given the time that the GRIN lenses are exposed to fluorescence through each optical filter, the lowest possible low-pass filter cut-off frequency was chosen which still permited the fluorescence to be transmitted at full amplitude.

The exposure time of the GRIN lenses to the fluorescence through an optical filter can be calculated if the geometry of the filter wheel and its rotation frequency are known. Figure 2.23 shows the first filter wheel used, drawn to scale, for which the low-pass filters were designed; the presently used wheel is similar, but its differences and their affect on signal transmission will be discussed at the end of this section. The filter wheel rotates at 2.00 Hz, so each quarter rotation (90°) of the filter wheel lasts 125 ms. A quarter rotation may be assigned to each optical filter of which the majority of the 90° is occupied by the filter, and a smaller portion is required for the structure of the opaque black plastic filter wheel. If the angles at the centre of the filter wheel which subtend the optical filter, θ_f, and the opaque plastic between optical filters, θ_o, are known, then the GRIN lens exposure time, t_{exp}, which is that fraction of the 125 ms during which the GRIN lenses are exposed to the fluorescence from the cuvette through a particular optical filter, may be calculated as:

$$t_{exp} = 125\,\mathrm{ms} \bullet \frac{\theta_f}{\theta_o + \theta_f} = 125\,\mathrm{ms} \bullet \frac{\theta_f}{90^\circ} \tag{2.13}$$

Given the exposure time, the fraction of the input signal amplitude transmitted through a low pass filter, V_o/V_i, can be calculated as[18]:

$$\frac{V_o}{V_i} = 1 - \exp\left(\frac{-t}{RC}\right) \tag{2.14}$$

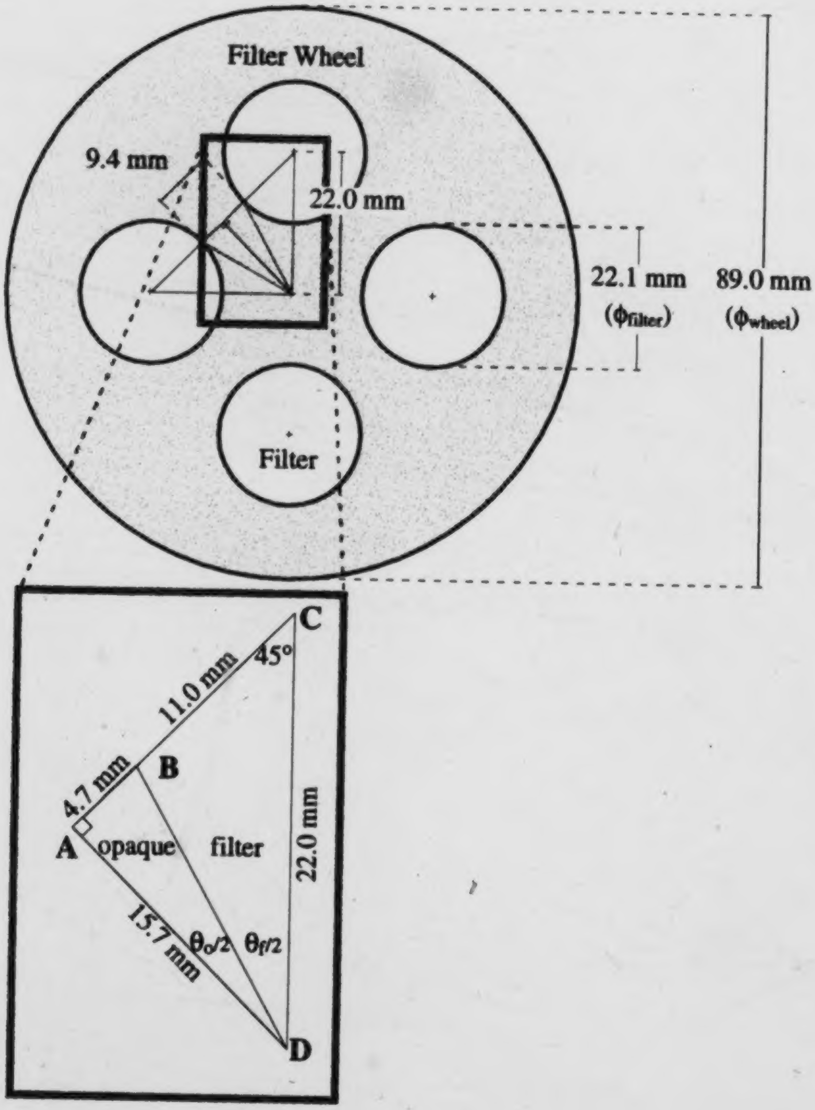
Filter Wheel
9.4 mm
22.0 mm
22.1 mm
(ϕ_{filter})
89.0 mm
(ϕ_{wheel})
Filter
C
45°
11.0 mm
B
4.7 mm
A
opaque
filter
22.0 mm
15.7 mm
$\theta_o/2$
$\theta_f/2$
D

Figure 2.23: Filter Wheel Geometry.

Measurements are used to calculate the exposure time of a GRIN lenses to its fluorescent spot; from the exposure time, the optimal time constant and cut-off frequency are determined for the low-pass electronic filters.

where R is the resistance (Ω) and C the capacitance (F) of the low-pass filter (gain of 1), and t is the time (s) that the imput voltage, V_i, has been applied. Solving equation (2.14) for RC, which is known as the filter's time constant, the appropriate cut-off frequency may be determined by the equation:

$$f_{co} = \frac{1}{2\pi RC} \tag{2.15}$$

where f_{co} is the cut-off frequency (Hz).

To calculate t_{exp}, trigonometry is applied to the filter wheel of Figure 2.23. Given the measurements taken on the filter wheel shown, angles θ_f and θ_o, can be determined approximately - a rigourous calculation would use circular arcs, but these are not easily measured experimentally:

$$\theta_o = 2\ \arctan(4.7\ \text{mm}/15.7\ \text{mm}) = 33.3°$$

and

$$\theta_f = 90° - \theta_o = 56.7°$$

From equation (2.13), t_{exp} is calulated:

$$t_{exp} = 125\,\text{ms} \bullet \frac{56.7°}{90°} = 78.8\,\text{ms}$$

The time constant RC is determined by rearranging equation (2.14), and assuming a high value of transmission, say 97%, for V_o/V_i:

$$RC = \frac{-t_{exp}}{\ln\left(1-\frac{V_o}{V_i}\right)} = \frac{-78.8\,\mathrm{ms}}{\ln(1-0.97)} = 22.5\,\mathrm{ms}$$

Equation (2.15) is then used to determine the appropriate cut-off frequency for the filter:

$$f_{co} = \frac{1}{2\pi \bullet 0.0225\mathrm{s}} = 7.1\,\mathrm{Hz}$$

The low-pass filters built used 22 nF capacitors and 1 MΩ resistors, such that $f_{co} = 7.2$ Hz, and $V_o/V_i > 97\%$.

A new filter wheel was inserted into the system (see section 2.2.3.B on data acquisition concerning the replacement of filter wheels) which was more compact since the filters were closer together, and still ran at 2.00 Hz. The effect of this change is a larger filter angle, θ_f, and hence exposure time, t_{exp}; since the low-pass filters were not changed, the transmission efficiency increased marginally.

2.3 Instrument Performance

Instrument performance is presented in two main areas, sensitivity evaluation (section 2.3.1) and four-colour DNA sequencing (section 2.3.2).

2.3.1 Sensitivity Evaluation

As a part of instrument characterisation, sensitivity was examined in two manners. First, a limit-of-detection (LOD) study was performed encompassing all 16 capillaries and the results are compared to those from a similar 5-capillary instrument from this group[24], and with LODs reported by other authors with multicapillary sequencers having completely different detection systems. By looking at all 16 capillaries and detectors, this study was additionally intended to highlight any relationship between the distorted image surface and sensitivity. Second, the signal-to-noise ratio (S/N) of the detection electronics of this instrument (independent of optical design) was compared to that of the 5-capillary instrument.

2.3.1.A Limits of Detection

Experimental: A 12.5 nM solution of fluorescein in a running buffer of 10 mM SDS (sodium dodecylsulphate, BDH, Toronto, Canada), 40 mM borate (sodium tetraborate decahydrate, Fisher), pH = 9.2 was used as the sample; an injection of this solution was made on up to 4 capillaries at a time in the following manner. The injection ends of the four capillaries, ~ 40 cm long, previously equilibrated with the running buffer flowing through them, were removed from a vial of running buffer and inserted into a vial of the 12.5 nM fluorescein solution along with the Pt electrode from the high voltage power supply, and +1 kV (~ 40 V/cm; some variation in capillary length) was applied for 2 or 3 s. The capillary ends and electrode were then removed from the sample and rinsed in two separate vials of running buffer to ensure that any fluorescein left on the outside of the capillaries or on the electrode would be removed before the capillary ends and electrode were inserted into a fresh vial of running buffer and 15 kV was applied. Approximately 4 minutes later, the fluorescein reached the sheath flow cuvette and fluoresced in the 488 nm laser beam, and the emitted light, passing through the 540 nm filter, generated a ~ 2 s wide peak on the one-colour electropherogram collected on Labview. Note that because only one fluorophore was being detected, just the Ar^+ laser beam ran unchopped, and the filter wheel was stationary with the 540 nm filter in the optical path; a simplified data acquisition programme was written by Darren Lewis of this group to continuously acquire from all capillaries simultaneously at 10 Hz. Otherwise, the detection system was identical to that used for 4-colour DNA sequencing.

An effort was made to ensure that none of the sample injection nor migration velocity were due to siphoning through the capillary. To eliminate siphoning, several siphoning injections of fluorescein were made as described above, save that no potential was applied during the injection; any fluorescein injected would thus be due to siphoning. Initially, the injection height was purposely made well above the sheath flow waste height, to induce a siphoned injection, and small peaks were observed in the electropherograms. The injection height was then reduced stepwise in subsequent siphoning injections, until the peak just disappeared; the height at which this occurred was marked and used for all subsequent electrophoretic injections. In calculations of detection limits, the effect of siphoning was thus justifiably omitted.

Results and Discussion: Detection limits were calculated in the following manner. The electropherograms were interpreted using statistical analysis in Igor Pro; the peak dimensions are presented in Table 2.5, along with the other data required to calculate the LODs. Note that all electropherograms were smoothed with a Savitzky-Golay, 21 point quadratic filter[25, 26], a running, least squares, second order polynomial smoothing function which, for each data point, uses that point plus the 10 points preceding and following the point. The following variables are defined: S_{spl} is the sample signal or peak height (V), equivalent to the

Filename	JC960731-10	JC960731-10	JC960731-10	JC960731-10	JC960731-17	JC960731-17
Capillary #	**1**	**2**	**3**	**4**	**5**	**6**
V_{bg} (V)	-0.420	-3.19	-1.42	-1.25	-2.92	-1.80
σ_{bg} (V)	2.25×10^{-4}	5.90×10^{-4}	4.71×10^{-4}	4.59×10^{-4}	9.21×10^{-4}	1.04×10^{-3}
V_{pk} (V)	-0.262	-2.46	-0.550	-0.832	-1.57	-0.347
C_{spl} (M)	1.25×10^{-8}	1.25×10^{-8}	1.25×10^{-8}	1.25×10^{-8}	1.25×10^{-8}	1.25×10^{-8}
L_{cap} (cm)	39.7	39.7	39.7	39.7	39.7	39.7
t_{inj} (s)	3	3	3	3	2	2
t_{mig} (s)	230	230	223	212	216	220
V_{inj} (kV)	1	1	1	1	1	1
V_{mig} (kV)	15	15	15	15	15	15
LOD (pM)	**54**	**30**	**20**	**41**	**26**	**27**
LOD (molec)	**22 000**	**12 000**	**8 500**	**18 000**	**7 400**	**7 600**

Table 2.5: 3σ Limit of Detection for Each Capillary.

Filename	JC960731-17	JC960731-11	JC960731-13	JC960731-13	JC960731-13
Capillary #	**7**	**8**	**9**	**10**	**11**
V_{bg} (V)	-2.11	-1.31	-4.84	-2.36	-2.50
σ_{bg} (V)	1.08×10^{-3}	6.83×10^{-4}	6.03×10^{-3}	9.11×10^{-4}	1.29×10^{-3}
V_{pk} (V)	-0.236	-0.690	-2.31	-1.47	-1.06
C_{spl} (M)	1.25×10^{-8}	1.25×10^{-8}	1.25×10^{-8}	1.25×10^{-8}	1.25×10^{-8}
L_{cap} (cm)	39.7	41.3	41.3	41.3	41.3
t_{inj} (s)	2	2	2	2	2
t_{mig} (s)	228	274	250	248	246
V_{inj} (kV)	1	1	1	1	1
V_{mig} (kV)	15	15	15	15	15
LOD (pM)	**22**	**41**	**89**	**39**	**34**
LOD (molec	**6 000**	**9 800**	**23 000**	**10 000**	**8 900**

Filename	JC960731-17	JC960731-14	JC960731-14	JC960731-14	JC960731-14
Capillary #	**12**	**13**	**14**	**15**	**16**
V_{bg} (V)	-0.906	-3.12	-1.10	-0.783	-1.21
σ_{bg} (V)	5.05×10^{-4}	1.37×10^{-3}	3.82×10^{-4}	9.00×10^{-4}	6.99×10^{-4}
V_{pk} (V)	-0.148	-0.814	-0.0632	0.126	-0.595
C_{spl} (M)	1.25×10^{-8}	1.25×10^{-8}	1.25×10^{-8}	1.25×10^{-8}	1.25×10^{-8}
L_{cap} (cm)	41.3	41.3	41.3	41.3	41.3
t_{inj} (s)	2	2	2	2	2
t_{mig} (s)	269	248	240	243	242
V_{inj} (kV)	1	1	1	1	1
V_{mig} (kV)	15	15	15	15	15
LOD (pM)	**25**	**22**	**14**	**37**	**43**
LOD (molec	**6 000**	**5 900**	**3 800**	**9 900**	**12 000**

difference between the peak maximum and the average of the adjacent baseline, or $|V_{pk} - V_{bg}|$; σ_{bg} is the noise of the background, measured as the standard deviation of the background baseline; LOD_{conc} and LOD_{molec} are the detection limits expressed as a concentration (M) or number of molecules; c_{spl} is the sample concentration (M); n_{spl} is the number of moles of sample injected; N_A is Avogadro's number (6.02 X 10^{23}/mol); Vol_{spl} and Vol_{cap} are the volumes of sample injected and volume of the capillary (L); t_{inj} and t_{mig} are the injection and migration times (s); V_{inj} and V_{mig} are the injection and migration potentials (V); and r_{cap} and l_{cap} are the inner capillary radius and capillary length (cm). Using the 3-standard deviation definition for a limit of detection, expressions for LOD_{conc} and LOD_{molec} may be written as:

$$LOD_{conc} = \frac{3\sigma_{bg}}{S_{spl}} \bullet c_{spl} \qquad (2.16)$$

and

$$LOD_{molec} = \frac{3\sigma_{bg}}{S_{spl}} \bullet n_{spl} \bullet N_A \qquad (2.17)$$

Now $n_{spl} = c_{spl} \bullet Vol_{inj}$, and the volume of the sample plug injected, Vol_{inj}, may be written as:

$$Vol_{inj} = Vol_{cap} \bullet \frac{t_{inj}}{t_{mig}} \bullet \frac{V_{inj}}{V_{mig}}$$

Substituting for n_{spl} and S_{spl}, equations (2.16) and (2.17) may be rewritten as:

$$LOD_{conc} = \frac{3\sigma_{bg}}{\left|V_{pk} - V_{bg}\right|} \bullet c_{spl} \tag{2.18}$$

and

$$LOD_{molec} = \frac{3\sigma_{bg}}{\left|V_{pk} - V_{bg}\right|} \bullet c_{spl} \bullet Vol_{cap} \bullet \frac{t_{inj}}{t_{mig}} \bullet \frac{V_{inj}}{V_{mig}} \bullet N_A \tag{2.19}$$

Capillary volume is simply:

$$Vol_{cap} = \frac{\pi r_{cap}^2 l_{cap}}{1000\,mL/L}$$

and so equation (2.19) becomes:

$$LOD_{molec} = \frac{3\sigma_{bg}}{\left|V_{pk} - V_{bg}\right|} \bullet c_{spl} \bullet \frac{\pi r_{cap}^2 l_{cap}}{1000\,mL/L} \bullet \frac{t_{inj}}{t_{mig}} \bullet \frac{V_{inj}}{V_{mig}} \bullet N_A \tag{2.20}$$

A spreadsheet programme written in Igor Pro was used to execute equations (2.18) and (2.20) and calculate all detection limits shown in Table 2.5.

The reader may note that the migration times for the fluorescein peaks are somewhat irreproducible: the fluorescein took either ~ 220 s (capillaries 1-7) or ~ 250 s (capillaries 8-16) to reach the detector. The variation in the migration times is thought to be due the fact that capillaries 1-7 and 8-16 were of slightly different length (39.7 and 41.3 cm for capillaries 1-7 and 8-16, respectively), and were from different batches from the supplier, Polymicro Technologies (Phoenix, Arizona). Migration time varies with the square of capillary length (see equation 1.13 in Chapter 1), so that effect alone would lengthen the migration time by 18 s:

$$220\,\mathrm{s} \bullet \frac{(41.3\,\mathrm{cm})^2}{(39.7\,\mathrm{cm})^2} = 238\,\mathrm{s}$$

Both groups of capillaries were untreated before use, but it is possible that the processing of the capillaries in their manufacture could have been slightly different, causing minor differences in the inner capillary surface and hence electroosmotic flow.

The biggest sources of quantitative uncertainty in the LOD values are thought to be injection time (2-3 s ± 0.25 s) and voltage (± 10%); these alone represent $\pm([(0.25\ \mathrm{s}/2\ \mathrm{s})^2 + 0.1^2]^{0.5} \times 100\%) = \pm 16\%$. Also, the voltage was observed to ramp up to the desired value over a fraction of a second, meaning that the effective injection voltage was somewhat less than 1 kV. The total error might be conservatively estimated at ± 25%.

The results seen in Table 2.5 are typical of the instrument, and may be compared to those of other instruments. The detection limits shown range from 3 800 to 23 000 molecules of fluorescein, or 14 to 89 pM, which is comparable to results obtained in other LOD studies performed on single capillaries at various stages of the instrument's ~ 2 year development. They also are close to the values of one LOD study seen with the five capillary instrument built by Jianzhong Zhang of this group (refer to p.81 of Zhang's thesis[24]), but inferior to those from a second study (p.112 of Zhang's thesis). While Zhang's and the 16 capillary instrument are both multicapillary sequencers with GRIN lenses and APDs as transducers, they differed in several respects that would affect sensitivity. In Zhang's instrument, detection was by means of single photon counting modules (SPCMs), which are APDs biased in the Geiger mode with frequency-counting electronics (see section 2.1.2.B on APDs); the author is unaware of a direct sensitivity comparison between APDs biased in the Geiger and linear modes, but suspects a difference in sensitivity likely exists. The 20X, 0.5 NA imaging lens in Zhang's instrument (which yields a collection efficiency of 6.7% versus 5.3% for the 16 capillary instrument), and the small object size, 5 capillaries @ 0.150 mm/capillary = 0.750 mm, allows the image spots to be collected at the manufacturer's specified focal distance. His LOD injections for the first study were performed by siphoning (no applied potential), and the fluorophore used was fluorescein isothiocyanate, or FITC; 3σ detection limits of 20 zmol, or 12 000 molecules, were obtained. In the second study, injections of fluorescein were made electrokinetically, and 3σ detection limits of 130 molecules were obtained.

Three other multicapillary instruments (see section 2.1.1 for a brief description of these instruments) have their LODs reported in the literature. In comparison with the ~ 10^{-11} M, or ~ 3 800 to 23 000 molecule LODs seen in Table 2.5, Yeung's on-column, CCD detection system produced ~ 10^{-9} to 10^{-10} M LODs using fluorescein as a fluorophore[12], and Takahashi and Kambara's post-column, concentric capillary sheath flow, CCD detection system produced 600 molecules or 10^{-13} M (2σ) LODs using Texas Red as a fluorophore[8, 9]. Mathies described a limiting sensitivity of ~ 10 amol of fluorescently-labelled DNA, or ~ 6 X 10^6 molecules[6]. The 1-or 2-decade less sensitive detection of Yeung's apparatus and ~ 2- or 3-decade less sensitive detection of Mathies' instrument are likely due at least in part to the fact that detection is on-column, and therefore suffers from curved boundaries of refractive index, which promote laser scatter, and hence higher background. Takahashi and Kambara's system shares with this 16 capillary instrument the optical advantages of a sheath flow cuvette, and so the detection optics and electronics may be compared; their ~ 2-decade better LODs may suggest that the use of non-magnifying optics and a CCD transducer is superior to the 18 X objective-GRIN lens-APD detection system described for this instrument, in terms of sensitivity.

There is no discernable relation between optical geometry and sensitivity (ie: sensitivity does not decrease for the outer capillaries for which the image surface has been most distorted - see section 2.2.4 describing detection optics): values for the central four capillaries range from 6 000 to 23 000 molecules, while for the outer four the range is from 9 900 to 22 000 molecules. It is likely that the range in detection limits is related to the variation in the extent of overlap in the optical alignment of the fluorescent spot to the GRIN lens spot from capillary to capillary (see section 2.2.4.A, B on optical alignment). While the GRIN lens positions used were optimised to the extent possible, there is still some variation from run to run in the fluorescent spot positions due to very small variations in capillary position, ~ ± 5 μm, as discussed in section 3.3.2.A, so that, while overall optical alignment is preserved (all capillaries are well detected each run), individual capillary sensitivity will fluctuate somewhat.

Optical/Electronic Cross-Talk: Using the current data acquisition system, there has never been any evidence for intercapillary optical or electronic signal cross-talk between the fluorescent spots, their images, the light conducted through the optical fibres, or the electronic signal at any point from the APDs through the transimpedance amplifiers and low-pass filters on to the computer. Since, in this LOD study, injections were made on up to four capillaries but data were acquired on all 16 capillaries for each run, an excellent opportunity existed to examine the electropherograms of unused capillaries for any cross-talk. Electropherograms for non-injected capillaries in two files, JC960731-10 and -14, were inspected overall, and in detail in the area where peaks occurred in the

Figure 2.24: Absence of Cross Talk in LOD Studies.

Raw data electropherograms of all 16 capillaries shown for LOD injections made on capillaries 13-16 (top, JC960731-14), and capillaries 1-4 (bottom, JC960731-10); no spurious peaks owing to cross talk appear. Seven peaks shown with solid arrows are one-point spikes and are similar to those discussed in section 2.2.5.F, likely arising from errors in the data acquisition software, and are not cross-talk. The peak for capillary 2 in the lower plot indicated with a dashed arrow is not a single point spike, and is likely due to some unknown impurity; it is not cross talk from the peak of capillary 3, as the maxima are distinct at 223.4 and 224.4 s for capillaries 2 and 3, respectively.

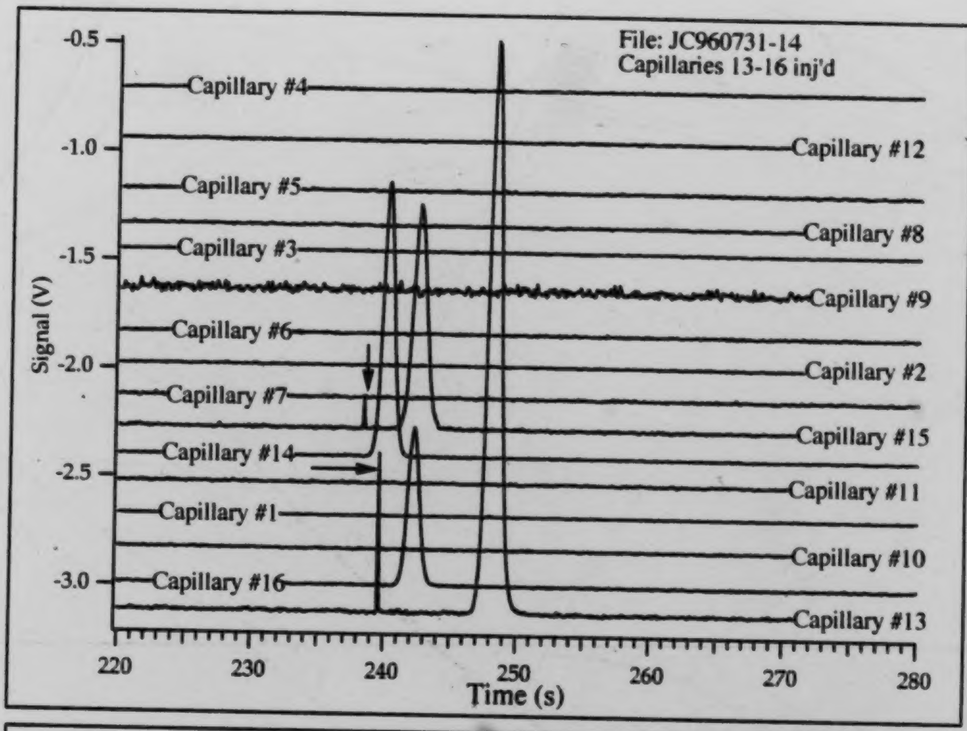
File: JC960731-14
Capillaries 13-16 inj'd
-0.5
-1.0
-1.5
-2.0
-2.5
-3.0
Signal (V)
Capillary #4
Capillary #12
Capillary #5
Capillary #8
Capillary #3
Capillary #9
Capillary #6
Capillary #2
Capillary #7
Capillary #15
Capillary #14
Capillary #11
Capillary #1
Capillary #10
Capillary #16
Capillary #13
220
230
240
250
260
270
280
Time (s)

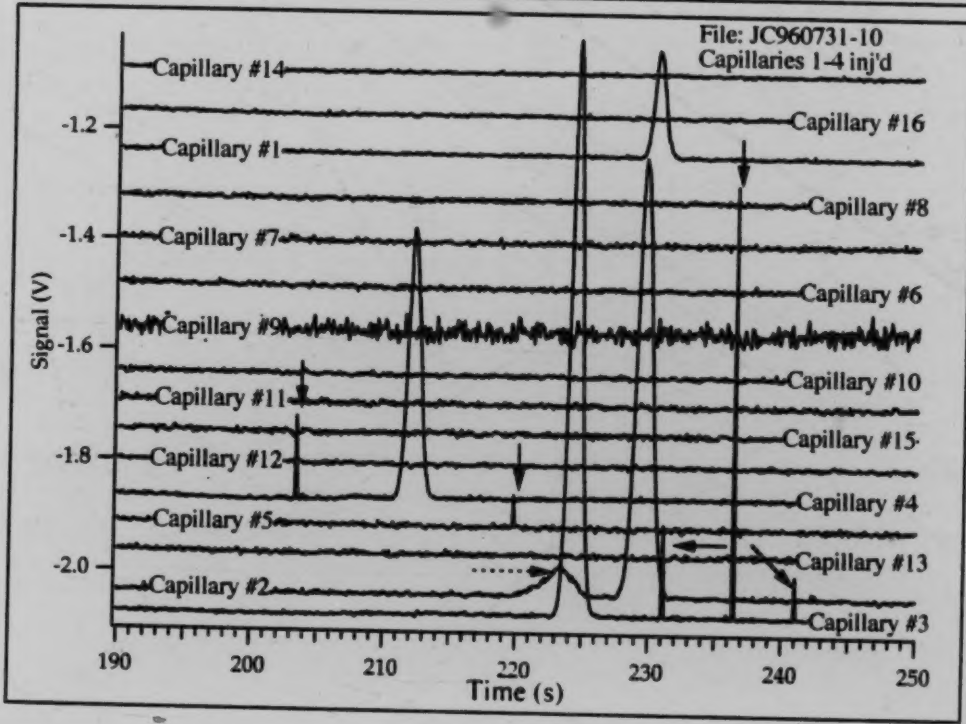
File: JC960731-10
Capillaries 1-4 inj'd
-1.2
-1.4
-1.6
-1.8
-2.0
Signal (V)
Capillary #14
Capillary #16
Capillary #1
Capillary #8
Capillary #7
Capillary #6
Capillary #9
Capillary #10
Capillary #11
Capillary #15
Capillary #12
Capillary #4
Capillary #5
Capillary #13
Capillary #2
Capillary #3
190
200
210
220
230
240
250
Time (s)

injected capillaries; no evidence for cross-talk was observed for any of the 16 capillaries. The time windows in which the fluorescein peaks appeared for the four capillaries injected in each run are shown in Figure 2.24.

2.3.1.B S/N Comparison of Linear Vs. Geiger APDs

An experiment using a flashing LED as the light source was performed to compare the sensitivity of the detection electronics of one of the APDs (#3) versus that of one of the single photon counting module (SPCM) detectors from Zhang's five capillary instrument.

Experimental: The apparatus for the APD was identical to that used for the APD biasing experiment (see section 2.2.5.B) except that the APD's bias was optimised for -30.0 °C, not -20.0 °C; a square wave signal trace was collected with the APD and detection electronics on. To test the SPCM under the same light source conditions, the GRIN lens was disconnected from the APD at the optical fibre to optical fibre FC connection (see section 2.2.4.C), and connected to the SPCM's identical FC connector. With the SPCM's signal output connected to the Apple computer, a similar square wave signal trace was acquired for the SPCM.

Results and Discussion: The data were processed in the same way as for APD biasing. The signal to noise ratios seen were 23 for the SPCM and 24 for APD #3. The sensitivity of the detection electronics in both instruments may thus be regarded as equal.

2.3.2 Example of Four-Colour DNA Sequencing

An example of a four-colour DNA sequencing run is presented to demonstrate the instrument's ability to perform the task for which is was designed.

Experimental: A four-colour, four termination, M13mp18 DNA sample was prepared as described in section 2.2.2.B. The one sample was injected onto all 16 capillaries simultaneously as described in section 2.2.1 with the following differences: the sample was injected at 100 V/cm for 30 s and capillaries were 43.1 cm long. The separation was performed at room temperature. Data acquisition (see section 2.2.3.B) was with the most current Labview programme wherein Pandora's box had been removed, but with the older chopper/filter wheel driving electronics lacking the auto-correction circuit for synchronisation of the two wheels. The filter/chopper wheel synchronisation was established at the beginning of the run, and verified at its conclusion to not have drifted.

Results and Discussion: The electropherograms collected on Labview were analysed in Igor Pro and were subjected to second order Savitzky-Golay 21 point smoothing, as described for the detection limit studies in section 2.3.1.A. The data acquired for this sample on one of the sixteen capillaries (capillary #7) are shown for the full ~ 2 hour separation in Figure 2.25; the full electropherograms of the other 15 capillaries are included in Appendix 1, and are virtually identical to the one shown. In the electropherogram, fluorescence intensity signal is plotted against separation time, and for each 10 minute time window, four traces, blue, green, yellow and red, are visible. These traces represent the data points gathered at 2 Hz per trace through the 540, 560, 580, and 610 nm filters for capillary #7 only. By looking at the relative intensities of the peaks of the 4 traces at any point in time, the terminal nucleotide of the fragment fluorescing at that time can be determined; this procedure is termed base-calling. If the electropherogram is base-called in the direction of increasing migration time, then the terminal nucleotide of increasingly long fragments is being read, or the complementary sequence to the original M13mp18 DNA

Figure 2.25: Example of 4-Colour DNA Sequencing Electropherogram. Data are displayed in 10 minute windows from 25 to 115 minutes. Sequence is called out to 450 bases before resolution degrades. The process of base-calling is depicted in Figure 2.26.

Capillary 7; File: 26/01/96#1

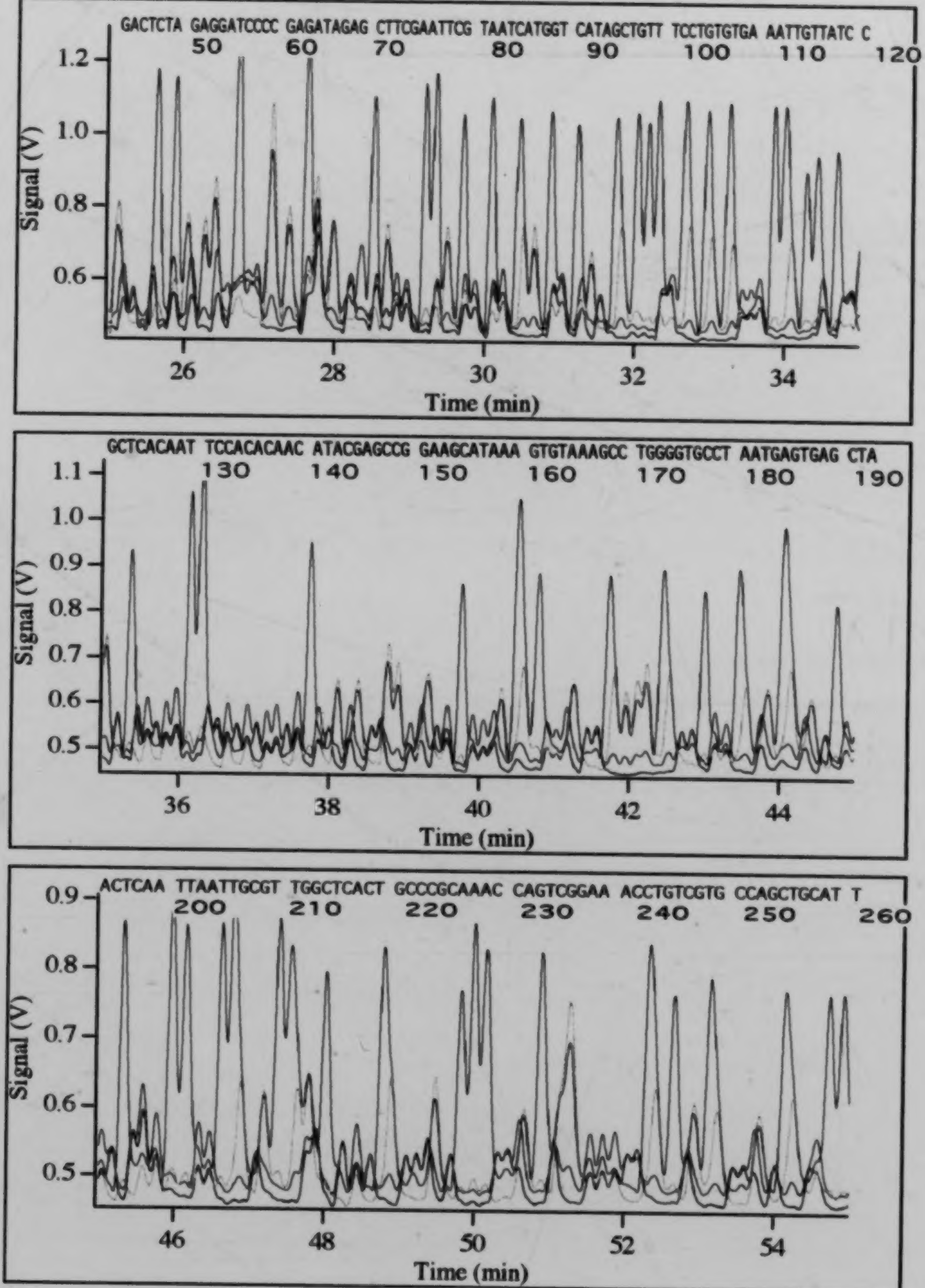

Capillary 7; File: 26/01/96#1

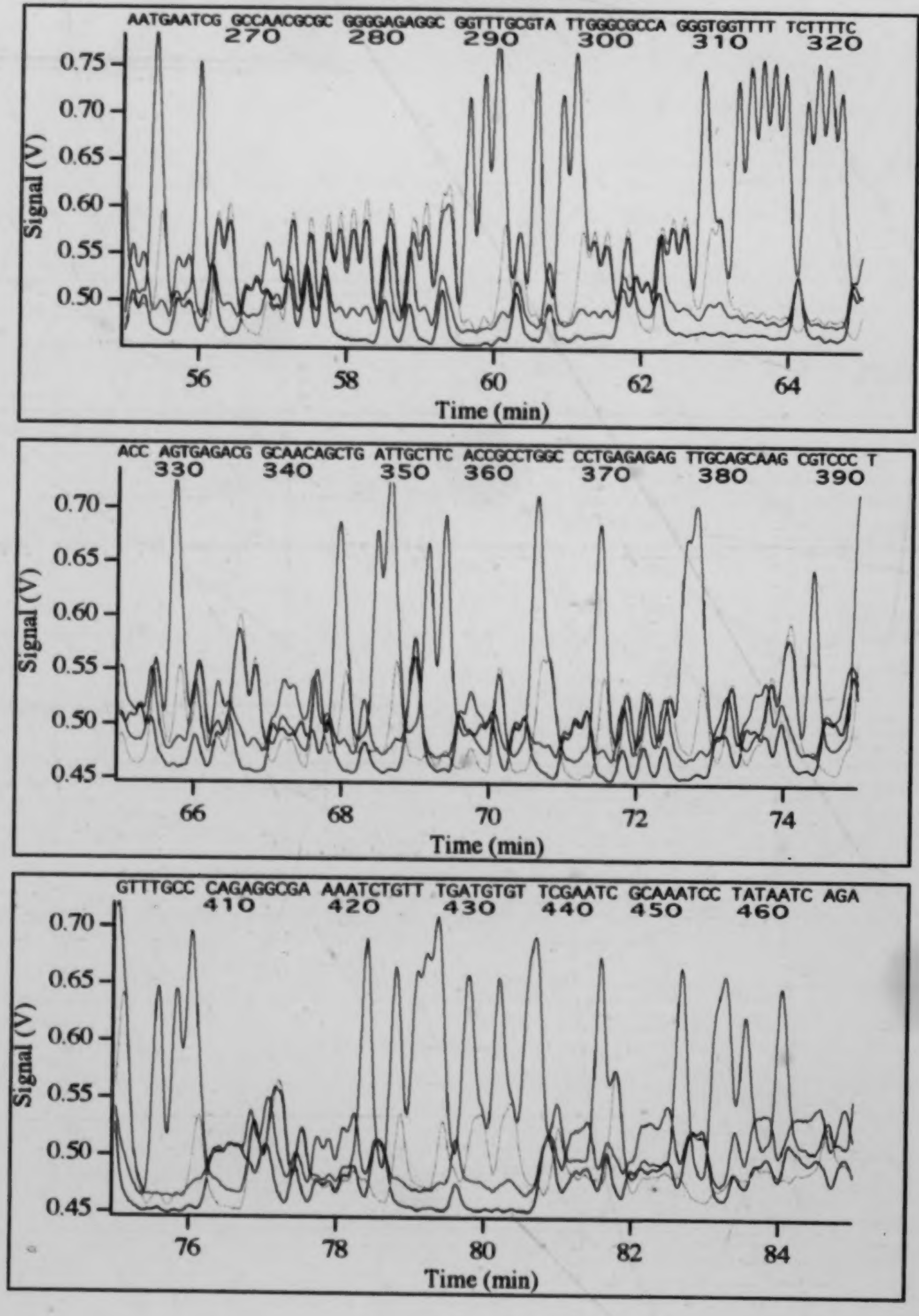

Capillary 7; File: 26/01/96#1

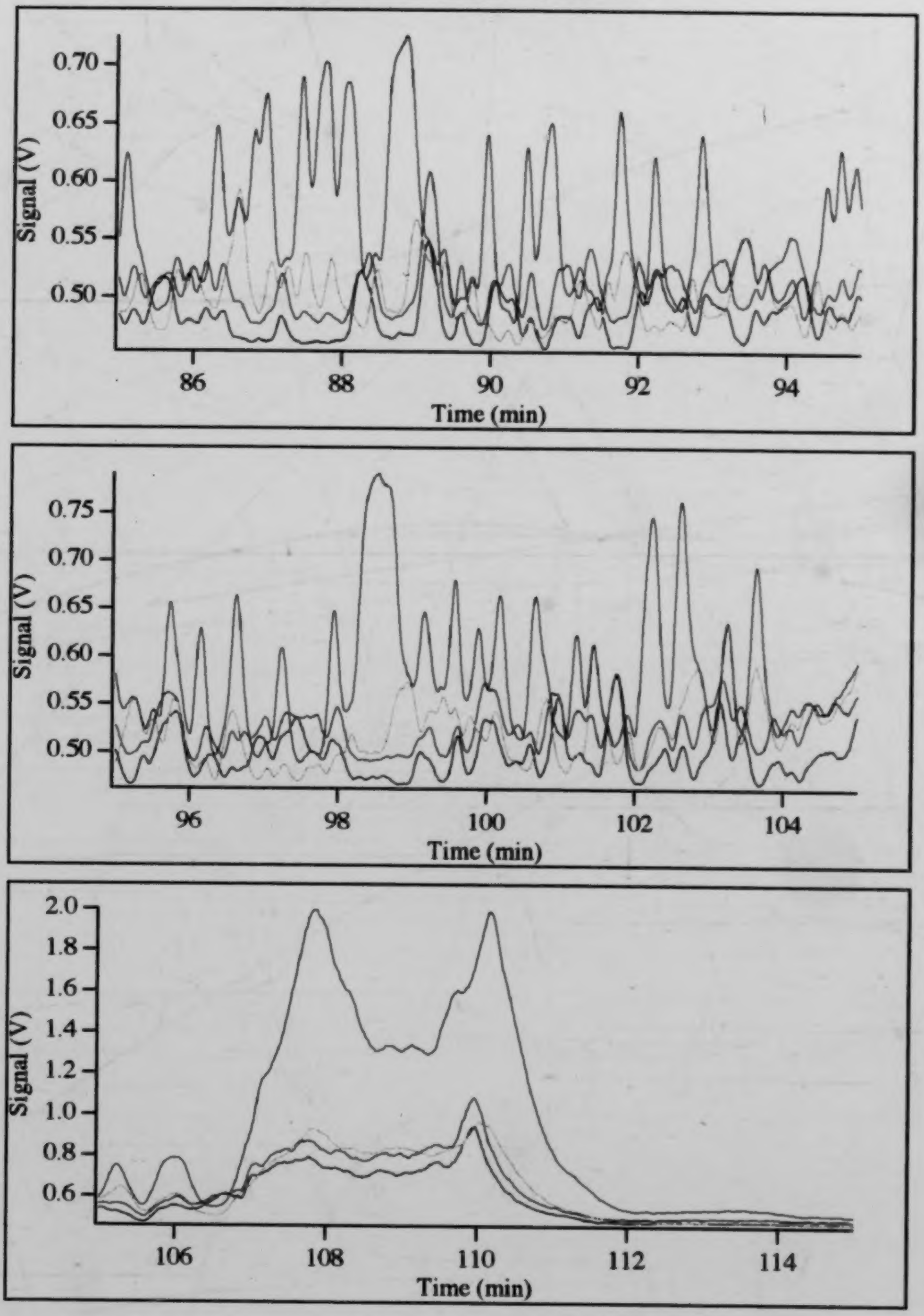

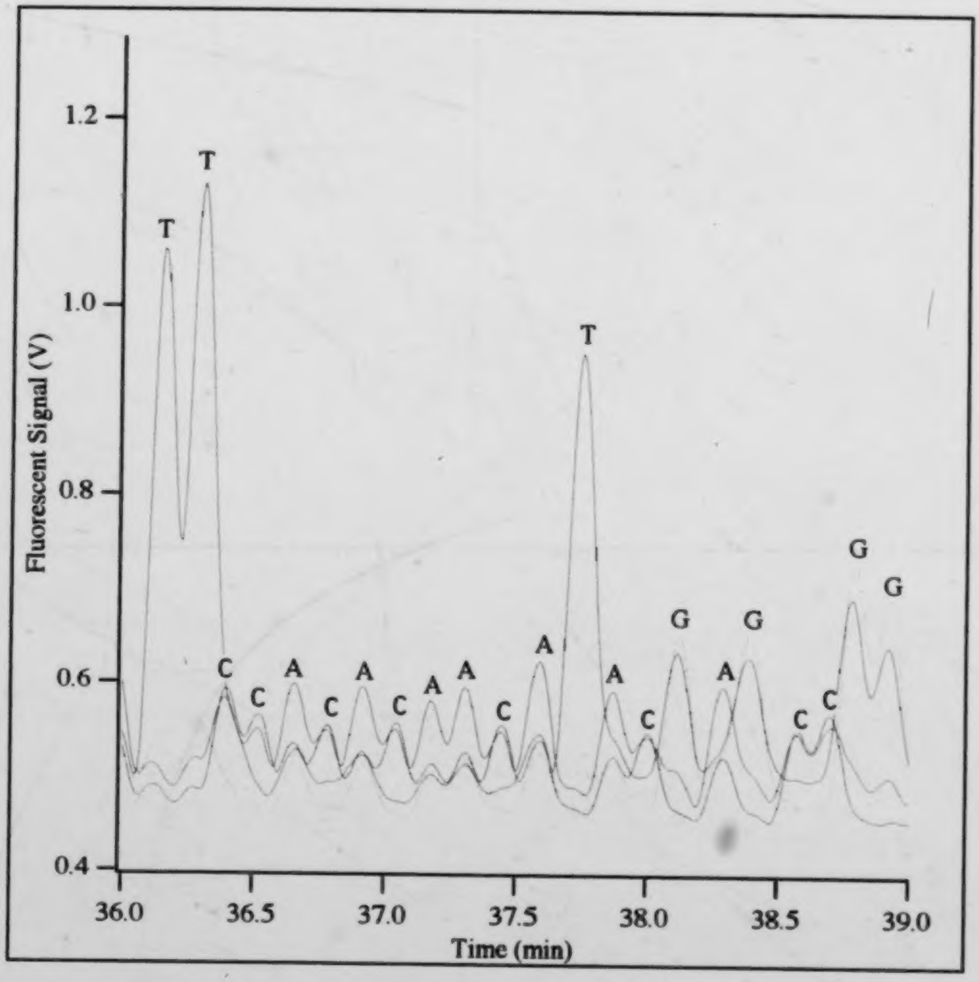

Figure 2.26: Base-Calling.

Red peaks are Ts, peaks equal in yellow and red intensity are Gs, those which are green and blue, 2:1 peak height intensity, are As, and peaks equal in green and blue are Cs.

template is being read from the primer position in the 3' direction of the complementary strand.

Base-calling is illustrated in Figure 2.26; peaks which are only red are Ts, peaks which are equal in yellow and red intensity are Gs, those which are green and blue, 2:1 peak height intensity, are As, while the equal intensity green and blue peaks are Cs. This protocol was used to base-call the first 460 nucleotides of sequence on capillary #7 electropherogram; the sequence and position in the M13mp18 sequence are listed above each trace. The called sequence is also listed with the known sequence of this segment of DNA in Table 2.6; the errors in the experimentally-read sequence are italicised and boldscripted, and are summed each ten nucleotides further along the sequence.

To illustrate that the data obtained in capillary #7 are representative of those in the other 15 capillaries, a small section of each of the 16 electropherograms was chosen in which the same series of peaks, representing the same portion of the M13mp18 sequence, occurs. The segment occurs at ~ 64 minutes into the separation of capillary #7 (Figure 2.25), and is characterised by a quintet of Ts, a C, followed by a quartet of Ts which are nucleotides 316 to 325 in the sequence. Figure 2.27 shows this same quintet-quartet for all 16 capillaries, and the resolution in each case is respectable, with ~ 2/3 of the separation time elapsed. The location of these peaks ranged from 63 to 71 minutes into the run from capillary to capillary, likely owing to inadvertant, minor variations in gel consistancy in the different capillaries.

It should be noted that, given current gel-preparation methods, compositions and sequencing protocols, 500 nucleotides of raw sequence per lane per run is considered acceptable; the good resolution seen in this run allows base-calling to extend to ~ 450 bases. Beyond 450 bases, the resolution and hence base-calling accuracy decrease dramatically. Table 2.7 shows the

Table 2.6: Base-Calling Comparison with Known Sequence.

Each set of three rows shows: the distance from the primer in base pairs (number of errors in bold) in the top row; the known sequence in the middle row; and the called sequence (errors in bold) in the bottom row.

10	20	30	40
TGTAAAACGA	CGGCCAGTGC	CAAGCTTGCA	TGCCTGCAGG
50	60	(4) 70	80
TCGACTCTAG	AGGATCCCCG	GGTACCGAGC	TCGAATTCGT
GACTCTAG	AGGATCCCCG	*A*G*A*TA••GAGC*T*	TCGAATTCGT
90	100	110	120
AATCATGGTC	ATAGCTGTTT	CCTGTGTGAA	ATTGTTATCC
AATCATGGTC	ATAGCTGTTT	CCTGTGTGAA	ATTGTTATCC
130	140	150	160
GCTCACAATT	CCACACAACA	TACGAGCCGG	AAGCATAAAG
GCTCACAATT	CCACACAACA	TACGAGCCGG	AAGCATAAAG
170	180	190	(1) 200
TGTAAAGCCT	GGGGTGCCTA	ATGAGTGAGC	TAACTCACAT
TGTAAAGCCT	GGGGTGCCTA	ATGAGTGAGC	TAACTCA•AT
210	220	230	(1) 240
TAATTGCGTT	GCGCTCACTG	CCCGCTTTCC	AGTCGGGAAA
TAATTGCGTT	GCGCTCACTG	CCCGCTTTCC	AGTCG•GAAA
250	260	270	280
CCTGTCGTGC	CAGCTGCATT	AATGAATCGG	CCAACGCGCG
CCTGTCGTGC	CAGCTGCATT	AATGAATCGG	CCAACGCGCG
290	300	310	320
GGGAGAGGCG	GTTTGCGTAT	TGGGCGCCAG	GGTGGTTTTT
GGGAGAGGCG	GTTTGCGTAT	TGGGCGCCAG	GGTGGTTTTT
330	(1) 340	350	(2) 360
CTTTTCACCA	GTGAGACGGG	CAACAGCTGA	TTGCCCTTCA
CTTTTCACCA	GTGAGACG•G	CAACAGCTGA	TTG••CTTCA
370	380	390	(4) 400
CCGCCTGGCC	CTGAGAGAGT	TGCAGCAAGC	GGTCCACGCT
CCGCCTGGCC	CTGAGAGAGT	TGCAGCAAGC	G•TCC•C••T
(2) 410	(1) 420	(1) 430	(2) 440
GGTTTGCCCC	AGCAGGCGAA	AATCCTGTTT	GATGGTGGTT
G•TTTG•CCC	AG•AGGCGAA	AATC•TGTTT	GATG•TG•TT
(2) 450	(2) 460	470	480
CCGAAATCGG	CAAAATCCCT	TATAAATCAA	AAGAATAGCC
C•GAATC•G	CAA•ATC•CT		

Figure 2.27: Comparison of 16 Electropherograms.

A small section of each of the 16 electropherograms was chosen in which the same series of peaks, representing the same portion of the M13mp18 sequence, occurs. The segment is characterised by a quintet of Ts, a C, and a quartet of Ts which are nucleotides 316 to 325 in the sequence; this segment occurs with ~ 2/3 of the separation time elapsed, at 63 to 71minutes, varying from capillary to capillary. Good resolution and signal can be seen for all 16 capillaries in this run.

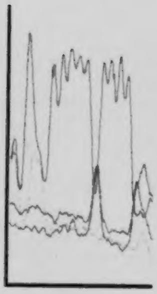

Capillary #1

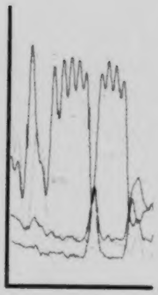

Capillary #2

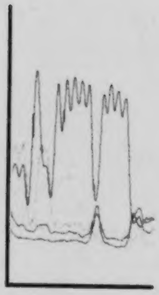

Capillary #3

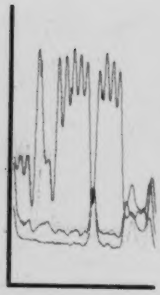

Capillary #4

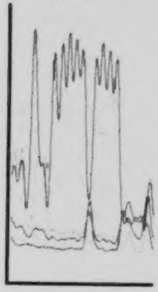

Capillary #5

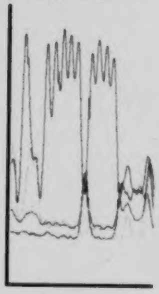

Capillary #6

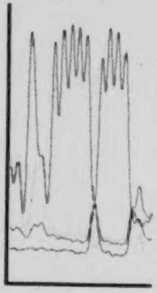

Capillary #7

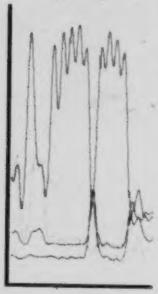

Capillary #8

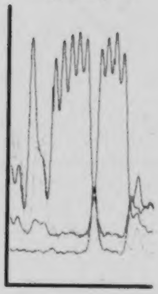

Capillary #9

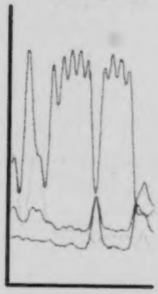

Capillary #10

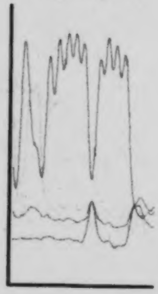

Capillary #11

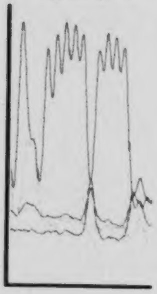

Capillary #12

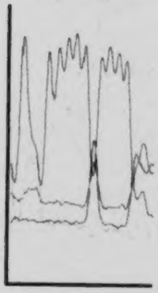

Capillary #13

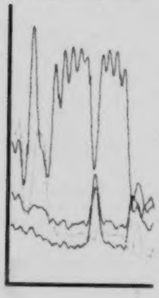

Capillary #14

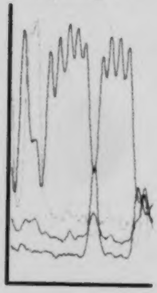

Capillary #15

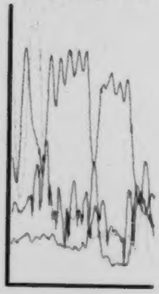

Capillary #16

Location in Sequence (nt)	Number of Errors	Accuracy	
		100-350 nt	50-450 nt
50-100	4	▨	94.8%
100-150	0	98.8%	
150-200	1		
200-250	1		
250-300	0		
300-350	1		
350-400	6	▨	
400-450	8		

Table 2.7: Base-Calling Accuracy.

Errors and accuracy in the base-calling of capillary #7's electropherogram are divided into 50 nucleotide segments of the whole sequence of M13mp18.

occurrence of errors and accuracy for the run. Note that, in the first, third and fourth columns, "nt" is the symbol for nucleotide.

This example of 16 simultaneous electropherograms all containing good quality separation data from which sequence may be read with high accuracy conclusively shows that the multicapillary sequencer is capable of separating and detecting the DNA fragments from 16 samples simultaneously. The potential for high-throughput sequencing may be extrapolated using ballpark figures. Assuming 500 nucleotides of sequence per capillary for a two hour run performed four times daily, 250 days per year, this sequencer would produce 8 Mb/year of raw sequence, or ~ 1 Mb/year of finished sequence. Recalling from section 1.1 that the objective of *the entire Human Genome Project* is 50 Mb/year of finished sequence, the potential impact of *this single instrument* is immediately obvious.

The tremendous high throughput potential of this sequencer must be qualified with the fact that, while such an impressive 1 Mb/year claim may ostensibly be made, it has proven difficult to reproduce the quality of the run shown in the example above, namely ~ 500 base read length for all capillaries with high accuracy, upon which this claim relies. Some examples of frequently encountered problems, possible causes and solutions are mentioned below.

Weak signal for some capillaries: If only observed in a single run, this could be attributed to a poor sample injection in those particular capillaries; however, when observed repeatedly and the operator is confident that sample injection was correctly performed, then the likely explanation is a lack of alignment of the fluorescent spot's image to the GRIN lens. The routine optical alignment performed at the beginning of each run (described in section 2.2.4.A) entails making a compromise in the cuvette's position to maximise the fluorescent spot-GRIN lens overlap *for all 16 capillaries*; invariably, some are better aligned than others. This misalignment is partly due to the small variations in capillary positioning within the cuvette from run to run; a V-shaped micromachined feature called a capillary stopper acts to stop and centre each capillary in the cuvette (see section 3.3.2.A), but is only effective if the capillary is pushed to the bottom of the V. On occasion, the capillaries which were properly seated in their Vs when sealed with epoxy pull up from this positioning feature when the capillaries are manipulated to effect injections, etc. Modifications to the cuvette holder to mechanically fix the capillaries better at the sheath flow cuvette holder might inhibit such movement inside the cuvette. Also, improving the instrument's overall sensitivity would allow weaker signals to be used, and would make optical alignment less stringent. Ideas for improved instrument sensitivity are suggested in section 4.2 on future directions.

When signal is non-existant for some capillaries, it is sometimes due to the poor gel quality in those capillaries. Despite efforts made in the pouring of gels to eliminate bubble formation, bubbles are periodically observed in capillaries. Prior to their insertion in the cuvette, gel-filled capillaries are inspected for bubbles under a microscope from the injection ends up to ~ 10 cm from the detection ends since the latter ends are kept in aqueous solution to keep the gels from drying out, but bubbles occurring in the 10 uninspected centimetres ruin separation. New gel chemistries and gel pouring protocols may eliminate the occurrence of bubbles.

Poor resolution: When, in a run, the resolution degrades early (such as after 200 bases), then it may be due to flawed gel preparation. In some cases an error committed in the gel-pouring protocol is recognised, but in other cases, no error is apparent. Updating gel-pouring protocols to enhance reproducibility and ensuring that reagents used are of the highest purity may aid in providing consistent gel quality.

Another possible cause is the use of overly concentrated samples; the need to keep samples dilute with regard to the running buffer in CZE has been highlighted by several researchers [27-29]. Concentrated sample zones cause the electric field to decrease locally, and inhomogeneities in the electric field adversely affect a zone's Gaussian concentration distribution. To regain the 100:1 = [running buffer]:[sample] ratio suggested as a general rule[29], the buffer concentration may be raised, or the sample concentration lowered. The former option has the disadvantage of increasing the current through the capillary and hence the production of heat (see equation 1.14 in section 1.2.1.C), which acts to degrade resolution of its own accord, so the better option is to use more dilute samples. This, in turn, can only be achieved with very sensitive detection. Thus improving the instrument's sensitivity would allow smaller amounts of sample to be injected and would likely result in better resolution and longer read lengths.

2.4 Conclusions

A sensitive, high throughput 16 capillary DNA sequencer has been developed. Many areas of instrument development have been dealt with at length, including separation apparatus, detection optics, detection electronics and data acquisition. One area of instrument development, that of the detection cell, or sheath flow cuvette, is dealt with exlcusively in Chapter 3. In terms of performance, the instrument has detection limits of approximately 10^3 -10^4 molecules of fluorescein, has electronic sensitivity comparable to that of an SPCM (single photon counting module, an APD biased in the Geiger mode), and is capable of four colour DNA sequencing on all 16 capillaries simultaneously. An example of DNA sequencing has been shown with 94.5% accuracy out to 450 bases.

2.5 References

1. *Understanding our Genetic Inheritance: The U. S. Human Genome Project-The First Five Years 1991-1995 (NIH Publication No. 90-1590)*; National Institutes of Health (U.S.), 1990.
2. *Human Genome News*; NIH/DOE (U.S.), 1993; Vol. 5, No. 4.
3. A. J. Kostichka, M. L. Marchbanks, R. L. Brumley, Jr., H. Drossman and L. M. Smith, *Bio/Tecnology* **10,** 78 (1992).
4. S. Bay and N. J. Dovichi, (in preparation).
5. N. J. Dovichi, *Review of Scientific Instruments* **61,** 3653 (1990).
6. R. A. Mathies and X. C. Huang, *Nature* **359,** 167-169 (1992).
7. R. J. Zagursky and R. M. McCormick, *BioTechniques* **9 (1),** 74-79 (1990).
8. H. Kambara and S. Takahashi, *Nature* **361,** 565-566 (1993).
9. S. Takahashi, K. Murakami, T. Anazawa and H. Kambara, *Analytical Chemistry* **66,** 1021 (1994).
10. X. C. Huang, M. A. Quesada and R. A. Mathies, *Analytical Chemistry* **64,** 2149 (1992).
11. J. A. Taylor and E. A. Yeung, *Analytical Chemistry* **65,** 956-960 (1993).
12. K. Ueno and E. S. Yeung, *Analytical Chemistry* **66,** 1424 (1994).
13. S. Terabe, K. Otsuka, K. Ichikawa, A. Tsuchiya and T. Ando, *Analytical Chemistry* **56,** 113-116 (1984).
14. *SELFOC Product Guide SPG0295*; NSG America, Inc.: Somerset, New Jersey, 1995, p 28.
15. K. D. Möller, *Optics*; University Science Books: Mill Valey, 1988.
16. J. D. Ingle, Jr. and S. R. Cro[illegible]*ctrochemical Analysis*; Prentice Hall: Englewood Cliffs, New Jersey, 1988.

17. H. Dautet, P. Deschamps, B. Dion, A. D. MacGregor, D. MacSween, R. J. McIntyre, C. Trottier and P. P. Webb, *Applied Optics* **32 (21)**, 3894-3900 (1993).

18. H. V. Malmstadt, C. G. Enke and S. R. Crouch, *Electronics and Instrumentation for Scientists*; The Benjamin/Cummings Publishing Company, Inc.: Menlo Park, California, 1981.

19. *Silicon Avalanche Photodiode (C30902E, C30902S, C30921E, C30921S) Data Sheet #ED-0017/03/88*; RCA ElectroOptics, Vaudreuil, Québec, Canada (Now EG&G), 1988.

20. D. Lewis, (in preparation).

21. S. Wu and N. J. Dovichi, *Journal of Chromatography* **480,** 141-155 (1989).

22. L. Coulson, Personal Communication, 1995.

23. *Dew Point Data Sheet*; Liquid Carbonic Canada, Ltd, 1980.

24. J. Zhang, Ph.D., University of Alberta, 1994.

25. *Igor Pro 3 Programming and Reference Manual*, 3 ed.; WaveMetrics: Lake Oswego, Oregon, 1996.

26. A. Savitzky and M. J. E. Golay, *Analytical Chemistry* **36,** 1627-1639 (1964).

27. F. E. P. Mikkers, F. M. Everaerts and T. P. E. M. Verheggen, *Journal of Chromatography* **169,** 11-20 (1979).

28. F. E. P. Mikkers, F. M. Everaerts and T. P. E. M. Verheggen, *Journal of Chromatography* **169,** 1-10 (1979).

29. W. G. Kuhr In *Capillary Electrophoresis - Theory and Practice*; Camilleri, P., Ed.; CRC Press: Boca Raton, 1993, pp 65-116.

Chapter 3

DESIGN, CONSTRUCTION AND EVALUATION OF MICROMACHINED, MULTICAPILLARY SHEATH FLOW CUVETTES

3.1 Introduction

This chapter describes the use of micromachining to make glass sheath flow cuvettes for laser-induced fluorescence detection, and the testing of the performance of these cuvettes.

A sheath flow cuvette is a flow through detection cell in which the stream of analyte is ensheathed in a fluid and guided to the detection region of an instrument. The sheath flow cuvette first appeared in 1947 as the detection cell for a light scatter smoke particle counter[1], and later in 1953 as applied to cell counting in flow cytometry[2]. In 1973, a square, quartz cuvette flow chamber was added in a dual sheath flow design[3], again for flow cytometry; since then, a variety of detection cell designs, many of which incorporate sheath flows and cuvettes, have been employed[4]. Sheath flow cuvettes have been used for post column detection via laser-induced fluorescence (LIF) in liquid chromatography[5] and flow injection analysis, in the latter case using Pyrex capillary[6]. In our group, sheath flow cuvettes have been employed for over 10 years as detection cells for LIF[7, 8], laser light scatter[9], chemiluminescence[10], refractive index[11] and thermal optical absorbance[12].

The sheath flow cuvettes which are discussed in this chapter are designed to act as the flow-through detection cell of a multicapillary DNA sequencing instrument, and, as such, have several requirements imposed on them. As for any other fluorescence detection cell, the cuvette must be of good optical quality. For example, the materials used must be transparent in the spectral regions of interest, in this case from ~ 480 nm to ~ 620 nm - most any clear glass satisfies this condition. One of the principle advantages of the sheath flow cuvette as a fluorescence detector is that both the incident laser beam and the emitted fluorescence pass through polished, planar boundaries of refractive index (four in total), a process which greatly lessens scattered light and resulting background detector signal compared to that seen with on-column detection. The sheath solution itself is carefully chosen to match in refractive index the analyte solution it ensheathes. While the cylindrical shape of the analyte solution leaving the ensheathed tube is intentionally preserved by the sheath flow up to the detection region, the curved boundary of refractive index disappears once the sheath and analyte solutions are in direct contact. In contrast, with on-column detection, these unpolished, cylindrical boundaries remain and scatter light. To ensure that the benefits of a sheath flow cuvette are reaped, the polishing protocol used on the optical cell must produce a high quality surface and, where polishing is not possible, the hydrofluoric acid etching protocol must do the same.

Unlike other flow cells, these cuvettes must allow for the fluorescence signal of up to 48 simultaneous separations in a linear array first, to be generated and second, to be detected. This arrangement is advantageous primarily because it allows tremendous parallelism in the analytical instrument using such a cuvette, which in turn leads to high information throughput with a significant reduction in instrumental cost. The design of this instrument is discussed in detail in Chapter 2. The optimum post-column position for fluorescence to be generated by the laser and collected for detection is directly beneath the capillary ends[7]. For optimum LIF detection for a linear array of capillaries, the capillary ends must be at the same height so that the laser can be brought up just beneath all the capillaries at once. In addition, for the laser to intersect all the capillaries' streams simultaneously requires the array to be very flat.

With regard to detection, there is a discrete, fixed detector positioned for each capillary's fluorescent spot; if the location of the spots is not reproducible when the capillaries are changed from one run to the next, the detection optics must be realigned each time. Thus the objective is to space the capillaries evenly and to place the spots directly beneath the capillaries. Capillary positioning is done by means of micromachined features in the cuvette, but these features which space and stop the capillaries must not disturb the laminar flow of the capillary eluent and sheath fluid.

Finally, from a practical standpoint, the cuvette features should facilitate capillary insertion to minimise run time and should also facilitate cuvette assembly.

The development of micromachined, multicapillary sheath flow cuvettes is described in this chapter. The patterned features in the cuvettes serve the mechanical function of capillary alignment inside the cell. An example of a 6 capillary micromachined cuvette alone and with capillaries inserted is shown in Figure 3.1. The micromachined multicapillary cuvettes are used in the DNA sequencer outlined in Chapter 2.

3.2 Experimental

Building a sheath flow cuvette involved 3 stages. The glass components were first micromachined and cut to size (section 3.2.1); they were then assembled into a cuvette, cut and polished (section 3.2.2); finally, the cuvette was integrated into a CE instrument and its performance was tested (section 3.2.3).

3.2.1 Micromachining

All micromachining was performed at the Alberta Microelectronic Centre, Edmonton, Alberta, and greatly benefitted from the assistance of Glen Fitzpatrick and Tran Tran. The technique of micromachining is described in Section 1.4.2.

3.2.1.A Mask

The designs for each mask were drawn on L-Edit, a circuit drawing programme (Tanner Research, Inc., Pasadena, California), sent electronically for

Figure 3.1: Photo of 6 Capillary Micromachined Sheath Flow Cuvette. Top photo shows 3.0 mm (h) X 2.0 mm (d) X ~ 20 mm (w) cuvette, with micromachined capillary-guiding features (horizontal lines) to right. Bottom photo shows the same cuvette with 6 capillaries inserted into their defined positions.

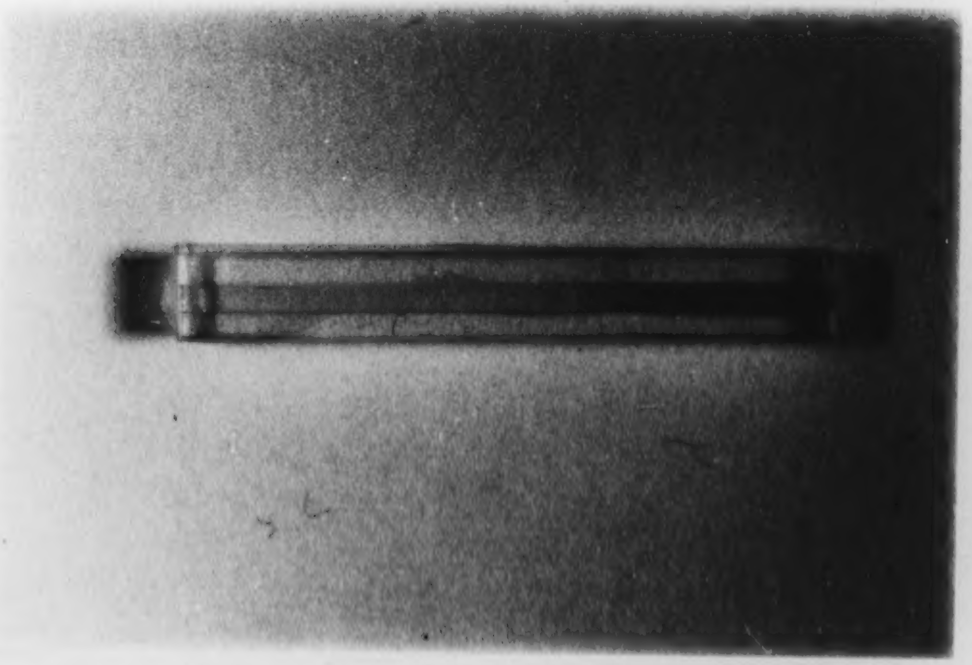

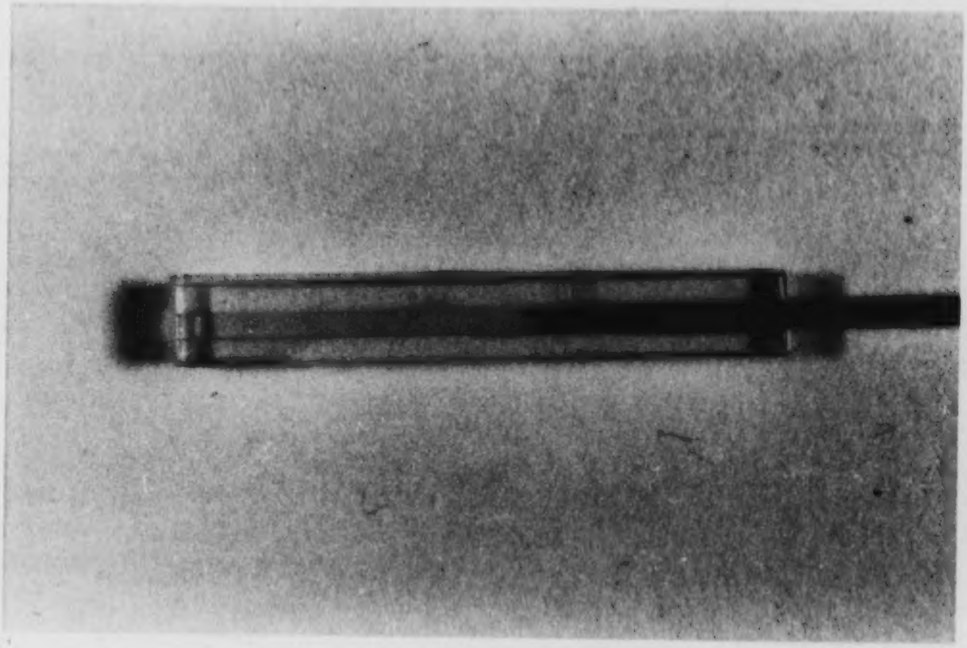

out-of-house mask fabrication (Precision Photomask (PPM), St-Laurent, Québec, Canada). Each mask contained 10 - 30 cuvette designs; a total of five masks were produced over 3 years. Figure 3.2 shows a photo of the first mask.

3.2.1.B Substrate preparation and metal plating

Glass substrates were purchased as 4" X 4" X 1.0 mm Pyrex #7740 plates (Paragon Optical Company, Inc., Reading, Pennsylvania). In all but some early etching experiments, substrates were annealed in a programmable oven to yield superior surface quality[13] under the advice of Dr. Harrison (Department of Chemistry, University of Alberta). The temperatures given by Corning[14] for strain, annealing and softening points of Pyrex #7740 are 510, 560 and 821°C, respectively. The three programmes shown in Table 3.1 were used for annealing various batches Pyrex #7740 plates. In each of the 3 stages in any programme, there is a total time duration, a temperature ramp and a target temperature, T_{target} ; each stage begins at the temperature of the previous stage (or at ambient temperature for stage #1), ramps the temperature to T_{target} at the rate specified, and holds at T_{target} for the remainder of the total time duration. While the three programmes differed somewhat, all seemed effective in relieving surface stresses, as witnessed in successful subsequent etches.

Prior to coating with metal, the substrates were washed in soap and water and then immersed in "piranha", a 3:1 volumetric mixture of 96% H_2SO_4 and 30% H_2O_2 (sulphuric acid and hydrogen peroxide from Olin Corp., Stamford, Connecticut), for 10 minutes in the clean room to remove any organic residue.

Metal deposition was performed either in an evaporation chamber (model SE 600 RAP, CHA Industries, Palo Alto, California) for a Cr, Au bilayer, or an Ar^+ plasma sputtering system (model 4410, Perkin-Elmer, Missisauga, Ontario,

Figure 3.2: Photo of Photolithography Mask.

Photo shows 25 rectangles (ca. 15 mm X 45 mm), each of which is a 6-capillary cuvette design. In the photo, each cuvette rectangle has a faint, ca. 2 mm X 15 mm rectangle centred along the top or left edge, running 1/3 of the cuvette length; these faint rectangles are the 7 capillary guides (see section 3.3.2 for a description of micromachined features). There are five designs of capillary stoppers on this mask (triangular and square pegs, 50 and 75 μm shelves, and one shelf), each of which was tried with 5 aspect ratios (1.4, 1.2, 1.0, 0.8 and 0.6:1). The three types of shelf designs for stoppers can be seen as ca. 2 mm X 26 mm bands beneath the capillary guides, while the peg stoppers cannot be seen except as faint dots to the right of the capillary guides in the two right-most cuvettes in the second and third rows from the bottom. The four solid black triangles and rectangles outside of the cuvette designs were Y- and T-shaped capillary connector prototypes.

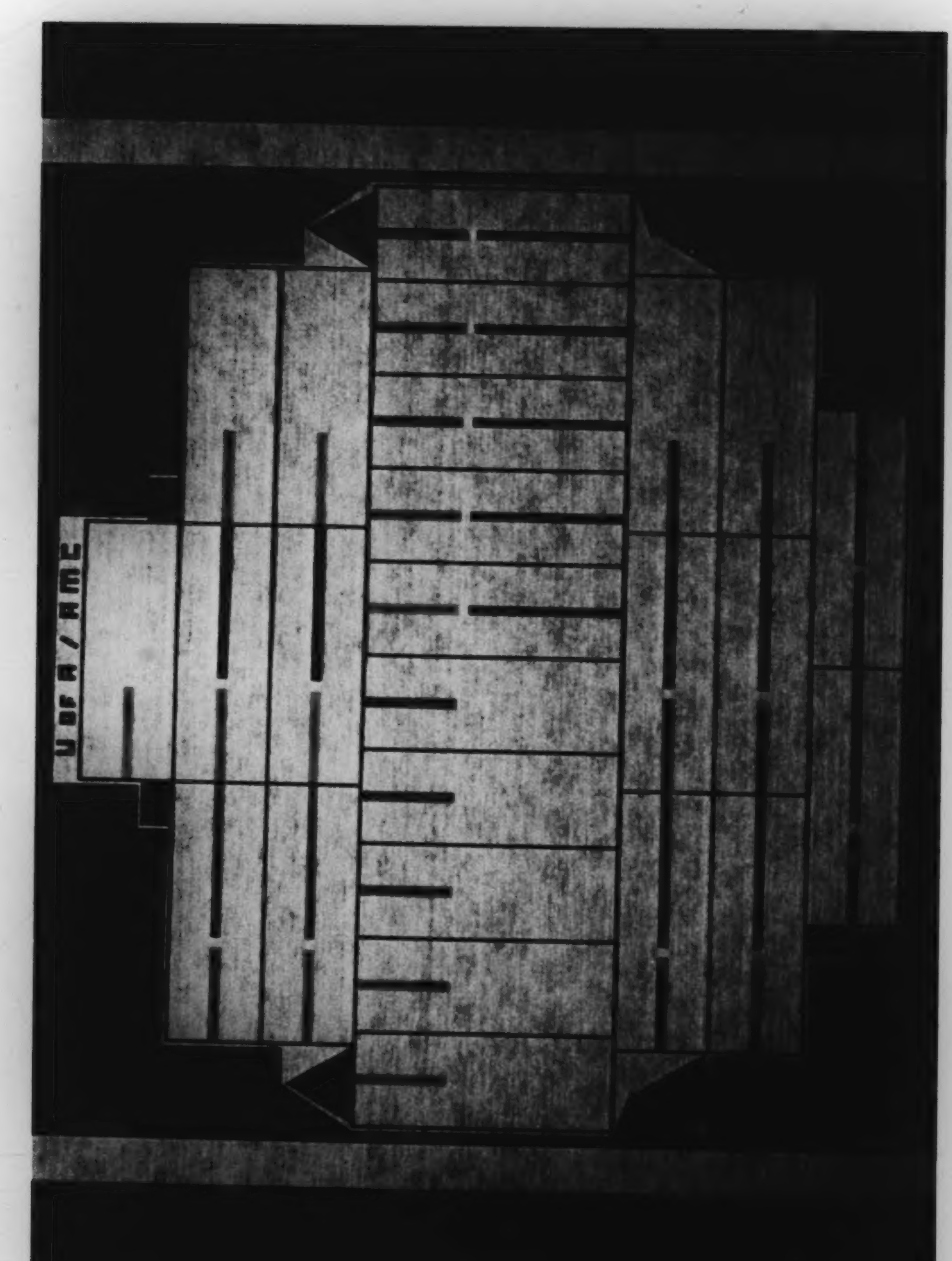
U OF A / AMC

Oven Stage	Duration (min.)	Ramp (°C/min)	T_{target} (°C)
Programme #1			
1	30	40	500
2	20	20	550
3	120	10	570
Programme #2			
1	30	40	500
2	30	20	550
3	120	10	570
Programme #3			
1	30	20	400
2	30	10	550
3	120	5	570

Table 3.1: Annealing Programmes for Pyrex 7740.

Annealing technique and programmes are those suggested by Dr. D. J. Harrison of this department.

Canada) for a Cr, Au bilayer, a Cu monolayer, a Cr, Au, Cr trilayer, and a Ni-Cr, Au, Ni-Cr trilayer.

3.2.1.C Photolithography

Photoresist (HRP 506, Olin Corp., Stamford, Connecticut) was spin coated onto the Pyrex substrate in two stages, 5 s @ 500 rpm and 30 s @ 2000 rpm (rpm = revolutions per minute), with a spin coater (model 5100, Solitec, Santa Clara, California) and was then softbaked for 30 min @ 110 °C. Next, the substrate was placed in the mask aligner (model MA4, Karl Süss KG-GmbH & Co., München-Garching, Germany), oriented underneath the mask and exposed to a UV lamp for ~ 5 s, depending on the age of the lamp. Once exposed, the photoresist was then developed with a 5 s water prewet @ 500 rpm, 70 s NaOH @1000 rpm, 90 s water rinse @ 1000 rpm, and 30 s dry @ 1500 rpm, and hard baked just prior to etching for 30 min @ 120 °C.

Once the photoresist had been patterned, the pattern was propagated through the underlying layers of metal by etching with aqua regia (a 3:1 volumetric ratio of 37% HCl to 70% HNO_3, hydrochloric and nitric acids from Olin Corp., Stamford, Connecticut) for Au and Cu layers, and Chrome Etch (contains ceric ammonium nitrate, nitric acid and water, Olin Corp.) for Cr and NiCr layers.

3.2.1.D Etching and Solutions

Several glass etching protocols were investigated to evaluate etchant composition and temperature. Solutions used were buffered and unbuffered HF. Unbuffered HF (Olin Corp., Stamford, Connecticut) was a mixture of concentrated HF (49%), concentrated HNO_3 (70%) and water, 20%, 14% and 66% by volume respectively. Buffered HF, buffered oxide etchant or BOE (Olin

Corp., Stamford, Connecticut) was specified as volumetric ratios of concentrated NH_4F (40%) to concentrated HF e.g.: 50:1, 10:1, 7:1, increasing in strength. Etching reactions were performed at room temperature (~ 20 °C) or at 45 °C. Typical etches in 10:1 BOE lasted ~ 25 hours for a 25 µm-deep etch; substrates were periodically removed from the etching solution so that their depth of etch could be monitored with a profilometer (model 10-02000, Tencor Instruments, Mountainview, California). Once the required depth of etch had been attained, the remaining photoresist and metal layers were removed with acetone and appropriate acids.

3.2.2 Cuvette Assembly

Cuvette assembly consists of cutting the etched cuvette pieces, gluing them and the cover slips together, and cutting and polishing the assembled cuvette.

3.2.2.A Cutting

The individual cuvette pieces were cut from the substrate on a wafer dicing saw (Micro Automation model 1100, General Signal, Freemount, California) for subsequent assembly. The substrate was mounted onto adhesive tape using a mounting station (Model 150, Micro Automation General Signal, Freemount, California), and placed on the saw's chuck. The saw, equipped with a 0.25 mm-thick circular resinoid blade (diamond-impregnated resin) spinning at 22 000 rpm, was programmed to cut depthwise through the 1 mm thick substrate in two 0.5 mm-deep passes, advancing horizontally at 1-2 mm/s.

3.2.2.B Assembly

The cuvette was assembled by gluing or fusing two identical etched pieces with two channel pieces or cover slips. An example of an etched piece with some of its micromachined features is shown in Figure 3.3. The four pieces were oriented and crudely assembled, as shown in Figure 3.4, and then fine alignment was achieved under microscope. Gentle pressure was carefully applied with plastic tweezers to the cover slips, forcing them inwards to bring all four pieces into alignment, as shown in Figure 3.5. Once aligned, as depicted in Figure 3.6, they were exposed at ~ 15 cm to 366 nm UV radiation from an 18.4 W UV lamp (model UVGL-58, UVP Inc., San Gabriel, California) for ~ 30 min., then heat cured in an oven (12 hours @ 50 °C).

The non-patterned channel pieces were initially also made of Pyrex #7740, polished to ~ 125 µm, and were fused with the two patterned pieces in an oven. Reproducible production of thin channel pieces of the correct thickness, ~ 150 µm, was labour intensive, and alignment of all four pieces for subsequent fusion in the oven proved difficult.

The method of assembling cuvettes using UV-curing glue (Norland Optical Adhesive #61, Norland Products, Inc., New Brunswick, New Jersey) described above yielded four advantages over a fusion assembly. First, it allowed the use of standard, non-Pyrex #7740, microscope cover slips, ~ 155 µm thick, cut to appropriate dimensions, and polished along the inner long edge. It proved advantageous to control the thickness of the cover slips by immersing them in 10:1 BOE after cutting and polishing. The thickness can be controlled to within ~ 5 µm by etching, and the polished edge remains intact after etching. Second, the use of glue allowed relatively easy manipulation of the four pieces for alignment prior to exposure to a U. V. lamp - the glue acts like a lubricant, allowing the four pieces to slide over each other smoothly; when the pieces are

Figure 3.3: Cuvette Design.

An illustration of a micromachined cuvette piece, one of two used to make a cuvette. Some of the features used to guide capillaries and cover slips are shown.

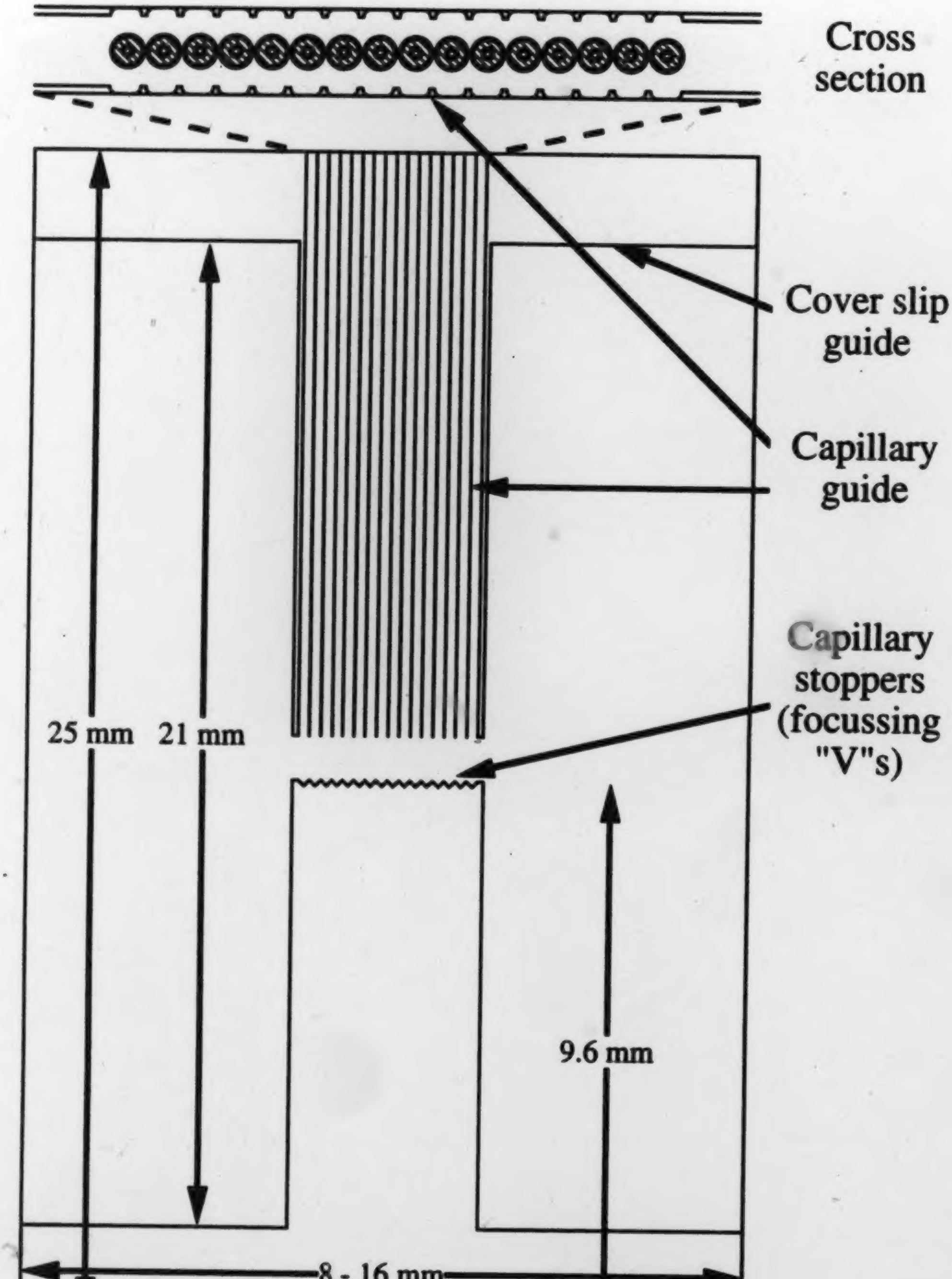
Cross section
Cover slip guide
Capillary guide
Capillary stoppers (focussing "V"s)
25 mm
21 mm
9.6 mm
8 - 16 mm

Figure 3.4: Cuvette Assembly I: Orientation and Crude Alignment. The orientation of the four glass pieces used to make a cuvette. Note that UV curing glue has been applied to the two micromachined pieces.

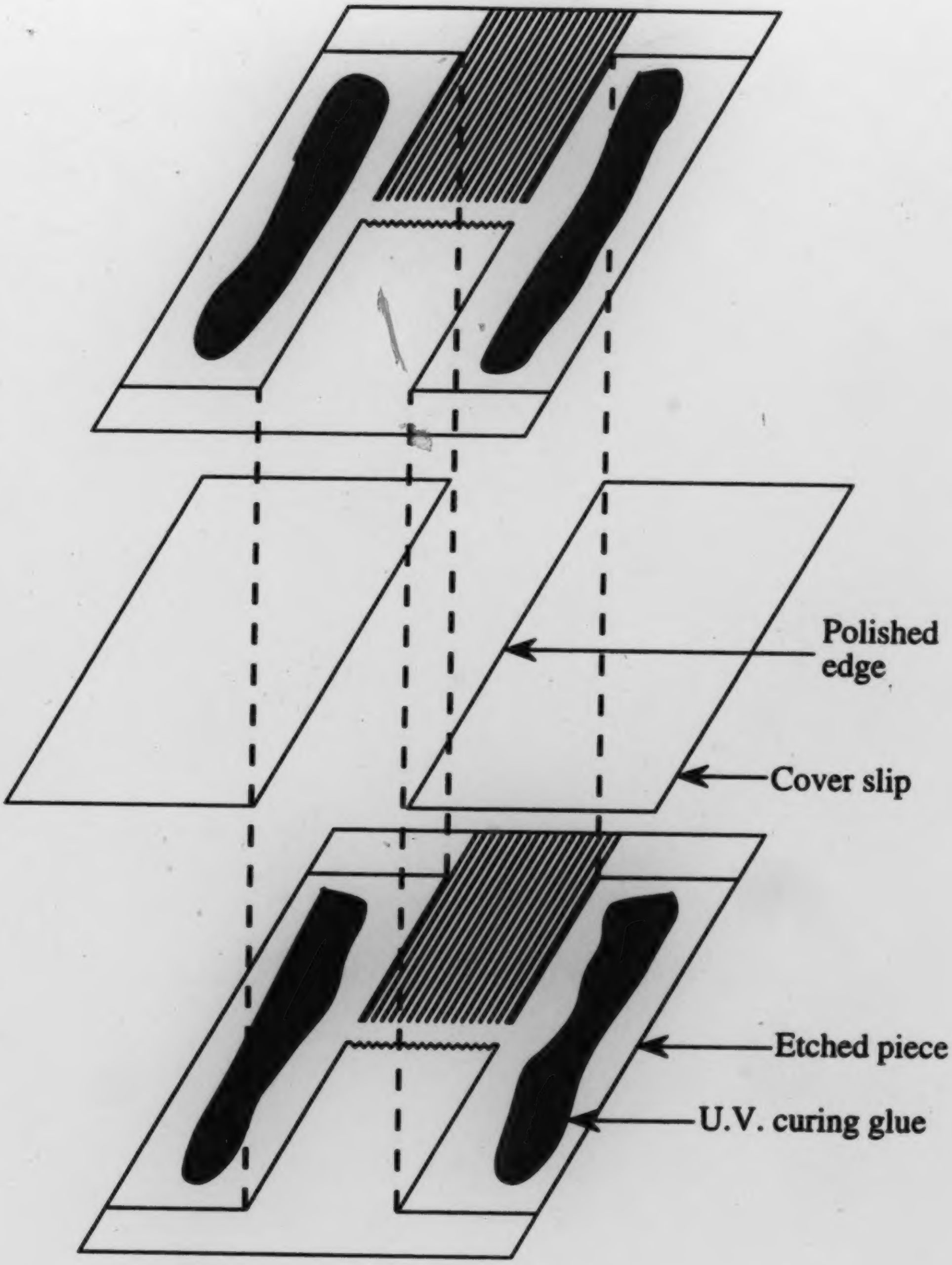
Polished edge
Cover slip
Etched piece
U.V. curing glue

Figure 3.5: Cuvette Assembly II: Fine Alignment.

The two cover slips are pushed in gently until they stop.

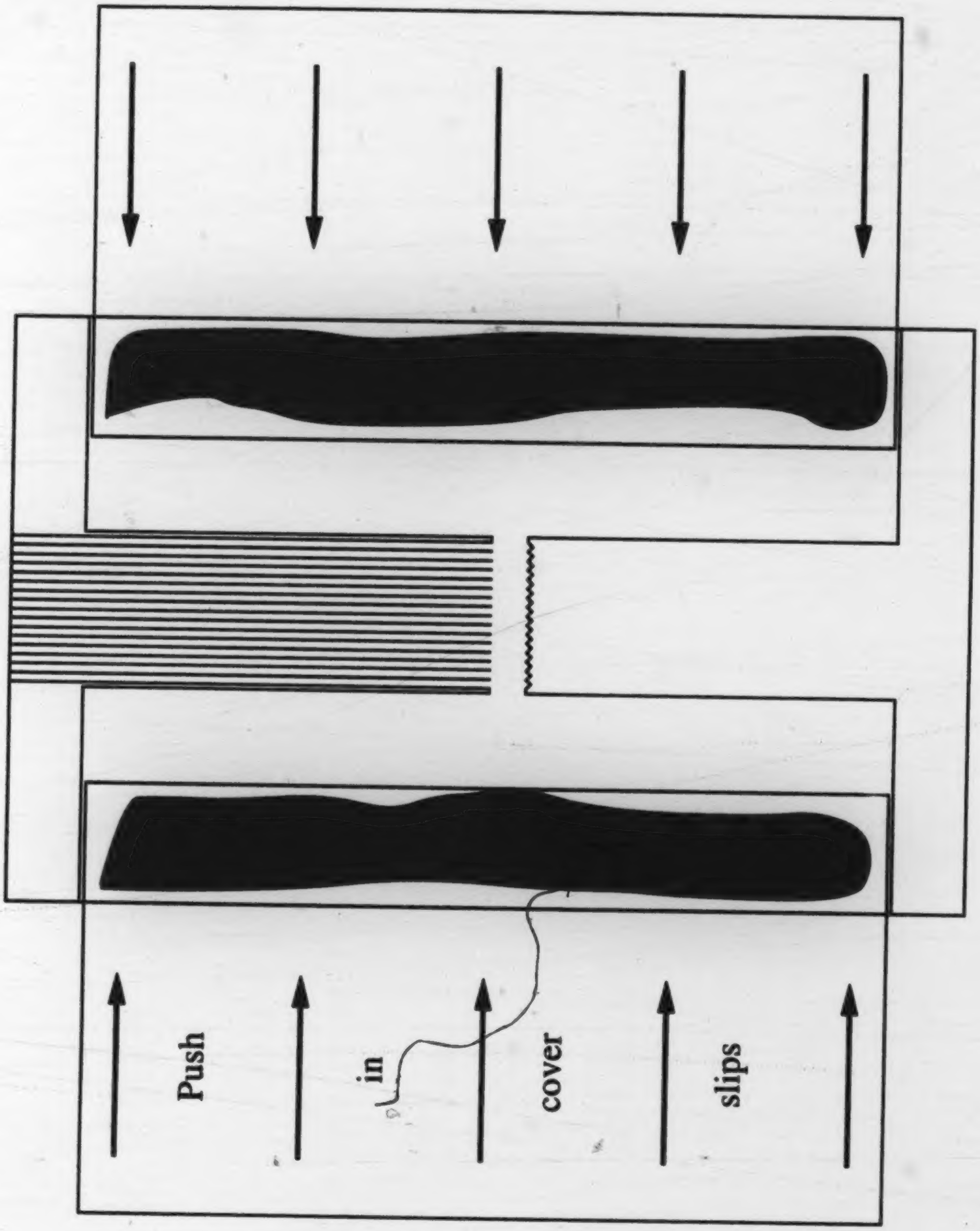
Push in cover slips

Figure 3.6: Cuvette Assembly III: Glue Curing, Cutting and Polishing.

The cuvette is exposed to UV light and heat to cure the glue, and is then cut along the lines shown, and polished along the long cut edges.

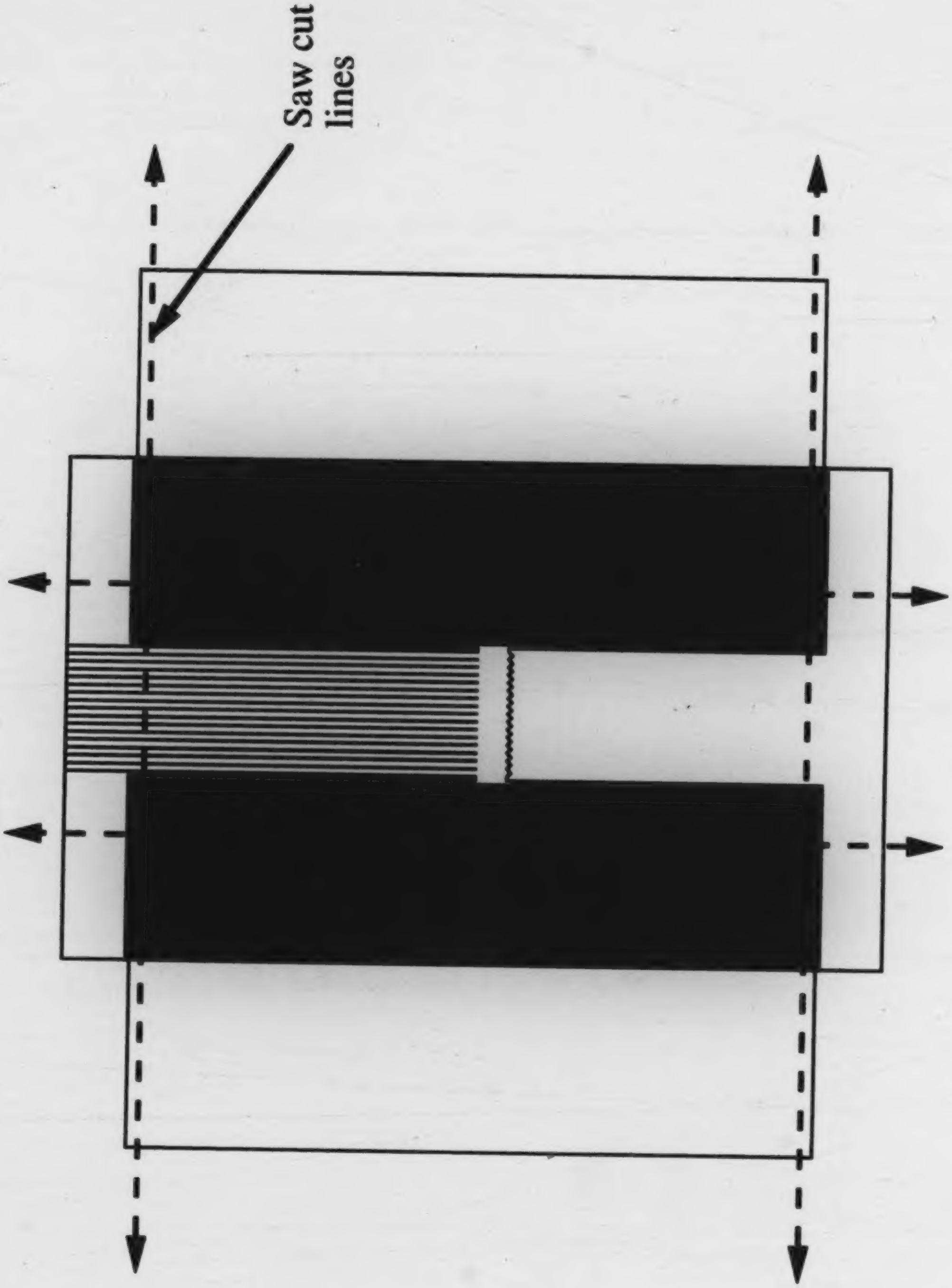
Saw cut lines

assembled for fusion, the lack of "glue lubrication" makes the alignment more difficult. Third, no loss of alignment is caused by U. V.-curing, as the lamp is simply brought overtop of the cuvette assembly and turned on; for fusion, the assembled cuvette must be delicately inserted into the oven, and weights must be placed on top of the cuvette, all without disturbing the alignment of the four pieces, a daunting task. Fourth, the weights required to ensure a good glass-to-glass bond during fusion left striations on the outer surface of the cuvette on which they rested. The cuvette outer surfaces resulting from fusion and gluing are compared in Figure 3.7. For these reasons, the UV-curing glue method was used throughout.

3.2.2.C Cutting and Polishing

Once the cuvette had been assembled and the glue cured, the cuvette was cut to size with the wafer dicing saw along the lines shown in Figure 3.6, 100 μm oversize along the edge to be polished and onto which the laser beams were to be incident. Several cuvettes were then mounted on a ~ 2" X 1" glass plate along with longer stabilising dummies, and were polished using 400 and 800 grit paper, then 3000, 8000 and finally 12000 grit diamond paste on a lapidary machine (Buehler Ecomet #, Lake Bluff, Illinois). Polishing lasted ~10 minutes at each grit size with the lapidary wheel spinning at ~ 150 - 300 rpm. The cut and polished cuvette is shown in Figure 3.8.

3.2.3 Cuvette Testing

3.2.3.A Cuvette Holder

Locally built cuvette holders were designed specifically to house the cuvette, to spread the capillaries into an array, feed them and their sheath flow

Figure 3.7: Photo of Striations on Outer Cuvette Surface.

Photo to the left shows the appearance of the outer surface of cuvette which was fused with weights on top; vertical striations can clearly be seen. Unfocussed features to the right are the capillary guides in the centre of the cuvette, 1 mm beneath the outer surface.

Photo to the right shows the same surface for a cuvette which was glued; the outer surface has no striations, since no weights are use in gluing. Dark objects at top of photo are the six capillaries inserted into this cuvette, again 1mm beneath the outer surface.

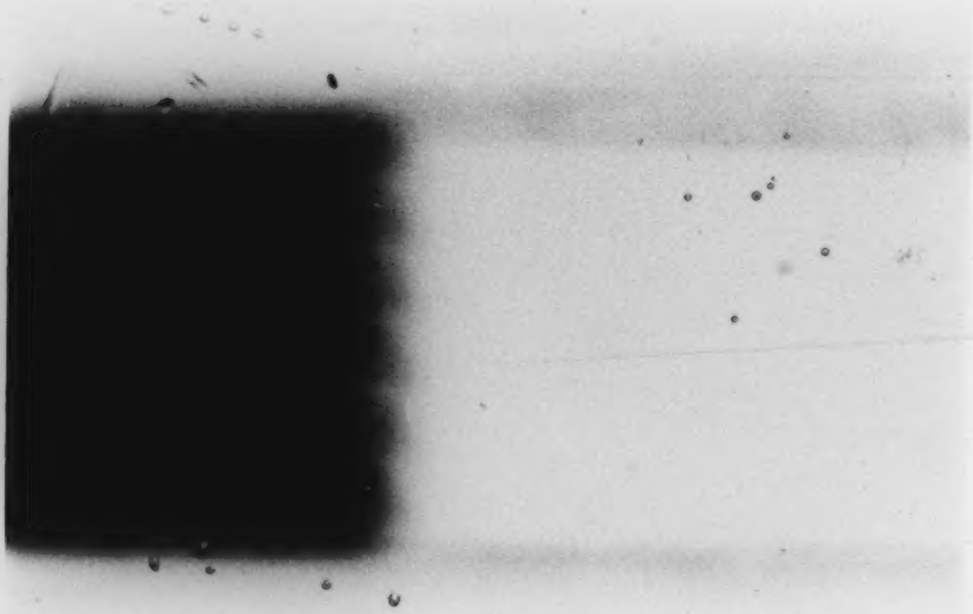

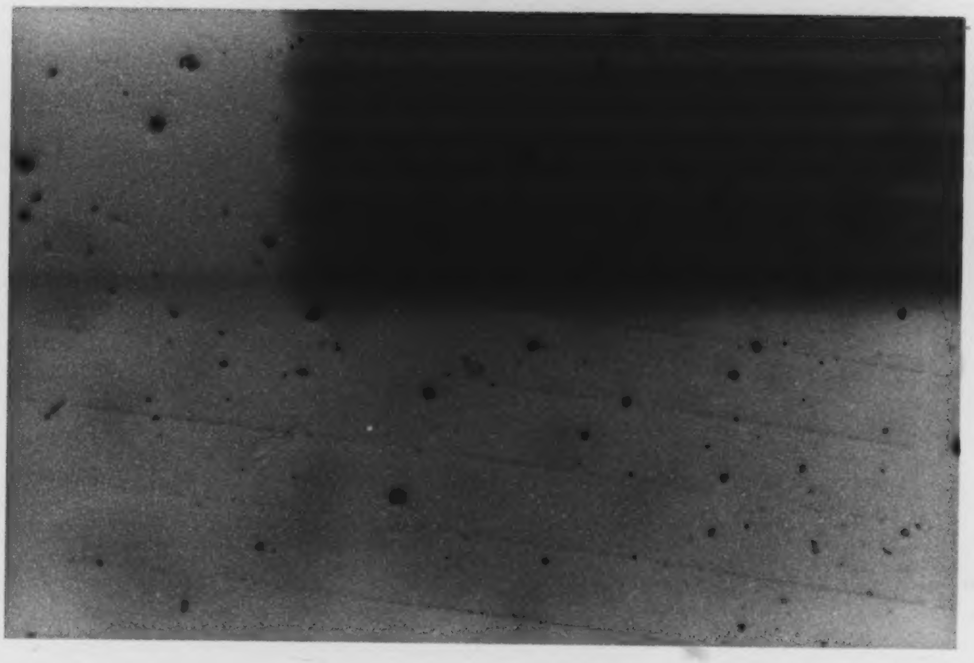

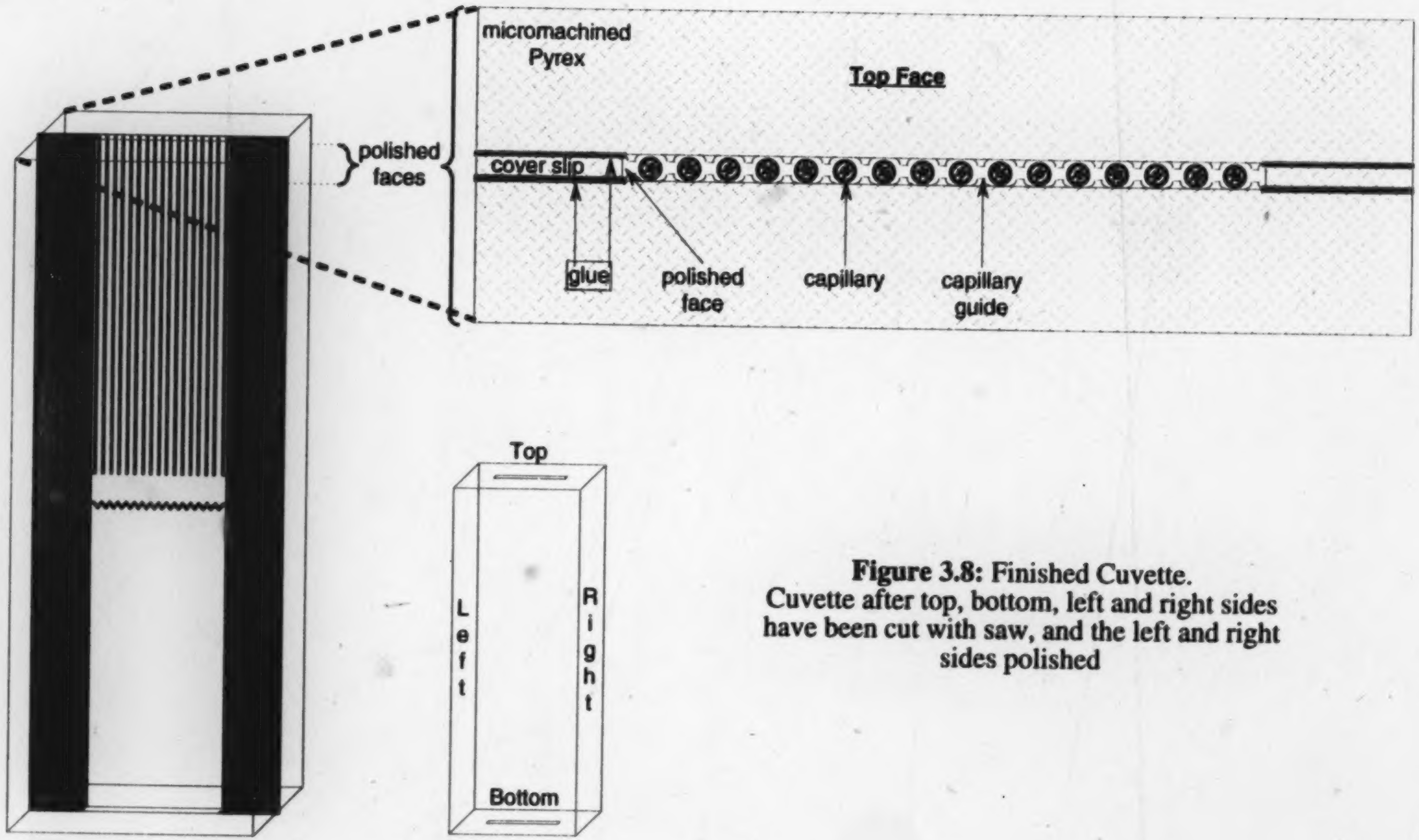
micromachined
Pyrex
Top Face
polished
faces
cover slip
glue
polished
face
capillary
capillary
guide
Top
Left
Right
Bottom

Figure 3.8: Finished Cuvette.
Cuvette after top, bottom, left and right sides have been cut with saw, and the left and right sides polished

into the cuvette and carry the capillary eluent and sheath flow to waste. The cuvette holder was mounted onto a vertical translation stage and two orthogonal horizontal stages to allow translational movement along three axes; the holder was also grounded to the optical table, completing the circuit for the electric field applied to the capillaries to effect electrophoresis. The cuvette in its holder constituted the detection cell of a capillary electrophoresis instrument.

Four cuvette holders were built, accommodating 6, 8, 16 and 32 capillary cuvettes The designs for the most recently built holder which accommodates some 16 capillary cuvettes with 225 or 300 μm spacing and some 32 capillary cuvettes with 150 μm spacing may be found in Appendix 2 of this thesis. This holder is currently used in the sequencer described in Chapter 2. A close-up photo of a 16 capillary cuvette in its holder, and as it appears integrated into the sequencer with the blue Ar^+ laser incident upon it is shown in Figure 3.9.

3.2.3.B Testing

To evaluate a particular cuvette's performance, the cuvette was mounted into its cuvette holder, capillaries were inserted into the cuvette, and a solution of fluorescent dye was pumped through the ~ 40 cm long, 50 μm I. D., 150 μm O. D. capillaries (capillaries have exterior polyimide coating to enhance flexibility; Polymicro Technologies, Phoenix, Arizona), either by gravity or by electrophoresis. The streams of dye were observed as they exited from the capillaries and passed through the laser beam incident upon the sheath flow cuvette just beneath the capillaries. The dye-laser combinations used were tetramethylrhodamine isothiocyanate (Molecular Probes, Eugene, Oregon) and rhodamine 6G (Aldrich, Milwaukee, Wisconsin) with either a 5 mW, 543.5 nm HeNe laser (#05-LGR-193-S, Melles Griot, Nepean, Canada) or a 10 mW, 532 nm frequency doubled Nd-YAG laser (Coherent 532-10, Santa Clara, California), or

Figure 3.9: Photos of 16 Capillary Sheath Flow Cuvette Mounted in Holder.

Photo to left shows 16 capillaries coming down from top into the stainless steel holder (viewed from front) and into cuvette, stopping half way down. Teflon tubes to left and right act to bring in sheath flow and expell bubbles; tube leaving beneath cuvette takes capillary and sheath solutions from bottom of cuvette to waste.

Photo to right shows cuvette and holder (viewed from back) integrated into sequencer. Gold-coloured capillaries can be seen coming out of the top of the holder, curving to the left; blue Ar+ laser is incident from right side. Viewing microscope on translation stage can be seen in foreground, while black box containing detection optics is in background (instrument optics are described in section 2.2.4).

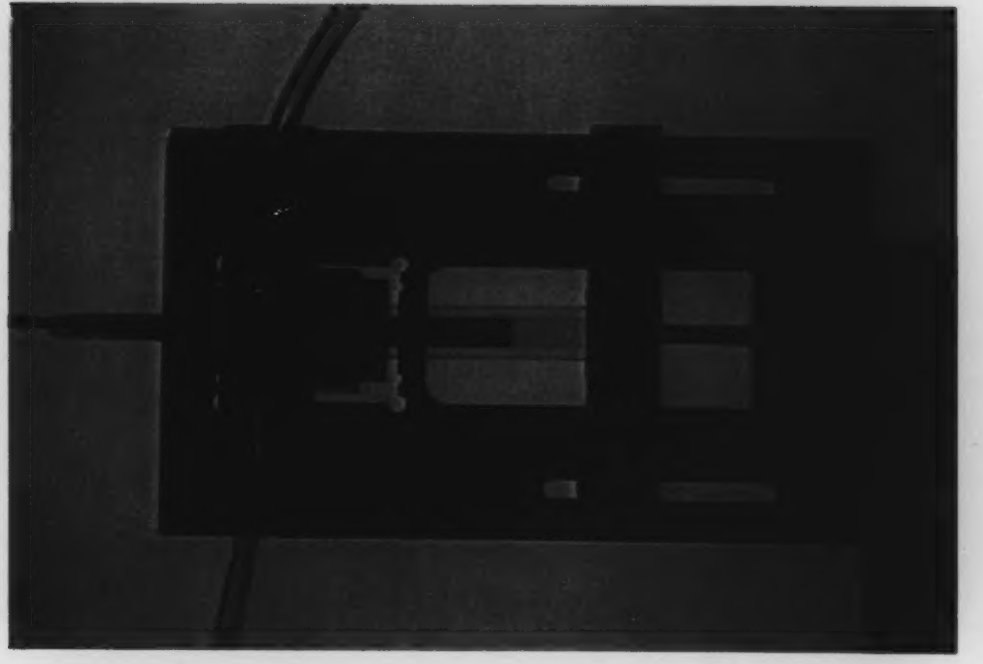

fluorescein with a 488 nm Ar^+ laser (Cyonics 2213-755L, San Jose, California); typically the dye concentration was ~ 10^{-7} M, easily visible to the eye. The cuvette's performance was observed through a microscope (Melles Griot Nepean, Canada), using objectives ranging in power from 4 X to 18 X. Flow rates of eluents and sheath flow were adjusted to produce a ~ 25 μm fluorescent spot at the hydrodynamic focus.

3.3 Results and Discussion

Two main areas are dealt with in this section: those results pertaining to micromachining methodology (glass treatment and etching procedures), and those pertaining to cuvette design.

3.3.1 Micromachining Methodology

Table 3.2 shows some qualitative and quantitative results with respect to etching conditions and annealing. It may be seen that the etching rate increases with acid concentration, as well as with temperature. Surface quality changes dramatically with temperature, solution and annealing, as seen in the scanning electron micrographs shown in Figure 3.10 a-c. Figure 3.10-a shows the result of a 45 °C etch in unbuffered HF on an unannealed Pyrex plate; 5 of the 7 capillary guide ridges can be seen, with some of the Cr and Au layers still attached. The glass between these ridges has pronounced striations and craters, and is not of optical quality. In both Figures 3.10-b and 3.10-c, Pyrex plates were etched in 10:1 BOE at room temperature, but in Figure 3.10-c, the plate has also been annealed. The view in Figure 3.10-b is as for 3.10-a, only magnified further, focussing on the upper left corner of the lowest capillary guide. The striations are no longer visible, but the craters remain. In Figure 3.10-c, the view is magnified still further, but the annealed substrate clearly has no striations or craters visible.

	Etching Solution, Temperature				
	50:1 BOE	10:1 BOE	7:1 BOE	Unbuffered HF	
	21 °C			21 °C	44 °C
Etching Rate (μm/min)	0.0061	0.017	0.033	0.46	11
Surface Appearance (Unannealed)	frosty	frosty	frosty	frosty	very frosty
Surface Appearance (Annealed)	clear	clear	clear	clear	N.D.

Table 3.2: Effect of Etching Conditions and Annealing for Pyrex 7740.

Figure 3.10: Scanning Electron Micrographs of Etched Glass Surfaces.

In each image, the magnification and scale are given along the upper border.

a) (opposite) unannealed Pyrex in unbuffered HF at 45 °C; pronounced craters and striations are visible.

b) (next page, top) unannealed Pyrex in 10:1 BOE at room temperature; pronounced craters are visible.

c) (next page, bottom) annealed Pyrex in 10:1 BOE at room temperature; smooth surface is seen.

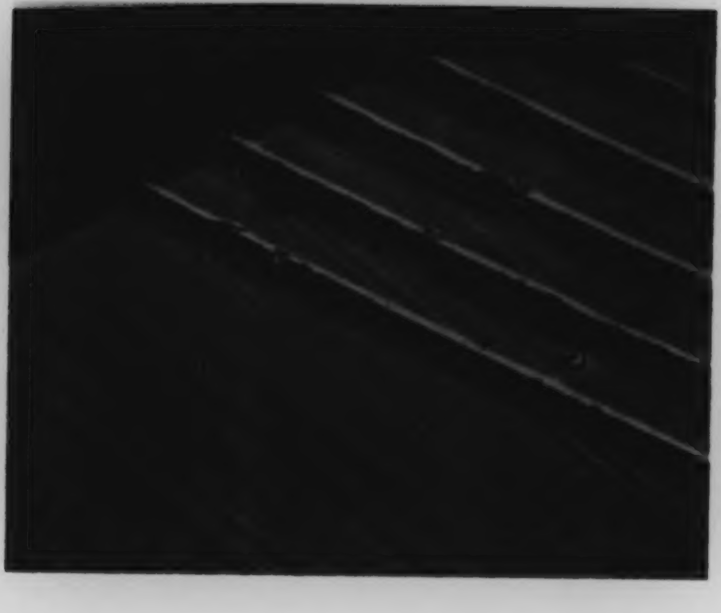

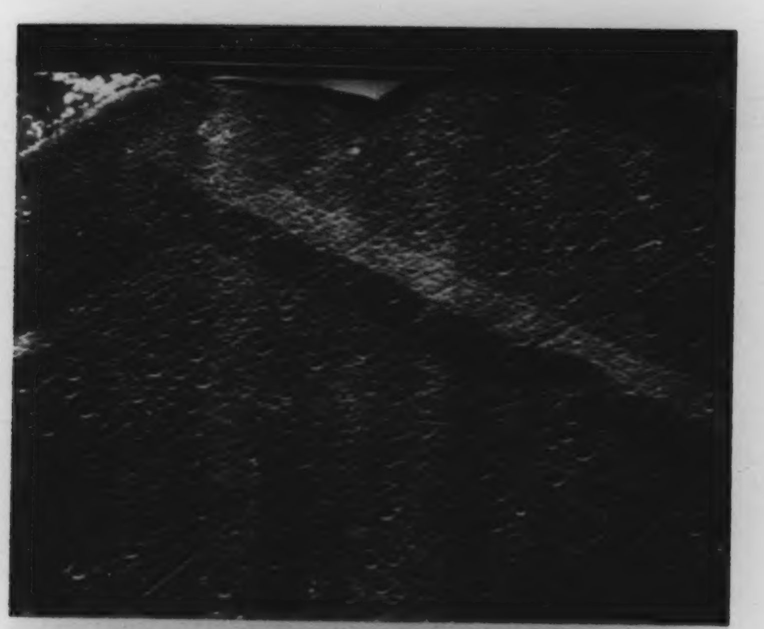

An additional feature worthy of note is that the capillary guide in Figure 3.10-c reaches full height, as compared to the flattened capillary guide of the unannealed plate in Figure 3.10-b. By reducing surface stress, annealing also seems to improve the adhesion of the metal layers; in the unannealed plate of Figure 3.10-b, the metal layers lifted during the etch, allowing the etchant to "undercut". This aspect of the quality of etch is quantified as the aspect ratio (horizontal : vertical etch ratio); the aspect ratios were measured on the profilometer, and for the unannealed and annealed plates of Figures 3.10-b and 3.10-c were ~ 15:1 and 1.5:1, respectively. The optimum conditions, namely a 10:1 BOE solution used at room temperature with annealed substrates, were chosen based on these scanning electron micrographs, and were used in all subsequent work.

3.3.2 Cuvette Design

The results of cuvette design iteration are displayed in Table 3.3, which lists cuvette design features in one of four categories, the objectives these design features were meant to address, and whether the numbered objectives were met. The four categories for design features are capillary stoppers, capillary guides, cover slips and their guides, and aspect ratio. Simply put, capillary stoppers are meant to stop the capillaries at the same level, capillary guides are meant to space the capillaries evenly apart, cover slips are the pieces of glass in the cuvette through which the laser is shone, cover slip guides aid in positioning the cover slips during assembly, and aspect ratio is the horizontal to vertical etch ratio. In each category, one or several of the features are italicised to indicate that they most closely met the objectives sought. Figure 3.11 shows a close-up photo of a 6 capillary cuvette with and without capillaries inserted, in the region where the micromachined features guide and stop the capillaries. The effect of changing the

Features Tested	Objectives		
	Description	Met	Not Met
1. Capillary Stoppers			
square pegs	1. stop capillaries 2. no turbulence 3. centre capillaries	2	1, 3
triangular pegs		2	1, 3
50 µm shelves		2	1, 3
75 µm shelves		2	1, 3
one shelf		1, 2	3
one shelf - Vs		*1, 2, 3*	*3.*
V slope of 1	1. centre capillaries 2. hold capillaries	1.	1, 2
V slope of 2		*1, 2*	
V slope of 3		*1, 2*	
2. Capillary Guides			
tapering at inlet	1. aid capillary insertion	*1*	
150 µm spacing	1. repr. spot spacing 2. no turbulence	2	1
160 µm spacing		2	1
225 µm spacing		1, 2	1.
300 µm spacing		*1,2*	
1 mm from stoppers	1. fix capillaries 2. no turbulence	2	1
100 µm from stoppers		*1, 2*	

Table 3.3: Cuvette Design Features.

Table shows four main areas of design, the area's design features, the objectives the features were meant to address, and whether the objectives were met.

Features Tested	Objectives		
	Description	**Met**	**Not Met**
3. Cover Slips (cs), Cover Slip Guides (csg)			
0 csg	1. ease of assembly		1
1 csg		1.	1.
2 csg		*1*	
cs (155 µm)	1. right thickness (flat array) 2. alignment (no spot compression)	2	1
cs (150 µm)		1, 2	1.
cs (145 µm)		1, 2	1.
cs (140 µm)		*1, 2*	
cs (135 µm)		*1, 2*	
cs (130 µm)		2	1
cs (125 µm)		2	1
4. Aspect Ratio (lateral : vertical etch)			
0.6 : 1	1. fits the aspect ratio seen		1
0.8 : 1			1
1 : 1		*1*	
1.2 : 1			1
1.4 : 1			1
1.5 : 1			1
2 : 1		*1*	

Figure 3.11: Photo of Capillaries, Guides and Stoppers in a 6 Capillary Cuvette. Top photo shows the horizontal, rectangular capillary guides, and square capillary stoppers; note that each feature is seen in duplicate, since it is present in the same location on both etched pieces. The centre-to-centre distance between guides and stoppers is 150 μm, and the stoppers are 1 mm from the guides. The somewhat chipped edges of the coverslips lying directly above and beneath the micromachined features can be seen. The boundary of UV-curing glue is shown by the curved line running through the lower cover slip, meaning that in this cuvette, the glue did not effectively spread accross the cover slip surface to make a water-tight seal.

Bottom photo shows the same cuvette with capillaries inserted and stopping at the square peg stoppers.

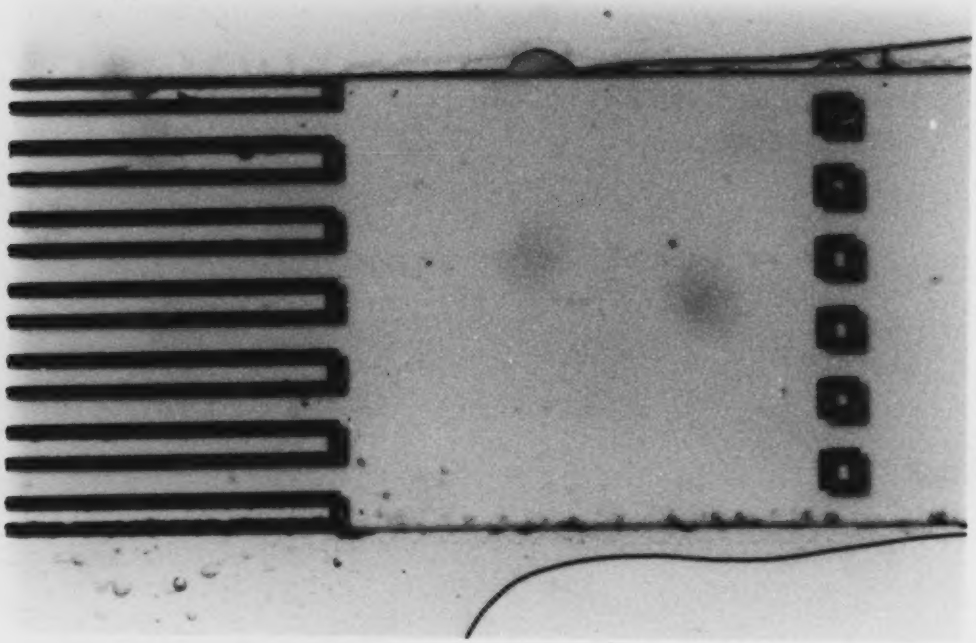

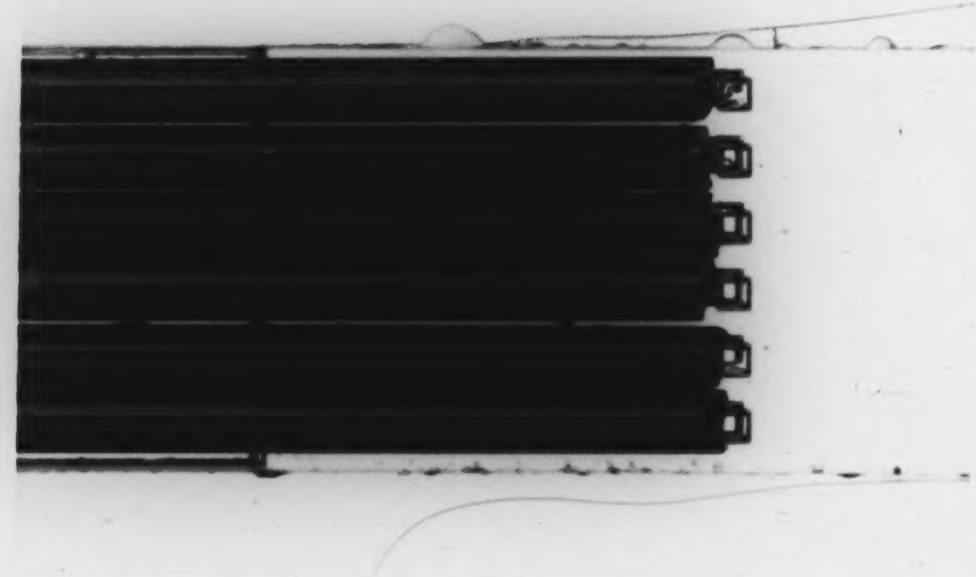

features in each of the four categories is explained in the following sections, and illustrated in Figures 3.12 to 3.20.

3.3.2-A Capillary Stoppers

Figure 3.12 a-f shows four capillaries lying in their slots as defined by the micromachined capillary guides and capillary stoppers in the cuvette. Six geometries are shown, with the preferred "one shelf with Vs" being used presently. The idea of a V-shaped stopper was conceived of by Dr. J. Z. Zhang of this department. Of the other five stopper designs, the square and triangular pegs, 50 and 75 µm shelves did not stop the capillaries at all, and the one shelf design stopped but did not centre the capillaries. When capillaries were inserted into a cuvette with pegs or shelves as stoppers, capillaries would often bend and squeeze between two stoppers to get past them, meaning the stoppers were ineffective. A highly magnified view of capillaries stopped at their square peg stoppers is given in Figure 3.13.

Shown in Figure 3.14 are the three V shapes investigated for the "one shelf with Vs"design. Slopes of $m = 1$, 2 and 3 were tried, with trade-offs seen in their performance; a slope of 2 was found to be optimal. The deeper Vs were conceived to better hold the capillaries by allowing them to wedge into the bottom of the Vs, but this was effective only to a point. Vs of $m = 2$ held the capillaries better that for $m = 1$, but there was no appreciable benefit to using $m = 3$; furthermore, the higher slope has the undesirable effect of stopping capillaries of marginally different outer diameters at different heights more pronouncedly than for lesser slopes. This same effect also occurs if the cuvette chamber width changes marginally across the cuvette. These effects can be visualised in terms of the stopping mechanism of the V stoppers, which is depicted in the lower section of Figure 3.14. Viewed along the capillary axis, the capillary stops when a chord

S

Figure 3.12: Capillary Stoppers.

Different types of capillary stopper geometries shown are shown: a) one shelf, b) one shelf with Vs, c) 50 µm shelves, d) 75 µm shelves, e) triangular pegs and f) square pegs.

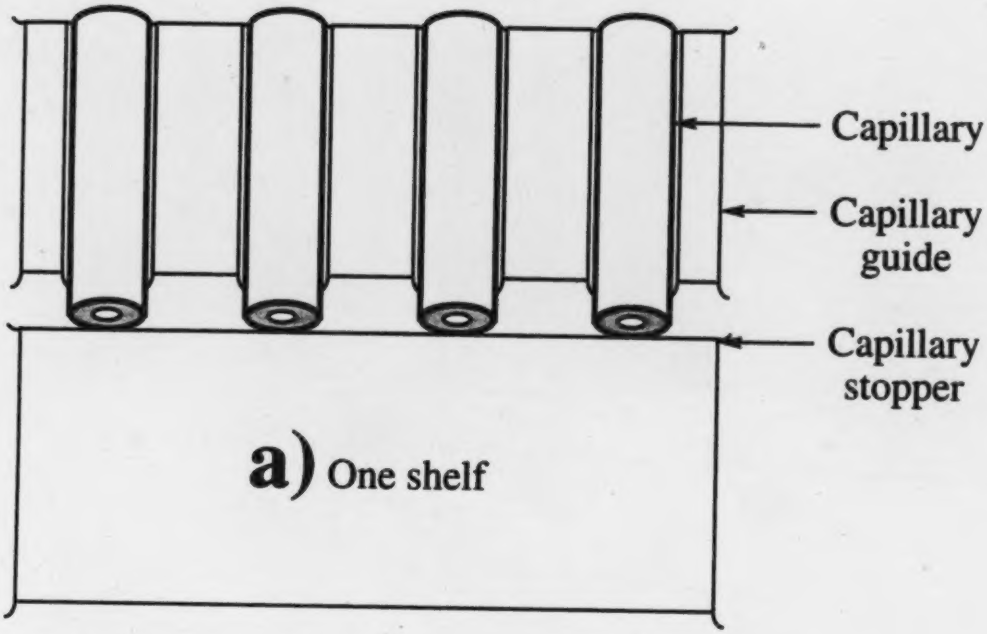
Capillary
Capillary guide
Capillary stopper

a) One shelf

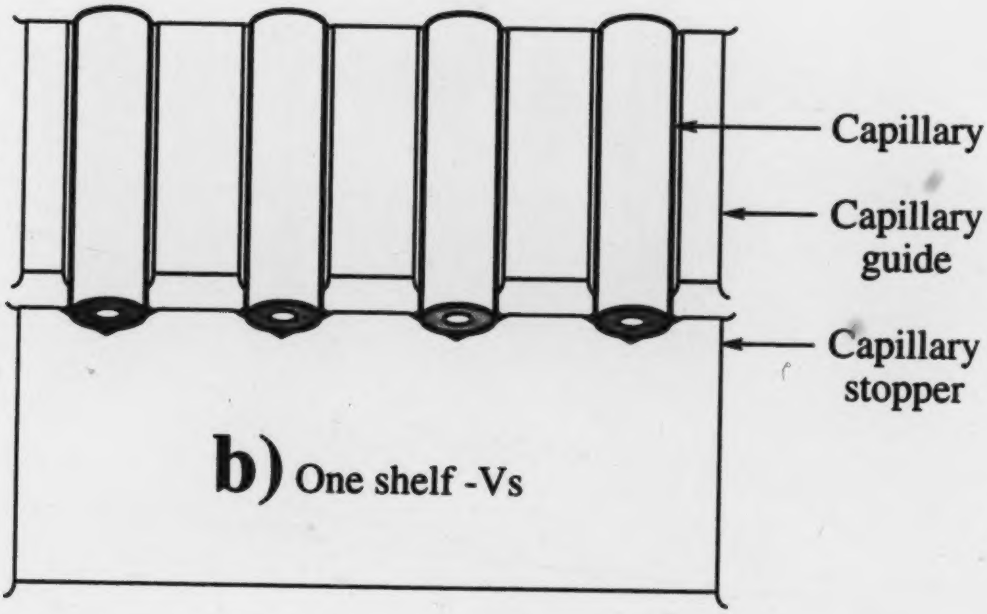
Capillary
Capillary guide
Capillary stopper

b) One shelf -Vs

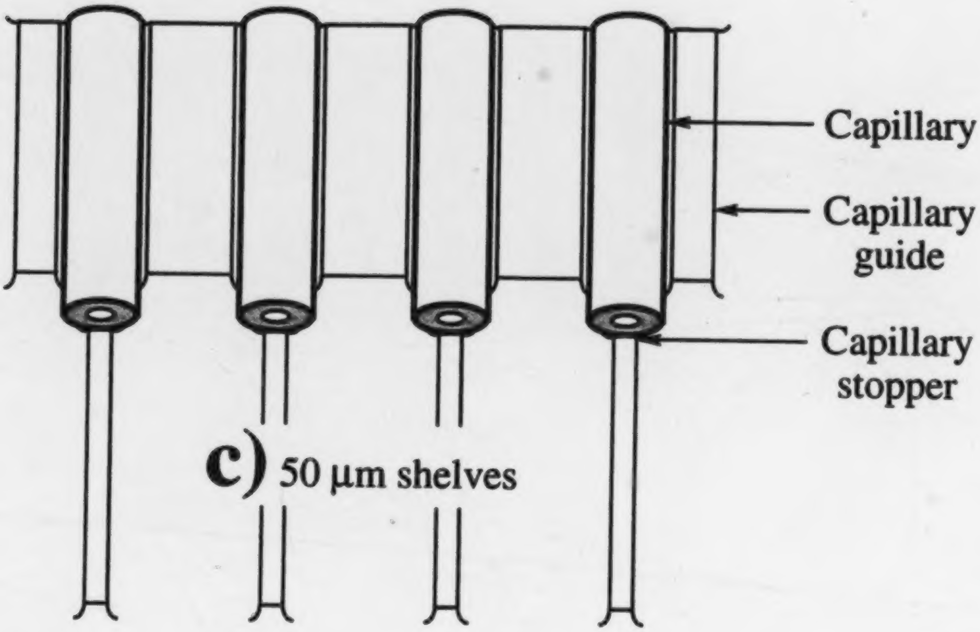
Capillary
Capillary guide
Capillary stopper

c) 50 µm shelves

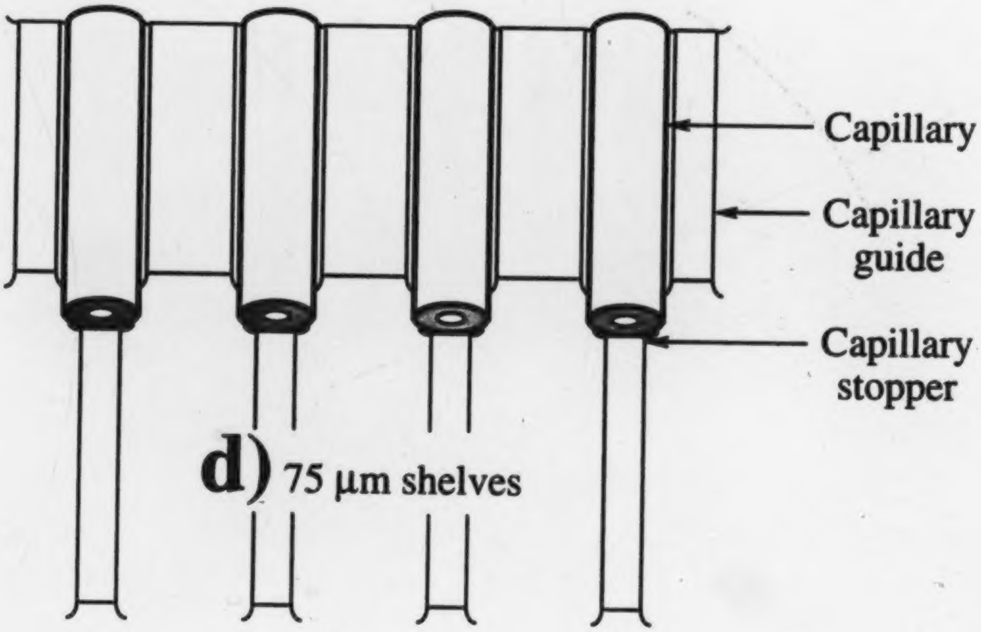
Capillary
Capillary guide
Capillary stopper

d) 75 µm shelves

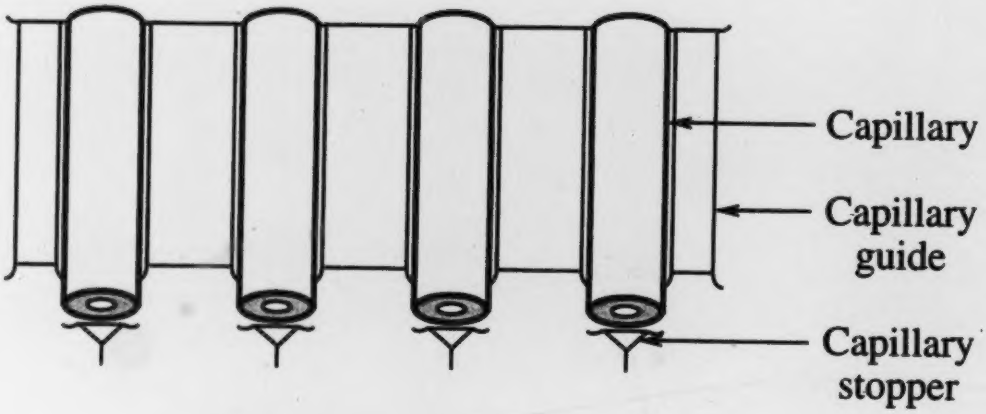
Capillary
Capillary guide
Capillary stopper

e) triangular pegs

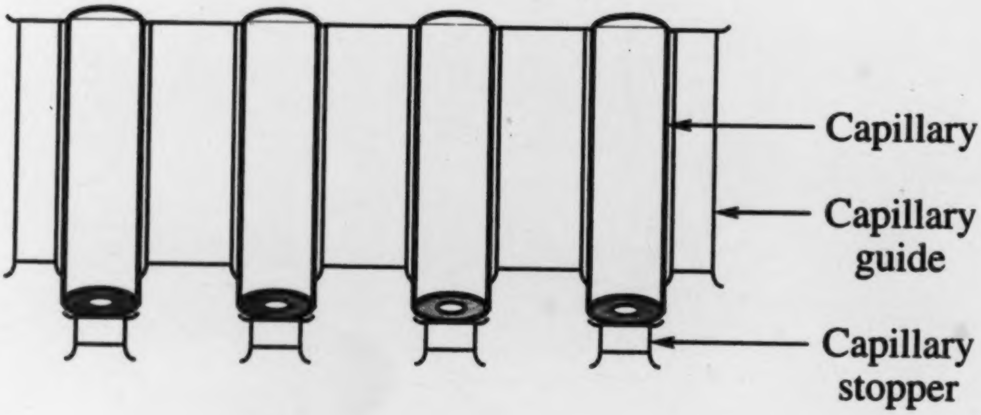
Capillary
Capillary guide
Capillary stopper

f) square pegs

Figure 3.13: Photo of Capillary Ends and Square Peg Stoppers.

Three capillary ends and the square pegs stopping them can be seen. Capillary ends were cut crudely with a silicon chip, not by the wafer dicing saw method described in Chapter 2, which is why they are not blunt. Centre-to-centre distance of capillaries and stoppers is 150 μm.

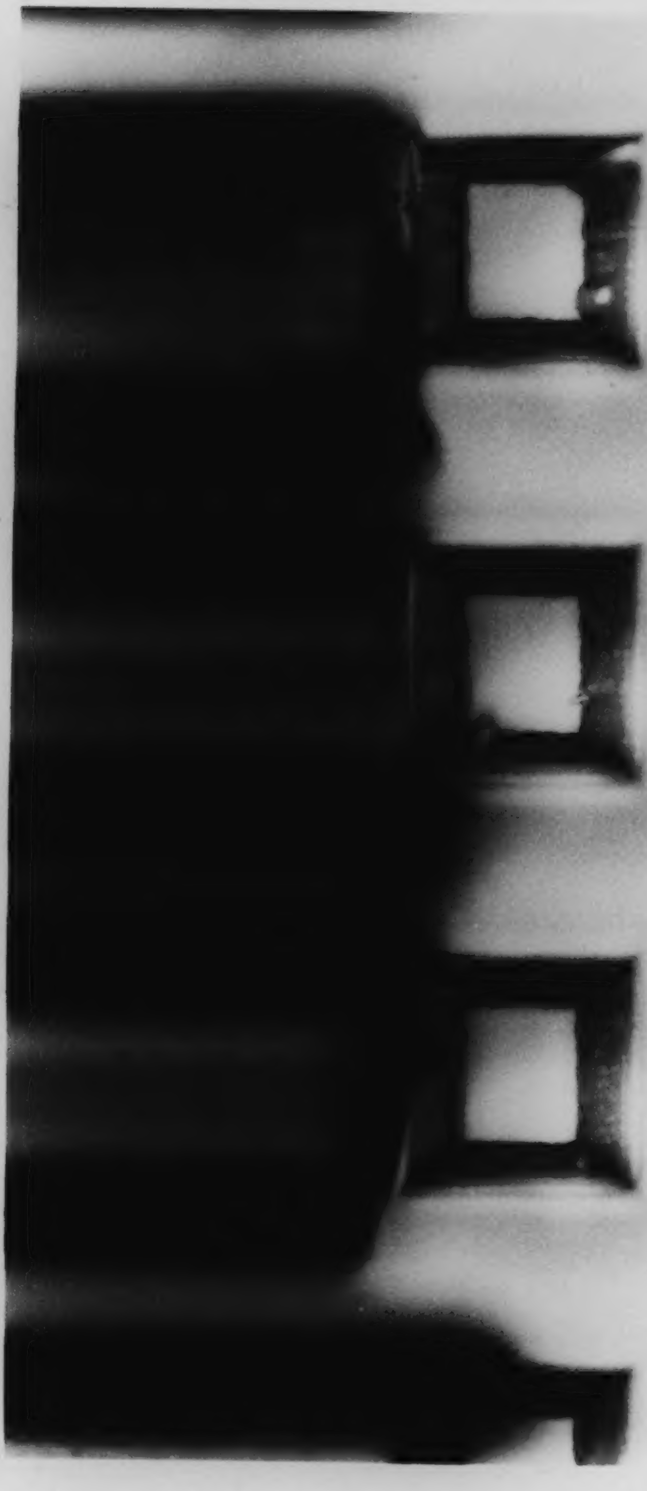

Figure 3.14: Shape of V in Capillary Stoppers.

For the one-shelf with Vs design in Figure 3.12-b, several different shapes were tried to improve their capillary fixing and centring ability; a slope of two was found to be optimal. Diagrams are to scale.

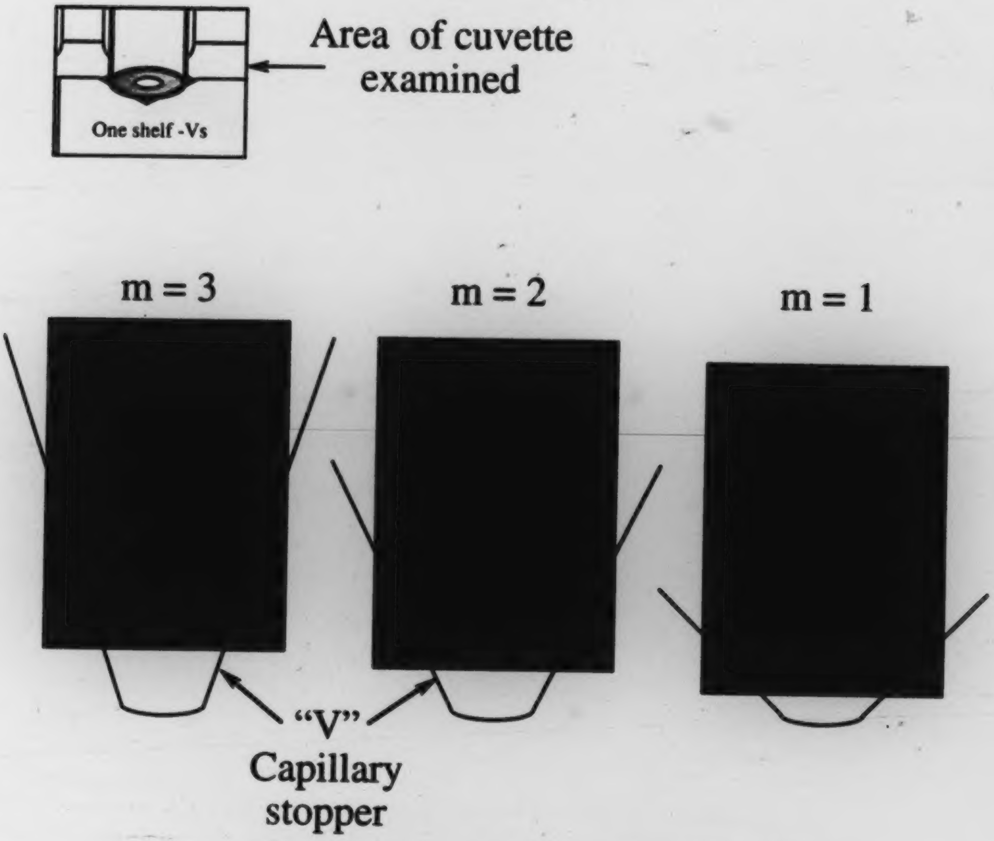
Area of cuvette examined
One shelf -Vs
m = 3
m = 2
m = 1
"V" Capillary stopper

Capillary Cross-Section

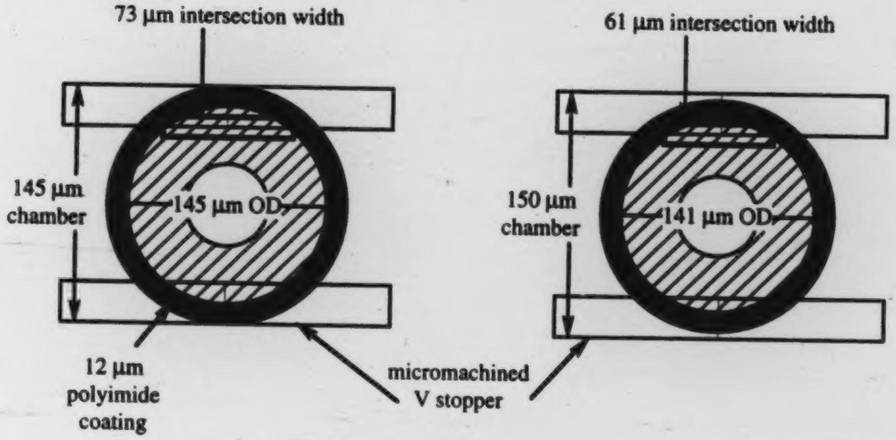
73 µm intersection width
145 µm chamber
145 µm OD
12 µm polyimide coating
61 µm intersection width
150 µm chamber
141 µm OD
micromachined V stopper

25 μm from the capillary's outer surface (ie: the height of the micromachined features) is equal to the V width; this width will be referred to as the intersection width. The V stoppers tend to cut through the 12 μm polyimide capillary coating, so this chord is drawn only accross the quartz portion of the capillary's cross-section. Two examples are shown in the lower portion of Figure 3.14, which is drawn to scale: a 145 μm OD capillary in a 145 μm-wide capillary slot in the cuvette, and a 141 μm OD capillary in a 150 μm-wide location. The intersection widths for these two cases are 73 and 61 μm respectively, meaning that these two capillaries will stop at different heights in the V. The greater the slope of the Vs, the greater the height differences between where capillaries stop, and the further from their ends some capillaries' streams will be sampled by the laser (recall from section 3.1 that capillaries should be sampled directly beneath their ends).

Restrictions in mask fabrication require no acute angles nor features smaller than 5 μm, so producing deep Vs with slopes of 2 or 3 necessitated a 6 μm flat segment at the bottom of the V in the mask. The flat bottom in the mask produces Vs with rounded bottoms ~ 50 μm-wide in the patterned cuvette pieces, as shown in Figure 3.14. In cases where smaller OD capillaries are used and/or the cuvette widens, the capillary may be stopped at the bottom of the V, and some of the centring capacity of the V may be lost.

3.3.2-B Capillary Guides

Two variables concerning capillary guide design are shown in Figures 3.15 and 3.16, capillary guide - capillary stopper separation and capillary spacing, respectively. First, as seen in Figure 3.15, capillary guides were initially designed to end 1 mm above the intersection of the capillaries with their stoppers so that the sheath fluid would expand to fill the space created by the absence of the capillary guides before reaching the ends of the capillaries. Any turbulence

Figure 3.15: Capillary Guide-Capillary Stopper Separation.
Reducing the 1mm separation to 100 μm better holds the capillaries in the centre of their channels.

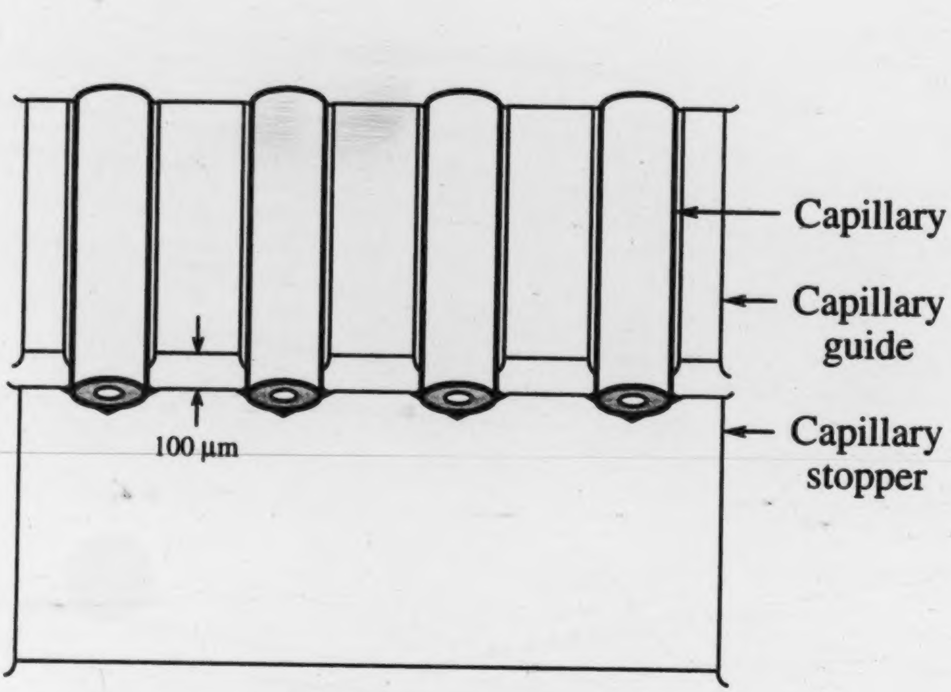
Capillary
Capillary guide
Capillary stopper
100 µm

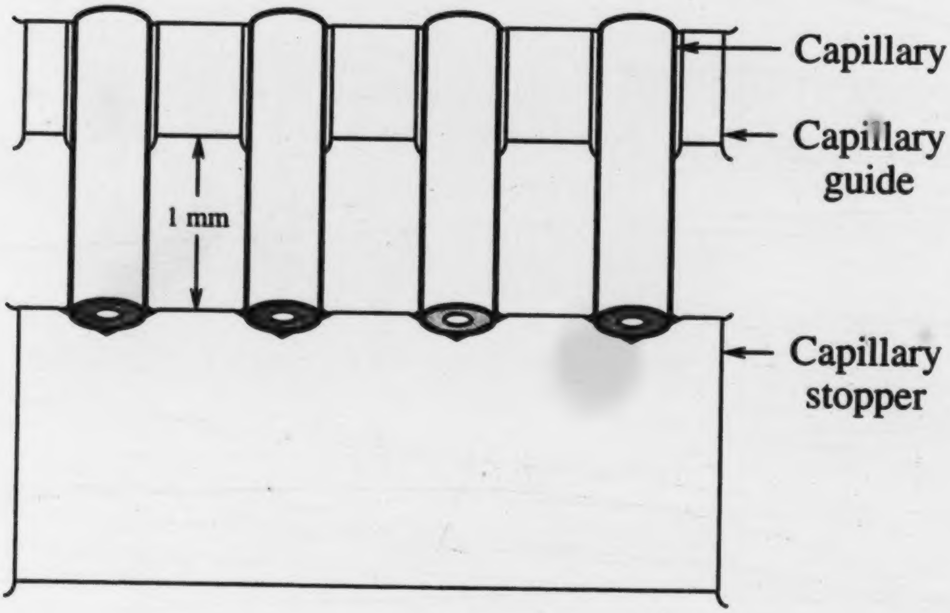
Capillary
Capillary guide
1 mm
Capillary stopper

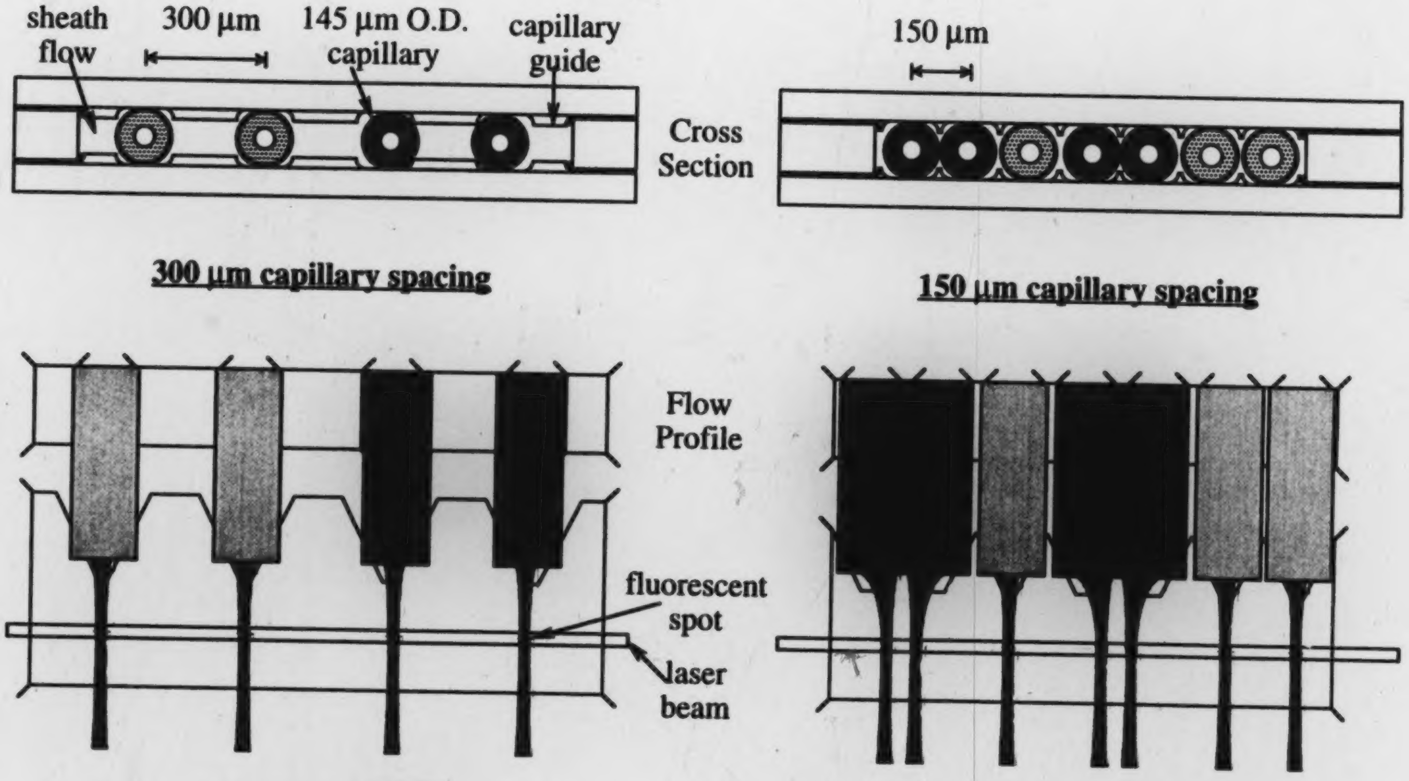
sheath flow
300 μm
145 μm O.D. capillary
capillary guide
Cross Section
150 μm
300 μm capillary spacing
150 μm capillary spacing
Flow Profile
fluorescent spot
laser beam
Centred capillary ▨
Off-centred capillary ■

Figure 3.16: Effect of Capillary Guide Spacing. 300 μm capillary spacing to left yields even and reproducible fluorescent spot spacing, while 150 μm spacing to right does not

generated at the ends of the capillary stoppers would have subsided by the ends of the capillaries, where the capillary flow is sheathed. The result, however, was that the capillaries, unguided for the last millimetre in the cuvette, would bend around their stoppers and proceed into the path of the laser beam. The capillary guides were thus brought to 100 μm from the capillary stoppers, which fixed the capillaries so that they were not able to circumvent the stoppers; no turbulence was observed in the sheath flow with the lower capillary guides.

Second, changing the capillary spacing by means of changing the capillary guide width is shown in Figure 3.16, the effect of which is quite dramatic. At 150 μm spacing, the capillaries (nominally 150 μm OD but typically ~ 145 μm OD) are very close to each other, and the fluorescent spot pattern beneath the capillaries is uneven since the spots do not fall directly beneath the capillaries. The spot pattern is also irreproducible: from one run to the next, the old capillaries are exchanged for new ones, and a different uneven spot pattern results. If the intercapillary distance is increased to 225 or 300 μm, the spot spacing becomes regular and reproducible, more so at 300 μm. Such spacing is crucial, as the cuvette is to be used as the detection cell in a high-throughput capillary electrophoresis DNA sequencing instrument, and if the location of the spots is not reproducible, the detection optics must be realigned each run. The effect of capillary spacing on spot spacing is demonstrated in the photographs of Figure 3.17.

The cause of more even and reproducible fluorescent spot spacing may be rationalised if one considers the magnitude of sheath flow involved. While the micromachined features in these cuvettes are designed to perfectly fix the position of each capillary in the centre of its channel, the latter are still capable of some movement, perhaps ± 5 μm. With all the capillaries evenly spaced, the area available for sheath flow (and hence the sheath flow itself) on either side of a

Figure 3.17: Photo of Evenly and Unevenly Spaced Capillaries in Cuvette.
Top photo shows a cuvette with 150 μm OD capillaries spaced 225 μm apart and evenly spaced fluorescent spots in laser beam beneath.
Bottom photo shows a cuvette with only 150 μm spacing for the 150 μm OD capillaries; the fluorescent spots beneath are not evenly spaced, nor reproducibly spaced from run to run.

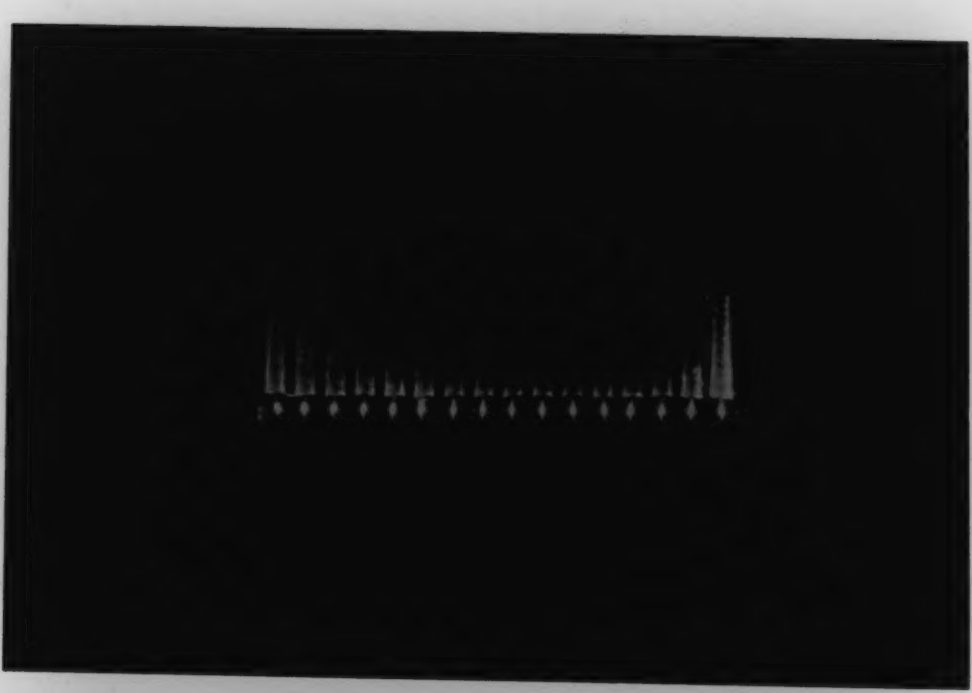

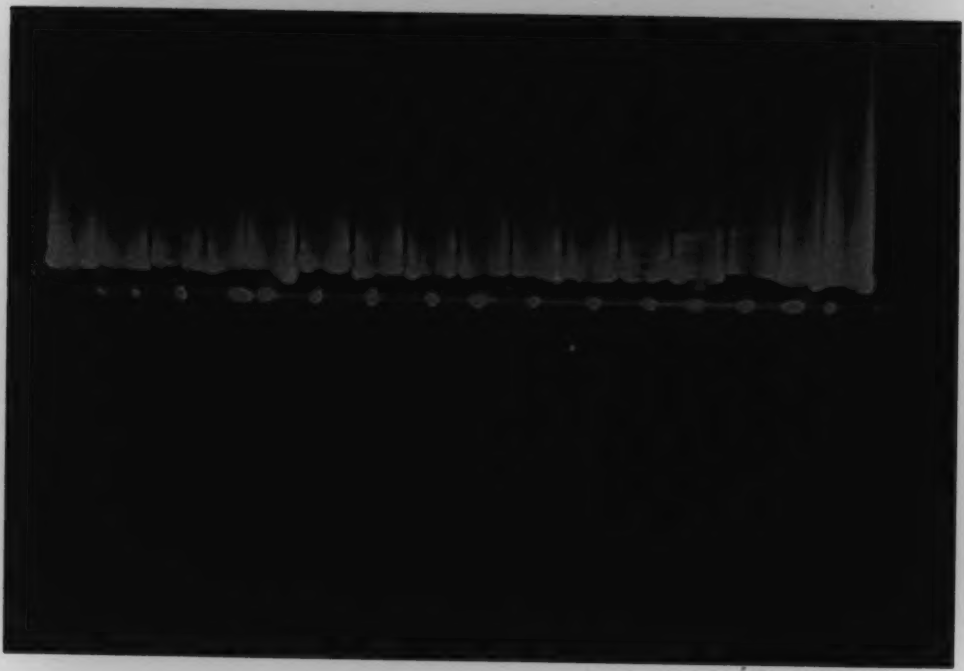

capillary is equal, and the spots should fall directly beneath the capillaries. If two capillaries pinch together, however, the area between them (*inner* area) decreases, while that between each of them and their nearest neighbours (*outer* area) increases. With 145 μm O. D. capillaries spaced 150 μm apart, two capillaries each moving 2.5 μm towards each other makes the outer area 1.55 times greater than the inner area, whereas for the same capillaries spaced 300 μm apart, the factor is only 1.07. Thus by increasing the capillary spacing, the relative change in inner/outer sheath flow decreases, and so spot spacing is less susceptible to small capillary movements.

3.3.2-C Cover Slips, Guides

Figures 3.18 and 3.19 illustrate the effect of varying cover slip thickness and of using cover slip guides, respectively. As shown in Figure 3.18, the thickness of the cover slips determines whether and how well the patterned features inside the cuvette control the position of the capillaries. A series of cuvettes was fabricated with cover slip thicknesses ranging from 125 μm to 155 μm, and the optimum thickness was found to be 135 μm or 140 μm. At this thickness, there is sufficient room for the capillaries so that they may be easily inserted into the cuvette, yet the fit is snug enough so that the capillaries are fixed in the centres of their channels and are forced into a linear array (ie: a straight line can pass through all the capillary axes). With thicker cover slips, the capillaries have room to move from their designated position. It is crucial that capillary spacing be regular and reproducible for detection optics, as previously mentioned, but it is also crucial that the capillaries be held in a linear array so that the laser beam (which generates fluorescence) may intersect all the capillary simultaneously.

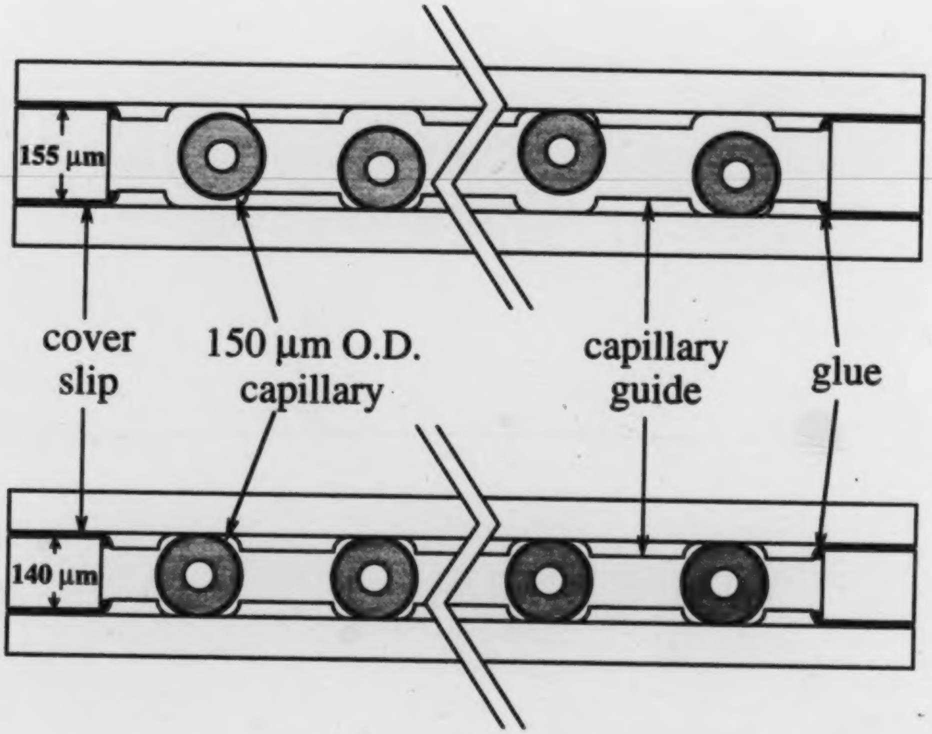
155 µm
cover slip
150 µm O.D. capillary
capillary guide
glue
140 µm

Figure 3.18: Cover Slip Thickness.

Excessively thick cover slips render the micromachined features incapable of positioning the capillaries. With capillaries fitting snugly in the cuvette, as seen with the use of 140 µm thick cover slips, micromachined features are effective.

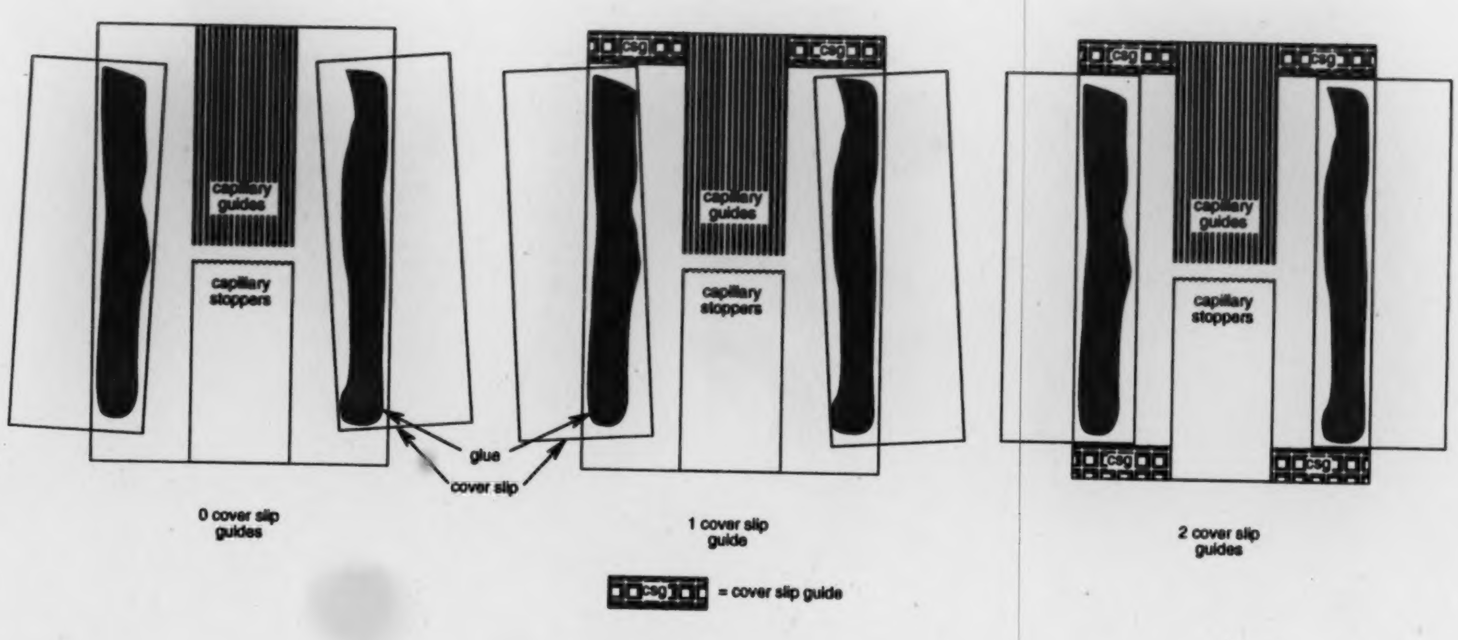
capillary guides
capillary stoppers
glue
cover slip
0 cover slip guides
csg
1 cover slip guide
2 cover slip guides
csg = cover slip guide

Figure 3.19: Cover Slip Guides.
Use of 2 cover slip guides per cover slip significantly aids in cuvette assembly by keeping the cover slips aligned during cuvette assembly; this benefit is not realised with 0 or 1 cover slip guide per cover slip.

The use of cover slip guides, shown in Figure 3.19, is merely to facilitate cuvette assembly. The cover slip guides are patterned exactly 21.000 mm apart, 21.050 mm after etching. The cover slips are cut with the wafer dicing saw to 21.00 ± 0.01 mm, so once in their groove, the cover slips cannot rotate and can only move closer into position beside the capillary guides and stoppers until they come into contact with the latter. Without these guides, cover slips often rotate, spreading glue into the centre of the cuvette - an assembly failure.

3.3.2-D Aspect Ratio

Aspect ratio is (horizontal etching rate):(vertical etching rate). In Figure 3.20, the two successful aspect ratios of the seven tried are depicted. To produce the same feature, in this case a 25 μm-wide capillary guide, under different conditions yielding different aspect ratios, it is necessary to provide different mask dimensions. Given a 25 μm depth of etch, a 1:1 aspect ratio dictates that the mask and hence the metal and photoresist layers on the substrate should extend 25 μm beyond the desired dimensions of the end product; for a 2:1 aspect ratio, the same depth of etch requires the mask to be 50 μm oversized to produce the "same" result. The result is not truly identical for both cases - the curvature depends on the aspect ratio - but performed equally well for our purposes.

Ideally, the aspect ratio observed in amorphous glass should be 1:1 = (horizontal etch rate) : (vertical etch rate), as the hydrofluoric acid should etch in all directions equally[15]. If, however, the metal and photoresist masking layers do not adhere well to the glass substrate, then HF is allowed between the glass and metal, enhancing the lateral etch rate, yielding a high aspect ratio. The two methods of metal deposition, evaporation and sputtering, tended to produce different results in terms of the aspect ratio observed in the subsequent etch, which is likely a function of the quality of the deposited metal layer(s). Typically,

Figure 3.20: Aspect Ratio Observed During Etching.
As examples, aspect ratios of 1:1 and 2:1 = (horizontal etch):(vertical etch) are illustrated. Note that the masking features have purposely been adjusted to yield approximately the same features: the larger the aspect ratio generated by various patterning conditions, the wider the mask shape needed to produce the desired feature.

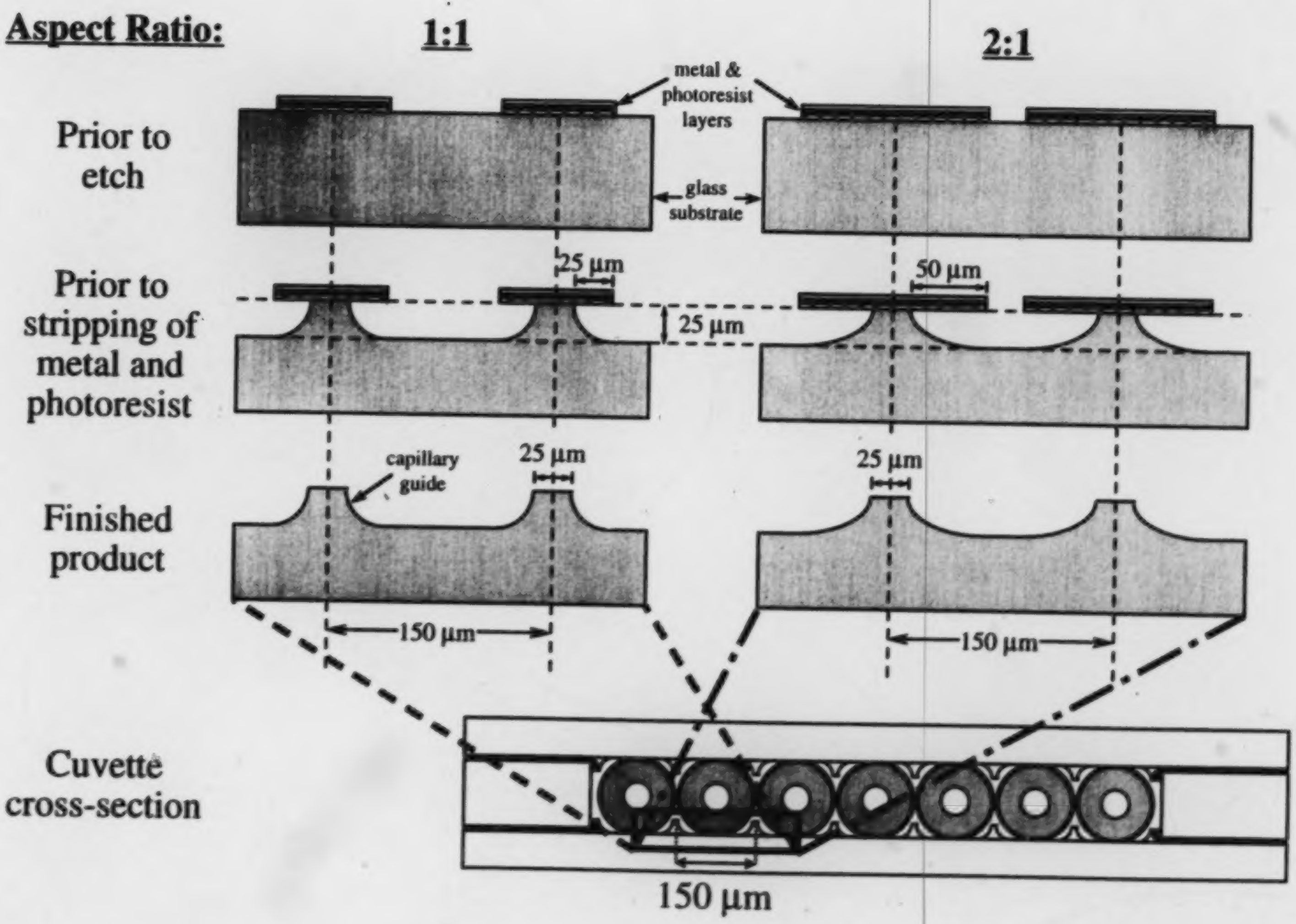
Aspect Ratio:
1:1
2:1
metal & photoresist layers
glass substrate
Prior to etch
Prior to stripping of metal and photoresist
25 µm
50 µm
25 µm
Finished product
capillary guide
25 µm
25 µm
150 µm
150 µm
Cuvette cross-section
150 µm

evaporated metal layers led to a 2:1 aspect ratio, while sputtered layers were closer to the ideal 1:1 ratio. Metal layers were sputtered whenever equipment allowed.

3.4 Conclusions

Over the last three years, 33 micromachined cuvette features (listed in Table 3.3) were implemented in 74 different cuvette designs housing from 1, 6, 8, 16, 32 or 48 capillaries, and the refinements made through an iterative design-build-test loop have allowed the production of a 16 capillary cuvette (1:1 aspect ratio, 300 μm capillary spacing, one-shelf with Vs (slope of 2) as capillary stoppers, 2 cover slip guides per cover slip, 140 μm thick cover slips, tapered capillary guides ending 100 μm above the capillary stoppers, Pyrex #7740 etched pieces, non-Pyrex glass coverslips). This cuvette is in regular use in the multicapillary DNA sequencer described in Chapter 2. 32, 48 and single capillary cuvettes were produced and integrated as the detection cells in other capillary electrophoresis instruments variously applied to DNA and protein separations in our lab.

Methodologies have been developed for glass pre-treatment, photolithography and aqueous hydrofluoric acid etching, cuvette assembly, cutting, and polishing, to allow low cost batch production of these sheath flow cuvettes.

3.5 References

1. F. T. Gucker, Jr., C. T. O'Konski, H. B. Pickard and J. N. Pitts, Jr, *Journal of the American Chemical Society* **69,** 2422 (1947).
2. P. J. Crosland-Taylor, *Nature* **171,** 37 (1953).
3. J. A. Steinkamp, M. J. Fulwyler, J. R. Coulter, R. D. Hiebert, J. L. Horney and P. F. Mullaney, *Review of Scientific Instruments* **44,** 1301 (1973).
4. J. A. Steinkamp, *Review of Scientific Instruments* **55,** 1375 (1984).
5. L. W. Hershberger, J. B. Callis and G. D. Christian, *Analytical Chemistry* **51,** 1444 (1979).
6. T. A. Kelly and G. D. Christian, *Analytical Chemistry* **54,** 1444 (1982).
7. Y. F. Cheng, S. Wu, D. Y. Chen and N. J. Dovichi, *Analytical Chemistry* **62,** 496 (1990).
8. N. J. Dovichi, *Review of Scientific Instruments* **61,** 3653 (1990).
9. F. Zarrin and N. J. Dovichi, *Analytical Chemistry* **57,** 1826 (1985).
10. J.-Y. Zhao, J. Labbe and N. J. Dovichi, *Journal of Microcolumn Separations* **5 (4),** 331 (1993).
11. Y.-F. Cheng and N. J. Dovichi, *Mikrochimica Acta* **III,** 351-357 (1986-7?).
12. Y.-F. Cheng and N. J. Dovichi, *Canadian Journal of Spectroscopy* **34 (3),** 70-75 (1989).
13. Z. H. Fan and D. J. Harrison, *Analytical Chemistry* **66,** 177 (1994).
14. *Laboratory Glassware Specifications Guide*; Corning Glass Works, Corning, New York, 1985.
15. W. Kern and C. A. Deckert, *Chemical Etching*; Academic Press: New York, 1978.

Chapter 4

CONCLUSIONS AND FUTURE DIRECTIONS

4.1 Conclusions

This thesis has demonstrated the design, construction and performance of a 16 capillary DNA sequencer, as well as of a variety of multicapillary, micromachined sheath flow cuvettes, one of which was integrated into the sequencer as its detection cell.

With regard to sheath flow cuvettes, a reproducible methodology for their manufacture has been developed. An iterative design process spanning three years has allowed experimentation with some 33 cuvette micromachined features all with the objective of yielding a cuvette which would reproducibly fix capillaries in a linear, evenly spaced array within. When integrated into a multicapillary electrophoresis instrument using laser-induced fluorescence detection, such a cuvette affords a real advantage in conserving optical alignment between the capillaries' fluorescent spots and their detectors. A 16 capillary sheath flow cuvette with features refined by iteration as described in Chapter 3 was used in the DNA sequencer described in Chapter 2; other micromachined cuvettes have been made for and are in use in a 32 capillary DNA sequencer under development and a single capillary CZE instrument, both from this laboratory.

The DNA sequencer described in Chapter 2 is capable of simultaneous, 4 colour, 16 capillary DNA sequencing, and of ~ 10^3 - 10^4 molecules or ~ 10^{-11} M detection limits. The instrument can be described as a 16 capillary gel electrophoresis DNA sequencer with laser-induced fluorescence detection in a sheath flow cuvette using two laser-, four spectral filter-discrimination for the four ABI dye system. Fluorescence detection is by means of optically aligned GFIN lenses connected by optical fibres to individually optimised avalanche photodiodes and associated amplification and filtration electronics. Data are acquired sequentially across the 16 capillary array with a programme written in-house to maximise fluorescence intensity as well as noise filtration.

4.2 Future Directions

The methodology developed for micromachining sheath flow cuvettes could be applied to other areas of microfabrication, such as electrophoresis separation chambers, T-connectors for capillaries, reaction mixing chambers, etc. Additionally, etching protocols for sheath flow cuvettes made of quartz could be developed for applications using other areas of the spectrum where Pyrex absorbs, but quartz does not[1, 2].

The instrument is currently being used by Sue Bay to sequence the genome of the bacteriophage M13 wild-type; several modifications have already been made or begun to enhance its performance in this capacity, and several shortcomings in performance have surfaced. In order to increase the denaturing environment of the capillary and reduce the number of compressions[3, 4], as well as reduce separation time, the capillaries are thermostated with an air circulation system at 40 °C. Multiple capillary sample injection using gold-plated microtiter plates and pressurised refilling of capillary gels have also begun to be studied, and are described briefly next. A brief perspective on the instrument's shortcomings and possible solutions are then offered, followed by a look at other approaches being pursued for multicapillary sequencing in this group.

A high throughput sequencer will require an efficient manner of sample injection. Sixteen different samples, to be injected one on each capillary, may be injected in series by the method of section 2.2.1, requiring $\geq 16 \bullet 40$ s = ~ 11 min., or in parallel from a microtiter plate, in the time of one sample. A microtiter plate is a ~ 5 X 10 cm plastic plate with a 8 X 12 array of ~ 5 mm wells, each used to hold a small volume (< 0.5 mL) of solution. With its surface plated with gold, the microtiter plate can serve as a 16 sample injection container and electrode in the following manner. 16 DNA samples may be pipetted into 16 wells of the microtiter plate, and a capillary inserted into each of the wells used. If a potential is applied to all the samples simultaneously, then the time required for the injection of 16 samples is identical to that for one sample. This protocol is obviously an advantage to the experimentalist, since both the time (decreasing from about 15 minutes to 40s) and repetitive nature of sample injection are reduced sixteen-fold, but the protocol also reduces the effect of diffusional broadening incurred over a lengthy injection. The benefit of the gold plate is that the electrical connection for all 16 samples may be made with a single electrode connected to the gold surface of the plate either directly with a metal to metal connection, or by inserting the electrode in one of the solutions of the microtiter plate. The plate as an electrode obviates the need for 16 electrodes having to be precisely aligned to come into contact with small sample volumes in each of the different microtiter plate wells.

Refillable gels in the capillaries would offer the advantage of not having to replace capillaries for each run. This would result in a savings of ~ 30 minutes required to insert and seal the 16 capillary array into the cuvette for each set of samples. The process of refilling the capillaries itself would perhaps take as long, but would not be demanding in terms of time or skill; a simple plumbing connection to the injection ends of the capillaries from a pressurised container of the gel solution should suffice to allow fresh gel to be pumped in, replacing the old gel. Another benefit of the refillable gel approach is that a single batch of gel could be prepared and used over many sequencing runs, which would help to overcome inconsistencies presently observed in gel quality from run to run (since each run requires a new gel preparation). Also, the cost per run would be less, since fewer gel reagents and capillaries would be required.

An idea of equal merit to refillable gels would be to develop a gel which was reusable for a number of runs. This would allow for the least time loss between runs and hence the highest throughput, and would otherwise yield all the gains of refillable gels.

As mentioned in section 2.3.2, good quality DNA sequencing runs effected on all 16 capillaries simultaneously have been difficult to reproduce, as witnessed in the M13 project. In particular, certain capillaries' electropherograms have weak signals or poor resolution, and cannot be base-called to an adequate read length or degree of accuracy. It is thought that improving sensitivity will likely reduce *both* problems of weak signals and poor resolution. Assuming that the detectors are achieving their maximum sensitivity *electronically*, as shown in the APD biasing procedure (see section 2.3.1.B), and that this sensitivity is comparable to that of an SPCM detector used in Zhang's instrument[5] (see section 2.2.5.B), then the two order-of-magnitude difference in detection limits observed between this and Zhang's instrument (see section 2.3.1.A) must logically lie in the optical domain.

The suggested approach would be to first confirm the supposition of equivalent electronic sensitivity, and second to test optical components for their transmission performance and spatial alignment. The electronic equivalency could easily be verified by performing the sensitivity comparison of section 2.2.5.B, using an SPCM or PMT as a reference detector. Verification of the transmission of optical components would likely be a more involved process, but might again use an SPCM or PMT which could be detached from its optical fibre as a reference detector, and the flashing LED as the reference optical source. The signal generated by the LED could then be measured directly with a PMT, and with a PMT connected to a GRIN lens by optical fibre with an FC connection. A comparison of the signal intensities from these two arrangements would reflect directly on optical losses incurred through GRIN lenses, optical fibres and connectors. Spatial alignment of the GRIN lenses to the image of the 18 X lens could be investigated with a ray-tracing programme, as could the optical geometries of other imaging objectives which might have better collection efficiencies and produce a less distorted image surface.

Several of the more problematic or labour-intensive areas of instrument development seen in the construction of this instrument have been circumvented in other instruments currently being built in our laboratory. The 32 and 96 capillary DNA sequencers under construction both use CCD cameras for detection; the advantage lies in the ability to use software programming to select and bin camera pixels to capture the images of fluorescent spots. This replaces the use of individual GRIN lenses, APDs, amplifiers and low pass filters; the optical and electronic complexity of such an instrument is greatly reduced, and is hopefully replaced with far fewer new challenges in programming and non-magnifying optics.

4.3 References

1. *Laboratory Glassware Specifications Guide*; Corning Glass Works, Corning, New York, 1985.
2. R. H. Doremus, *Glass Science*; John Wiley and Sons: Toronto, 1973.
3. J. Z. Zhang, Y. Fang, J. Y. Hou, H. J. Ren, R. Jiang, P. Roos and N. J. Dovichi, *Analytical Chemistry* **67**, 4589-4593 (1995).
4. Y. Fang, J. Z. Zhang, J. Y. Hou, H. Lu and N. J. Dovichi, *Electrophoresis* **in Press** (1996).
5. J. Zhang, Ph.D., University of Alberta, 1994.

Appendix 1

FOUR COLOUR ELECTROPHEROGRAMS FROM A DNA SEQUENCING RUN

6

The electropherograms collected for capillaries 1-6 and 8-16 during a single DNA sequencing run on the same sample are displayed in this appendix. In section 2.3.2, the particulars of the run are described, and the electropherogram for capillary 7 is shown as an example to illustrate base-calling, read length and accuracy. The other 15 separations are included here to substantiate the claim of comparable resolution for all 16 separations.

Capillary 1; File: 26/01/96#1

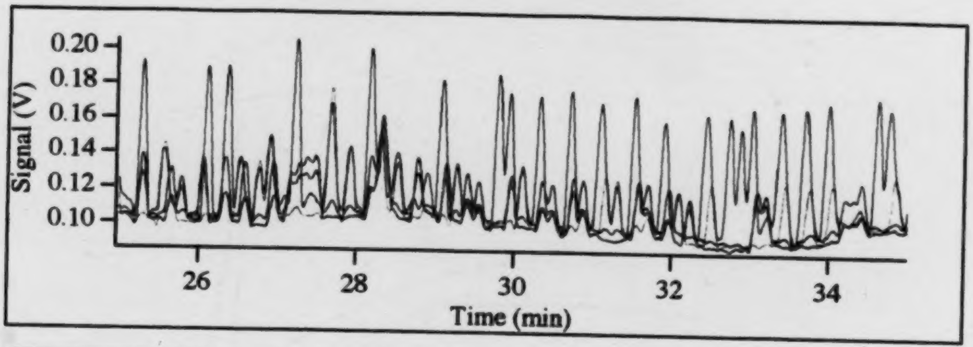

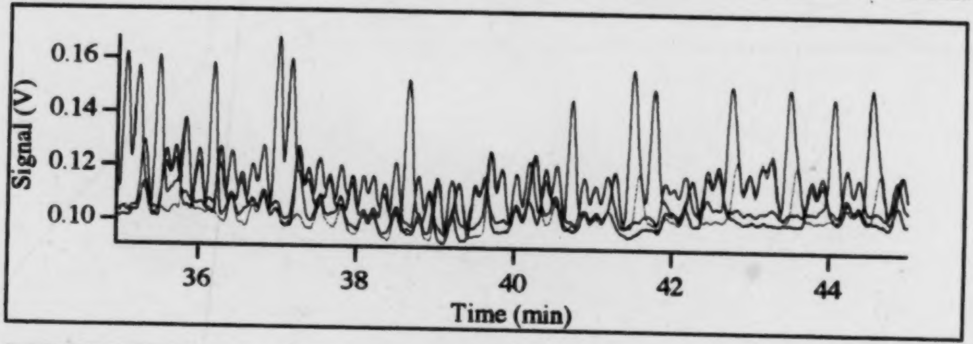

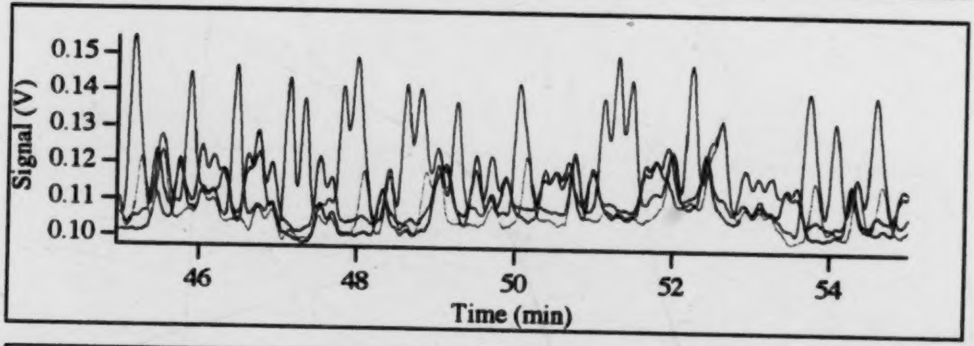

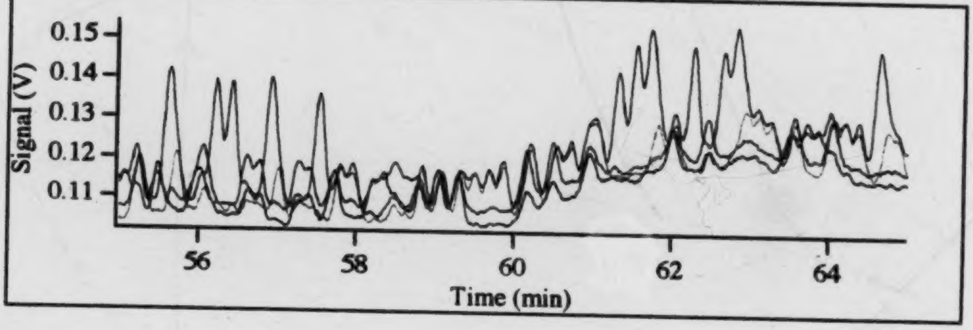

Capillary 1; File: 26/01/96#1

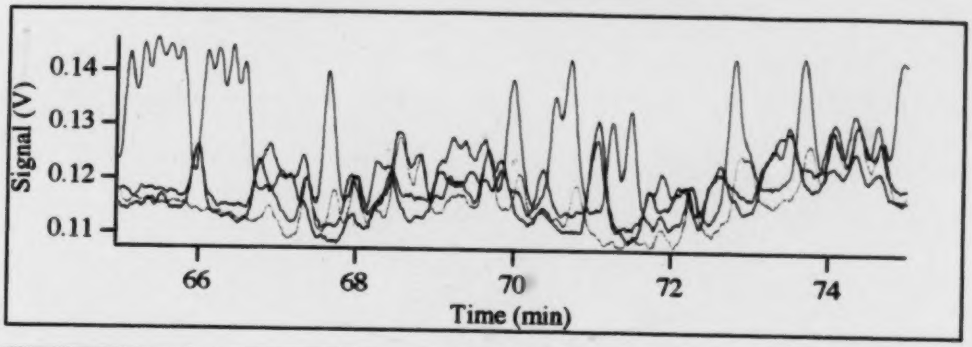

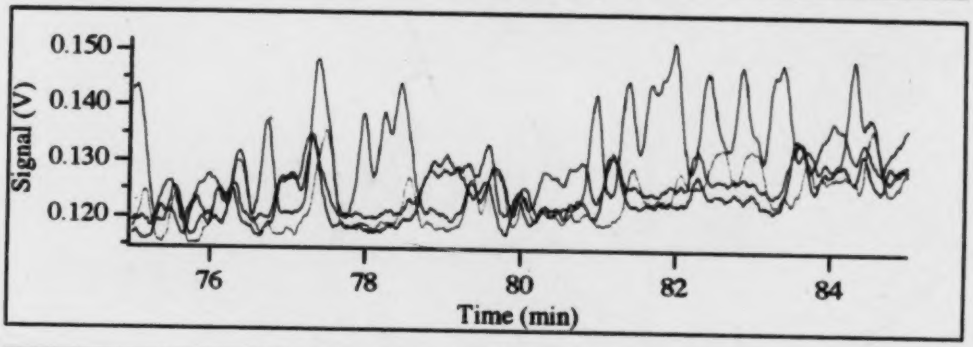

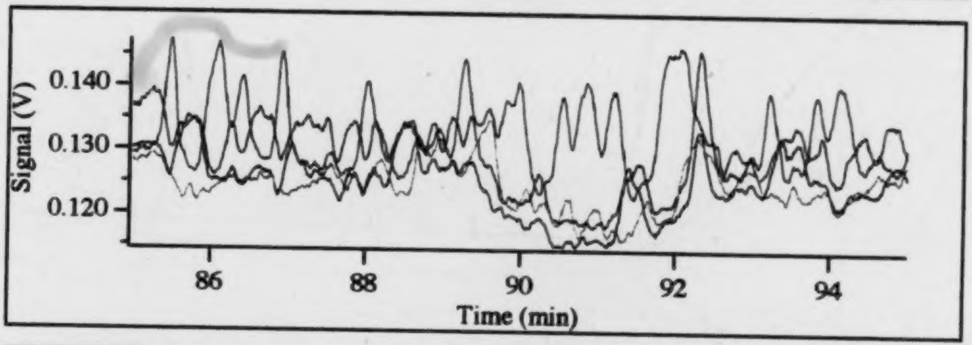

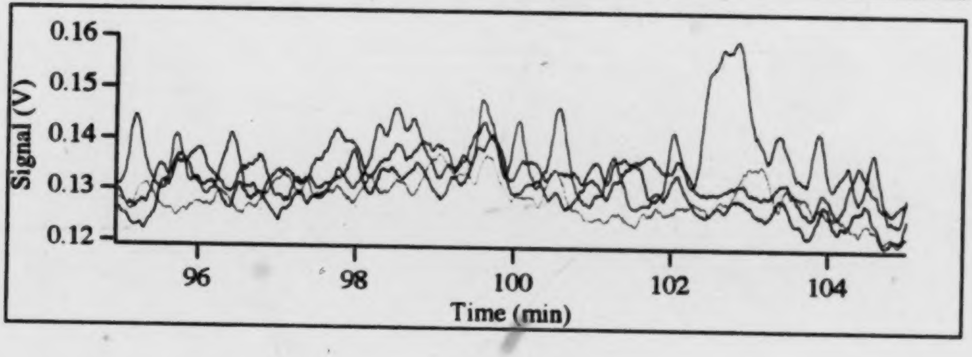

Capillary 2; File: 26/01/96#1

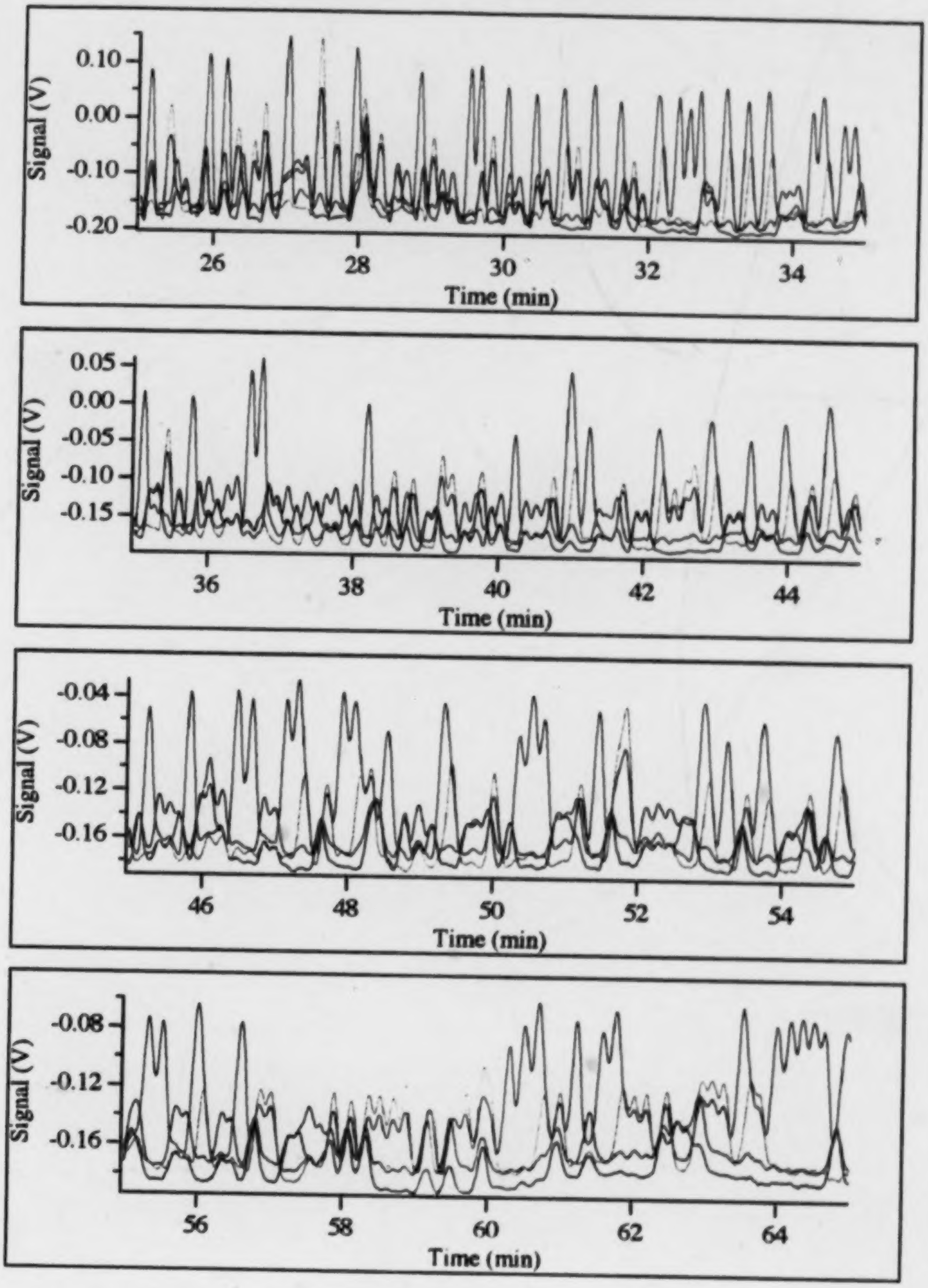

Capillary 2; File: 26/01/96#1

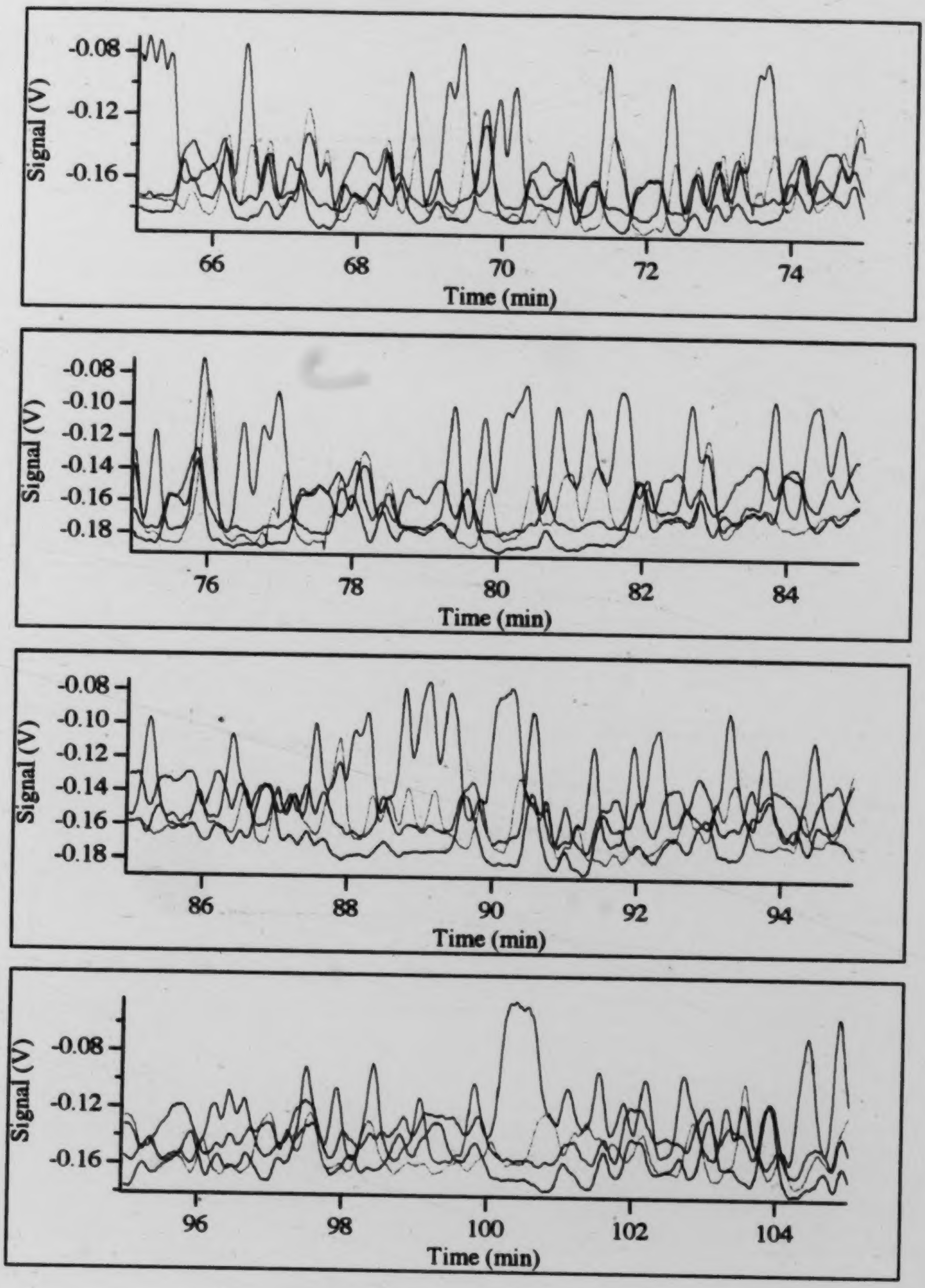

Capillary 3; File: 26/01/96#1

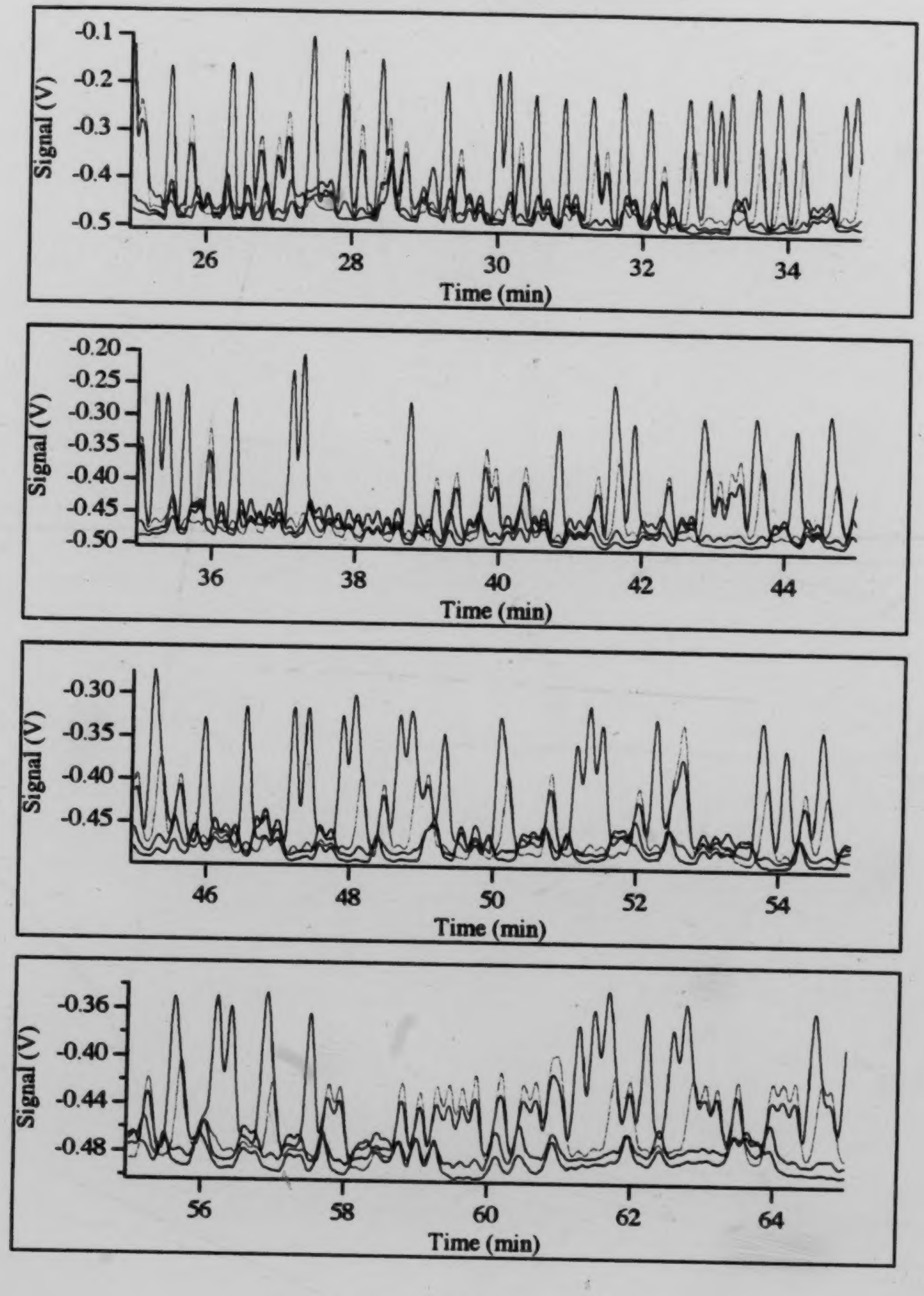

Capillary 3; File: 26/01/96#1

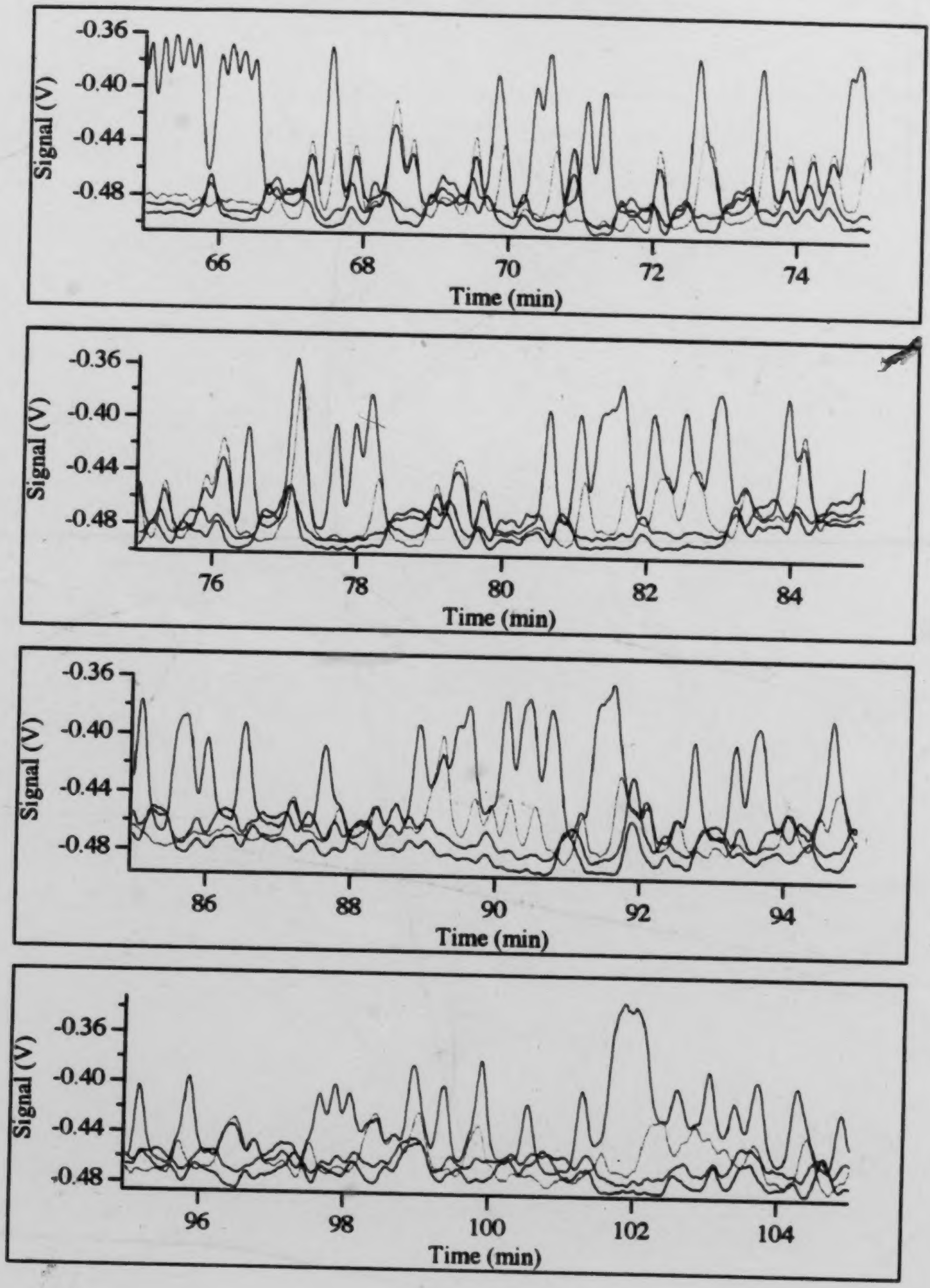

Capillary 4; File: 26/01/96#1

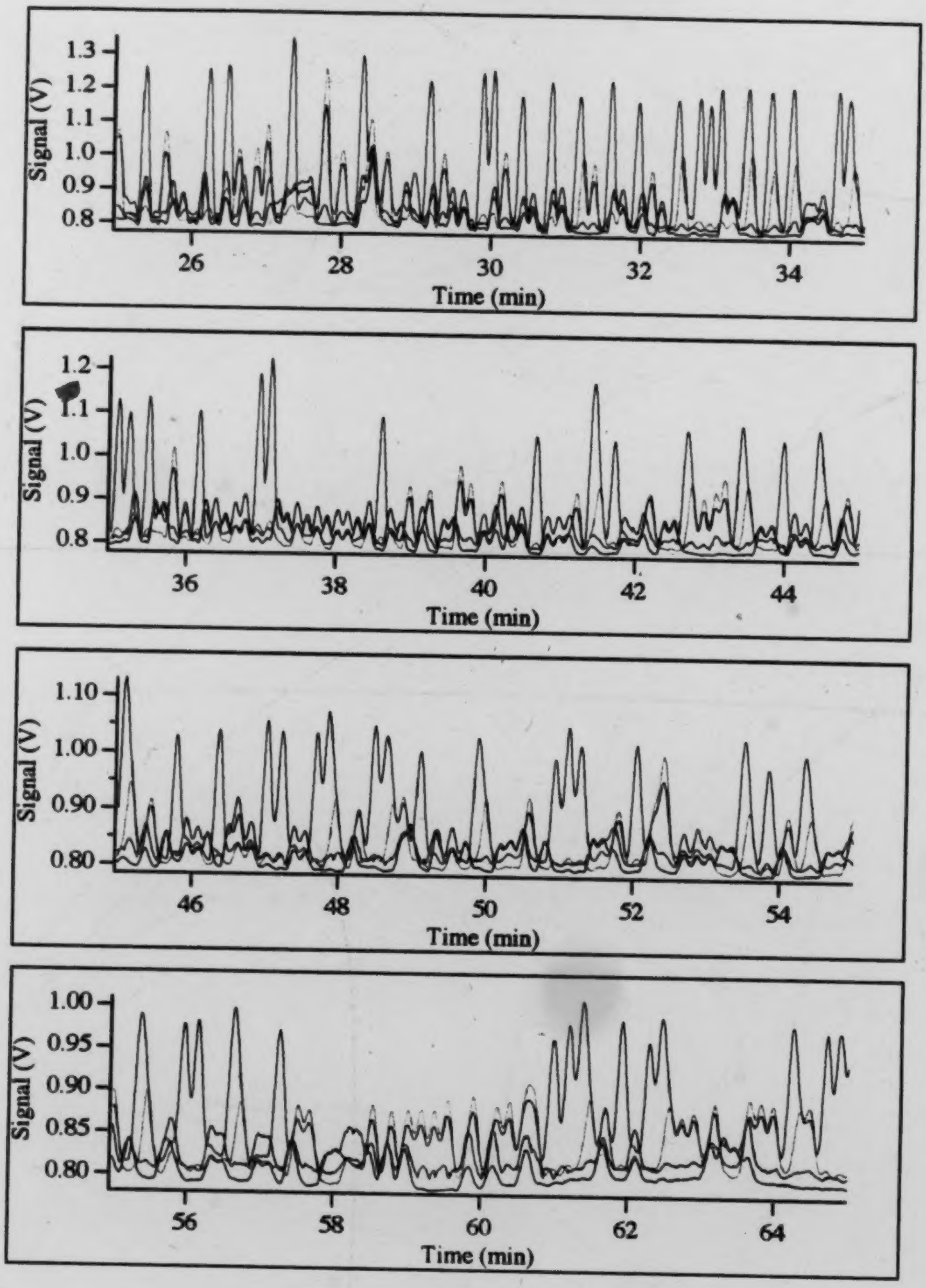

Capillary 4; File: 26/01/96#1

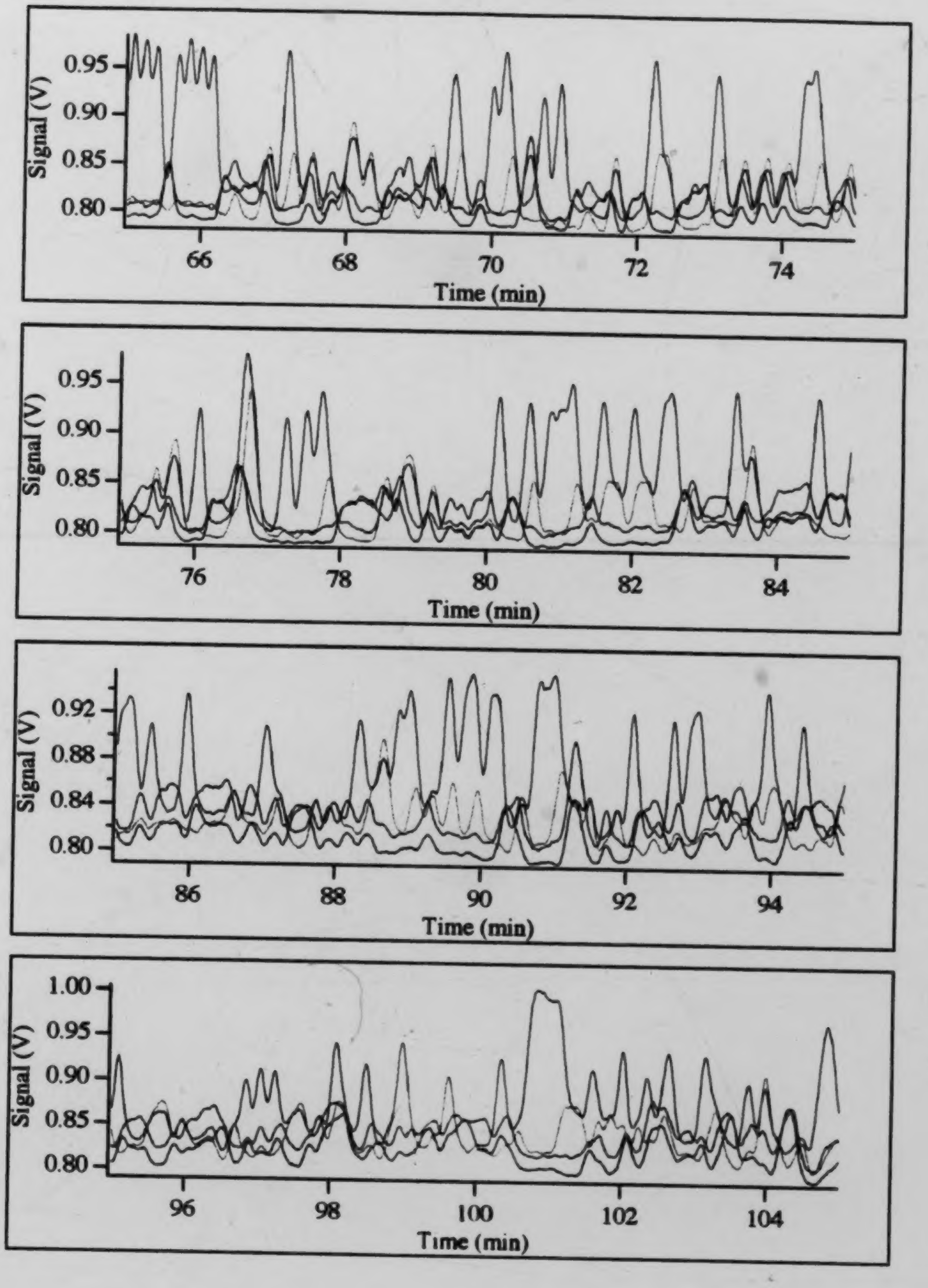

Capillary 5; File: 26/01/96#1

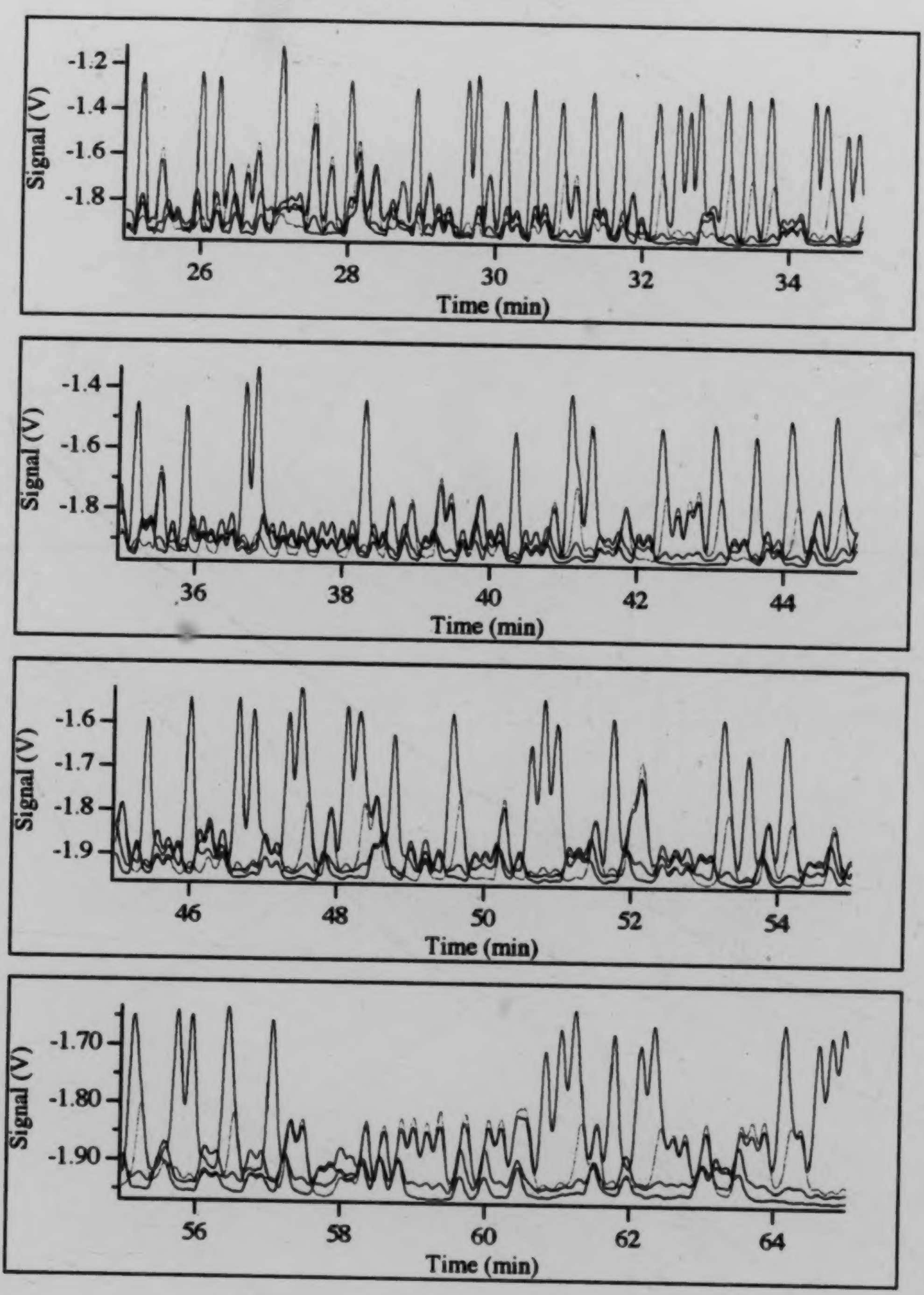

Capillary 5; File: 26/01/96#1

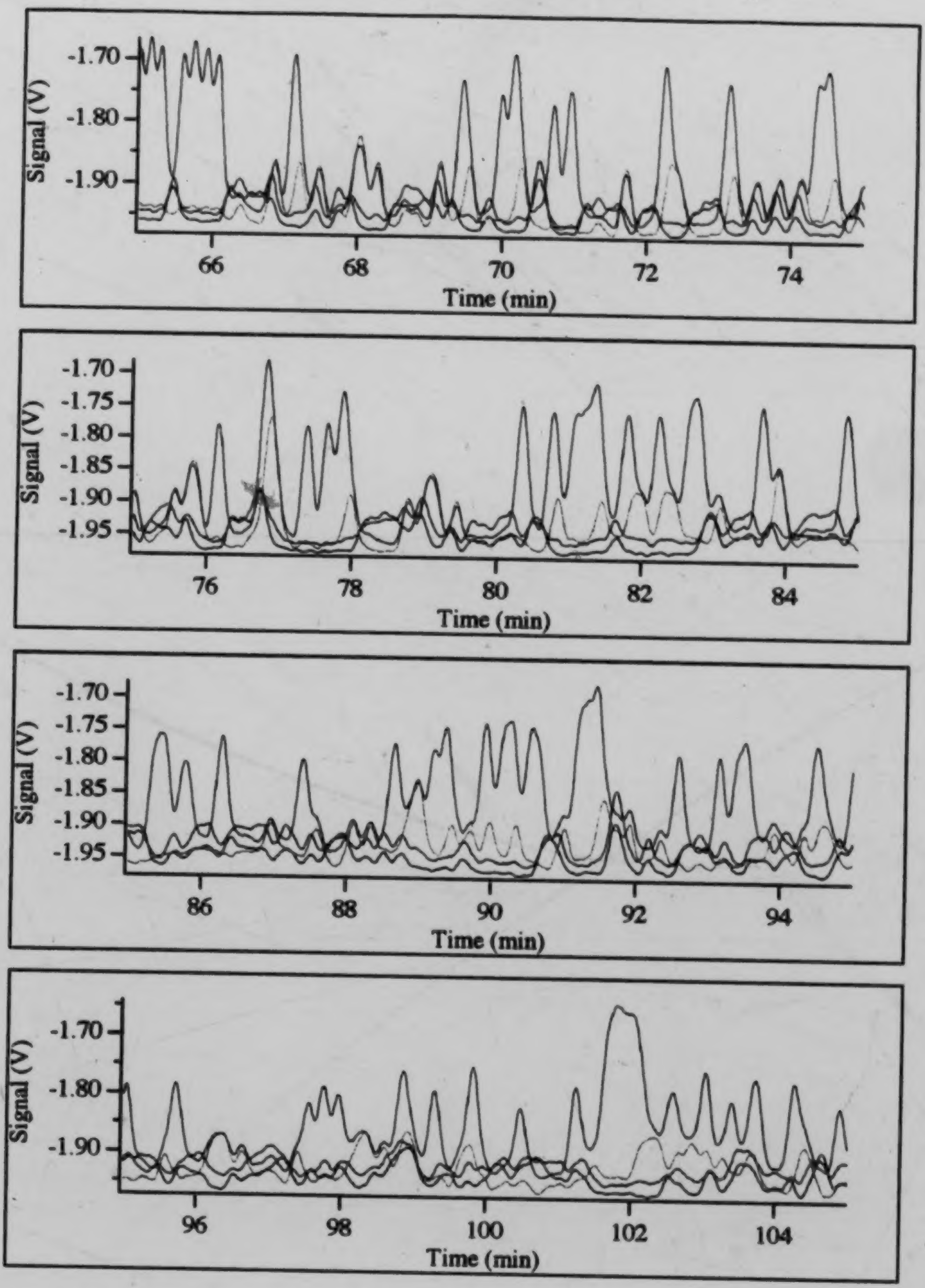

Capillary 6; File: 26/01/96#1

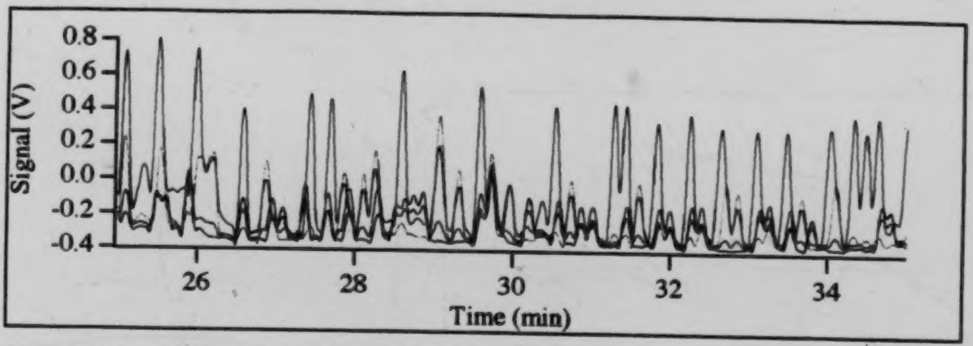

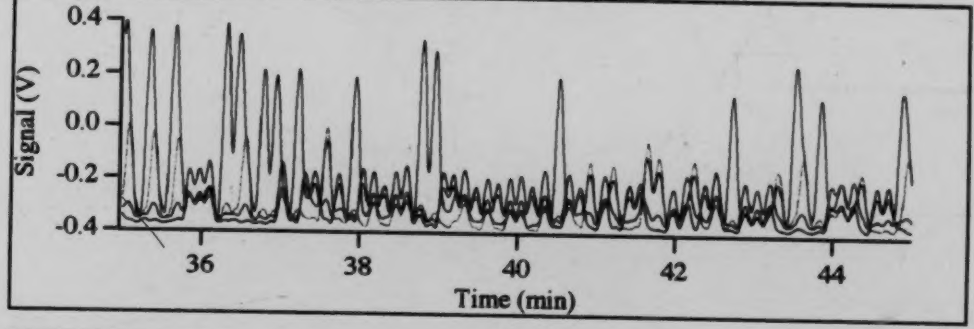

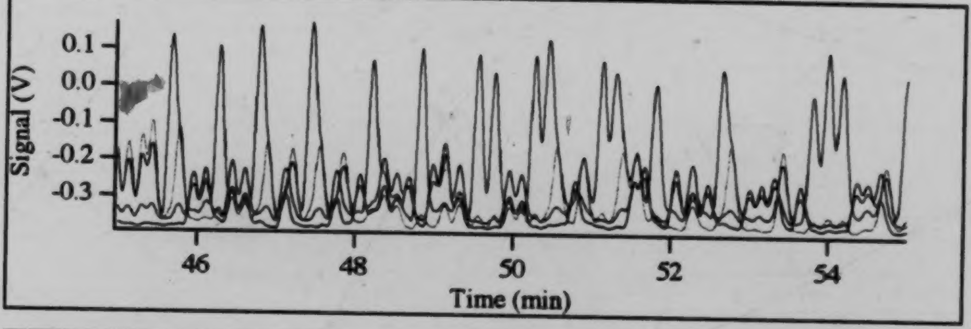

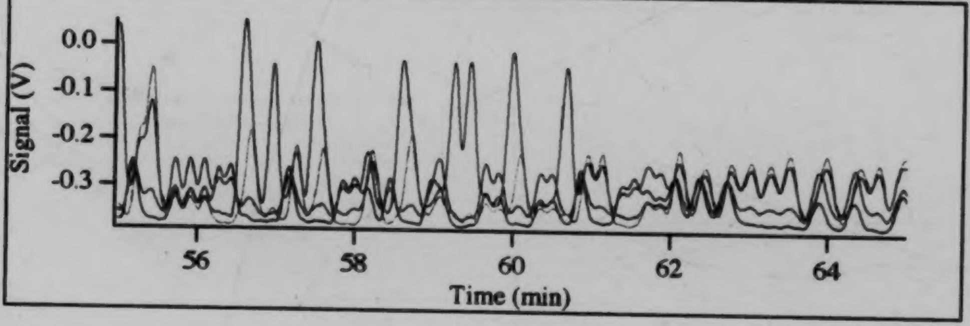

Capillary 6; File: 26/01/96#1

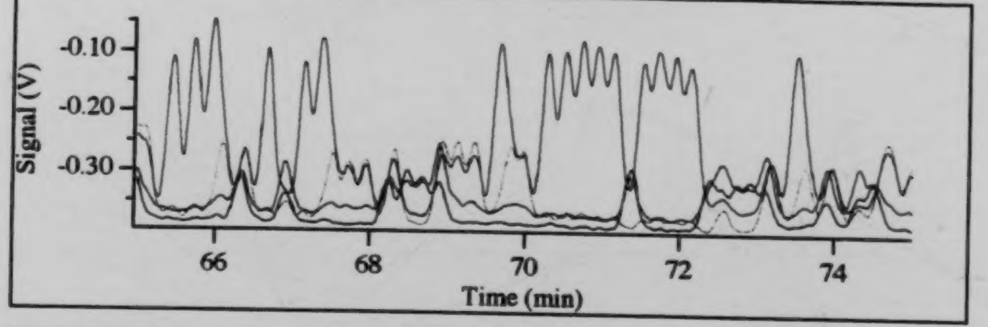

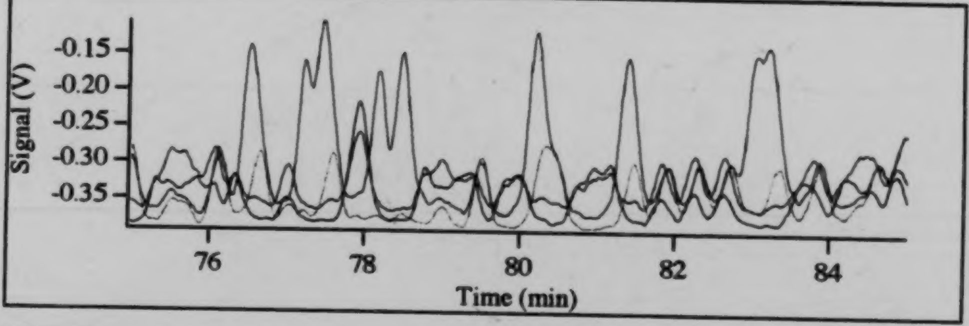

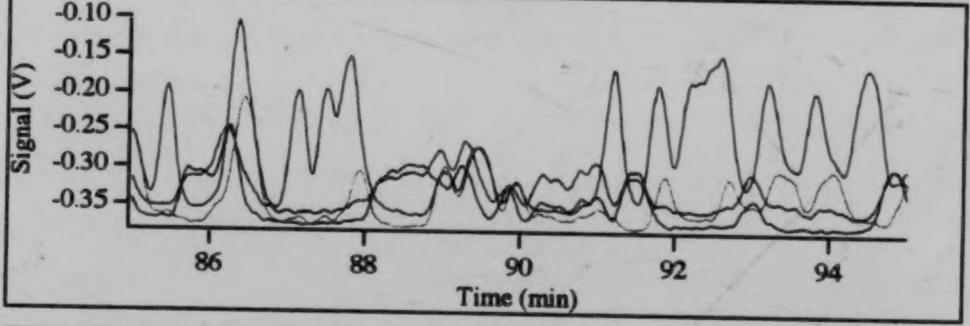

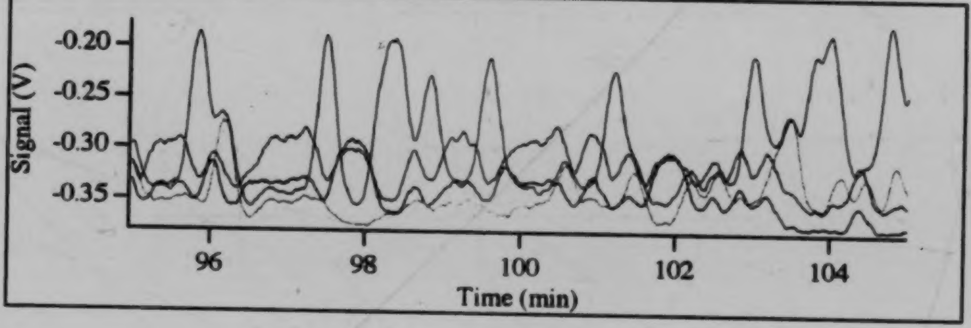

Capillary 8; File: 26/01/96#1

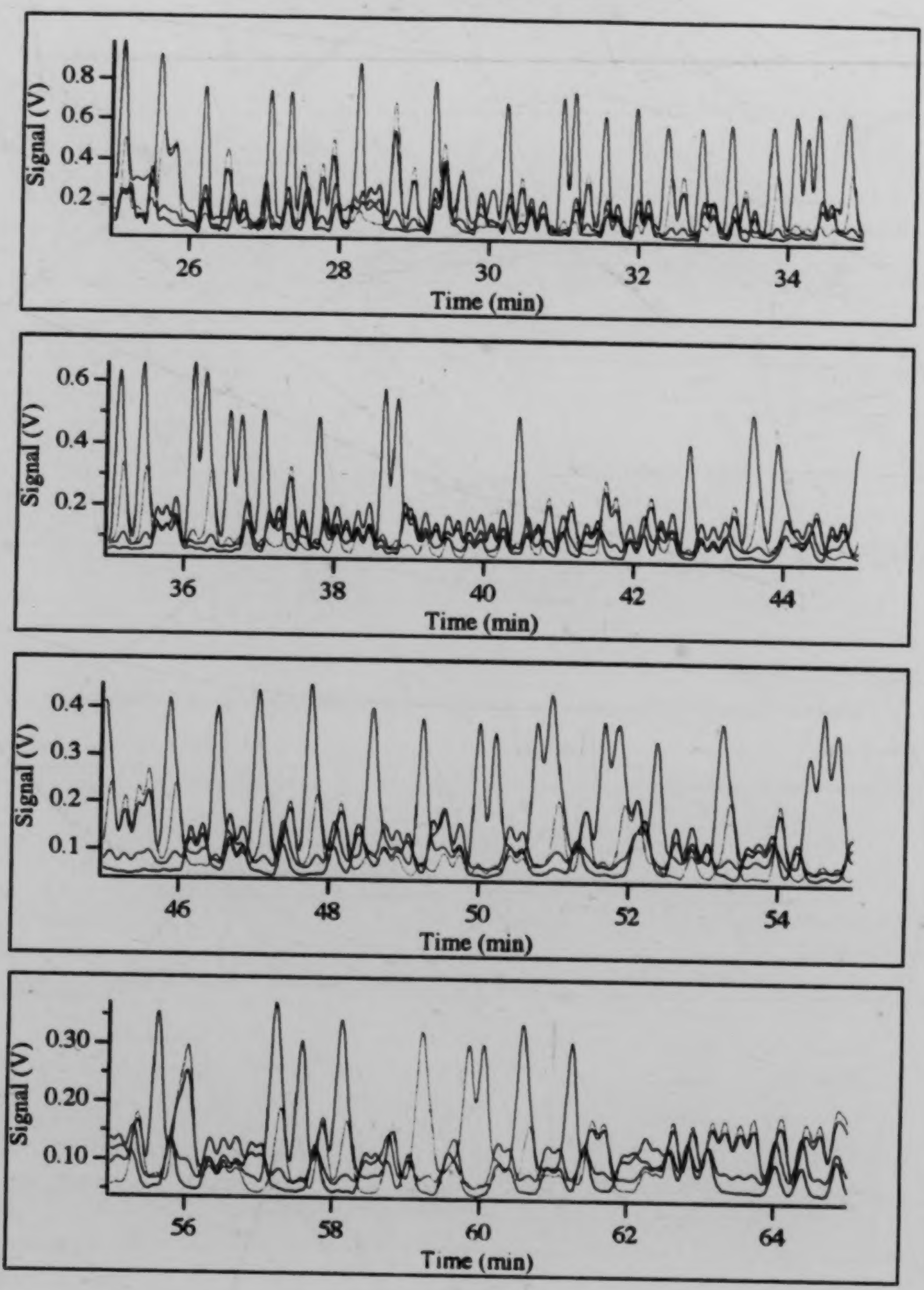

Capillary 8; File: 26/01/96#1

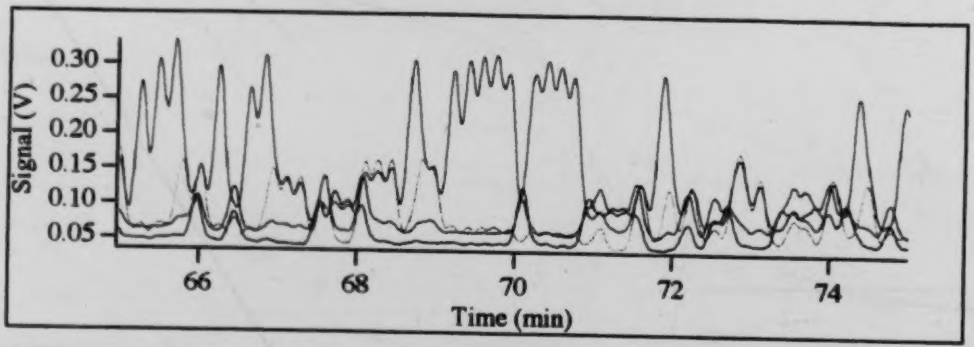

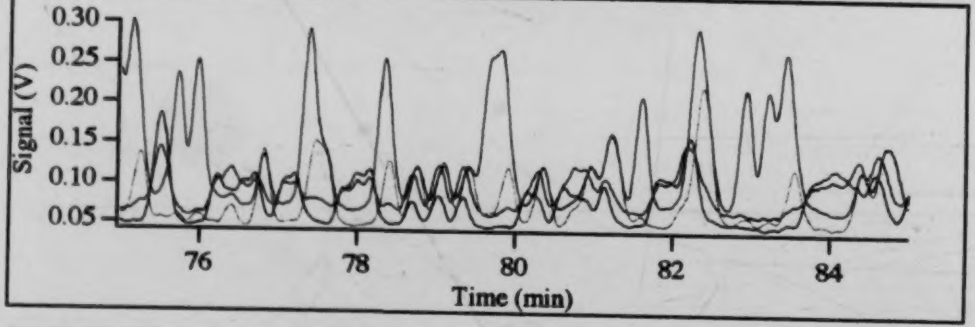

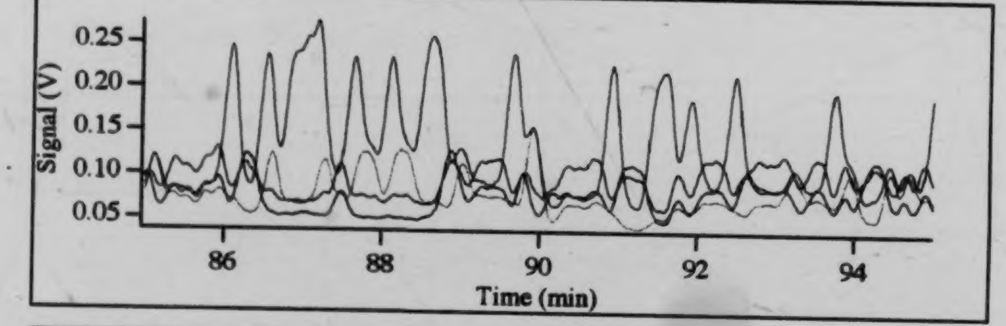

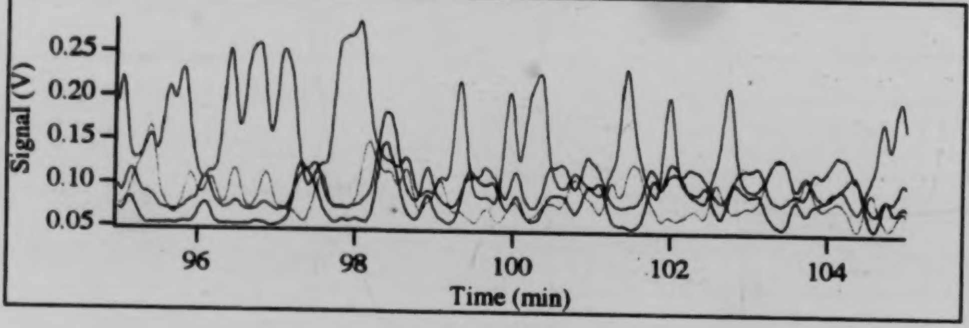

Capillary 9; File: 26/01/96#1

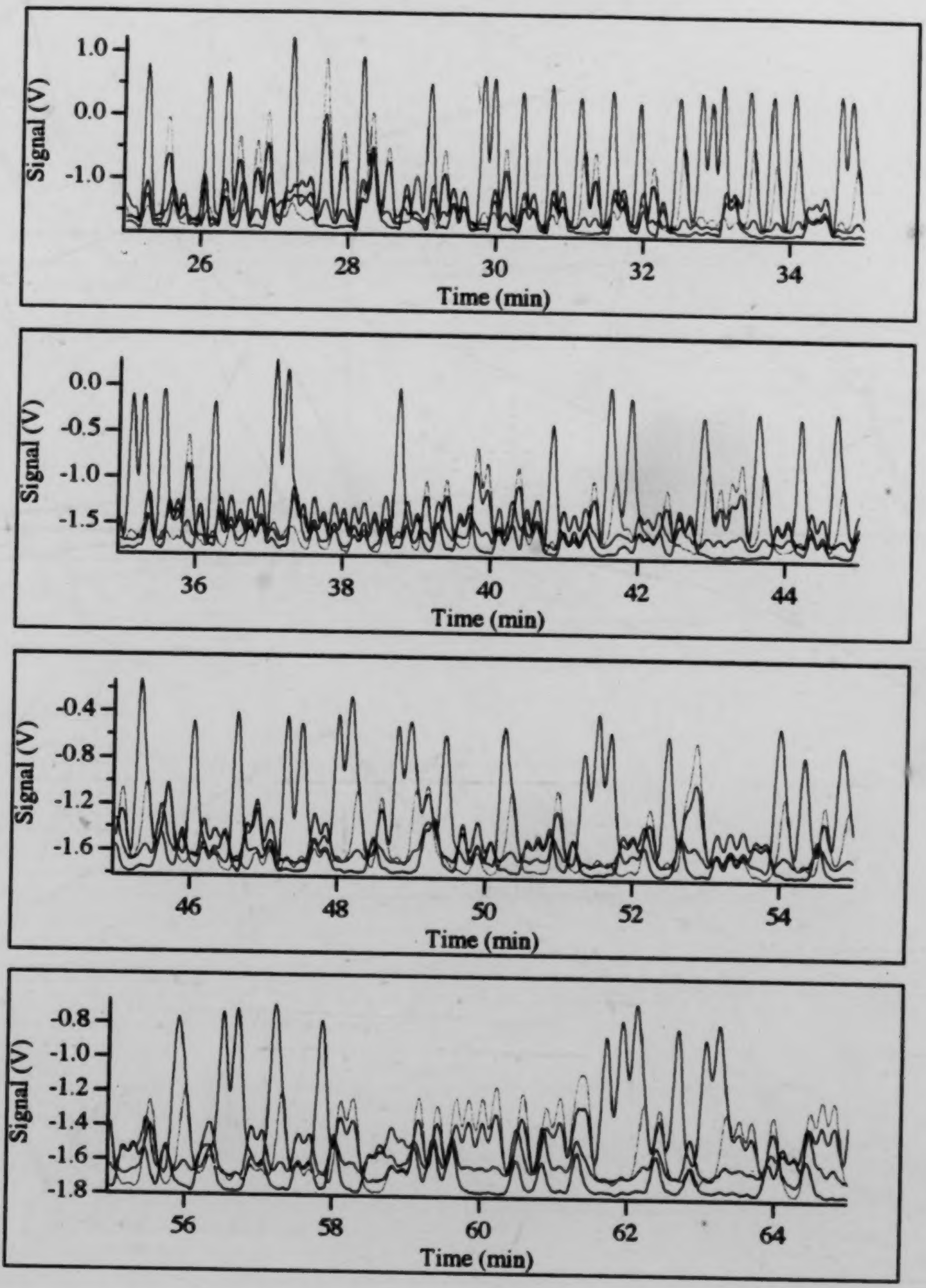

Capillary 9; File: 26/01/96#1

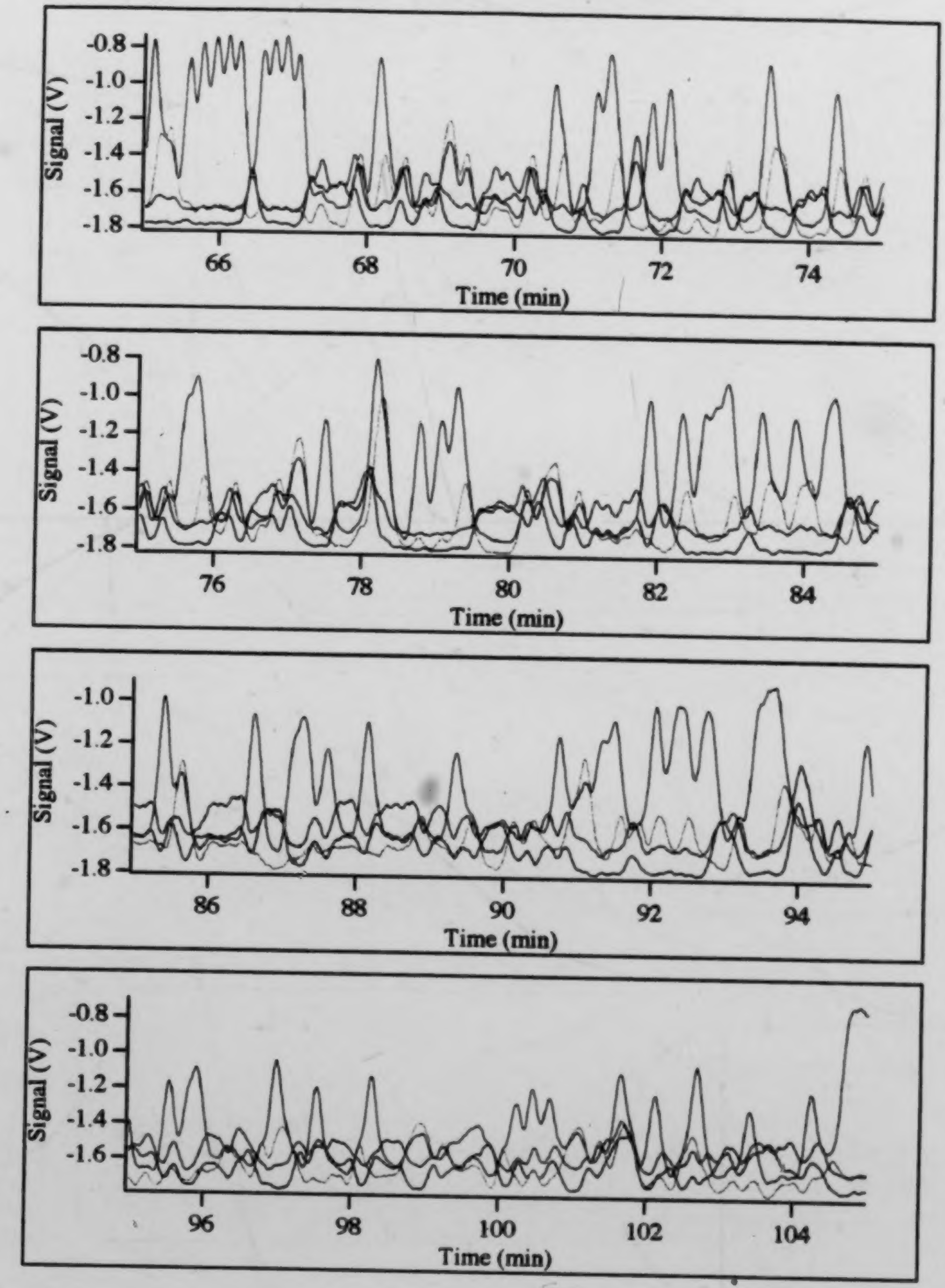

Capillary 10; File: 26/01/96#1

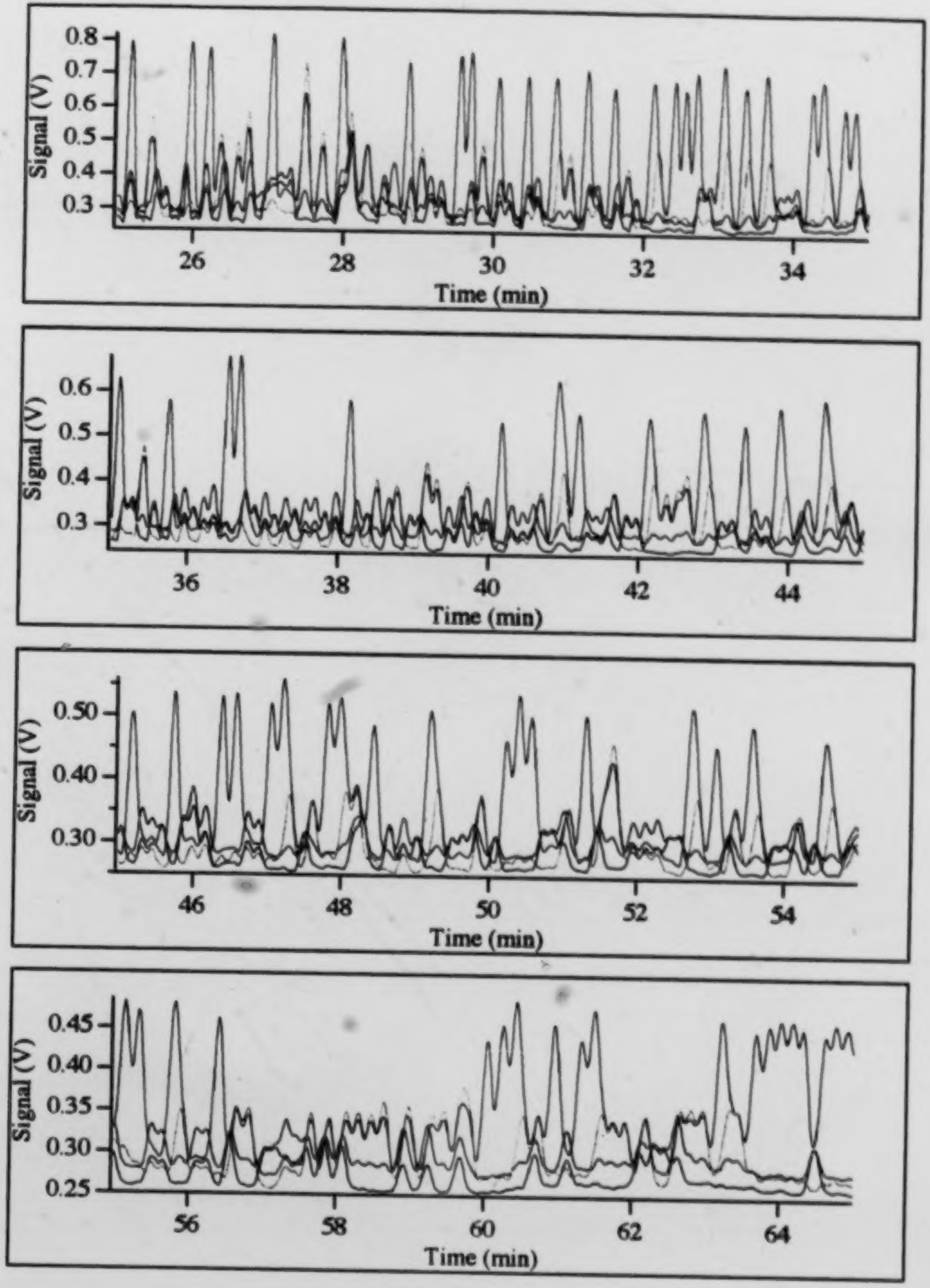

Capillary 10; File: 26/01/96#1

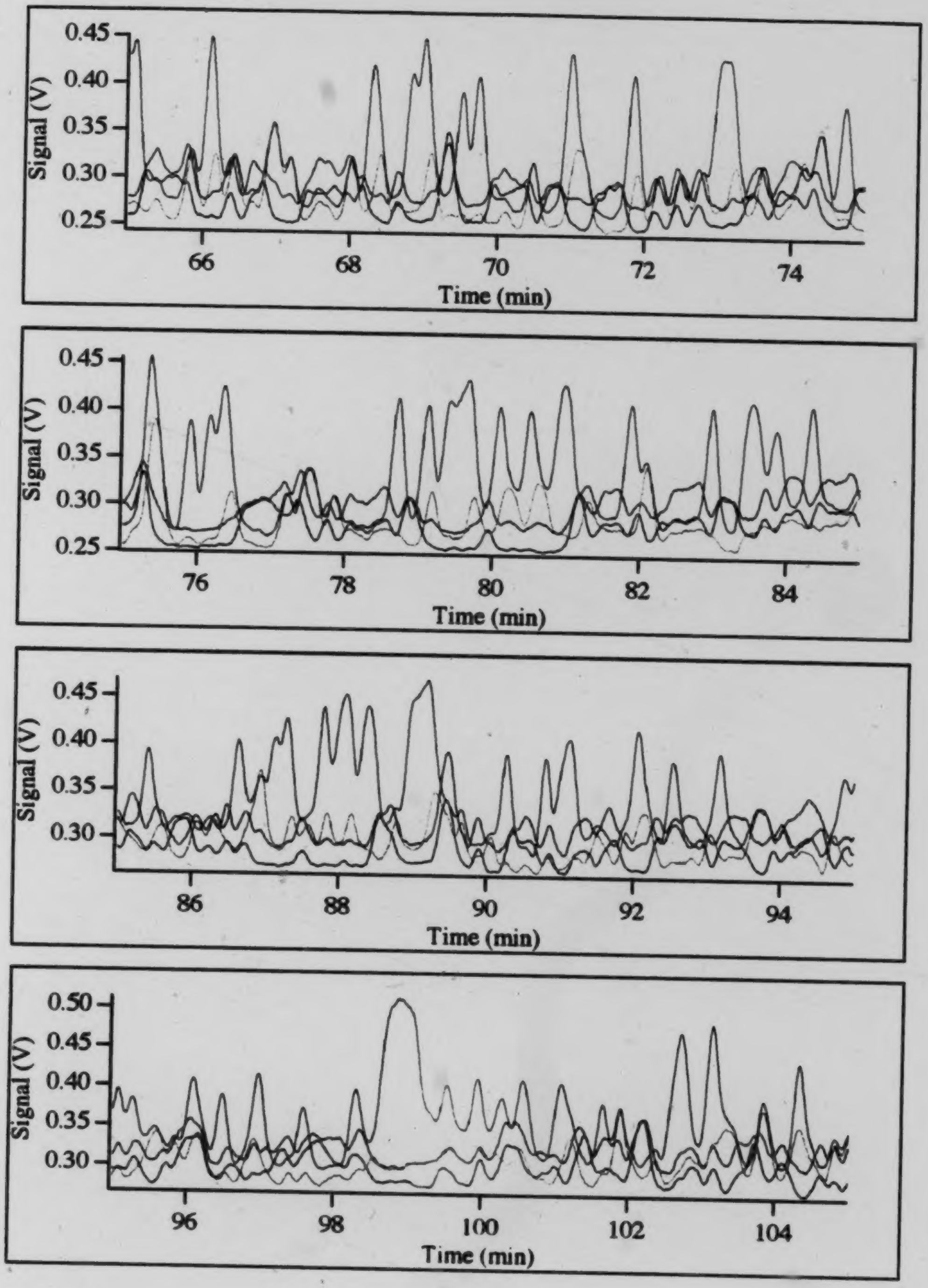

Capillary 11; File: 26/01/96#1

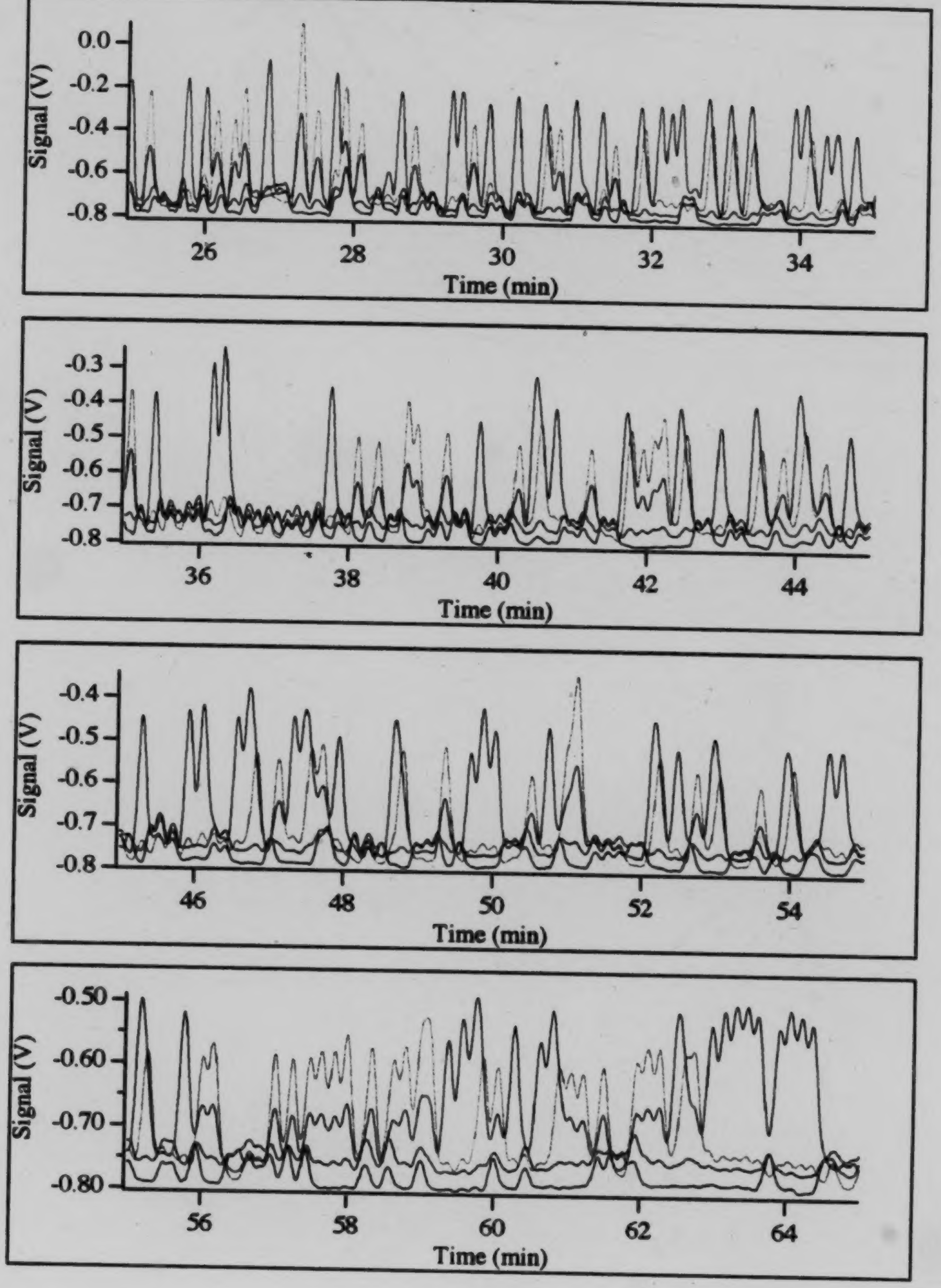

Capillary 11; File: 26/01/96#1

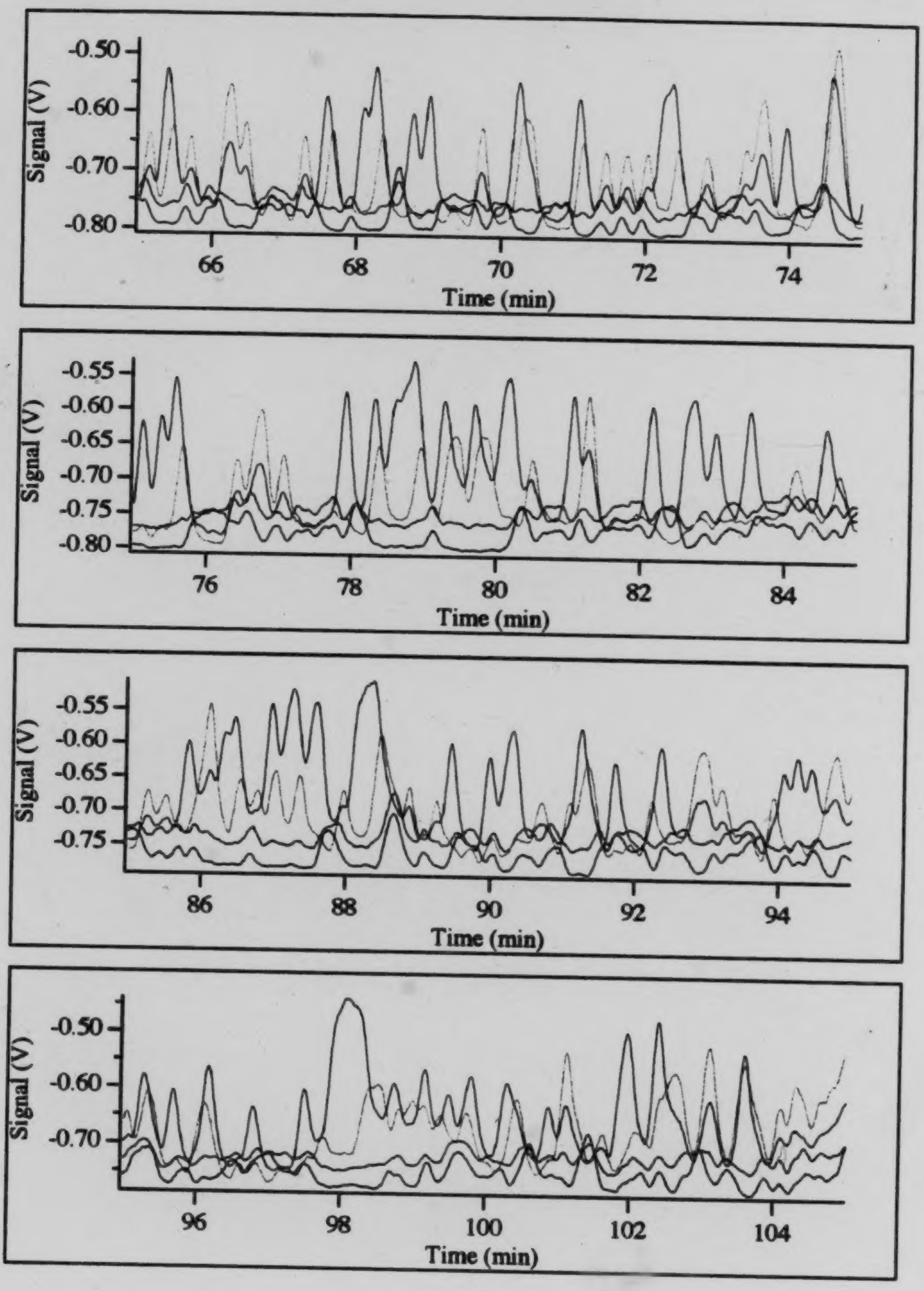

Capillary 12; File: 26/01/96#1

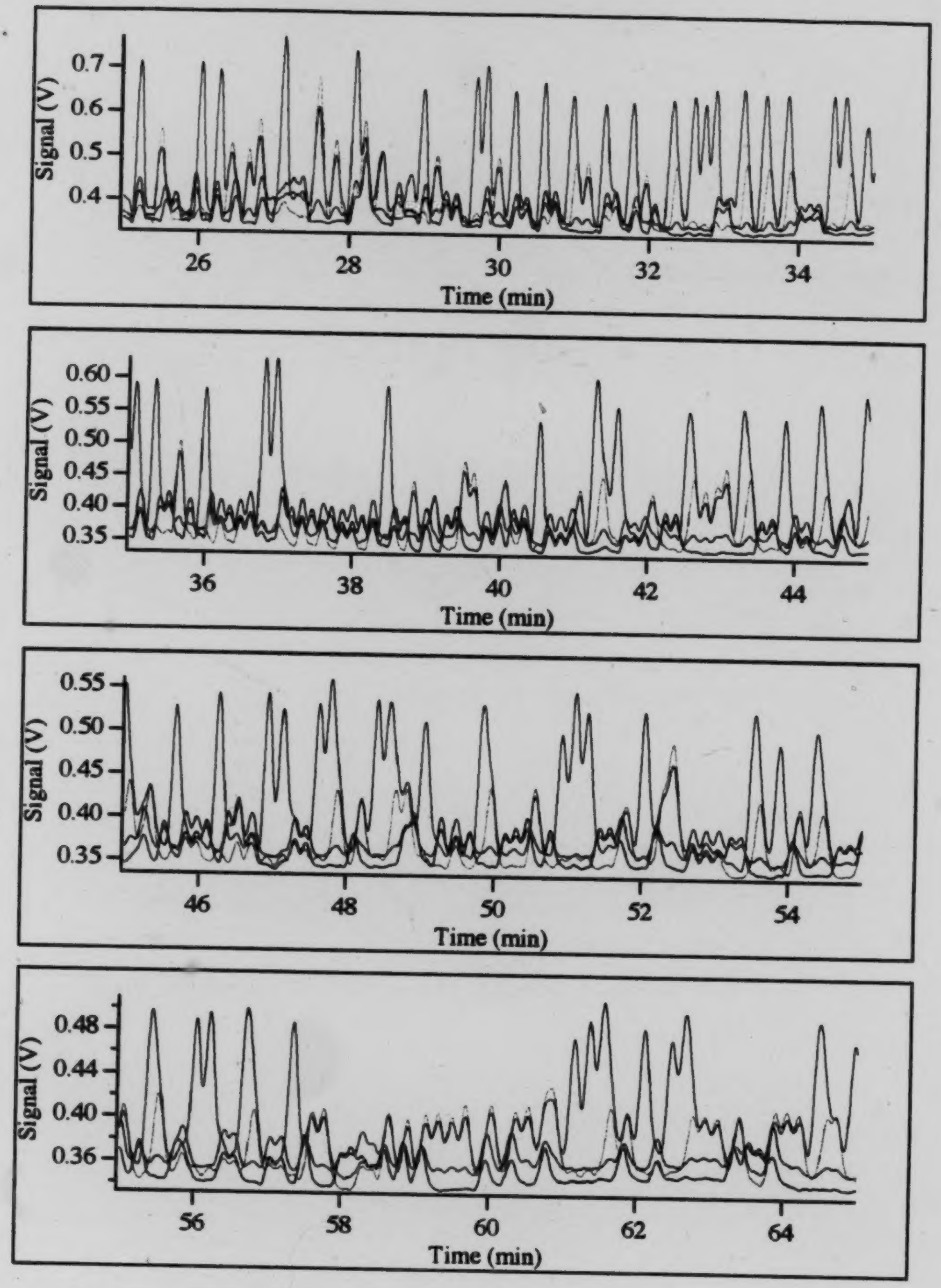

Capillary 12; File: 26/01/96#1

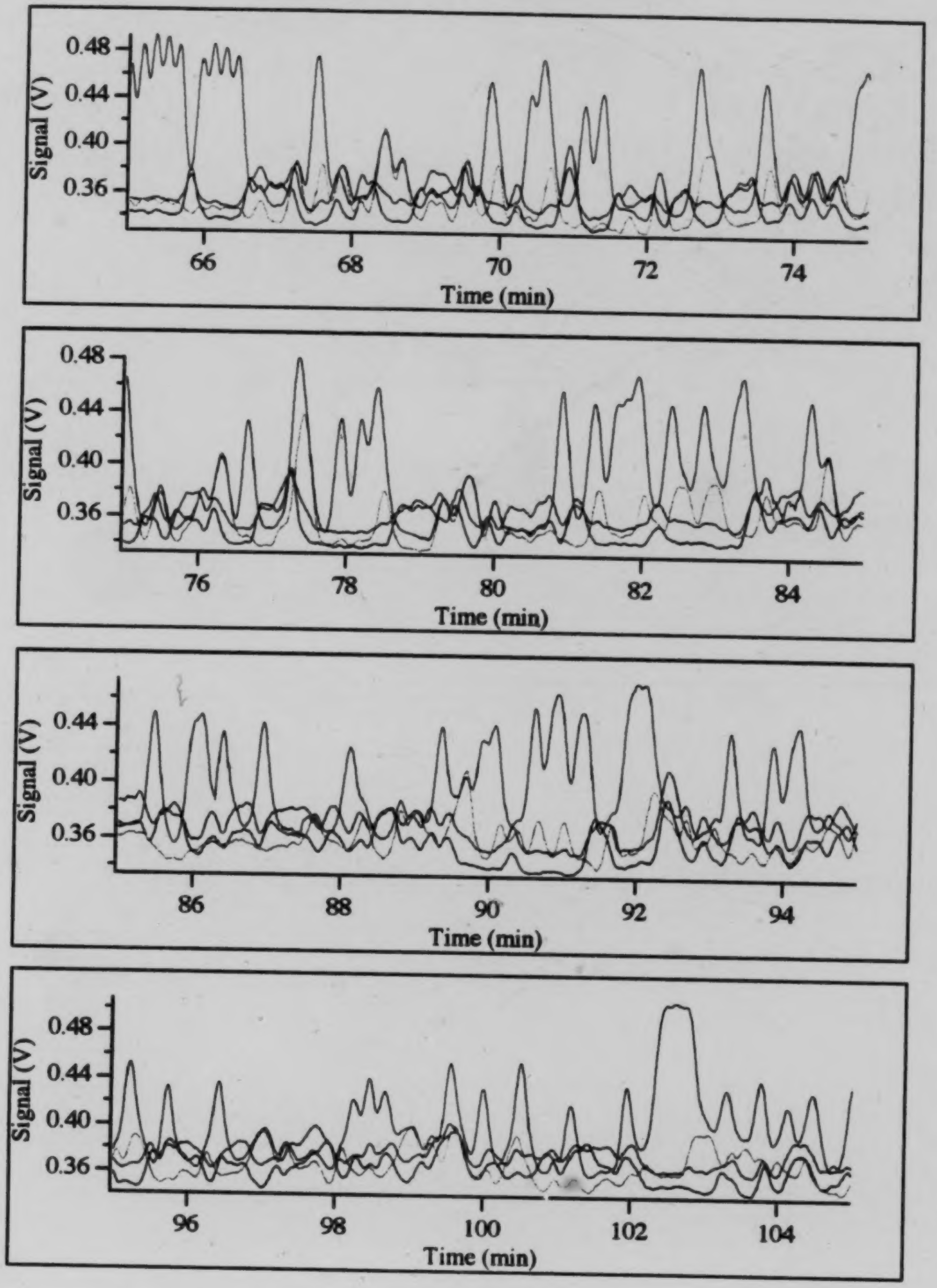

Capillary 13; File: 26/01/96#1

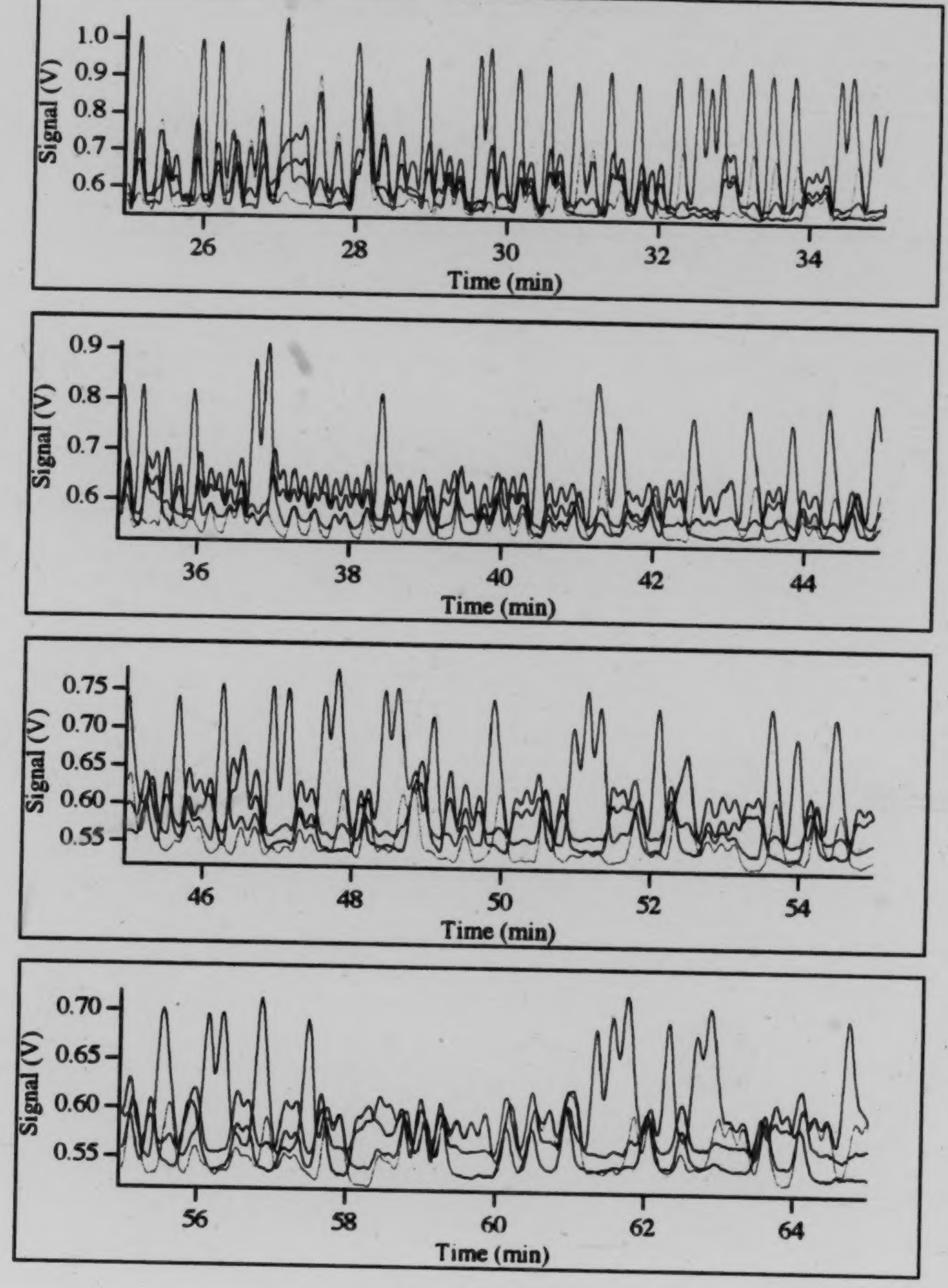

Capillary 13; File: 26/01/96#1

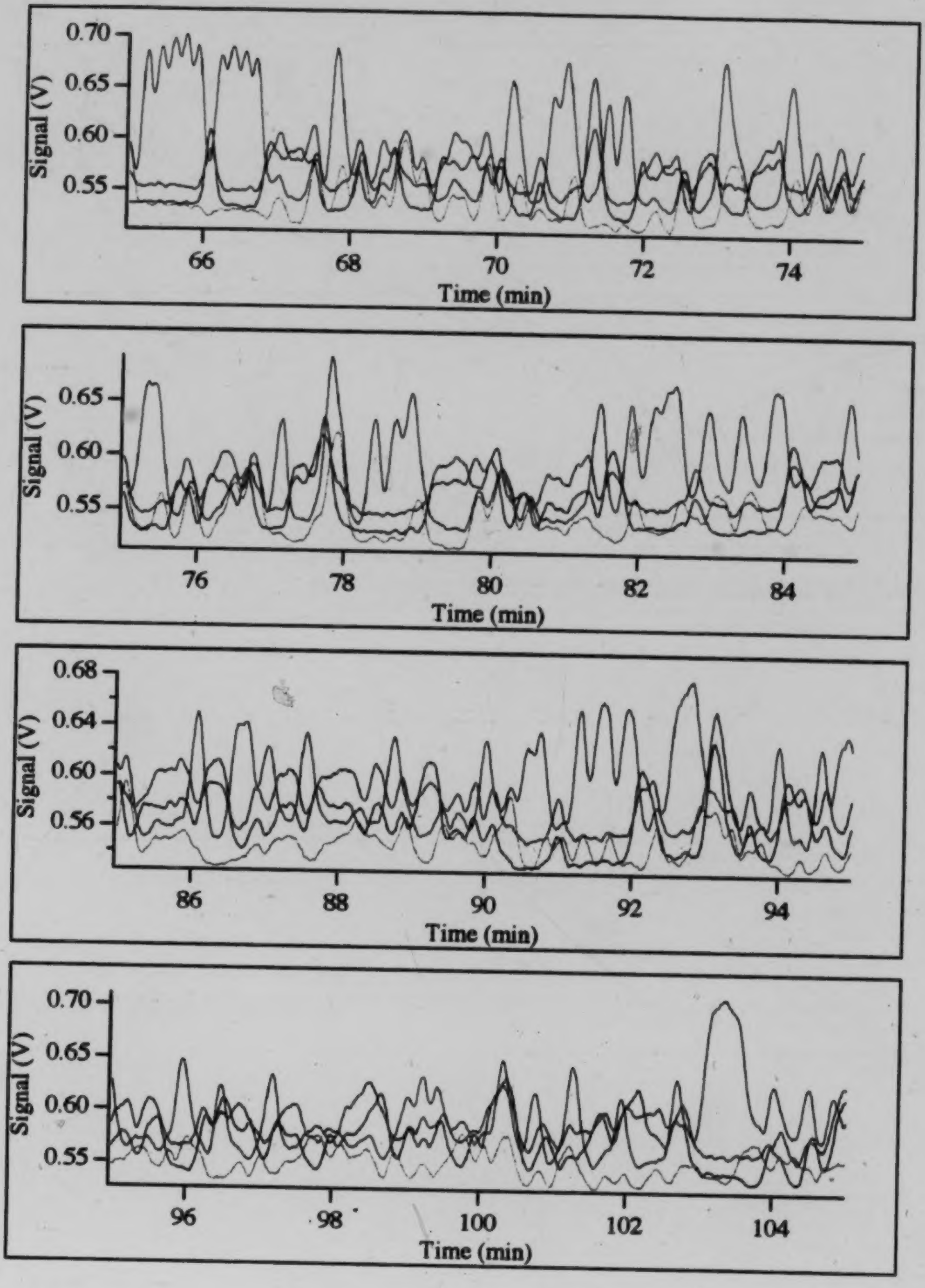

Capillary 14; File: 26/01/96#1

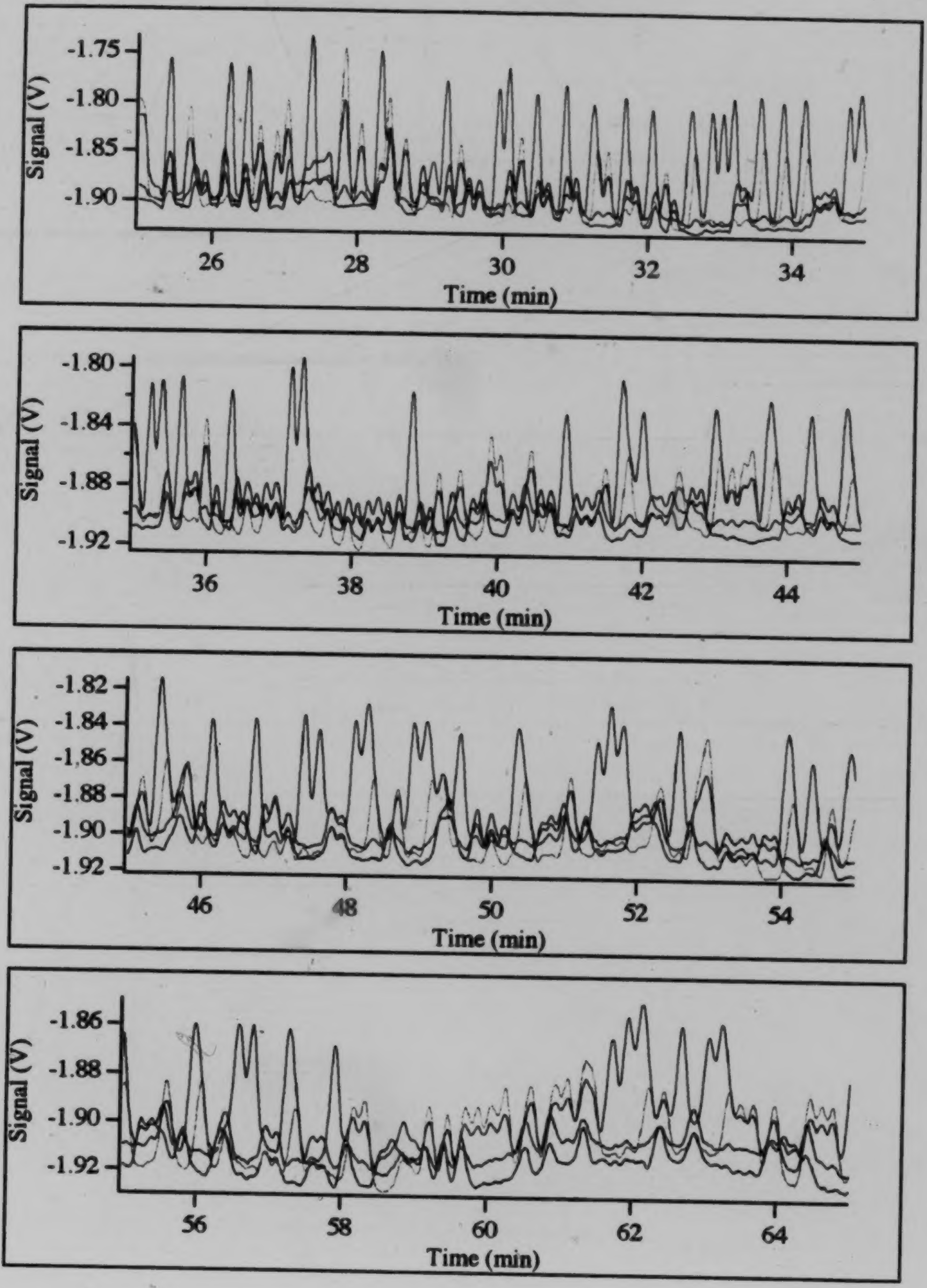

Capillary 14; File: 26/01/96#1

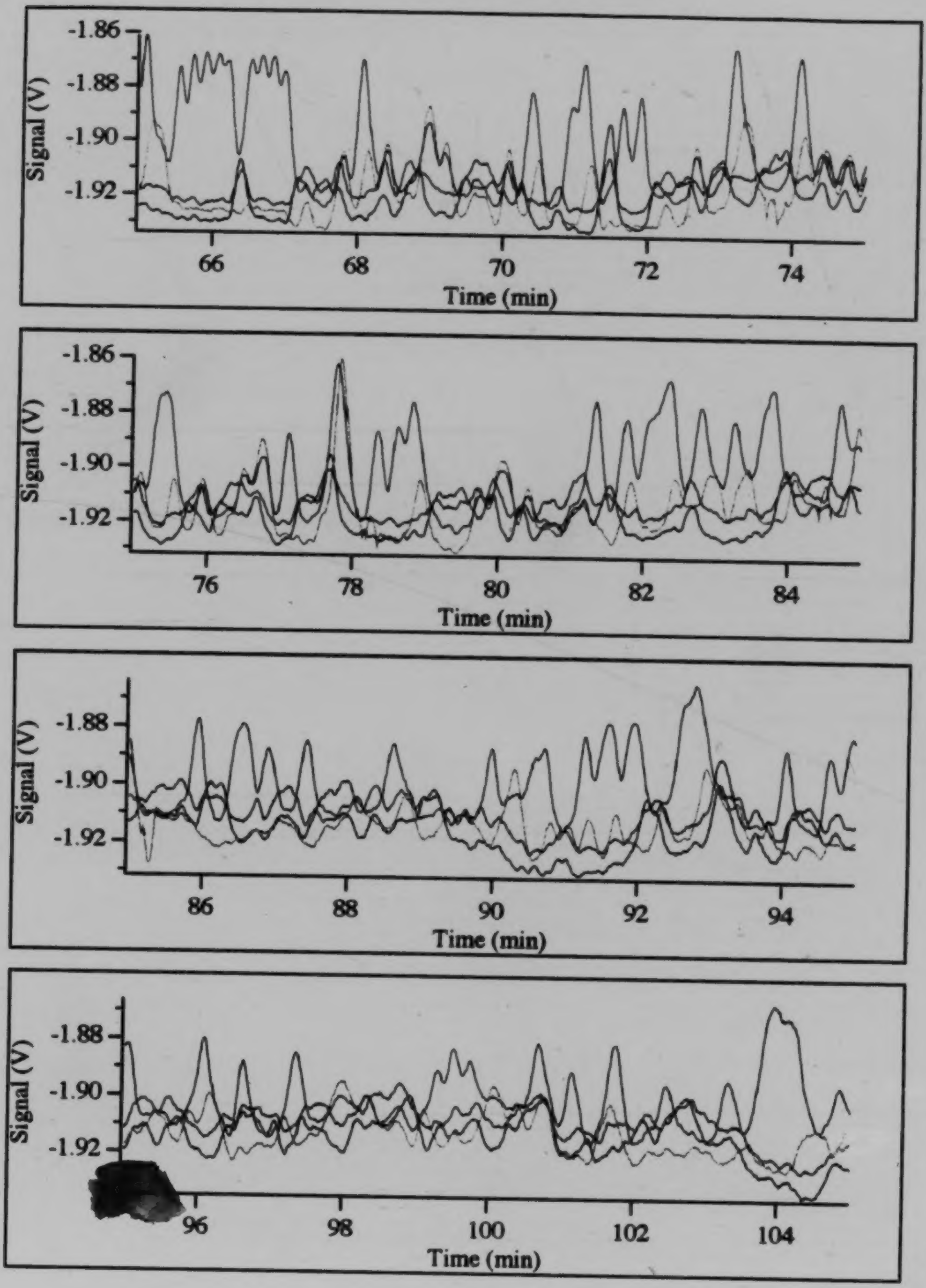

Capillary 15; File: 26/01/96#1

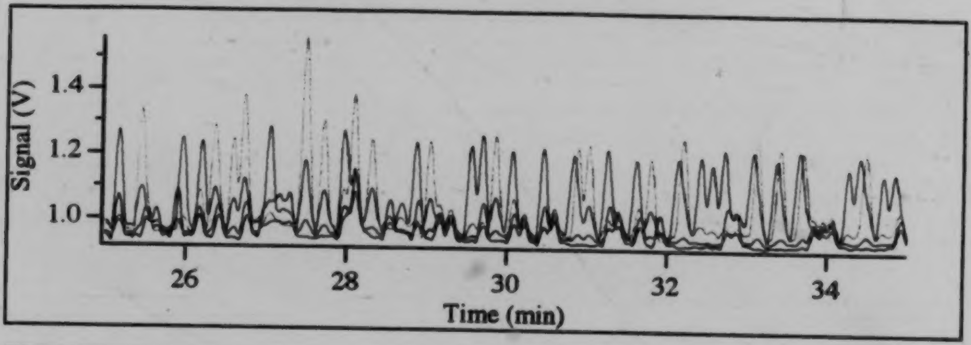

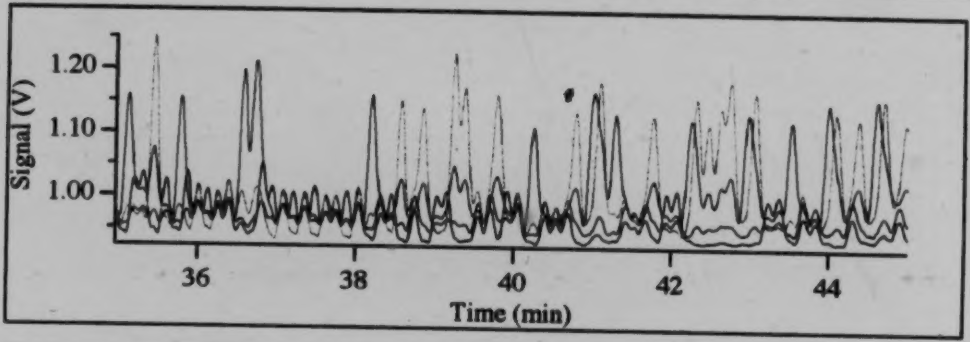

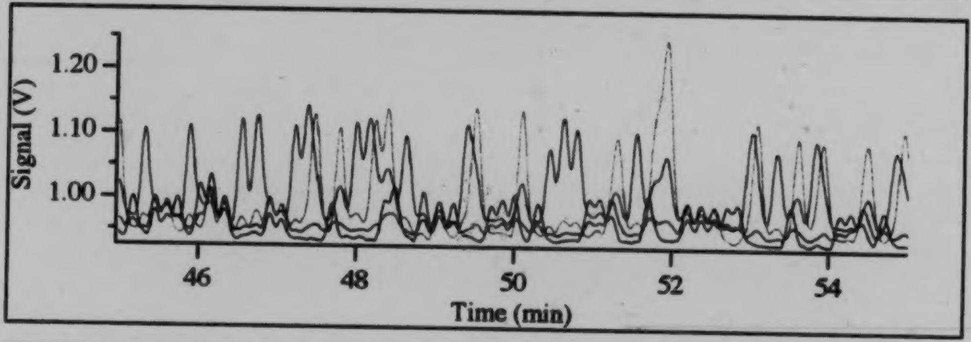

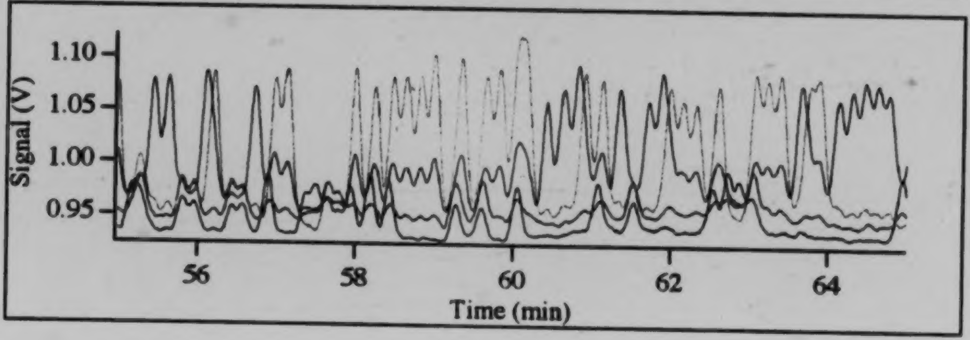

Capillary 15; File: 26/01/96#1

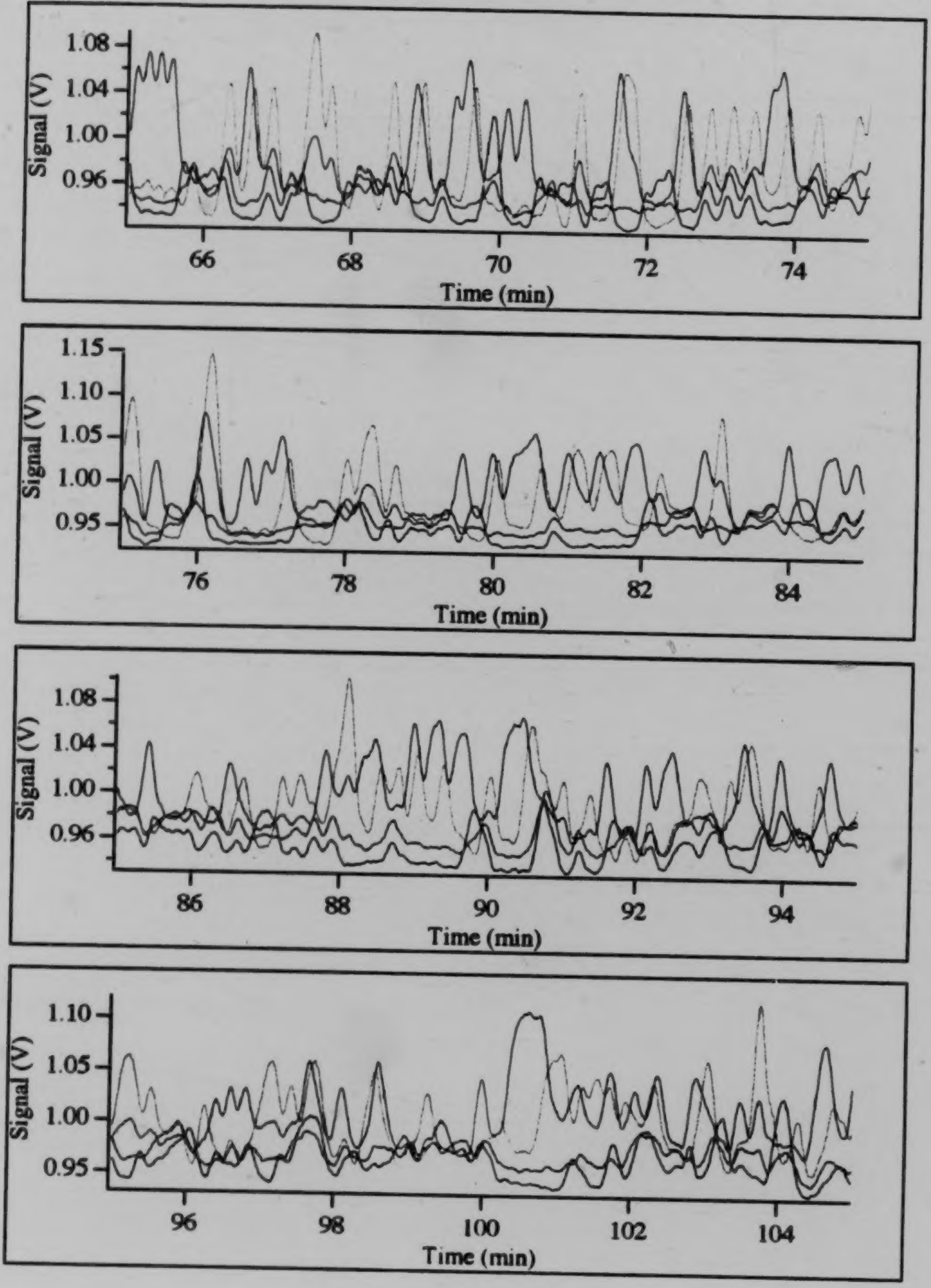

Capillary 16; File: 26/01/96#1

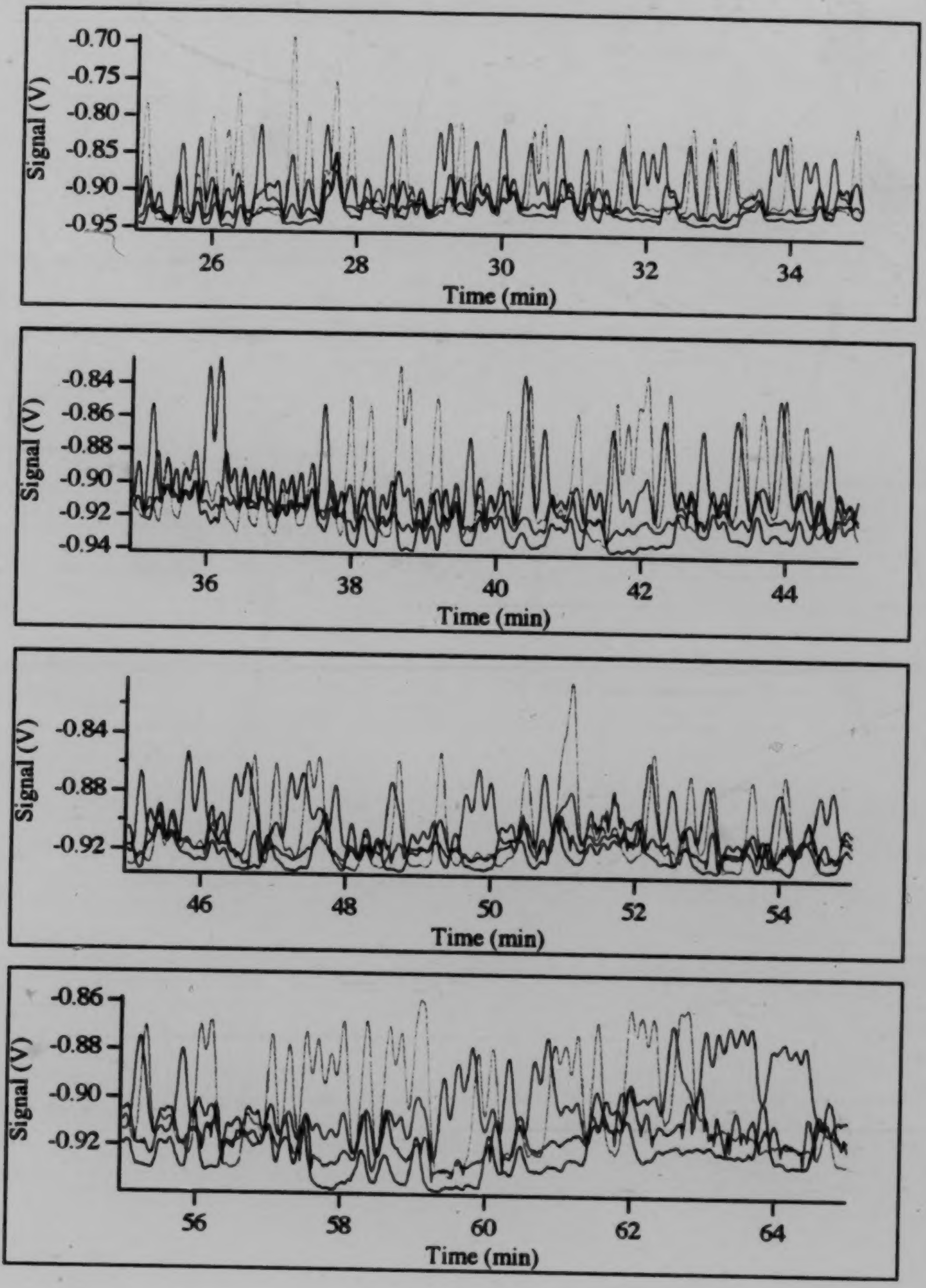

Capillary 16; File: 26/01/96#1

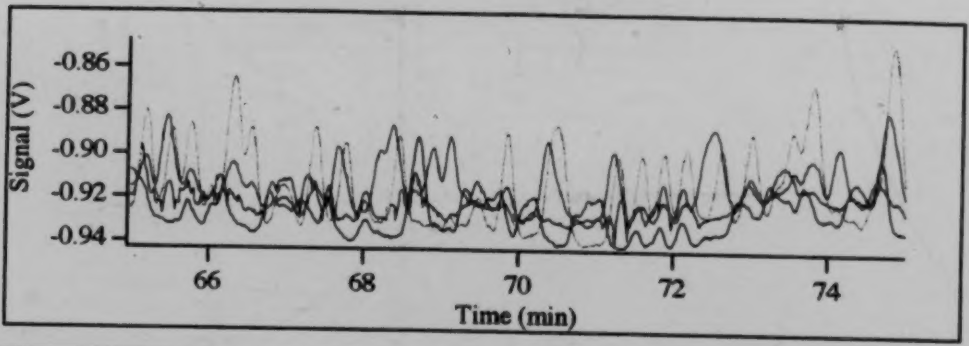

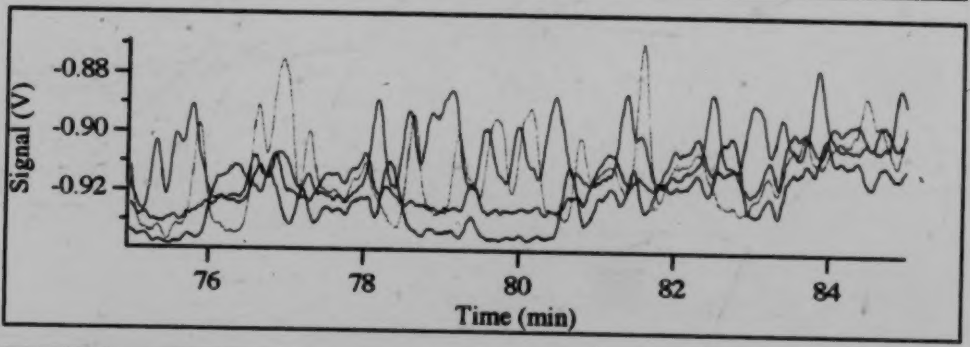

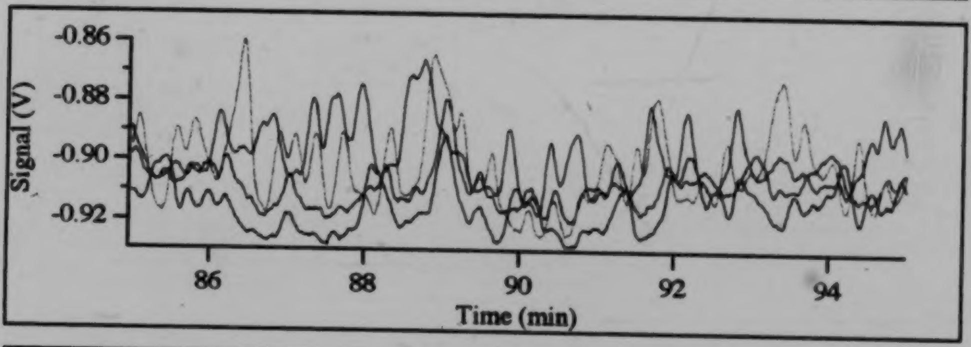

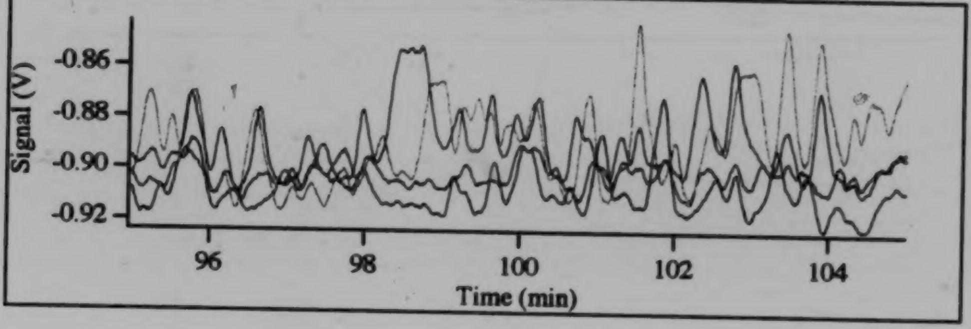

Appendix 2

DESIGNS FOR A MULTICAPILLARY SHEATH FLOW CUVETTE HOLDER

The purpose of the cuvette holder is to rigidly position the cuvette, guide the capillaries and sheath flow into the cuvette, allow "optical access" to the cuvette, and form the electrical connection to ground for the high voltage applied during an electrophoretic separation. The holder should prevent solution leakage from the cuvette, allow purging of bubbles in the sheath flow, allow the cuvette to be viewed on two sides with microscopes of short (~ 3 mm) working distances (optical axis of lenses perpendicular to capillary array plane), allow the laser beams to be incident on the cuvette at a right angle to the capillary axes and to the optical axis of the detection objective, and finally, afford some convenience during regular use. The cuvette holder detailed in this appendix was specifically designed to meet, and ostensibly does meet, these criteria. It should be noted that the design of this cuvette holder greatly benefited from Dr. Jian Zhong Zhang's descriptions of recurrent problems in the very different 5 capillary sheath flow cuvette holder, as well as from the creativity and very capable workmanship of Roman Lipiecki of this department's machine shop who built all four versions.

The sheath flow cuvette holder described accommodates cuvettes which are 7.2 mm across, namely cuvettes which contain 16 capillaries spaced 225 or 300 µm apart, or 32 capillaries spaced 150 or 160 µm apart. The three predecessors to this holder were very similar in concept to the one shown, except that the linear capillary array was not as wide for the 6, 8, and 16 capillary cuvettes spaced at 150 or 160µm. The other difference is that in this holder, the *slot pieces* attach to the back plate, versus the *top piece* in earlier versions. This modification came about to allow the capillaries to be changed from one DNA sequencing run to the next without disturbing the optical alignment of the cuvette: presently, the top piece is detached from the slot pieces, and the capillaries are changed (the cuvette position remains intact), whereas previously the bottom piece was lowered, the cuvette was removed, and the capillaries were changed.

There are five main parts to the cuvette holder; their relation to each other may be seen in the front and side views of the assembled cuvette holder. When integrated into the multicapillary instrument, the detection imaging objective approaches from the front, the experimentalist observes the cuvette through the viewing microscope from the back, and the lasers are incident from the left hand side. Sheath flow buffer enters through one of the top piece's horizontal tubes (bubbles may be flushed out the other), passes through the cuvette and exits from the bottom piece. Capillaries enter through the top piece, pass through the slot pieces and into the cuvette; an epoxy seal is made between the capillaries and a short length of Teflon tubing connected to the top piece's vertical tube. A wire is connected from the back brace to the optical table to establish electrical ground.

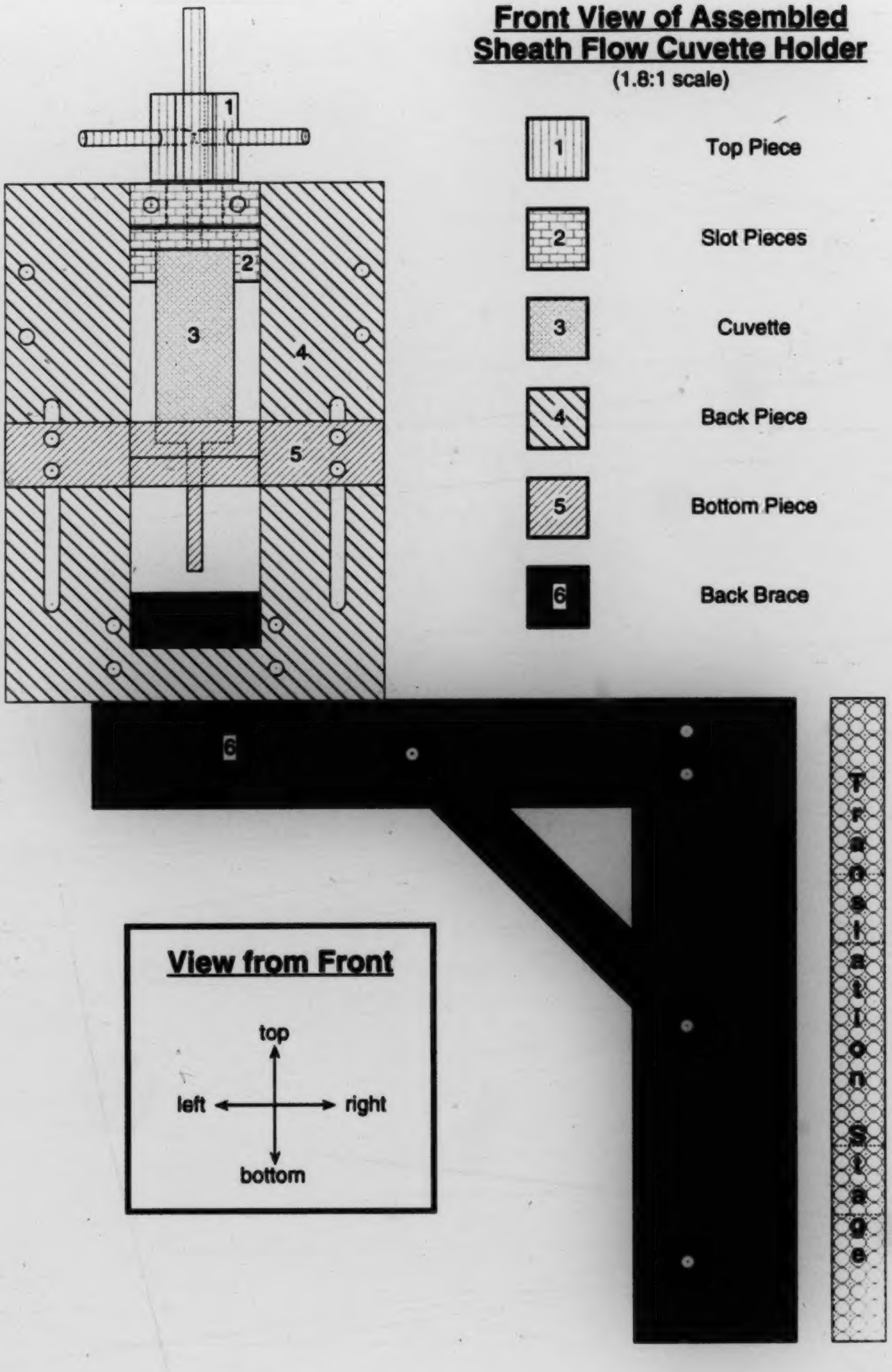

Front View of Assembled Sheath Flow Cuvette Holder

(1.8:1 scale)

1
2
3
4
5
6
1 Top Piece
2 Slot Pieces
3 Cuvette
4 Back Piece
5 Bottom Piece
6 Back Brace
Translation Stage
View from Front
top
left
right
bottom

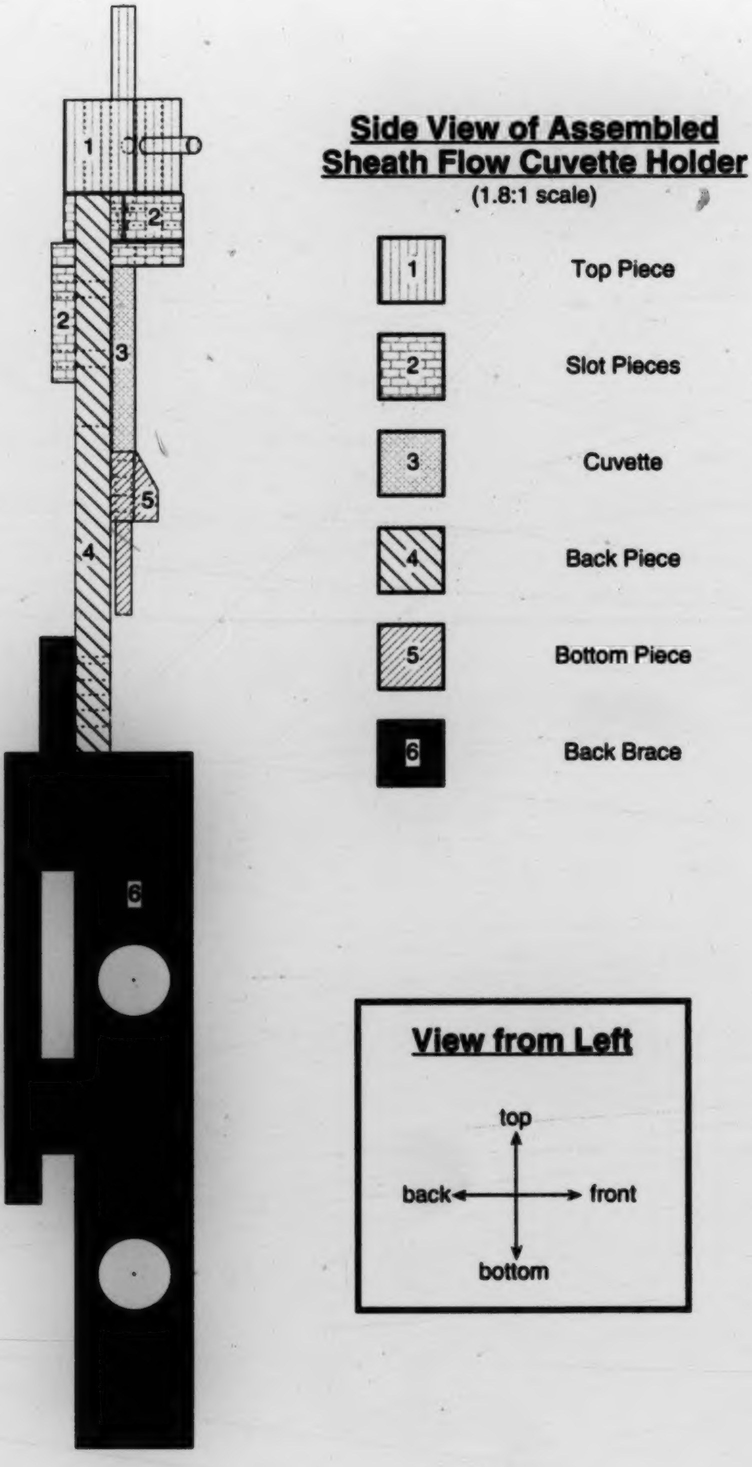

Side View of Assembled Sheath Flow Cuvette Holder
(1.8:1 scale)

1
2
2
3
4
5
6
1 Top Piece
2 Slot Pieces
3 Cuvette
4 Back Piece
5 Bottom Piece
6 Back Brace
View from Left
top
back
front
bottom

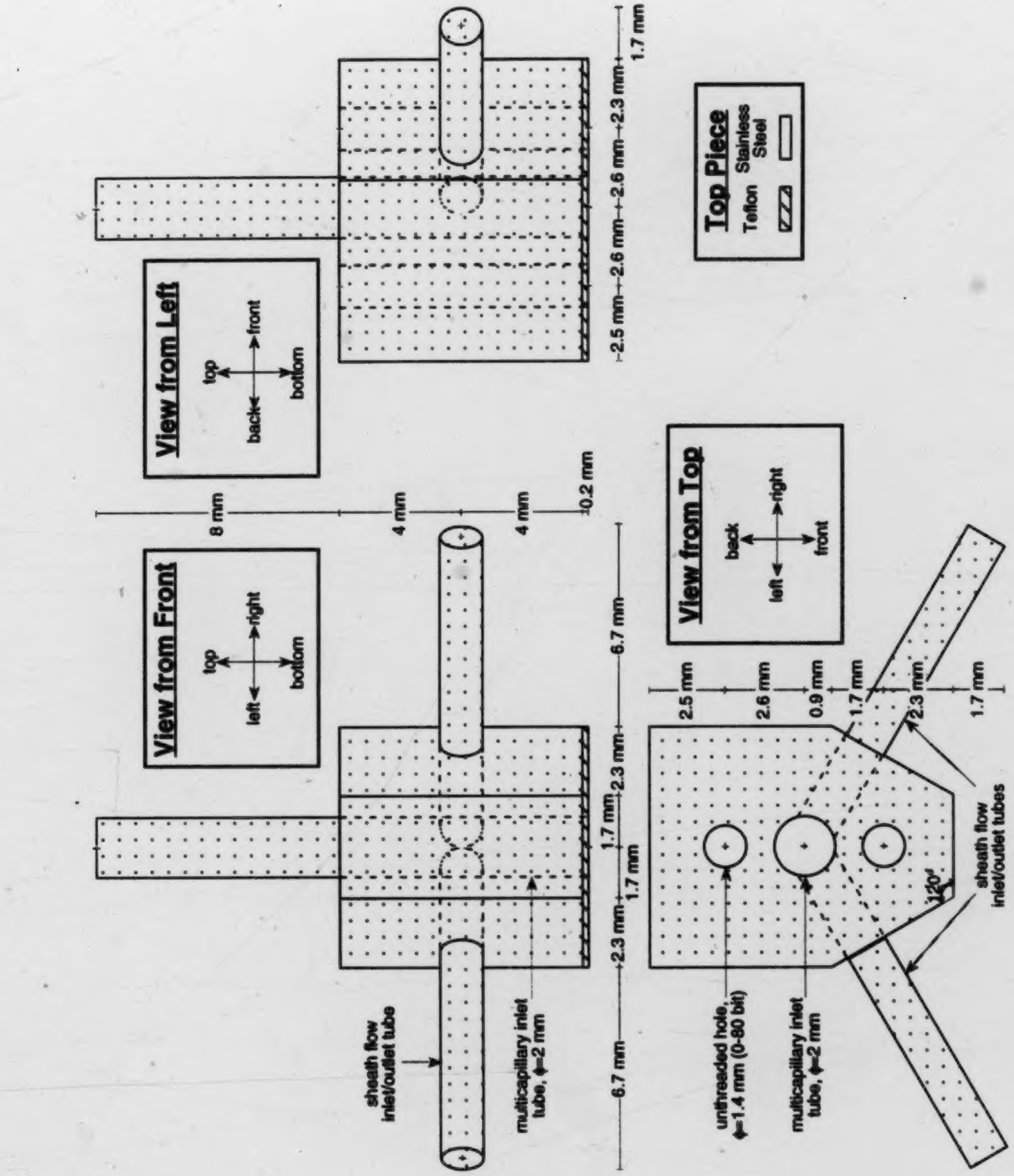
View from Front
top
left
right
bottom
View from Left
top
back
front
bottom
View from Top
back
left
right
front
Top Piece
Teflon ▨
Stainless Steel ☐
8 mm
4 mm
4 mm
0.2 mm
6.7 mm
2.3 mm
1.7 mm
1.7 mm
2.3 mm
6.7 mm
2.5 mm
2.6 mm
2.6 mm
2.3 mm
1.7 mm
2.5 mm
2.6 mm
0.9 mm
1.7 mm
2.3 mm
1.7 mm
120°
sheath flow inlet/outlet tube
multicapillary inlet tube, ϕ=2 mm
unthreaded hole, ϕ=1.4 mm (0-80 bit)
multicapillary inlet tube, ϕ=2 mm
sheath flow inlet/outlet tubes

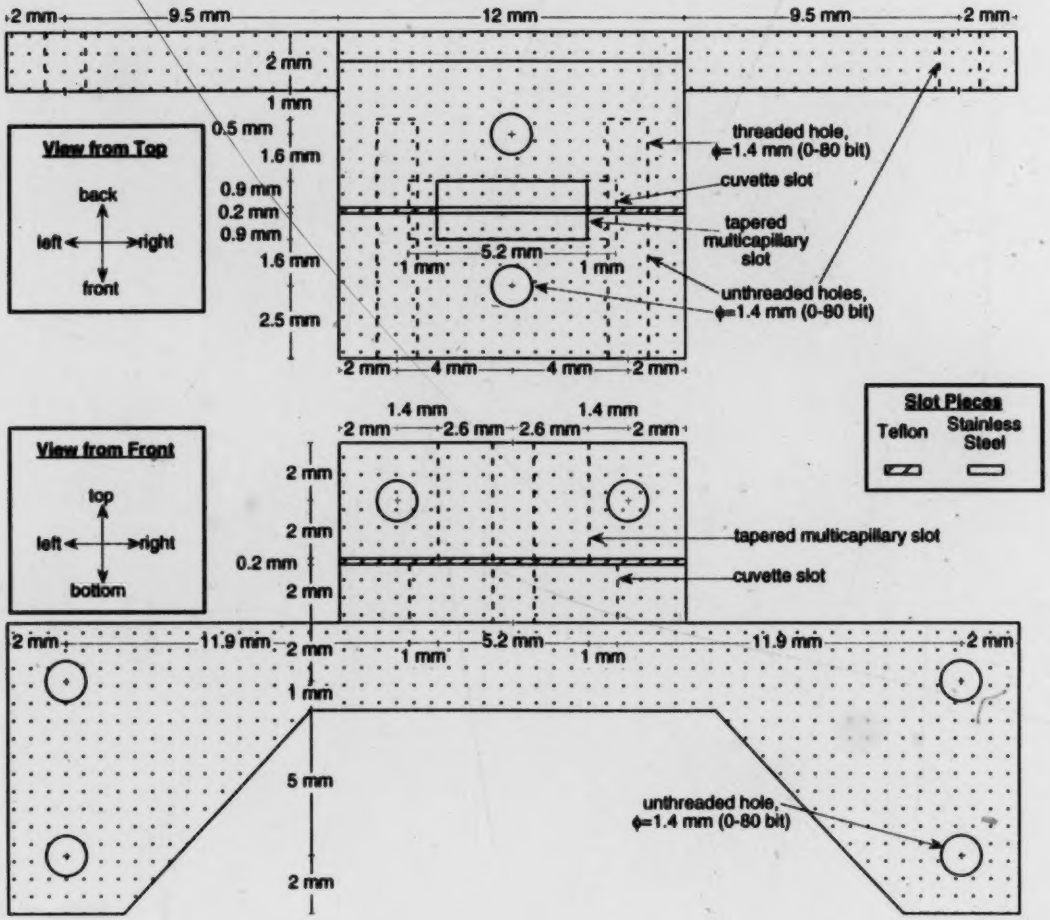
2 mm
9.5 mm
12 mm
9.5 mm
2 mm
2 mm
1 mm
0.5 mm
1.6 mm
0.9 mm
0.2 mm
0.9 mm
1.6 mm
2.5 mm
View from Top
back
left
right
front
threaded hole,
ϕ=1.4 mm (0-80 bit)
cuvette slot
tapered
multicapillary
slot
unthreaded holes,
ϕ=1.4 mm (0-80 bit)
5.2 mm
1 mm
1 mm
2 mm
4 mm
4 mm
2 mm
Slot Pieces
Teflon
Stainless Steel
1.4 mm
1.4 mm
2 mm
2.6 mm
2.6 mm
2 mm
View from Front
top
left
right
bottom
2 mm
2 mm
0.2 mm
2 mm
tapered multicapillary slot
cuvette slot
2 mm
11.9 mm
2 mm
5.2 mm
11.9 mm
2 mm
1 mm
1 mm
1 mm
5 mm
2 mm
unthreaded hole,
ϕ=1.4 mm (0-80 bit)

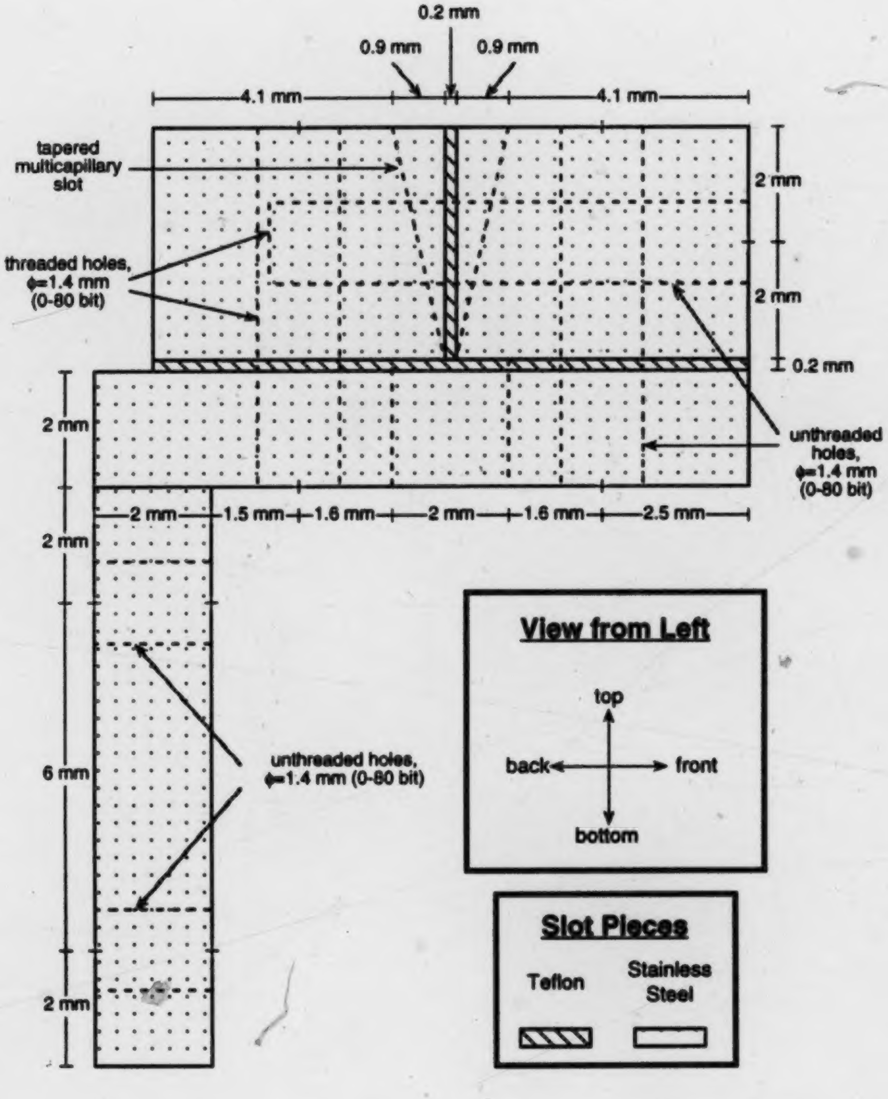
0.2 mm
0.9 mm
0.9 mm
4.1 mm
4.1 mm
tapered multicapillary slot
threaded holes, ϕ=1.4 mm (0-80 bit)
2 mm
2 mm
0.2 mm
2 mm
unthreaded holes, ϕ=1.4 mm (0-80 bit)
2 mm
1.5 mm
1.6 mm
2 mm
1.6 mm
2.5 mm
2 mm
6 mm
2 mm
unthreaded holes, ϕ=1.4 mm (0-80 bit)
View from Left
top
back
front
bottom
Slot Pieces
Teflon
Stainless Steel

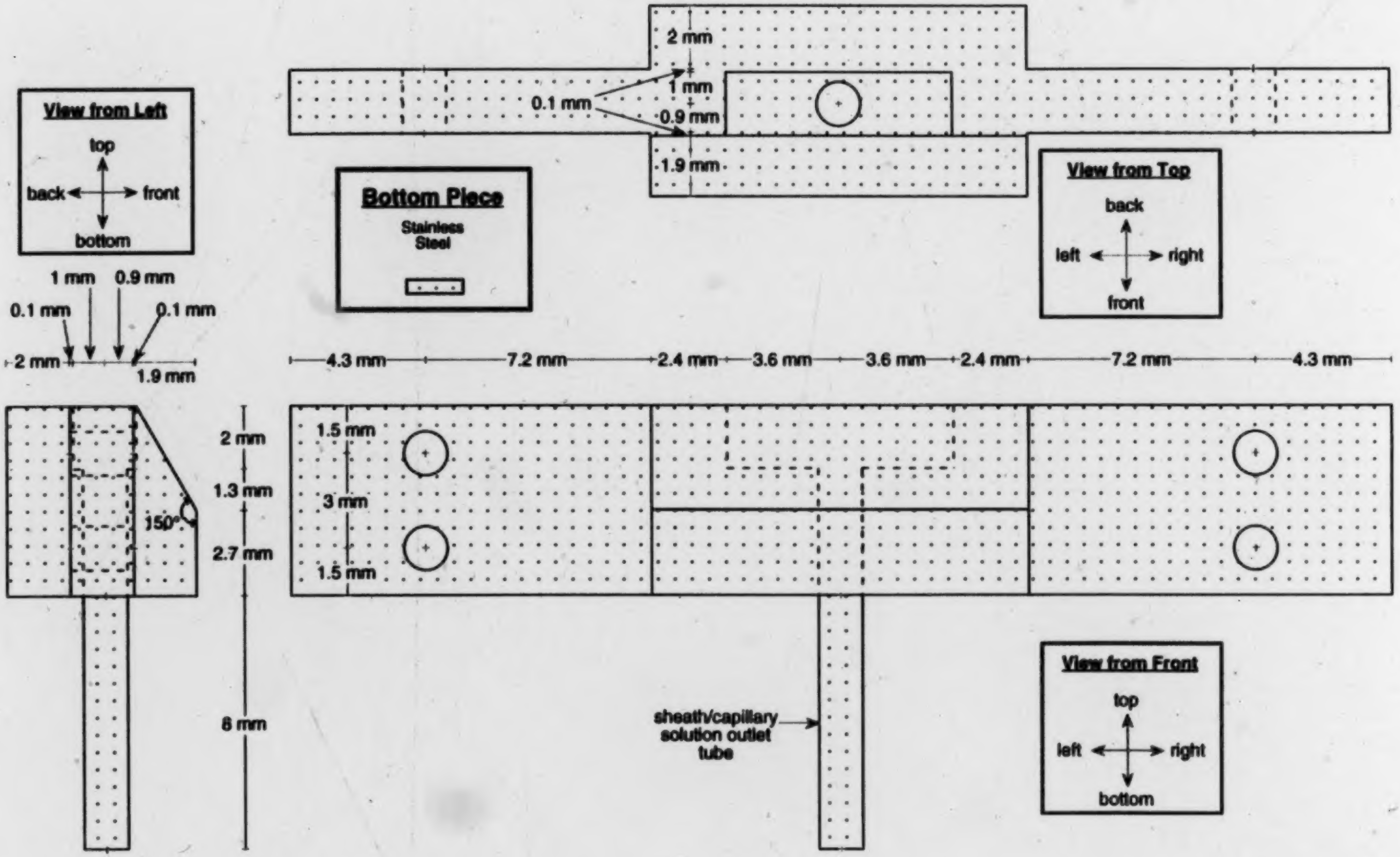
View from Left
top
back
front
bottom
1 mm
0.9 mm
0.1 mm
0.1 mm
2 mm
1.9 mm
150°
2 mm
1.3 mm
2.7 mm
8 mm
Bottom Piece
Stainless Steel
2 mm
1 mm
0.1 mm
0.9 mm
1.9 mm
View from Top
back
left
right
front
4.3 mm
7.2 mm
2.4 mm
3.6 mm
3.6 mm
2.4 mm
7.2 mm
4.3 mm
1.5 mm
3 mm
1.5 mm
sheath/capillary solution outlet tube
View from Front
top
left
right
bottom

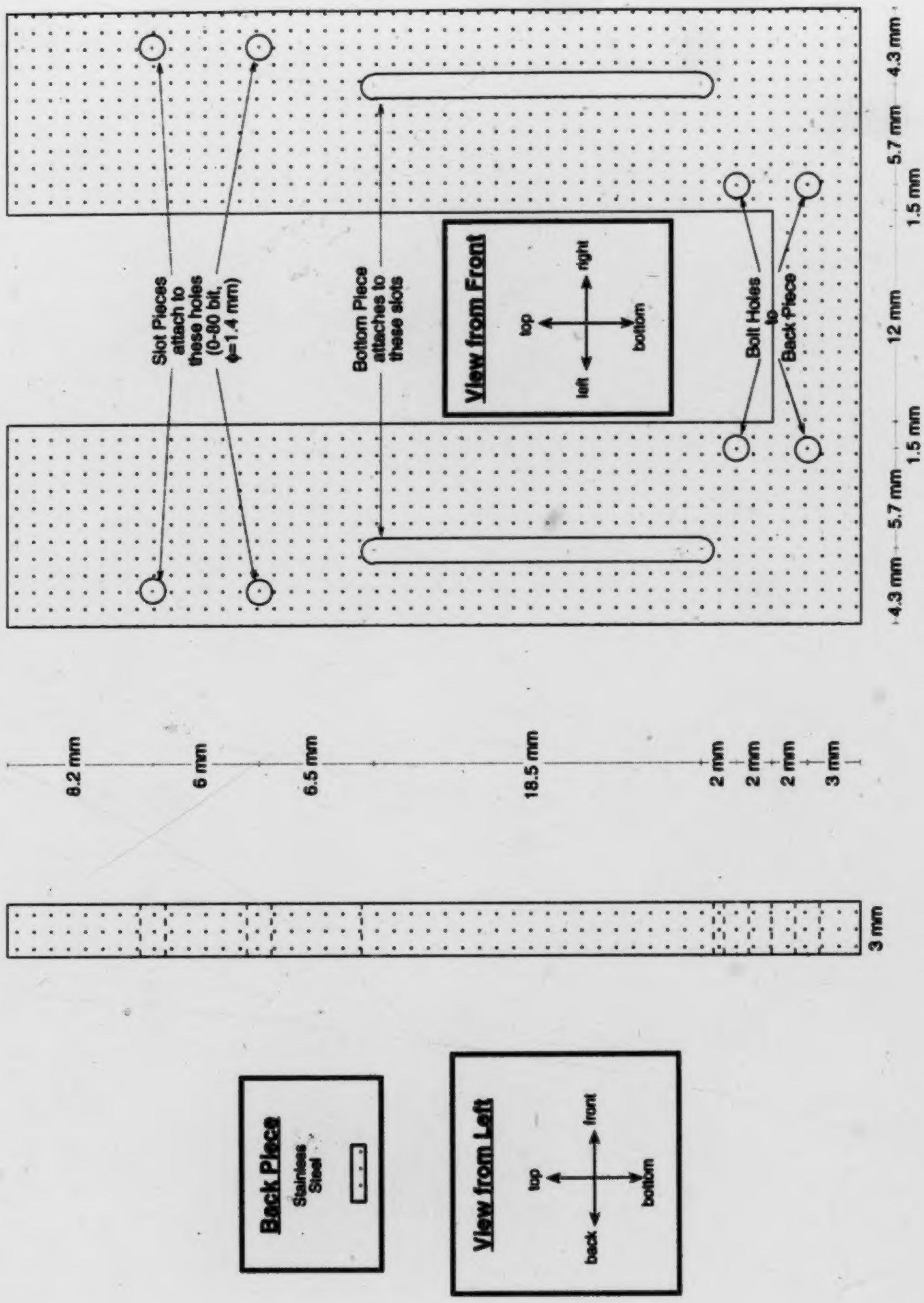
Slot Pieces attach to these holes (0-80 bit, ϕ=1.4 mm)
Bottom Piece attaches to these slots
View from Front
top
left
right
bottom
Bolt Holes to Back Piece
4.3 mm
5.7 mm
1.5 mm
12 mm
1.5 mm
5.7 mm
4.3 mm
8.2 mm
6 mm
6.5 mm
18.5 mm
2 mm
2 mm
2 mm
3 mm
3 mm
Back Piece
Stainless Steel
View from Left
top
back
front
bottom

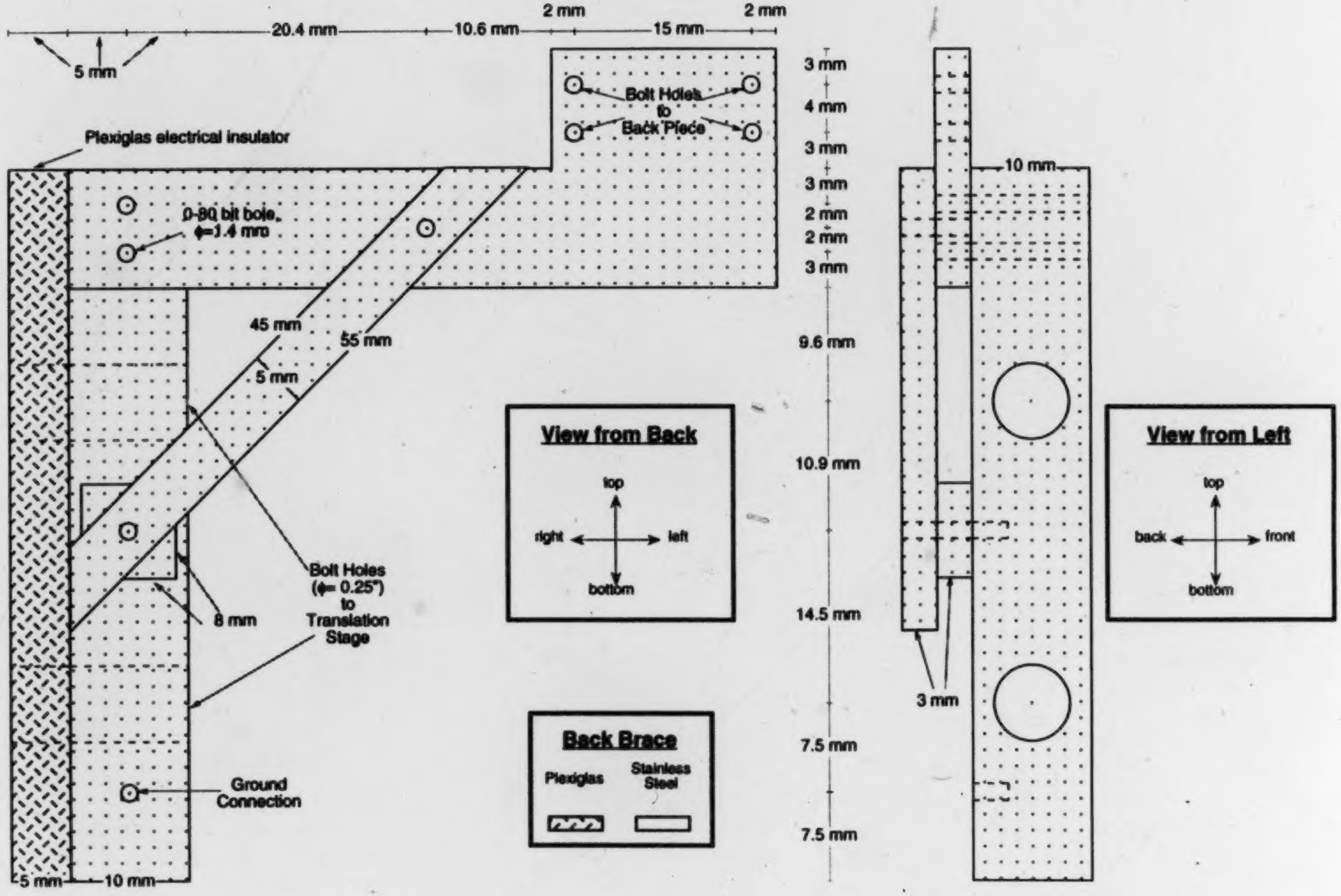
20.4 mm
10.6 mm
2 mm
15 mm
2 mm
5 mm
Plexiglas electrical insulator
Bolt Holes to Back Piece
0-80 bit hole, ϕ=1.4 mm
45 mm
55 mm
5 mm
8 mm
Bolt Holes (ϕ= 0.25") to Translation Stage
Ground Connection
5 mm
10 mm
3 mm
4 mm
3 mm
3 mm
2 mm
2 mm
3 mm
9.6 mm
10.9 mm
14.5 mm
7.5 mm
7.5 mm
10 mm
3 mm
View from Back
top
right
left
bottom
View from Left
top
back
front
bottom
Back Brace
Plexiglas
Stainless Steel